Latent Heat Fluxes Through Nano-engineered Porous Materials

by

Matthew J. Traum

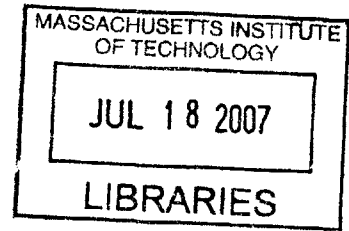M.S., Mechanical Engineering (2003)
Massachusetts Institute of Technology

Submitted to the Department of Mechanical Engineering in
Partial Fulfillment of the Requirements for the Degree of
Doctor of Philosophy in Mechanical Engineering

at the

Massachusetts Institute of Technology

June 2007

Signature of Author..................................... ....
Department of Mechanical Engineering
May 4, 2007

Certified by............................... ....
William A. Peters
Executive Director, MIT Institute for Soldier Nanotechnologies
Thesis Supervisor

Certified by.....................
Edwin L. Thomas
Morris Cohen Professor of Materials Science and Engineering
Thesis Supervisor

Accepted by...........................
Lallit Anand
Chairman, Department Committee on Graduate Students

Latent Heat Fluxes Through Nano-engineered Porous Materials

by

Matthew J. Traum

ABSTRACT

Micro- and nano-scale truss architectures provide mechanical strength, light weight, and breatheability in polymer barriers. Liquid evaporation and transport of resulting vapor through truss voids (pores) cools surfaces covered by the barriers, suggesting the possibility for simultaneous protection of humans from mechanical and thermal stresses. Design of real systems employing this technique requires quantitative understanding of vapor transport within the truss pores and accompanying latent heat lift under ambient temperature and pressure. One application is desert Soldier protection.

Need exists to clarify whether smaller pore diameters affect surface cooling and water vapor transport owing to fluid rarefaction or surface interactions. Contrasting previous studies where pressure within capillaries of fixed diameter was modulated, in this thesis Knudsen Number (Kn) was systematically varied by changing pore diameter at constant pressure (one atmosphere). Cooling efficacy was assessed for porous membranes with pore diameters ranging from 39 to 14,400 nm, varied in regular increments. Evaporative cooling experiments simulated combined daytime desert solar and metabolic thermal load on humans by heating an evaporation chamber partially filled with liquid water and capped with a porous membrane. Hot, dry gas was swept over the membrane, simulating desert ambient conditions. By continuously weighing the entire evaporation apparatus, intrinsic pore diffusion coefficients for dilute water vapor in air were deduced for each membrane by correcting for upstream and downstream boundary layer mass transfer resistances. Pore diameter impact on evaporative cooling of an underlying surface by water vapor transport across two types of porous polymer membranes with micro/nano-scale truss architecture was quantified. This research showed that transition diffusion regime theory predicted observed transport rates to better than ± 35% for pore diameters between 14,400 nm and 60 nm (0.01 < Kn < 3). Despite low membrane porosity, substantial Fractional Accomplished Cooling (up to 60% maximum achievable) was demonstrated via latent heat transport. The absolute magnitude of achieved surface cooling was 3.7 K to 14.0 K. An engineering design correlation was developed linking latent heat transport at various Knudsen Numbers (pore diameters) to evaporative cooling efficacy. Results of this research inform design of porous mechanical barriers that permit evaporative cooling of underlying surfaces.

Thesis Supervisor: William A. Peters

Title: Executive Director, MIT Institute for Soldier Nanotechnologies

Thesis Supervisor: Edwin L. Thomas

Title: Morris Cohen Professor of Materials Science and Engineering

Biographical Note

Matthew J. Traum is a researcher at MIT's Institute for Soldier Nanotechnologies (ISN). He has been a doctoral candidate in MIT's Department of Mechanical Engineering since June 2003. Traum earned his master's degree in mechanical engineering from MIT in 2003 through MIT's Cryogenic Engineering Laboratory where he focused on the development of a miniaturized Collins cycle cryocooler. Traum graduated Cum Laude from The Henry Samueli School of Engineering at the University of California, Irvine in June 2001. He holds a B.S. in mechanical engineering and a B.S. in aerospace engineering from UC Irvine; in addition, he is the recipient of a minor in Women's Studies. Traum also attended the University of Bristol, UK as a non-matriculating visiting scholar where he completed an M.Eng thesis in the Department of Aerospace Engineering studying low-speed autogyro pitch instability. Upon completing his MIT doctoral degree, Traum will join the faculty of the Mechanical and Energy Engineering Department at the University of North Texas as an assistant professor.

Matthew J. Traum is a member of Phi Beta Kappa national honor society, Tau Beta Pi national engineering honor society, Pi Tau Sigma international mechanical engineering honor society, and Sigma Xi scientific research society. His professional affiliations include the American Society of Mechanical Engineers (ASME), the American Institute of Aeronautics and Astronautics (AIAA), Association of Energy Engineers (AEE), the American Society of Heating, Refrigerating, and Air-Conditioning Engineers (ASHRAE), the American Society for Testing and Materials (ASTM), the American Institute of Physics (AIP), and the National Society of Professional Engineers (NSPE).

Acknowledgments

Livermore is the one that I wish I could fold up and put in my pocket to take with me to the next phase of my life.

Of course, I would never have come this far without the continuous emotional and financial support of my parents, Robert and Valerie Traum. My father taught me never to lower my standards. My mother taught me never to give up.

My warmest thank you is reserved for my wife, Sharon. If it weren't for her constant motivating influence, I would still be on page 17 of my master's thesis and living in a single room on the fifth floor of a 100-year-old undergraduate dormitory with no elevator. Her continuous love, attention, and support provided the backdrop against which I found myself miraculously able to tackle each impossible task laid before me to earn this degree. Dr. Traum simply would not have happened without her.

While the Ph.D. is nice, the most valuable asset I earned at MIT was my Mr. Degree.

Table of Contents

List of Symbols

A	Arbitrary Molecular Species
a	Sonic Velocity
A_i	Area of i
B	Arbitrary Molecular Species
C	Total Concentration
$C_{f,x}$	Local Skin Friction at Station x
$C_{f,x,smooth}$	Local Skin Friction at Station x Over a Smooth Surface
C_i	Molar Concentration of Species i
C_p	Specific Heat at Constant Pressure
C_v	Specific Heat at Constant Volume
d	Channel or Cylinder Diameter
D	Diffusion Coefficient
dA	Differential Area
$D_{A,B}$	Diffusion Coefficient of A in B
$D_{H2O,Air}$	Diffusion Coefficient of Water Vapor in Air
d_e	Effective Pore Diameter
d_h	Hydraulic Diameter
D_K	Knudsen Diffusion Coefficient
F	Arbitrary Constant
g	Gravitational Acceleration
h	Lumped Natural Convection Coefficient
h_{BL}	Mass Transfer Coefficient for a Boundary Layer
$\overline{h}_{BL}$	Average Mass Transfer Coefficient for a Boundary Layer
h_i	Thermal Transport Coefficient of i
h_m	Mass Transfer Coefficient
j_i	Diffusion Flux of Species i
k	Boltzmann Constant ($1.3806503 \times 10^{-23}$ m^2-kg/s^2-K)
k_i	Thermal Conductivity of i
L	Thickness, Length
L_f	Trailing Edge Location
L_i	Thickness of i
L_o	Leading Edge Location
M	Mass
$\dot{m}$	Mass Transport Rate
$\dot{m}_{ave}$	Apparatus-specific Overall Average Mass Transfer
$\dot{m}_i$	Mass Transport Rate of i
Ma	Mach Number
M_i	Molecular Weight of i
n_i	Molecular Density of i
N_i	Total Flux of i
P	Pressure
p	Perimeter
p_i	Momentum of Gas i
P_i	Pressure of i

Pr	Prandtl Number
$\dot{Q}_{in}$	Heat Flux In
$\dot{Q}_{lost}$	Unaccounted Heat Leakage
r	Channel or Cylinder Radius
Ra_L	Rayleigh Number Based on Length L
R_{axial}	Axial Thermal Resistance
$R_{BL,downstream}$	Mass Transport Resistance in the Boundary Layer Downstream of the Membrane
R_{DS}	Downstream Apparatus Mass Transport Resistance
Re	Reynolds Number
Re_D	Reynolds Number Based on Diameter
Re_L	Reynolds Number Based on Distance Down a Flat Plate
$Re_{L,tr}$	Transition Reynolds Number
$R_{electrical}$	Resistance, Electrical
Re_r	Reynolds Number Based on Radial Coordinate
Re_x	Local Reynolds Number Based on Coordinate x Along a Flat Plate
Re_Θ	Local Momentum Thickness Reynolds Number
$R_{headspace}$	Mass Transport Resistance in the Apparatus Headspace
r_i	Radius of i
R_i	Mass Transport Resistance of i
R_{mem}	Membrane Mass Transport Resistance
r_o	Outer Radius of the Membrane
R_{radial}	Radial Thermal Resistance
R_u	Universal Gas Constant (8.314472 J/K-mol)
R_{US}	Upstream Apparatus Mass Transport Resistance
R_{VSL}	Mass Transport Resistance of the Viscous Sub-layer
s	Entropy
Sc	Schmidt Number
Sh	Sherwood Number
$Sh_{L,membrane}$	Membrane Sherwood Number
$\overline{Sh}_L$	Average Sherwood Number over Length L
Sh_x	Local Sherwood Number Based on Coordinate x Along a Flat Plate
T	Temperature
t	Time
T_1	Apparatus Base Temperature
$T_{1,closed}$	Apparatus Base Temperature, Closed Chamber
$T_{1,mem}$	Apparatus Base Temperature, Porous Membrane in Place
$T_{1,open}$	Apparatus Base Temperature, Open Chamber
T_2	Upstream Membrane Temperature
T_3	Downstream Membrane Temperature
T_{amb}	Ambient Temperature
T_b	Bare Thermocouple Temperature
T_e	Epoxy Beaded Thermocouple Temperature
U	Free Stream Velocity
$\bar{u}$	Mean Molecular Velocity
$u^+(x)$	Dimensionless Velocity at Station x

U_b	Characteristic Buoyancy-driven Velocity
u_τ	Friction Velocity
$\forall$	Volume
$\dot{\forall}$	Volume Flow Rate
$\forall_i$	Partial Molar Volume of Species i
V_i	Velocity at Radial Station i
v_i	Bulk Velocity of Species i
V_{rms}	Voltage, Root Mean Squared
w_i	Molar Flux of Species i
X	Edge Length
X_{tr}	X Coordinate Marking Transition from Laminar to Turbulent Flow
$y^+(x)$	Dimensionless Boundary Layer Thickness at Station x
y_i	Mole Fraction of i

List of Symbols (Greek)

λ	Mean Free Path
α	Thermal Diffusivity
β	Thermal Expansion Coefficient
ω	Euler's Constant (0.5772...)
γ	Specific Heat Ratio
$\delta(x \text{ or } r)$	Boundary Layer or Viscous Sub-layer Thickness at Coordinate x or r
$\bar{\delta}$	Average Viscous Sub-layer Thickness
ΔH_{fg}	Latent Heat of Evaporation
Δr	Infinitesimal Control Volume Thickness
ΔT	Temperature Difference
Δt	Infinitesimal Time Step
δ_ρ	Mass Concentration Boundary Layer Thickness
ε_v	Void Fraction (Porosity)
ζ	Membrane Number
Θ	Fractional Accomplished Cooling
Λ	Dimensionless Power Ratio: Latent Heat Transfer Rate vs. Power Input
ν	Kinematic Viscosity
ξ	Downstream Station Where Mass Transfer Begins
ξ_i	Diameter of Molecule i
Π	Power
ρ	Density
ρ_i	Mass Concentration at Station i
σ_v	Tangential Momentum Accommodation Coefficient
τ	Tortuosity
Φ_M	Dimensionless Temperature Ratio
Φ_o	Dimensionless Temperature Ratio for Open Chamber Mode
ΔC	Log Mean Concentration Difference

List of Acronyms

MEMS	Micro Electro Mechanical Systems
MIT	Massachusetts Institute of Technology
ISN	Institute for Soldier Nanotechnologies
FOCs	Force Operating Capabilities
CMOS	Complementary Metal–Oxide–Semiconductor
CVD	Chemical Vapor Deposition
Kn	Knudsen Number
CNT	Carbon Nano-tube
SEM	Scanning Electron Microscope
CIA	Computer Image Analysis
ID	Inner Diameter
FIB	Focused Ion Beam
LN_2	Liquid Nitrogen
SEMs	Scanning Electron Micrographs
HAMTA1	Heat- And Mass-Transfer Apparatus 1
HAMTA2	Heat- And Mass-Transfer Apparatus 2
OD	Outer Diameter
DI	De-ionized
VAC	Volts, Alternating Current
PID	Proportional-Integral-Derivative
RH	Relative Humidity
Ave	Average
WVTR	Water Vapor Transmission Rate

1   Introduction

This thesis investigates cooling of solid surfaces by non-boiling evaporation (latent heat transfer) through various micro/nano-engineered membranes with pore diameters from 39 to 14,400 nm. Membrane pore width is shown to be significant in modulating mass transfer through the membranes, latent heat transport away from the surface being cooled, and the resulting temperature of that surface. A further motivation of this thesis is to elucidate integration of nano-scale and nano-enabled materials to enhance human survivability in practical-scale systems.

1.1   Heat and Mass Transport

Latent and sensible heat carried through porous soft materials by vapor transmission can make an appreciable contribution to the total transported energy, augmenting or exceeding purely conductive heat transfer. Using a latent heat carrier concentration gradient, thermal energy can be moved parallel to, without, or opposed to a temperature gradient that drives thermal conduction. Moving latent heat against a temperature gradient can thus neutralize incoming heat or cool a heat source, which is relevant to humans for maintaining normal body temperature in hot, dry environments despite metabolic heat generation and exterior solar radiation.

1.2   Multi-functionality

Mass transport through porous membranes has been extensively studied [Cussler (1997)] for desalination [Findley (1969)], human comfort [McCullough, et al. (2003)], and human protection [Gibson, et al. (2001)]. Pore diameters from 1 to 15,000 nm are of interest for potential heat management applications in multi-functional nano-structures, MEMS, and macro systems based thereon that exploit nano- and micro-scale building blocks to multiplex functionalities, e.g., the work of Johnson, et al. [Johnson, et al. (2003)]. In this thesis, materials with micro- and nano-scale pores show promise to combine, in one lightweight material, substantial mechanical energy absorption for blast or ballistic protection with evaporative cooling for thermal comfort. However, quantitative investigations in the 1 − 15,000 nm size range are challenging because length-scale phenomena, e.g., non-continuum hydrodynamics [Karniadakis and Beskök (2002)], curvature, wetting [Gennes, et al. (2004)], and fluctuations, e.g. in species concentration at interfaces [Luo, et al. (2006)], may confound experimental design and interpretation.

Micro/nano-fabricated membranes are of interest for their capacity to scaffold two or more capabilities. For example, so-called *nano-trusses* are polymeric materials whose ordered

15

networks of micro- to nano-scale rods, struts, cells, and channels (Figure 1.1) provide light weight, high porosity, and extraordinary absorption of mechanical energy [Jang, *et al.* (2006)]. Design of practical integrated systems requires knowledge of tradeoffs in the strength, porosity, weight, and cooling efficacy of the nano-structure, which demands quantitative understanding of how pore width and geometry impact evaporative cooling of surfaces overlaid by the nano-trusses. This thesis quantifies how pore size impacts transport of latent heat by directly measuring rates of water vapor transport and deducing an apparatus-independent pore diffusion coefficient for water vapor in air through each membrane.
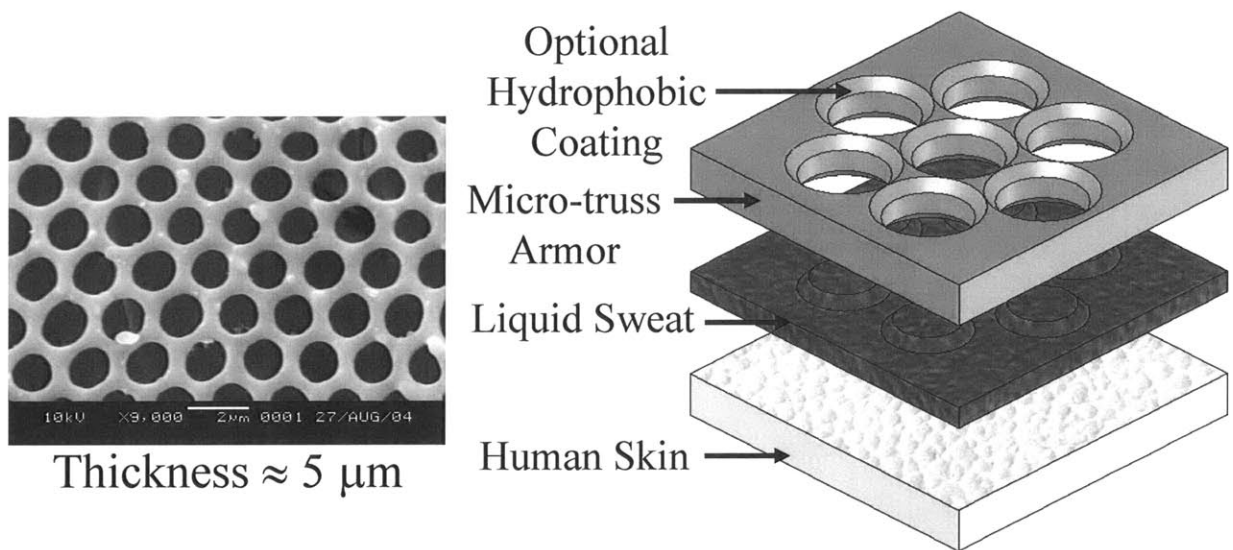
Figure 1.1: (Left) a micrograph of two-dimensional nano-frame demonstrates regular, porous geometry [Micrograph courtesy of Dr. Ji-Hyun Jang and Taeyi Choi, Thomas Group, MIT]. (Right) nano-truss can be designed and augmented with other functional components (i.e. surface coating) to create membranes providing both evaporative cooling and ballistic protection.

1.3 Tie-in to MIT's Institute for Soldier Nanotechnologies (ISN)

This thesis was conducted as part of the fundamental research program of MIT's Institute for Soldier Nanotechnologies (ISN). Through partnering of MIT, the Army, and industrial companies, the mission of the ISN is to discover and develop nano-enabled materials, devices, and systems to provide unprecedented advances in Soldier survivability. The original goal of this particular project was to demonstrate the integration of two or more nano-enabled components from the ISN's research portfolio to create useful, multifunctional modules to enhance Soldier survivability.

This research therefore draws upon nano/micro-trusses, bi-continuous polymer/air nano structures, which are being studied by ISN colleagues as mechanical energy absorbing materials for potential applications in blast or ballistic protection. Their concept is to design material with substantial energy absorbing properties, but with overall reduced weight compared to bulk material due to periodic connected voids in the structure. This thesis research capitalizes upon the voids in nano/micro-truss (and simulant materials) as conduits to allow fluid to travel through the material, enabling evaporative cooling of a surface or volume overlaid by the nano/micro-truss. One example is cooling of the skin of a Soldier. This "sweating body armor" capitalizes on the large latent heat absorbed as water undergoes its liquid-to-vapor phase change to provide a source of cooling for the Soldier.

1.4 Impact of Operating Theater on Soldier Cooling Requirements

To quantify Soldier cooling requirements, ambient conditions in Baghdad, Iraq were selected as a reference point. At midday in July and August, the temperature may reach 120 °F (48.9 °C). Intense daytime heat is somewhat mitigated by low relative humidity (10 to 50 percent) [NOAA (2007)]. Additional design point guidance is provided by the Army through TRADOC Force Operating Capabilities (FOCs). The Soldier of the future must function in ambient temperatures from -60 °F to +120 °F with use of additional special equipment and procedures limited to snow, moderate ice, rain, sand, dust, salt water spray, and when exposed to battlefield contaminants. Thus, "sweating body armor" is designed to operate in a low-humidity environment with 120 °F (48.9 °C) ambient temperature. Potential applications to higher humidity conditions are not the focus of this thesis.

1.5 Integrating Ballistic and Thermal Protection

Modern body armor is designed to protect the dismounted Soldier from certain pistol and smaller caliber rifle rounds. Ceramic inserts plus Kevlar can stop 0.30 caliber ammunition (i.e., from an AK-47). However, body armor has not been designed for thermal comfort in hot climates. As a result, the clothing between the Soldier's skin and armor can become saturated with perspiration and can increase in temperature, literally cooking the Soldier's body. Anecdotal evidence from recent desert engagements suggests that Soldiers sometimes remove their armor for a short time to allow themselves to cool and dry off [Dean (2003)]. This practice puts the Soldier at risk. Thus, focusing on enabling evaporative cooling for body armor will provide significant impact to Soldier thermal regulation and threat protection in desert environments.

1.6   Thesis Objectives

Using bench-scale experiments that mimic heating of a desert Soldier, together with interpretive mathematical modeling the specific objectives of this thesis are to:

1) Quantify the rates and extents of evaporation of a pure liquid (water) from a flat solid surface through a porous membrane as affected by the diameter of the membrane pores;

2) Determine how steady state surface temperatures are affected by the diameter of the pores in the membrane during evaporative cooling;

3) Illuminate the underlying mechanisms responsible for beneficial and unwanted effects of the size of membrane pores, on evaporative cooling of an underlying surface.

4) Use the results of (1) – (3) to identify operating conditions that accelerate or hinder surface cooling, with particular interest in beneficial and inhibitory impacts of nano scale size and geometric effects.

5) Drawing on the results of (1) – (4) and other information as appropriate, develop a preliminary engineering design correlation for a system to cool a surface by evaporation of a liquid through a nano-engineered porous membrane.

6) Focus the design on cooling Soldier body armor constructed from porous materials such as nano/micro-trusses.

1.7   Human Perspiration and Heat Rates

The required heat removal from the Soldier to maintain thermal equilibrium in the desert must be quantified, and the amount of self-cooling enabled by perspiration evaporation must be known. In sufficiently dry air, perspiration evaporates as rapidly as it is formed, and the skin remains virtually dry. During an extremely hot day in the desert, as much as 12 liters of perspiration may be produced, giving an average human perspiration rate of over 1 liter per hour [Schmidt-Nielsen (1979)] for a 12-hour period. However, the reported perspiration rate of humans varies widely from one study to the next. Table 1.1 summarizes human perspiration rates for various desert-like ambient environments reported by different researchers; the total water expenditure for perspiration formation in humans can easily reach 15 liters per day. The rate of perspiration is not changed by moderate dehydration or excessive consumption of water; it is only adjusted by the need for heat dissipation [Schmidt-Nielsen (1979)]. Good water economy would be best realized via reduced overall perspiration production by deriving maximum cooling benefit from the perspiration that is produced and evaporated.

Table 1.1: Human sweat rates reported by various researchers under desert-like conditions suggest the rate is between 0.5 and 4 liters per hour, with a typical rate of about 1 liter pre hour for extended periods. *Data from Schmidt-Nielsen (1979).*

Researcher	Sweat Rate	Conditions
[ ]	[liters/hour]	[ ]
Ladell	0.5	Arabian Desert
Adolph & Dill	1.3 - 1.7	Nevada Desert
Moss	2.6	Coal Mine
Eichna	1.24 - 3.88	33.5 °C @ 100% RH

To maintain constant body temperature, the Soldier must expel heat at the same rate it arrives at, or is produced in, his or her body. Major sources of heat include solar radiation (about 1000 watts/m^2) and metabolic heat (about 350 watts/m^2 for heavy exercise [ASHRAE (2005)]). To benchmark the amount of heat that must be removed, this thesis assumes that the heat dissipation requirement is evenly distributed across the torso. Thus, any Soldier cooling system must eliminate a peak load 1350 watts/m^2 to maintain thermal equilibrium under marching conditions. It is also assumed that the human perspiration rate is 1 liter per hour and that sweat generation is uniform over the surface of the body.

These assumptions provide a reasonable benchmark against which to compare various candidate cooling technologies, but they do represent oversimplifications. For example, the distribution of sweat glands (and the production of perspiration) is not uniform across the body. The most numerous types of sweat glands, the so-called *eccrine glands*, are concentrated on the forehead, neck, back, palms of the hands, and soles of the feet. Sweat generation for thermal management (and nervousness) is concentrated in these areas [Shier, *et al.* (1996)].

1.8   Down-selection of Cooling Techniques

Several potential Soldier cooling approaches were analyzed using the climate and loads of the design point: 50 °C ambient environment, 1000 w/m^2 insolation, and 350 w/m^2 metabolic heat generation. This analysis is presented in Appendix 3. It was assumed that no metabolic regulation (no sweating) occurred unless the technique under scrutiny specifically enabled it. Convention was assumed to occur only from buoyant effects – no wind was blowing on the Soldier. Finally, it was assumed that the Soldier uses no additional thermal management coping mechanisms (such as standing in the shade) to mitigate heat. This analysis therefore represented

an upper bound on the heat load that the Soldier must dissipate. Under these assumptions, the following potential cooling techniques were analyzed: 1) Evaporating Perspiration, 2) Evaporation of Exotic Materials, 3) Cryogenic Thermal Energy Storage, 4) Cryogenic Thermal Energy Storage Plus Fuel, 5) Mechanical Refrigeration, 6) Super Insulators and Reflectors, and 7) Endothermic Chemical Reactions.

Each cooling approach was evaluated using five metrics: 1) was the approach physically possible, 2) what weight and bulk was required to meet 1 hour of peak heat load, 3) how much power was required for implementation 4) how easily could an approach be integrated into the Soldier battle suit and Army supply chain, and 5) how amenable was the approach to improvements by nanotechnology research. Evaluations were applied in order. If an approach failed a test, the analysis was terminated, i.e., the remaining figures of merit were not applied.

1.8.1 Evaporation of Water – the Superior Cooling Approach

The results of the analysis indicate that evaporation of liquid water from the Soldier is the best solution for desert thermal management. A similar conclusion was reached by Nellis, *et al.* [Nellis, *et al.* (Feb. 2003)], in an Army-funded study that rated several cooling techniques for personal heat removal. An abridged version of the Nellis, *et al.* study is also available [Nellis, *et al.* (Aug. 2003)].

At a perspiration rate of 1 liter per hour (1 kg/hr) the Soldier mitigates almost half of the total peak heating load. At a perspiration rate of 2.25 liters per hour, which is within the realm of realistic peak perspiration rates, the entire heat load is mitigated. No weight associated with mechanical systems is required. However to avoid serious or potentially fatal dehydration, the Soldier must have access to sufficient water to replenish that lost by sweating.

Drinking water is already part of Army supply chain, and water can also be found in and utilized from the surrounding environment. To a limited extent, the Soldier can "store" excess water by super-hydrating himself before going on patrol. Excess water can be carried in simple containers, but a weight penalty is incurred. So, if water is carried as part of the logistic chain or onboard the Soldier, this extra weight must be accounted for.

A further benefit of sweating is that the perspiration rate is monitored and regulated by mechanisms in the body. No exogenous feedback control is necessary. Provided the human sweat flux rate does not exceed the rate at which water evaporates from the system, the Soldier perspires just as much as is required to effect adequate cooling.

1.9 Bio-inspired Model: The Camel

Uniquely adapted for desert survival, the camel employs a wide assortment of thermal and water management techniques that enable it to survive while exposed to hot, dry climates for extended periods. These techniques are detailed in Schmidt-Nielson's book [Schmidt-Nielsen (1979)], which also covers techniques utilized by other desert-dwelling animals. Inspiration for the cooling concept featured in this thesis arises from the evolution of camel fur for efficient evaporative cooling, water management, and thermal protection.

Camel fur allows sweat evaporation directly from the skin's surface while the fur provides a layer of thermal insulation, as shown in Figure 1.2. The fur has evolved to stand on end with enough hair-to-hair separation to retard sweat wicking to the surface; whereas fur of mammals evolved for cold conditions mats to the skin and causes liquid sweat to wick through and evaporate from the fur's surface. For these non-desert mammals, sweat evaporation gives less efficient cooling because the liquid-to-vapor boundary is displaced from the skin's surface, and the latent heat is assimilated not directly on the skin but rather on the surface of the matted fur. The practical thermal regulation consequence is that camel fur maintains the same skin temperature as other mammals but requires less sweat evaporation under the same environmental conditions [Schmidt-Nielsen (1979)].

1.10 Creating "Sweating Body Armor" from Nano Components

A major hypothesis of this thesis is that light-weight ballistic protection and vapor transport for evaporative cooling can be integrated to create "sweating body armor". Substantial improvements in Soldiers' ability to cool themselves by sweating could be achieved by making water-vapor-permeable body armor that behaves like camel fur. Conventional lithography, interference lithography, extrusion/skiving, and track etching (among other nano-fabrication techniques) can be utilized to make arrays of straight-through pores in many soft polymer materials as well as CMOS materials like silicon. Interference lithography allows large arrays of perfectly identical micro-scale through-channels to be fabricated with almost any desired shape, size, and orientation [Toader, *et al.* (2004), Ullal, *et al.* (2004)] into many photolithographic polymers.
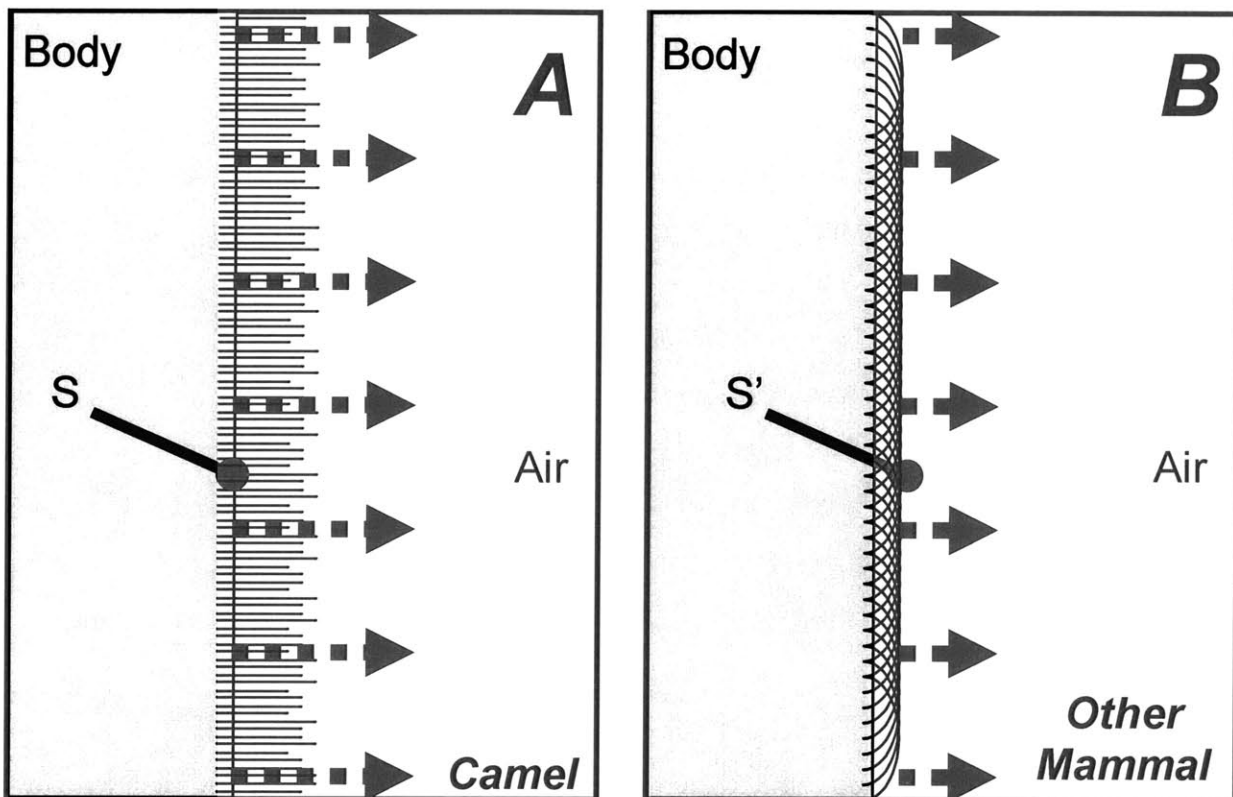
Figure 1.2: Camel fur (left) allows evaporation of liquid sweat directly from the skin's surface (S) giving superior cooling while the fur provides thermal insulation. Non-desert mammal fur (right) mats to the skin and causes liquid sweat to wick through and evaporate from the fur's surface (S'). The camel's adaptations provide substantially improved thermal and water management in the desert than mammals not evolved for desert survival. *Figure based on original in Schmidt-Nielsen [Schmidt-Nielsen (1979)].*

Researchers working at the ISN have demonstrated substantial energy absorption using arrays of micro-frame and micro-truss [Choi (2006)]. A goal of these researchers is to create body armor that is lighter than conventional armor but more protective against ballistic or blasts threats (or both). These capabilities are enabled by a regular pattern of connected voids in the material that reduce weight without retarding energy absorption. These voids can also serve as conduits for vapor transmission.

Design guidance comes from camel fur, which stands on end allowing perspiration to evaporate at the skin's surface. Utilizing control of the evaporation front location, high cooling effectiveness of latent heat removal is located where it will have the highest impact i.e., at the Soldier's skin. Sweating body armor will force perspiration to vaporize from near the Soldier's skin and transport the resulting vapor through pores in the armor to the high-temperature/low-

humidity ambient environment. The body armor effectively becomes a thermal insulation layer akin to the camel fur.

Micro/nano-fabrication techniques can make through-holes, but to more fully mimic the camel's capabilities, further treatment would be required to prevent liquid sweat from wicking into the pores. As shown in Figure 1.1, the surfaces of nano-truss pores could be treated with a hydrophobic coating to prevent liquid from wicking into the pores and reaching the outside surface of the body armor. This would in turn keep the liquid/vapor evaporation front close to the skin and thus mimic the efficient evaporative cooling arrangement utilized by camels in the desert.

Direct contact between liquid and porous membrane is intentionally avoided in experiments within this thesis by experimental apparatus design. An air gap between the liquid and the porous membrane prevents this contact. In the functional Soldier system, the armor would not directly contact the skin. An undershirt would be utilized to provide separation and retain the solids from the evaporated perspiration to avoid fouling the armor pores. In the real system, nano-coating techniques, such as chemical vapor deposition (CVD), could be employed to apply a hydrophobic coating to some or all of the micro-truss channel walls. Porous membranes could also be fabricated from material that is already hydrophobic to prevent the need to coat the pores for evaporation front control.

2 Background and Literature Review

This thesis is concerned with the transport of water vapor through porous membranes and the associated latent heat carried away from the system, which provides cooling. By capitalizing on micro/nano-fabrication techniques, membranes can be created with pores run straight-through from one exterior membrane face to another. In addition, the pores are approximately cylindrical in shape, representing a nearly ideal system from the standpoint of mathematical modeling.

A key dimensionless parameter for defining diffusion transport efficacy of straight-through cylindrical pores is the Knudsen Number (Kn), which is a ratio of the mean free path of water vapor diffusing in air, λ, to the pore diameter, d:

$$Kn = \frac{\lambda}{d} \qquad \text{(Equation 2.1)}$$

For small pores or at low pressure (large mean free path), the Knudsen Number exceeds unity, which means that the diffusing water molecules begin to collide with the channel walls more often than with molecules of air through which they are diffusing. According to the prevailing model, a molecule striking the pore wall exchanges momentum with the molecules of the channel and is diffusely reflected; that is, reflected in a random direction unrelated to the direction at which it arrived [Kärger and Ruthven (1992)]. The so-called *Knudsen diffusion regime* can be characterized by momentum transfer to the wall by a diffusing gas species substantially exceeding the momentum transfer to the host gas.

In their classical work on gaseous diffusion in long capillary tubes, Pollard and Present [Pollard and Present (1948)] provide derivations for self-diffusion gas transport in infinitely long tubes for two extreme limits: Kn >> 1 and Kn << 1. For Kn >> 1 (very small pores), the expression for theoretical diffusion coefficient, D, is

$$D = \frac{2}{3}\bar{u}r\left[1-\left(1.2264+\frac{3}{4}\ln\left(\frac{\lambda}{2\omega r}\right)\right)\frac{r}{\lambda}...\right] \qquad \text{(Equation 2.2)}$$

where $\bar{u}$ is the mean molecular speed, r is the capillary radius (d/2 = r), λ is the mean free path of the diffusing species, and ω is Euler's constant. For Kn << 1 (very large pores), the expression for D is

$$D = \frac{1}{3}\bar{u}\lambda\left[1-\frac{3}{8}\frac{\lambda}{r}\right] \qquad \text{(Equation 2.3)}$$

In Equation 2.3, the mean free path for a single molecular species, λ, can be replaced by the mean free path of molecule A diffusing through a background of molecule B [Dushman (1962)] through the following expression

$$\frac{1}{\lambda_A} = \sqrt{2}\pi n_A \xi_A + \pi n_B \xi_{AB}^2 \left(1 + \left(\frac{M_A}{M_B} \right)^2 \right)^{\frac{1}{2}}$$
(Equation 2.4)

where n_A and n_B are the molecular densities of species A and B respectively, ξ_A is the molecular diameter of species A, ξ_{AB} is the average molecular diameter of species A and B, and M_A and M_B are the molecular weight of species A and B respectively. Equation 2.4 assumes that the temperatures of species A and B are the same. Also note that because Equation 2.2 assumes that the diffusing species only interacts with the channel wall and not with the background gas, it is appropriate to use the self-diffusion mean free path of water vapor in Equation 2.2.

Equation 2.2 and Equation 2.3 (using λ_A from Eq. 2.4) are plotted in Figure 2.1. While the assumptions underlying these curves break down as Kn $\rightarrow$ 1 and the expressions are valid only for channels of infinite length, the theory indicates that as pore diameter drops (Kn increases) the diffusion coefficient of water vapor through the pores also falls off to nearly zero.

This thesis includes a design correlation concerned with the impact of pore diameter on mass transport and ultimately cooling efficacy from $0.05 < \text{Kn} < 5$. Therefore, theory that is robust around Kn = 1, the so-called *transition regime* where both intermolecular and molecule-wall impacts are important, is required. Kärger and Ruthven [Kärger and Ruthven (1992)] suggest modeling the transition regime by summing the momentum transfer components associated with intermolecular collisions and wall collisions, and setting that expression equal to the total momentum transfer for the diffusing molecules. This expression becomes

$$-\frac{1}{kT}\left(\frac{dp_A}{dz} \right) = \frac{N_A}{D} = \frac{N_A}{D_K} + \frac{N_A - y_A(N_A + N_B)}{D_{A,B}}$$
(Equation 2.5)

Where k is the Boltzmann constant, T is the temperature of the gas, the derivative dp_A/dz represents momentum transferred out of the gas per unit volume, N_A and N_B are the total fluxes of species A and B respectively, y_A is the mole fraction of species A, D is the total observed diffusion coefficient, D_K is the Knudsen diffusion coefficient (associated with wall collisions) and, $D_{A,B}$ is the continuum diffusion coefficient of species A in species B (associated with intermolecular collisions). Solving Equation 2.5 for $1/D$ reduces the expression to

$$\frac{1}{D} = \frac{1}{D_K} + \frac{1}{D_{AB}}\left[1 - y_A\left(1 + \frac{N_B}{N_A}\right)\right]$$

(Equation 2.6)

For the evaporative cooling arrangement studied in this thesis, water vapor diffuses through a quiescent background of air. Therefore N_B, the diffusive flux of air in Equation 2.6 is zero. Furthermore, even for totally saturated air at 50 °C, the partial pressure of water vapor is only 12,247 Pa, and hence the water vapor mole fraction, y_A, represents less than 12.1% of the total pressure of the air-water mixture. Therefore, for systems of interest in this thesis, Equation 2.6 can be simplified to the following expression, which is accurate to better than ±12.1% over the range 0.05 < Kn < 5:

$$\frac{1}{D} = \frac{1}{D_K} + \frac{1}{D_{AB}}$$

(Equation 2.7)

Kn (λ/d)
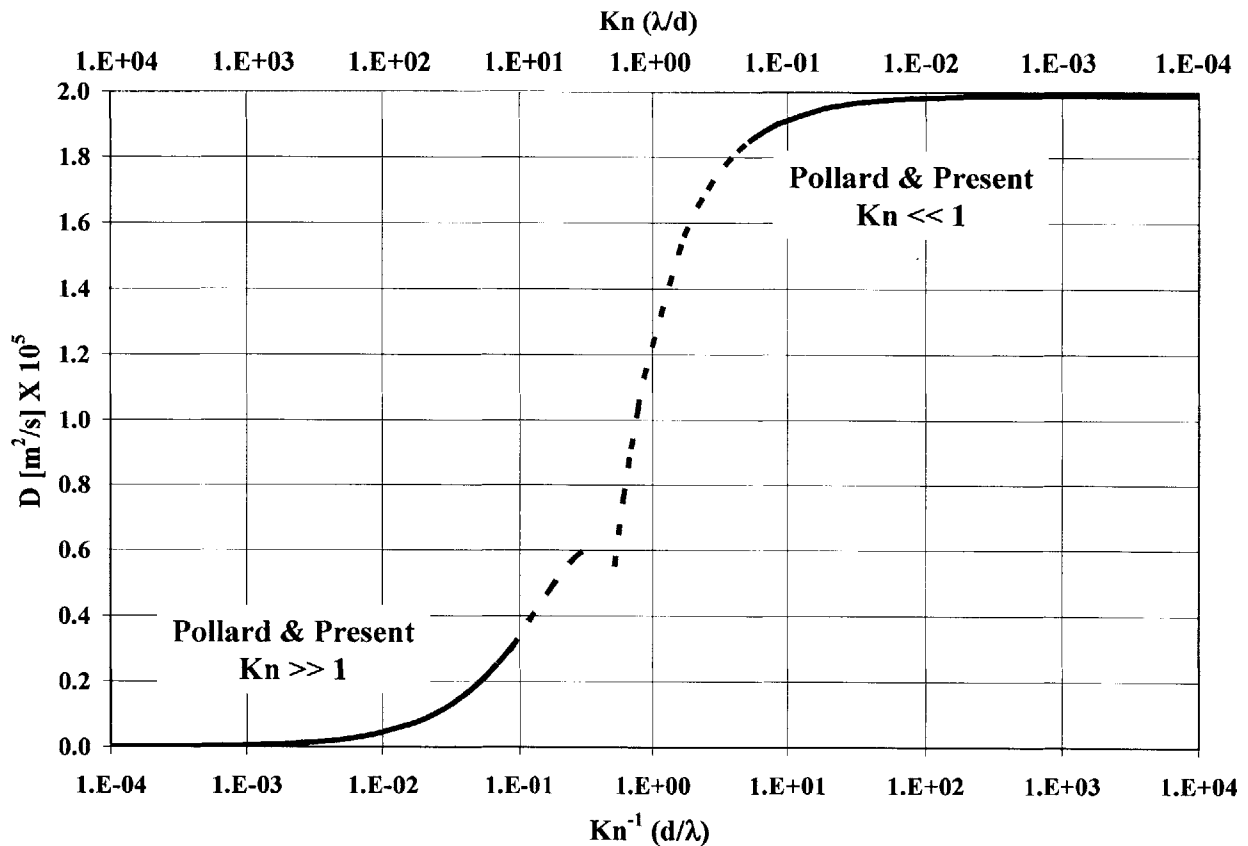
Figure 2.1 The theoretical work of Pollard and Present (1948) describes how molecules diffusing in capillary tubes of infinite length behave at the extreme cases of Kn >> 1 and Kn << 1 (solid black curves). These models break down as Kn → 1 (dashed black curves). Nonetheless, Pollard and Present predict a reduction in diffusion coefficient as compared to the continuum regime as Knudsen Number increases (pore diameter drops).

The expression for the continuum diffusion coefficient of water vapor in air ($D_{A,B}$, which is hereafter called $D_{H2O,Air}$) is calculated using an empirical correlation including temperature and pressure, given in Mills [Mills (1999a), p. 947];

$$D_{H_2O,air} = 1.87 \times 10^{-10} \left(\frac{T^{2.072}}{P} \right) \text{ for } 280K \leq T \leq 450 \qquad \text{(Equation 2.8)}$$

where T is the temperature in Kelvin and pressure, P, is given in atmospheres. The units of the resulting $D_{H2O,Air}$ value is [m^2/s]. If a temperature difference exists across a porous membrane, temperature is taken as the average temperature between the upstream and downstream membrane faces. Since evaporative cooling processes in this thesis occur at atmospheric pressure, the pressure is taken to be one atmosphere, plus a small correction accounting for the presence of water vapor (inside the chamber).

To check the accuracy of Equation 2.8, it was compared against an experimental continuum regime result reported in Deen [Deen (1998), p. 12], of 2.59 x 10^{-5} m^2/s at 308 K and one atmosphere for water vapor diffusing in nitrogen. Equation 2.8 returned 2.68 x 10^{-5} m^2/s for identical conditions (although against a background of air, not nitrogen), an error of less than 3.5 percent.

The expression for Knudsen diffusion, D_K, is obtained using the kinetic theory of gasses, and can be found in Kärger and Ruthven [Kärger and Ruthven (1992)] or Mills [Mills (1999a), p. 811];

$$D_K = 97 \left(\frac{d}{2} \right) \sqrt{ \left(\frac{T}{M_{H_2O}} \right) } \qquad \text{(Equation 2.9)}$$

where d is the pore diameter (in meters), T is the temperature (in Kelvins) of the gas within the pore, and M_{H2O} is the molecular weight of water (in grams/mole). The units of the resulting D_K value are [m^2/s].

Substituting Equations 2.8 and 2.9 into Equation 2.7, an expression is obtained for the diffusion coefficient of water vapor diffusing in air through straight-through cylindrical porous channels. This expression is the canonical model for mass transport through porous membranes of interest in this thesis:

$$\frac{1}{D_{mem}} = \left(\frac{1}{1.87 \times 10^{-10} \left(\dfrac{T^{2.072}}{P} \right)} + \frac{1}{97\left(\dfrac{d}{2}\right)\sqrt{\left(\dfrac{T}{M_{H_2O}}\right)}} \right)$$ (Equation 2.10)

Equation 2.10 can be thought of in analogy to a pair of electrical resistors in series [Mills (1999a), p. 811]. As pore diameter, d, decreases, diffusing water vapor molecules collide with the pore walls more often, and the Knudsen diffusion "resistor" begins to dominate over the continuum diffusion "resistor". Thus, the Knudsen term can be interpreted as an increasing resistance to diffusion, slowing down the mass flux rate through the membrane.

In fact, the overall governing equation for 1-dimensional steady state mass transport, a special case of Fick's Law, is analogous to Ohm's Law for circuits:

$$\frac{dm}{dt} = -\frac{A_1 (\rho_0 - \rho_1)}{\sum R_{mass\_transport}}$$ (Equation 2.11)

where dm/dt is the rate of mass transport from station 0 to station 1, A is the cross sectional area through which mass is transported, ρ_0 and ρ_1 are mass concentrations at stations 0 and 1 respectively, and $R_{mass\_transport}$ represents that various resistances to mass transport between station 0 and station 1.

The mass transport resistance associated with a porous membrane, R_{mem}, is expressed as follows

$$R_{mem} = \frac{L_{mem}\tau}{D_{mem}\varepsilon_v}$$ (Equation 2.12)

Where L_{mem} is the membrane thickness, D_{mem} is the expression for porous membrane diffusion coefficient derived in Equation 2.10, τ is the tortuosity of the membrane, and ε_v is the membrane porosity. Membrane tortuosity and porosity will be treated in greater detail in Chapter 3.

To provide a sense of pore size impact on mass transport efficacy, Figure 2.2 plots mass transport across a 30% porous membrane with non-tortuous pores ($\tau = 1$) between two reservoirs at 20 °C and one atmosphere utilizing Equation 2.10. The first reservoir is at 100% relative humidity ($\rho = 0.171$ kg/m^3) while the second reservoir is at 0% relative humidity ($\rho = 0$ kg/m^3). The membrane is 100 microns thick and covers an area of 1 square centimeter.

28
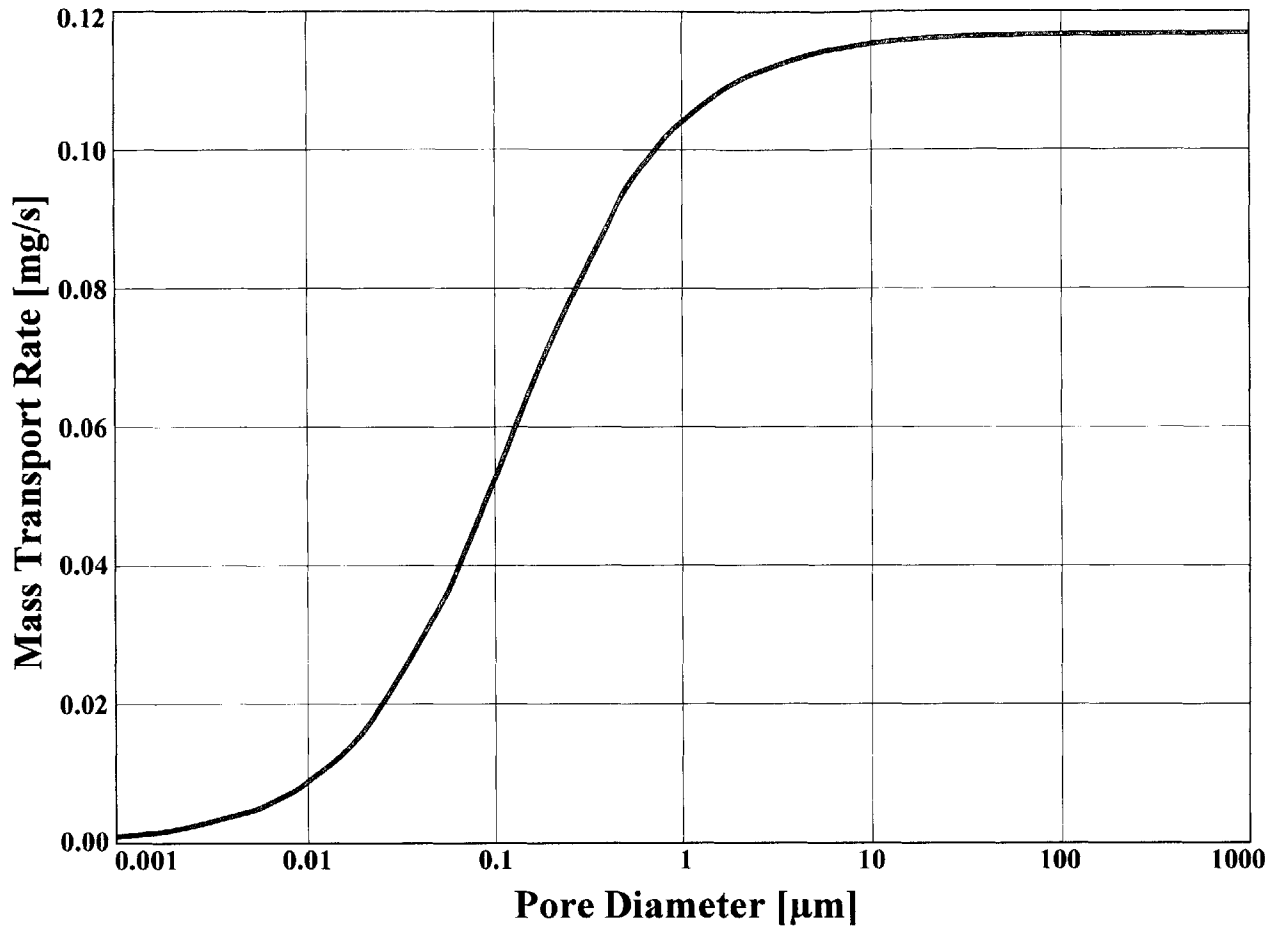
Figure 2.2 A representative example of water vapor diffusing through a porous membrane in a background of air (Equation 2.10). In this model, the porous membrane represents the only resistance to mass transport. Pore diameters from 0.001 to 1000 µm are plotted. This result assumes a uniform temperature of 30°C with 100% relative humidity at the upstream membrane face and 0% relative humidity on the downstream membrane face. The membrane is assumed to have a tortuosity of unity, 30% porosity, and a thickness of 100 µm.

Figure 2.2, demonstrates that decreasing pore diameter becomes detrimental to mass transport for this system at a pore diameters of roughly 10 microns. In the regime of pore diameter between 1 micron and 1 nanometer, the mass transport rates drops substantially (the so-called *transition regime*), but is not entirely extinguished. This diffusion regime is of particular interest to nano-systems integration because of emergent properties associated with nanometer length scales, which can be capitalized upon for multi-functionality. Thus, designers of multifunctional systems may need to utilize pore diameters below one micron to obtain some desirable nano-effect, combined with transport of vapor through the channels. One contribution of this thesis is to provide design parameters describing the mass and latent heat transport

efficacy attained by porous systems in the transition diffusion regime from 39 nm to 15 μm that combine evaporative cooling with some other nano-enabled feature.

2.1 Additional Micro- and Nano-channel Flow Considerations

While the theory described in the preceding section is well-understood, experimentalists have observed interesting deviations from theoretical results that might be explained by the emergence of nano-scale phenomena. Indeed, one of the major contributions of this thesis is exploration of the transition diffusion regime over a wide range of Knudsen Number (maintaining atmospheric pressure and similar temperature across membrane samples) while varying pore diameter over several orders of magnitude. The transition diffusion regime has been classically studied by measuring flow of a single gas species through a capillary of fixed inner diameter while varying pressure in the capillary [Knudsen (1952)]. This approach achieves high Knudsen Number by increasing the mean free path of the diffusing species through lowering pressure, which is adequate to probe fundamental processes but not applicable to practical engineering systems.

While important for design of real systems that function at standard pressure and temperature exposed to the ambient environment, the experiments within this thesis are also of fundamental scientific interest because pore diameter was modulated instead of pressure. In fact, the most prominent motivation for utilizing nanometer diameter pores was the hope that a never-before-seen nano-effect might emerge at atmospheric pressure and small pore diameter that could potentially enhance through-membrane mass transport and improve evaporative cooling efficacy. Experimental evidence for the existence of such effects has appeared in the recent literature. The following sections describe prior experiments that either fortify or weaken the possibility of nano-scale flow enhancements. These sections also describe the significant differences between this thesis and prior research.

2.1.1 Evidence of Enhanced Flow Through Micro/Nano Channels

Roy, *et al.* [Roy, *et al.* (2003)] devised a two-dimensional finite-element flow model that attempted to predict diffusion through a nano-channel 60 μm long and 200 nm in diameter. The authors provide modeling equations to handle the shift from slip to transition flow as Knudsen Number increases. To benchmark this model, data were collected on flow through a porous alumina disc with an array of well-defined cylindrical nano-diameter pores oriented perpendicular to the membrane. The gasses studied were Ag, N_2, and O_2. The model agreed with

experimental results to within 5 percent. Roy, *et al.* noted that a deviation from the Knudsen diffusion result may be observed at very small pore radii because molecule-wall interactions at that pore size can be different from the elastic interactions assumed in Knudsen diffusion.

In a follow-on study, Roy, *et al.* [Roy, *et al.* (2005)] presented experimental measurements of argon and oxygen gas flow through a 10 nm-pore-diameter polycarbonate membrane 6 microns thick. They reported flow rates an order of magnitude higher than predicted by the Knudsen diffusion model. Using simulations, they also found that a hydrodynamic model based on Poiseuille gas flow (with addition of a slip boundary condition) successfully predicted transport rates for Knudsen Numbers as high as 10, suggesting a change in molecule-wall interactions in the nano regime is responsible for enhanced flow rate at high Knudsen Number.

While these two papers by Roy and collaborators provide compelling experimental evidence of enhanced mass transport at high Knudsen Number, the experimental conditions do not cover all those of interest for real cooling systems. Pure, non-polar gasses were utilized as the working fluids, and the downstream face of the membrane was kept at vacuum pressure while the upstream face was pressured between 173 and 1127 torr (0.22 – 1.46 atmospheres). In addition, no independent characterization of the membrane samples was undertaken. Instead, manufacturer data for pore diameter, porosity, and membrane thickness were utilized. As will be shown in Chapter 3 of this thesis, manufacturer data for track-etched membranes are often inaccurate, and independent characterization is required to verify sample dimensions and topology. Finally, the work provided transport information but to temperature or heat flux measurement to tie in a heat transfer component. Coupling heat and mass transport to impact cooling efficacy is a critical contribution made by this thesis.

Enhanced rate of pure gas transport utilizing pores with very small channel diameter was also demonstrated experimentally by Holt, *et al.* [Holt, *et al.* (2006)]. These researchers report 16 to 120 times enhancement in gas transport over the rates predicted from the Knudsen diffusion model for pores of 2 nm in diameter. These authors used carbon nano-tubes (CNTs) to create nano-porous membranes through which pure gases were driven under a pressure gradient. The authors attribute the observed flow enhancement to the atomic smoothness of the nano-tube surfaces, a hypothesis they found to be consistent with literature predictions from molecular dynamics simulations. According to Holt, *et al.*, the molecule-wall collisions may change from purely diffuse (as in the Knudsen model) to a combination of diffuse and specular. While

31

molecules undergoing diffuse collisions depart the pore wall at a random angle, molecules undergoing specular collisions depart at an angle related to the angle of impact. So, mixed diffuse and specular reflections enable faster molecule transport through the channels than diffuse reflection alone.

The transport results by Holt, *et al.* had similar practical limitations to the papers by Roy, *et al.* with respect to realistic cooling applications as studied in this thesis. While a wider array of gasses was tested (H_2, He, Ne, N_2, O_2, Ar, CO_2, Xe CH_4, C_2H_6, C_3H_6, C_4H_6, C_4H_8), water vapor was not studied. Flow was induced across the membrane by maintaining the upstream face at 15 psi (1 atmosphere) and pumping the downstream face to vacuum. From compressible flow theory, the minimum pressure ratio required to induce chocked (sonic) flow is

$$\frac{P_0}{P_1} = \left[\frac{\gamma+1}{2}\right]^{\frac{\gamma}{\gamma-1}} \qquad \text{(Equation 2.13)}$$

where γ is the specific heat ratio of the flowing gas. For a representative value of $\gamma = 1.4$, sonic flow may occur for pressure ratios in excess of $P_0/P_1 = 1.9$ (see Appendix 1 for more details).

Despite viscous dissipation, high pressure ratio across the nano-pores in Holt, *et al.* created conditions similar to a sonic shock at the mouth of the pores. As in the work of Roy, *et al.*, this condition is not indicative of transport processes under ambient pressure of interest for practical systems such as Soldier gear. Holt, *et al.* also did not explore heat transfer implications of their system.

2.1.2 Evidence of Retarded Flow Through Micro/Nano Channels

Itaya, *et al.* [Itaya, *et al.* (1984)] performed experimental studies with membranes of alumina pores over a range of pore diameters (i.e. 10nm, 20nm, and 30nm) using H_2, He, N_2, CO_2, CO, C_2H_6, C_3H_8 as the diffusing species. They also collected data for a range of temperatures: 77, 195, 290, 322, and 370 K. Itaya, *et al.* reported gas permeability results consistent with Knudsen diffusion with no flow enhancement. As with studies highlighted in Section 2.1.1, these researchers pumped their system down nearly to vacuum and relied upon pressure gradients across the membrane to drive transport. In addition, there was no mention of heat transfer implications for their system.

The research presented in this thesis utilizes the diffusing species as a latent heat carrier to enable energy transport. In addition, the manuscripts outlined above study a single pore diameter (i.e. Roy, *et al.* [10 nm]) or a cluster of closely-spaced pore diameters (i.e. Itaya, *et al.* [10 nm, 30

nm, and 50 nm] and Holt, *et al.* [2 and 15 nm]). This thesis experimentally interrogates the mass transfer impact of pore width using a spectrum of pore diameters varied in a systematic manner ranging from the nano regime (39 nm) to the micro regime (14.4 µm). If there is a nano-scale enhancement effect as observed by Roy, *et al.* [Roy, *et al.* (2005)] and Holt, *et al.* [Holt, *et al.* (2006)], the series of experiments presented in this thesis will help establish pore diameter (and Knudsen Number) beyond which the enhancement is extinguished. This information will illuminate possible candidate mechanisms creating this effect. If no enhancement is observed, this thesis will provide confirmation that the model for transition regime mass transport through micro- and nano-porous channels given by Equation 2.10 is valid, even at ambient pressures by changing Knudsen Number via a range of pore diameters.

2.2 Multi-functional, Nano-enabled Textiles and Systems

In addition to making contributions to fundamental understanding of diffusion in nano pores, this thesis also provides an initial design framework to guide the development of multi-functional garments that integrate evaporative cooling with other capabilities both nano- and non-nano-enabled. Thus, the textile and membrane literature was also explored to determine how the research within this thesis could contribute to multi-functional design of nano-enabled textiles and systems.

2.2.1 Electro-spun Textiles

Gibson *et al.* [Gibson, *et al.* (2001)] studied the mass transport and human comfort properties of porous membranes made of Nylon 6,6 electro-spun nano-fibers, similar to those in Figure 2.3. The authors randomly deposited fibers with outer diameters between 200 and 500 nanometers to generate mats in a range of thicknesses depending on how much material was deposited. These membranes had high porosity (from 30% to 60%) with sub-micron pore size. By capillary flow liquid expulsion porosimetry, the authors estimated a pore throat diameter range of 0.1 to 0.8 microns. These small pores were designed to afford the membrane good resistance to chemical penetration and chem-bio agents while allowing water vapor transport to enable evaporative cooling.

Using an automated water vapor diffusion test method, Gibson *et al.* showed that these electro-spun membranes had a large resistance to pressure-driven convective flow of air compared to normal clothing. Pore size in conventional clothing is roughly 100 – 500 microns. However, the authors point out an advantage: the fiber diameters are of the same order as the

diffusing species mean free path. Thus, the no-slip approximation for macro-scale flow does not apply, and the actual pressure drop measured across the membrane is about 1/3 less than the classically-predicated result. Despite large resistance to convective flow, the membranes display much lower resistance to water vapor transport via diffusion than commercially available textiles.
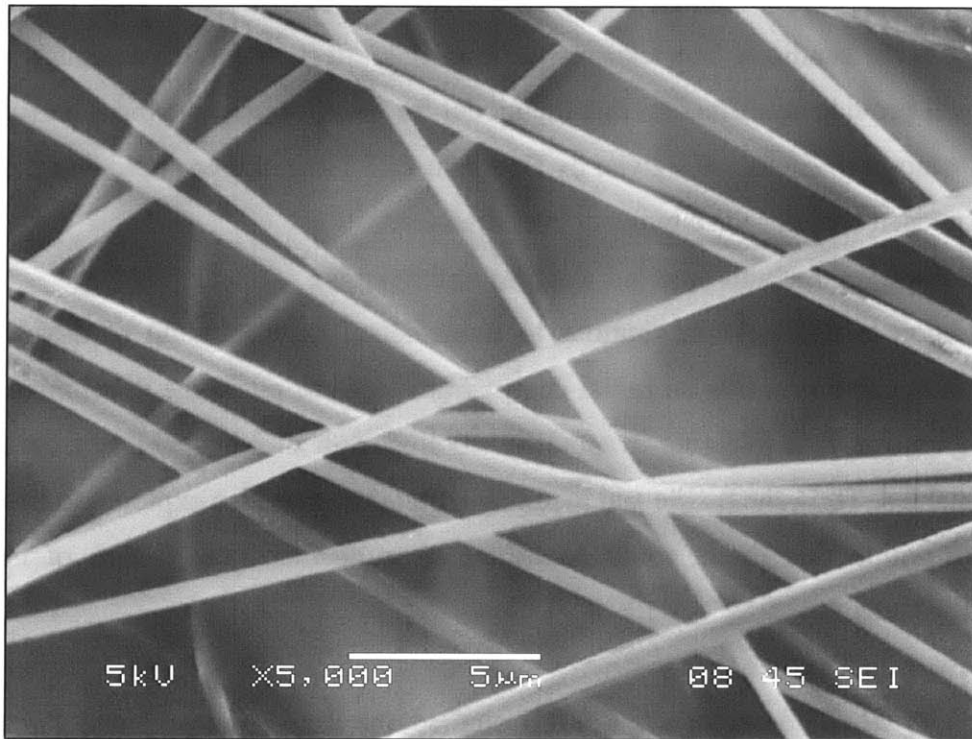
Figure 2.3: Micrograph of an electro-spun mat of PMMA [courtesy of Jian Yu (Rutledge Group, MIT)]. Gibson, *et al.* (2001) made similar mats from 200 to 500 nm diameter Nylon 6,6 fibers.

In this thesis, mass transport resistance is reported in units of [s/m], which is the most simplified form of the more complex dimensions [m^2-Pa/W], favored by ASTM International, (originally the American Society for Testing and Materials), for resistance of mass flow through fabrics. Physically, [m^2-Pa/W] can be thought of as the amount of power (in watts) required to drive water vapor against a gradient in partial pressure (in Pascals) through a surface area (in square meters). Since mass transport resistance appears in the denominator of Fick's Law (Equation 2.11), the term's dimensions are inverted.

Gibson, *et al.* [Gibson, *et al.* (2001)] state that intrinsic mass transfer resistance of the electro-spun mats is about 10 s/m, which is much lower than commercial fabrics with resistance values from 200 to 1500 s/m. The reported mass transfer resistance value is about 29% of the

34

expected value based on continuum diffusion not corrected for Knudsen Number (34.8 s/m for 30% porous mats at 0.87 mm thick). As a comparison, the 1 micron-pore-diameter DuPont porous membranes studied in this thesis present a mass transfer resistance of 72 - 91 s/m. The 14.4 micrometer-pore-diameter track-etched membranes studied herein present a mass transfer resistance of about 10 s/m, which increases to about 260 s/m as the pore diameter drops to 39nm.

The porous membranes utilized in this thesis for evaporative cooling have the potential to provide many of the human-protective features of electro-spun nano-fiber textiles, and to do so with several potential additional benefits with respect to control over rates of coolant vapor mass transfer. Electro-spun mats are not structured at the micro-scale; the pores have no regular pattern, size, or order, and there is a nearly-ten-fold range in pore size [Yu (January 2007)]. On the contrary, micro-truss pore shape and size can be specifically engineered via nano-fabrication techniques (e.g. conventional or interference lithography) to provide a specific type of desirable performance. For example, micro-truss pore diameters can be engineered to a very precise and uniform size to prevent transport of specific chem-bio agents, while allowing water vapor diffusion and providing ballistic protection.

2.2.2 Integrated Evaporative Cooling with Biological Decontamination

Johnson, *et al.* [Johnson, *et al.* (2003)] contacted liquid water from a reservoir into bundles of hollow fiber membranes, shown schematically in Figure 2.4, from which it evaporated to facilitate cooling of air in a duct. For this experiment, air blown over bundles of hollow fiber porous membranes caused water inside the hollow channels to evaporate. Water evaporation absorbed heat, effectively cooling the bundles, and the air passing over the bundles was in turn cooled and humidified. Hollow fiber membranes with small pore size (less than 100 nanometers) prevent microbes and bacteria from passing while allowing water vapor transfer. Therefore, the membrane served as a barrier to biological contamination between potentially dirty feed water in the hollow membrane and the duct carrying chilled air to into a building. This technology was therefore attractive for sanitary and hygienic cooling applications and potentially for water purification and desalinization.

Two types of membranes were studied by Johnson, *et al.* The first was a tubular configured polypropylene micro-porous hollow fiber membrane manufactured by Mitsubishi Rayon Co. with an inner diameter of 200 μm and an outer diameter of 242 μm (Figure 2.4). The effective pore size was 100 nm and the porosity was 46.7 percent (according to the manufacturer). Pore

tortuosity was experimentally measured using a Wilson plot [Wilson (1915)] to be 6.5. The second was a tubular polypropylene micro-porous hollow fiber membrane made by Celgard Inc. with an inner diameter of 240 μm and an outer diameter of 300 μm (Figure 2.4). The effective pore size was 30 nm, the porosity was 40 percent, and the pore tortuosity was 2.75 (according to the manufacturer).

Ø 0.03 μm

300 μm

240 μm
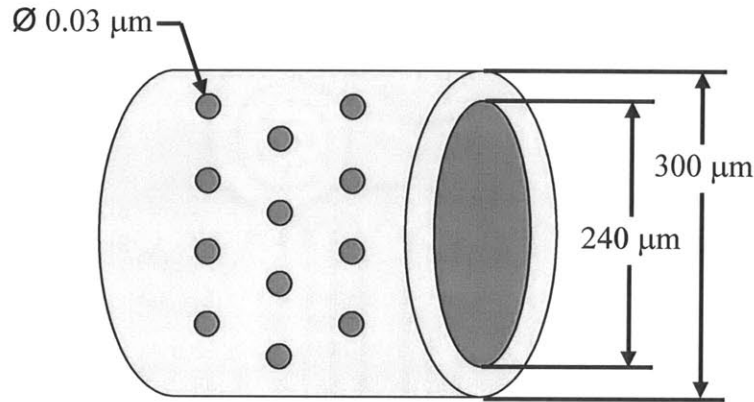
Figure 2.4: Important dimensions of polypropylene micro-porous hollow fiber made by Celgard, Inc. and used for multi-functional cooling and biological protection by Johnson, *et al.* (2003).

The authors used a textbook heat transfer correlation for flow over a cylinder to model heat transfer from the hollow-fiber membranes operating in cross flow:

$$Sh = 0.61\,\mathrm{Re}_D^{0.363}\,Sc^{0.33}$$ (Equation 2.13)

where Sh is the Sherwood Number, Re_D is the Reynolds Number (based on cylinder outer diameter), and Sc is the Schmidt number. Since the membranes used in Johnson *et al.* had very small pore diameter, diffusion through the pores was within the regime of $1.0 < Kn < 3.3$. Therefore the mass transfer coefficient through the pores, $\hbar_m$, is described by

$$\hbar_m = \frac{D_K \cdot \varepsilon_v}{\tau \cdot L_{mem}}$$ (Equation 2.14)

where D_K is the Knudsen diffusion coefficient (Equation 2.9), ε_v is the membrane porosity, L_{mem} is the membrane thickness, and τ is the channel tortuosity. Using these parameters, Johnson *et al.* [Johnson, *et al.* (2003)] formulated a dimensionless *membrane number*

$$\zeta = \frac{r \cdot \varepsilon_V}{\tau \cdot L}$$ (Equation 2.15)

where r is the pore radius. High ζ corresponds to better heat and mass transfer performance because it implies large pore diameter, high overall porosity, small tortuosity, and a thin membrane.

The rate of water evaporation through the pores was modeled as two resistances in series: 1) transport resistance through the membrane and 2) transport resistance through the air boundary layer adjacent to the membrane. This approximation was confirmed by comparison to heat transfer behavior predicted under the Chilton-Colburn analogy:

$$\hbar_{BL} = \frac{h_{BL}}{\rho \cdot C_p} \left(\frac{Pr}{Sc} \right)^{\frac{2}{3}}$$ (Equation 2.16)

where $\hbar_{BL}$ is the mass transfer coefficient of the boundary layer, h_{BL} is the heat transfer coefficient of the boundary layer, ρ is the density of air, C_p is the heat capacity of air, Pr is the Prandtl number, and Sc is the Schmidt number. By determining the heat transfer coefficients of interest and applying Equation 2.16, the authors estimated the mass transfer coefficients, which were then compared to the experimental results.

The authors measured the values of humidity and temperature in a duct at stations before the hollow membrane bundles and after. Mass flow rate of water was measured by the change in weight of a liquid water reservoir continuously feeding the hollow fiber membranes. Distilled water was used in this study to eliminate complications arising from using salt solutions, such as clogging of the membrane pores. Although Johnson, et al. did not address this concern, over time, the membrane filters would certainly clog and lose cooling efficacy. When clogging became too severe, the membranes would have to be cleaned or replaced.

From the collected data, experimental heat and mass transfer coefficients for the apparatus were determined. Convective boundary layer effects in the bundles dominated the heat transfer process. Thus, the global heat transfer coefficients remained relatively unchanged despite changes in ζ between membranes. The measured overall heat- and mass-transfer coefficients for the hollow fiber membranes were found to be slightly less than predicted by the model correlations. The authors found an intrinsic mass transfer resistance from the membrane bundles that ranged between 33 s/m and 67 s/m depending on the fiber bundle arrangement and the Reynolds Number over the bundles. Johnson et al. [Johnson, et al. (2003)] speculate that this result was due to the leading fibers shielding other fibers in the bundle from the free stream flow.

The authors also provided a definition for evaporative cooling effectiveness: the ratio between experimental air temperature decrease and the maximum theoretical decrease when air is cooled to the wet bulb temperature. For conventional evaporative cooling systems, this ratio is between 70 and 90 percent. The authors conclude that the proposed hollow fiber membrane bundle system showed promise in performing equally well to conventional systems while keeping the cooled air safe from biological contaminants.

The qualitative similarities between Johnson et al. [Johnson, et al. (2003)] and the evaporative cooling research contained in this thesis are important. The authors advanced a model for heat and mass transfer for evaporative cooling through nanometer-scale pores, and they tested this model with an experimental apparatus. In this thesis, heat and mass transfer modeling was executed using several tools including 1) a First Law heat balance, 2) natural convection correlations from the heat transfer literature, 3) forced and free convection coefficients for mass transfer, and 4) continuum and transition regime diffusion models to predict flow through porous membranes.

There are several differences between the work in Johnson, et al. [Johnson, et al. (2003)] and this thesis. The membranes studied by Johnson, et al. were tubular while the samples studied in this thesis were flat. In addition, the hollow fiber membranes being studied by Johnson et al. were made from polypropylene using a process that produced tortuous, irregular pores. These researchers had no control over the geometry of the pores in their membranes. In contrast, the membranes studied in this thesis had relatively straight-through channels of cylindrical cross section with their axis oriented essentially normal to the membrane face. Pore diameters were also well-controlled. These features were made possible because the membrane fabrication processes enabled good control over pore geometry.

2.2.3 Energy-absorbing and Rigid Structures

Sypeck and Wadley [Sypeck and Wadley (2001)] provide several examples of multi-functionality in open cell metallic truss including load supporting structures, mechanical impact/blast absorption, thermal management, noise attenuation, catalyst support, filtration, electrical energy storage, retardation of chemical reactions and/or fire, and scaffolding for in-growth of biological tissue. Using a textile synthesis approach of laminating two-dimensional wire metal mesh to form three-dimensional metallic truss, Sypeck and Wadley sought a geometric structure that provided efficient in-plane support, excellent mechanical energy

absorption, and high heat transfer conductivity. However, the reported process did not produce micro- or nano-scale features: the resulting samples were cubes on the order of 25 mm per side made of metal wires with 1 mm diameter.

While meeting many of the functional properties sought by Sypeck and Wadley, nano-truss and simulant materials studied in this thesis enjoy additional multi-functional advantages to metal mesh. By using lithographic polymers instead of drawn metal wires as the basic building block, nano-truss structures can be made substantially smaller, allowing the critical dimensions to be on the micro- or nano-scale. While beneficial for mass transport, these materials can also be used as photonic and phononic crystals. The design of phononic band gaps can be specified to impact physical material properties such as thermal conductivity and heat capacity [Gorishnyy, *et al.* (2005)].

2.3 Methods for Testing Water Permeability Through Fabrics

A substantial volume of porous material heat and mass transport research relevant to this thesis arises from the textile engineering literature. There exist several prescribed methods for testing mass transport through fabrics. McCullough, *et al.* [McCullough, *et al.* (2003)] survey five of the major methods: ASTM E 96 B (Upright Cup Method), ASTM E 96 BW (Inverted Cup Method), JIS L 1099 (Desiccant Inverted Cup Method), ASTM F 1868 (Sweating Hot Plate Method), and ASTM H 2298 DMPC Diffusion Test). The essential features of these methods are summarized in Figure 2.5.

Despite the existence of several accepted fabric testing methods, only the Sweating Hot Plate Method yields an apparatus-independent mass transfer resistance (subject to the assumption that apparatus contributions to mass transport resistance remain the same with and without the test fabric affixed). In this test, the apparatus mass transfer resistance is independently measured and subtracted from the total mass transfer resistance inclusive of the textile being tested. The other four methods surveyed by McCullough, *et al.* provide only mass flux rate through the fabric under specified conditions. While useful for comparing the mass transfer rates of various textiles under prescribed conditions of a particular test [Barker (2006)], these methods are less attractive for detailed engineering design computations.
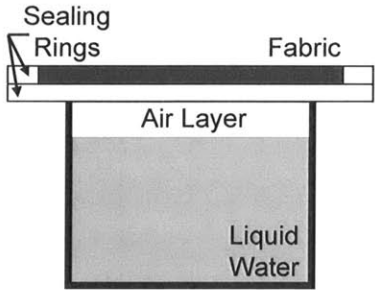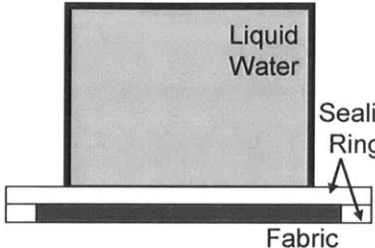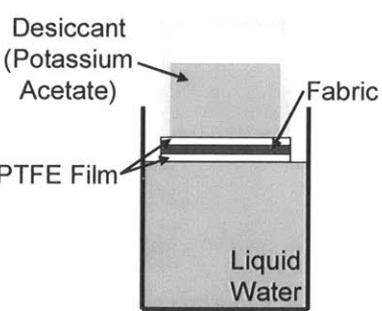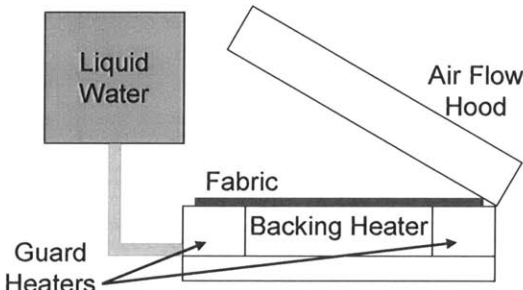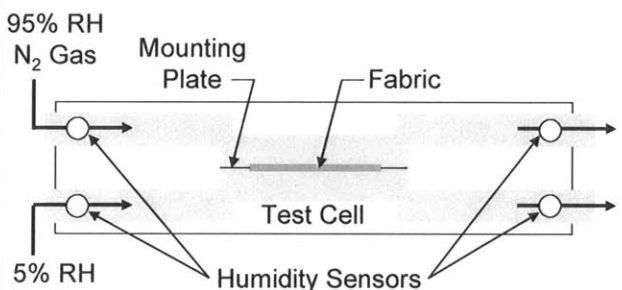
Upright Cup Method

Sealing Rings — Fabric — Air Layer — Liquid Water

$$WVTR = \frac{M/t}{A} = \left[\frac{grams}{hour-meter^2} \right]$$

Advantages:
Best simulation of sweaty skin and dry fabric
Disadvantages:
Lowest WVTR of any method
Long test (t ~ 30 hours)

Inverted Cup Method

Liquid Water — Sealing Rings — Fabric

$$WVTR = \frac{M/t}{A} = \left[\frac{grams}{hour-meter^2} \right]$$

Advantages:
Best simulation of soaked fabric

Disadvantages:
Only water-proof samples
Long test (t ~ 30 hours)

Desiccant Inverted Cup

Desiccant (Potassium Acetate) — Fabric — PTFE Film — Liquid Water

$$WVTR = \frac{M/t}{A} = \left[\frac{grams}{hour-meter^2} \right]$$

$$WVTR = \frac{4(M_1 - M_o)}{A} = \left[\frac{grams}{hour-meter^2} \right]$$

Advantages:
Short test (t ~ 15 minutes)
Inexpensive, easy to run
Disadvantages:
Chemical potential "artificial"
No accommodation for RH

Sweating Guarded Hot Plate Test

Liquid Water — Air Flow Hood — Fabric — Backing Heater — Guard Heaters

$$\sum R_{mass\_transfer} = \frac{A(P_2 - P_2)}{\Pi} = \left[\frac{Pascal-meter^2}{watt} \right]$$

Advantages:
R_{mem} not as susceptible to flow rate as WVTR
Test accounts for input power
RH level controlled by saturation of free air
Most accurate simulation of heat/mass transfer in skin/clothing

Moisture Permeation Cell

95% RH N_2 Gas — Mounting Plate — Fabric — Test Cell — Humidity Sensors — 5% RH N_2 Gas

$$\dot{m} = \frac{\rho_2 - \rho_1}{A} \dot{\forall} = \left[\frac{mass}{sec-meter^2} \right]$$

$$\sum R_{mass\_transport} = \frac{\Delta C}{\dot{m}} = \left[\frac{seconds}{meter^2} \right]$$

Advantages:
Same RH gradient at different levels testable
Disadvantages:
Nitrogen used instead of air
Expensive, requires computer automation

Figure 2.5: Overview of the fabric permeability tests surveyed by McCullough, *et al.* (2003), showing which properties are measured as well as advantages and drawbacks to each approach. WVTR is water vapor transmission rate, M is mass, t is time, A is area, P is partial pressure, Π is input power, ρ is mass concentration, $\dot{\forall}$ is volume flow rate, and ΔC is the log mean concentration difference across a sample. *Images in this figure are based on originals in McCullough,* et al. *(2003).*

2.3.1 Sweating Hot Plate Method

The Sweating Hot Plate Method apparatus is shown in Figure 2.6. The units of data derived from this test are [Pa-m^2/watt], which convert to [s/m]. Subject to a key assumption, this method provides an intrinsic (apparatus-independent) fabric mass transfer resistance because it experimentally accounts for the mass transfer impedances of all the components in the absence of the fabric being tested. The key assumption is that these other contributions to overall mass transfer, which are quantified in a separate control experiment, remain unchanged during the experiment with the fabric.
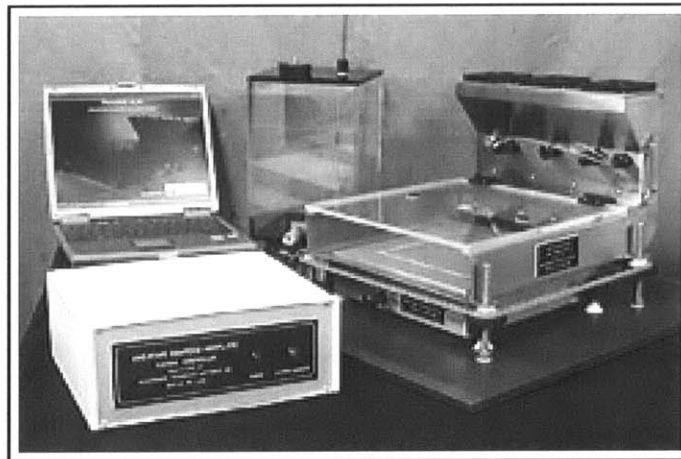
Figure 2.6: This commercially-available guarded sweating hot plate apparatus is distributed by Measurement Technology Northwest. *Image used with permission of Measurement Technology Northwest (see Thesis page 209).*

Guard heaters are utilized with great care to control undesirable parasitic heat leakage. Air of prescribed relative humidity is blown over the fabric surface to control the partial pressure of water vapor in the external boundary layer. The Sweating Hot Plate Method does not directly measure surface (skin) temperature because this variable is pre-selected. The experiment quantifies the rate of energy dissipation needed to drive just sufficient evaporation at a given ambient humidity to maintain the surface at that temperature. This information is of interest for thermal comfort purposes, and for a given pre-set skin temperature, complements the quantitative heat management information provided by the apparatuses described in this thesis (Chapter 4).

Nonetheless, the intrinsic resistance derived from the Sweating Hot Plate Method is not a true diffusion mass transport resistance competent for utilization in mass transport equations for engineering modeling and design. An important contribution of this thesis is description and

implementation of two heat and mass transport apparatuses (Chapter 4) that provide intrinsic mass transport resistance data for membrane samples of interest. An important difference between the various existing fabric transport testing techniques and the apparatuses described in this thesis is that experiments herein continuously measure weight lost from the system. Therefore the mass transported through the membrane is quantified, and these data are convertible to intrinsic mass transport resistance values.

2.4 Human Thermal Comfort

To understand how the cooling techniques studied in this thesis will impact the comfort and safety of the ultimate customer, the Soldier, basic knowledge of the thermal management functions of the human body are critical. When the human body encounters a warm environment with reduced opportunities for heat mitigation, blood flow to the skin increases. Enhanced blood flow rate may double or triple the transmission of heat from the body core to the skin, and the temperature of the skin can rise as high as one degree C below that of the deep tissues. If the added heat dissipation associated with increased blood flow is still unable to balance heat input, the body releases liquid from the sweat glands for evaporative cooling. If evaporation is inadequate to restore equilibrium, body temperature must increase, driving additional heat release. However, when deep body temperature rises more than 2 °C above 37 °C, humans begins to lose cognitive abilities. Core body temperature above 43 °C is lethal if endured longer than a few minutes [ASHRAE (2005)].

An average-sized human can generate as little as 40 w/m^2 of metabolic heating while sleeping to as much as 505 w/m^2 in short, very intense bursts of physical activity [ASHRAE (2005)]. About 200 w/m^2 is generated during light exercise such as calisthenics where the body is unencumbered by additional weight. Since this thesis studies peak Soldier thermal load situations, the metabolic output of 350 w/m^2 was selected as a representative metabolic heat load. This load is meant to represent the heat generated by a Soldier carrying a full march load (120 to 150 pounds) while sustaining the velocity of a rapid march or jog (about 3 m/s).

2.5 Membrane Characterization

A critical component to modeling and testing membrane transport processes is detailed characterization of the membrane to determine transport-impacting features including pore diameter, membrane porosity, and membrane thickness. Chapter 3 of this thesis details several membrane topology interrogation techniques including micrograph imaging and gravimetric

weighing utilized herein to characterize the membranes of interest. To inform development of these methods, a literature survey of porous membrane characterization techniques was conducted to reveal best practices, the results inspired new, innovative approaches.

According to Tomlins, *et al.* [Tomlins, *et al.* (2004)], random porous materials can be expected to have the following types of cavities. "Pores" (sometimes called thru-pores) are channels connecting two or more external faces of a sample that occur as open volumes within an otherwise solid material. "Through pores" are an engineered network of channels that permit mass transport from one external face or surface of a sample to another. "Blind pores" are pores connected to only a single external sample surface. "Closed cells" are voids isolated within an otherwise solid material that do not connect with any external surfaces.

Porosity, or void volume, is expressed as the ratio of cavity volume (including "closed cells") to the total volume of material. Measuring the porosity, dimensions, and distribution of pore sizes is difficult due to 1) lack of techniques to accurately probe pore penetration, 2) inability of computer programs to correctly analyze complex images, 3) limitations in the applicability of particular techniques to a wide range of sample types without causing damage, 4) need for tedious human work.

Tomlins, *et al.* compare porosity measurement methods reliant upon intrusion of fluid or inert gas (i.e. mercury porosimetry and helium pycnometry) to other techniques. A summary of this discussion is given in Table 2.1. Porosimetry is limited because only the volume of open (and to some extent blind) pores is accessible while voids are missed. Porosimetry can also damage pores because attempts to access the smallest pores of interest require pressures that compress or distort soft materials. In addition, according to Tomlins, *et al.* [Tomlins, *et al.* (2004)], porosimetry assumes that the pores within a structure are cylindrical in cross-section which is unlikely to be the case for random porous substrates.

In addition to porosimetry, there are several other ways to characterize porous membranes, including scanning electron microscopy (SEM) and gravimetric approaches. Historically, various types of porosimetry (e.g. mercury porosimetry, gas–liquid displacement porosimetry, and liquid–liquid displacement porosimetry) were the most accepted way to determine porosity and pore size. However, SEM characterization of micro-truss simulants such as track-etched membranes is now considered the most reliable standard for membranes in which surface pore radii remain essentially unchanged along the pore through the whole membrane [Calvo, *et al.*

(2004)]. All membranes studied in this thesis have straight-through pores that meet this extrapolation criterion.

Table 2.1: Techniques for investigating the microstructure of porous materials. *Table adapted from original* [Tomlins, *et al.* (2004)].

Technique	Information Available
Microscopy Electron microscopy Optical microscopy Confocal microscopy Optical coherence tomography Optical coherence microscopy	Pore shape, size and size distribution, porosity.
Micro X-ray computer tomography	Pore shape, size and size distribution, porosity (μm resolution)
Gravimetric analysis	Pore volume of capillary pores
Density determination	Porosity
Mercury porosimetry	Porosity, total pore surface area, pore diameter, pore size distribution (μm resolution)
Porometry	Median pore diameter (assuming cylindrical geometry), through pore size distribution
Diffusion of markers	Permeability
NMR	Pore size and distribution
Nitrogen adsorption (BET method)	Pore surface area

According to Calvo, *et al.* [Calvo, *et al.* (2004)], porosimetry is criticized in the literature for failure to provide reproducible results and for being extremely slow (5 to 8 hours for a single test). Porosimetry can also return incorrect results. For example, overpressure in the porosimetry apparatus can open pores with smaller radii than those being probed causing the deduced mean pore size to be too large. Inadvertent pore opening is not reversible. Calvo, *et al.* [Calvo, *et al.* (2004)] attempted to prove that the liquid–liquid displacement porosimetry technique (replacing water with alcohol) did not inadvertently open pores. However, their "before exposure" and "after exposure" data showed that the liquid-liquid process did change the pore radius (and membrane porosity) to an extent greater than can be explained by experimental error. It was implied that pore stretching under pressure was to blame for erroneous results.

Hernandez, *et al.* [Hernandez, *et al.* (1997)] utilize a Computer Image Analysis (CIA) SEM procedure similar to the method that was independently developed for this thesis to enable membrane characterization. The Hernandez, *et al.* SEM process characterized an entire 47 mm diameter membrane using properties measured from about 300 pores. Five to ten images of roughly 4200 nm x 3000 nm from randomly selected locations on each sample were used. At most 1.26×10^{-10} m^2 are imaged, representing roughly 0.000007% of 1.73×10^{-3} m^2 in a 47mm diameter membrane disk. More reliable membrane topology statistics were obtained in this thesis by taking hundreds of SEMs at systematically-selected locations over an entire 47mm diameter membrane.

3 Membrane Selection and Characterization

To study the impact of pore size on vapor transport and cooling efficacy, the ideal test specimens would be a series of membranes with perfectly straight-though pores. These pores would be circular in cross section and spatially distributed evenly across the surface of the membrane. The pores would come in a spectrum of diameters from 1 nm to 10,000 nm (10 μm) in regular intervals (e.g. 1 nm, 5 nm 10 nm, 50 nm, 100 nm, 500 nm, 1000 nm, 5000nm, and 10,000 nm), and the membrane material could be made hydrophobic or hydrophilic without any other significant chemical or physical change to the membrane. To isolate pore diameter for systematic study, each membrane would have identical thickness, identical porosity, be made of the same homogeneous material, and have uniform (extremely low) surface roughness. Moreover each membrane would be immune to chemical or physical changes induced by exposure to the liquids and vapors utilized in experiments or applications over the full temperature range of interest.

Membranes with two-dimensional micro-truss structures fabricated using interference lithography (Figure 3.1) show promise for simultaneously meeting requirements for pore size range as well as other characteristics desired for this thesis. Unfortunately, uniform periodic samples of micro-truss cannot yet be fabricated as individual pieces large enough to accommodate macro-scale mass transport tests using the apparatus developed for the present research [Thomas (2005)]. Thus, to conduct the research in this thesis, appropriate micro/nano-truss simulant materials were identified.

3.1 Selecting Micro-Truss Simulants

There are numerous commercially-available membranes that are potential simulant candidates for micro/nano-truss. In selecting an appropriate surrogate, candidate membranes must meet as many of the idealized criteria outlined above as possible. In addition the membranes must be commercially available in samples at least 30 mm in diameter to assure the targeted heat and mass transfer properties can be studied under practically meaningful conditions using the apparatuses developed for this research. Membranes explored for potential use in this research included anodized aluminum [Jessensky, *et al.* (1998)] (Figure 3.2a), Celgard membranes (made of polypropylene) [Celgard (2007)] (Figure 3.2b; cellulose filters [Choi (2005)] (Figure 3.2c), electro-spun mats (made of PMMA [Yu (2007)] or Nylon 6,6 [Gibson, *et al.* (2001)]) (Figure 3.2d), DuPont porous membranes [Kapur (2005)] (made of Nucrel® or

Hytrel®) (Figure 3.2e), Teflon (PTFE) filters [Millipore (2007a)] (Figure 3.2f), and polycarbonate track-etched filters (Figure 3.2g) [Millipore (2007b)]. Table 3.1 shows how many of the idealized criteria each of the candidate membranes meets. Based on their attributes, DuPont porous membranes and track-etched membranes were selected as top prospects for further research. Although anodized aluminum was also an attractive option, this metal-based material had significantly different thermal properties than micro-truss (which is made using soft materials, i.e. SU-8 photo-resist.); so, it was eliminated as a potential simulant.
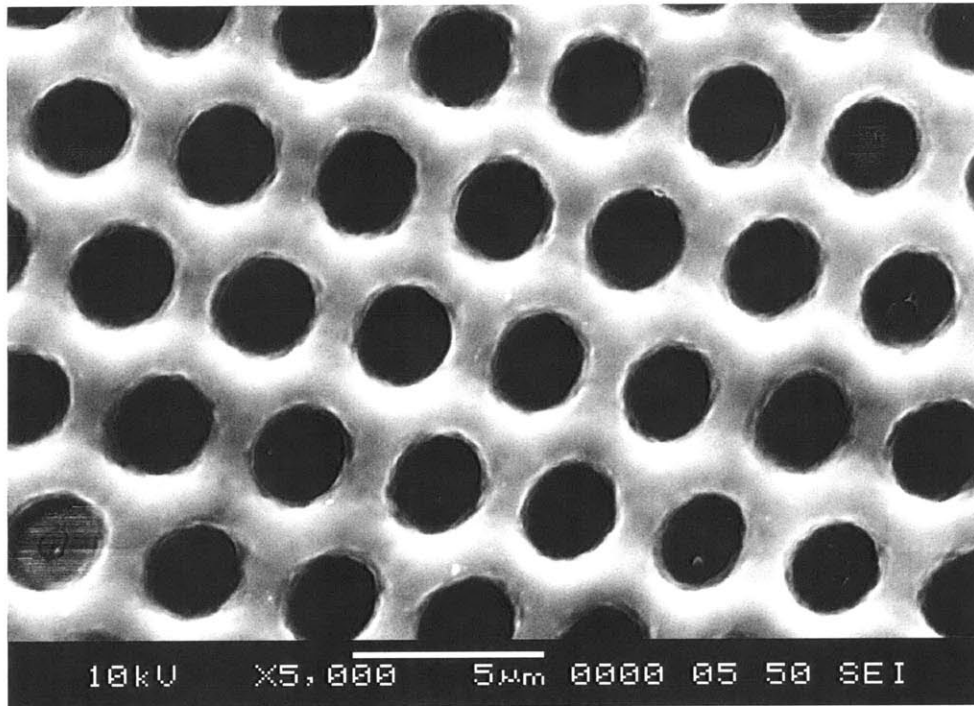
Figure 3.1: Scanning electron micrograph of two-dimensional micro-truss shows periodic straight-through pore geometry, ideal for mass-transport studies. Straight-through architecture is assured because the pores are generated via an etching process that dissolves material in the axial direction. *Micrograph courtesy Dr. Ji-Hyun Jang and Taeyi Choi, Thomas Group, MIT.*

Table 3.1: Attributes significant to mass transfer studies of various candidate porous membranes to serve as micro/nano-truss surrogates.

Membrane Type	Through Pores	circular cross section	distributed equally	Tight Diameter Control	spectrum of diameters	Adjustable Contact Angle	Identical thickness	Identical Porosity	Homogeneous Material
Anodized Aluminum		X	X	X	X		X		X
Celgaurd Membrane		X			X		X	X	X
Celulose Filter					X		X	X	X
Electrospun Mats						X	X		X
DuPont Membrane	X	X	X	X	X	X	X	X	
Teflon Filter					X		X	X	X
Track-Etched Filters	X	X		X	X	X	X	X	X

47

A: Anodized Aluminum[α]

— 100 nm

B: Celgard Membrane[β]

Celgard, Inc. Magnification 20,000x

C: Cellulose Membrane[γ]

D: Electrospun Mat[δ]

5kV   X5,000   5μm   08 45 SEI

E: DuPont Porous Mem.[ε]

5kV   X4,000   5μm   19 25 SEI

F: Teflon Membrane[ε]

2.5kV   X45 500μm

G: Track-etched Mem.[ε]

5kV   X750   20μm   r3b3rm
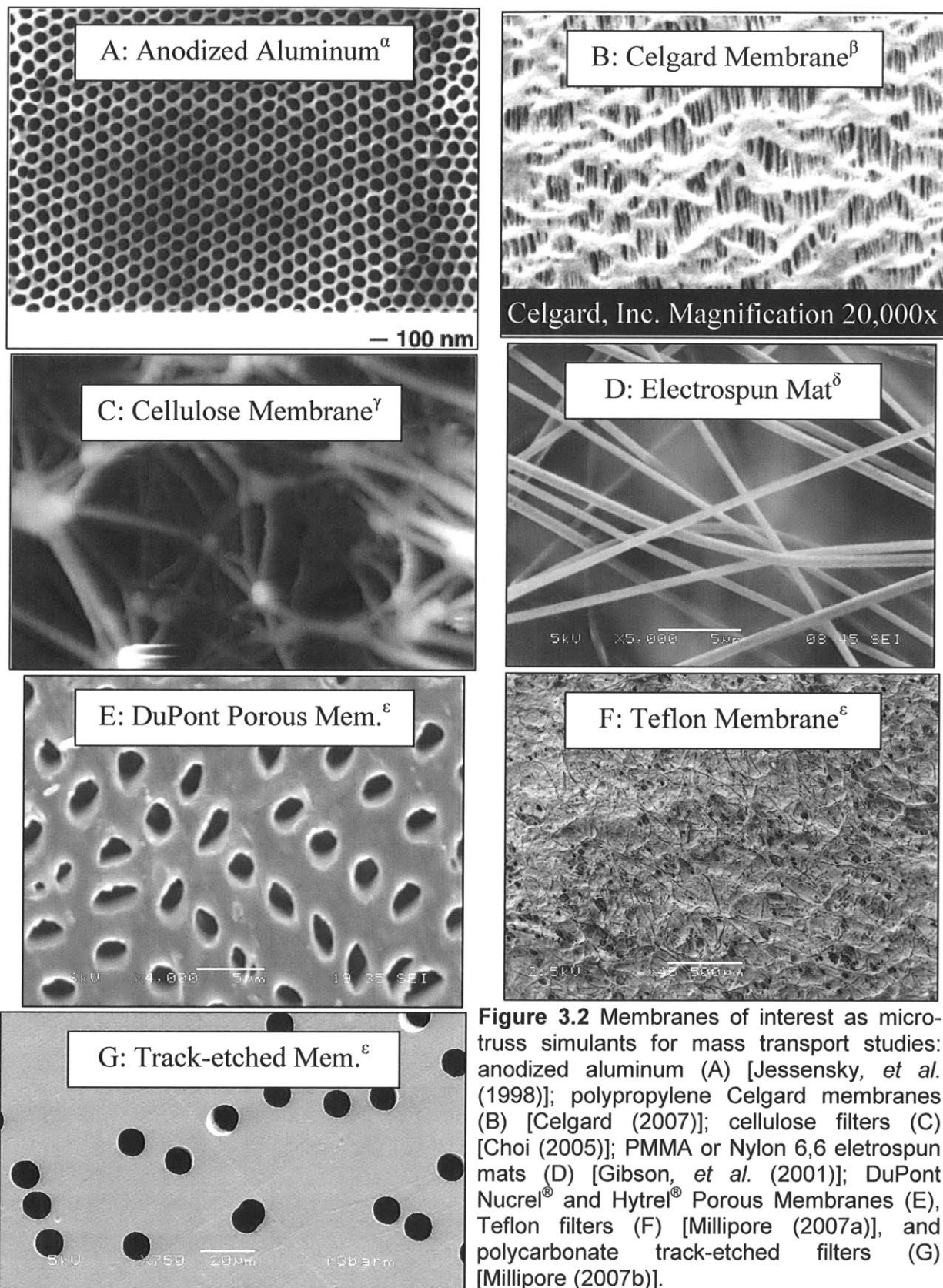
Figure 3.2 Membranes of interest as microtruss simulants for mass transport studies: anodized aluminum (A) [Jessensky, *et al.* (1998)]; polypropylene Celgard membranes (B) [Celgard (2007)]; cellulose filters (C) [Choi (2005)]; PMMA or Nylon 6,6 eletrospun mats (D) [Gibson, *et al.* (2001)]; DuPont Nucrel® and Hytrel® Porous Membranes (E), Teflon filters (F) [Millipore (2007a)], and polycarbonate track-etched filters (G) [Millipore (2007b)].

3.2 Overview of Candidate Simulant Samples

Details for DuPont porous membranes and track-etched membranes, derived from manufacturer data, are provided in the following sections.

3.2.1 DuPont Porous Membranes Background

DuPont porous membranes are a pre-commercial product developed by the DuPont Company. The membranes are created using a proprietary, patent-protected process that cannot be disclosed in this thesis due to a standing non-disclosure agreement between ISN and DuPont. This process results in membranes that are about 125 μm thick with straight-though pores. Nominally, the pores are circular in cross-section, but stretching can permanently deform the pores into long ovals. DuPont porous membranes can be made of many different materials and in many pore sizes [Kapur (2005)]. The samples used in this thesis were early examples of DuPont porous membranes and as such showed wider distributions of pore sizes and greater variability (i.e., more non-circularity in the pore cross sections) than the eventual commercial-quality product. The parent materials of the DuPont porous membranes used for this thesis, Nucrel® and Hytrel®, are both hydrophobic. According to DuPont, Nucrel® is a random copolymer of ethylene and methacrylic acid (12 weight percent), and Hytrel® is a random polyetherester copolymer formed by the condensation of terephthalic acid, tetramethylene glycol, and poly tetramethylene glycol. [Kapur (2005)] DuPont has the capability to make these porous membranes out of hydrophilic polymers as well.

According to DuPont, the Nucrel® membranes have pore diameters ranging from 1 to 2 microns with the majority of pores at about 1.5 microns. The method used by DuPont to determine this pore size information was the so-called *pressure burst test* in which membranes are soaked in liquid water until the pores are saturated. The samples are then subjected to an increasing pressure differential meant to blow the water out of the channels. Larger channels impose smaller capillary force on the water, and consequently water is blown out of these pores at a lower imposed pressure differential than for smaller ID channels. By measuring the amounts of water released from the channels as affected by successively higher pressures, DuPont was able to calculate the pore size distribution. DuPont did not perform pressure burst tests on the Hytrel® membranes. However, by electron micrograph analysis, DuPont reports that the pore size for Hytrel® samples is between 20 and 25 micrometers [Kapur (2005a)].

3.2.2 Track-etched Membranes Background

According to Hanot, *et al.* [Hanot, *et al.* (2002)], track-etched membranes (Figure 3.3) are thin polymer films with discrete pores formed through a combination of charged-particle bombardment (or irradiation) followed by chemical etching. Particle bombardment forms damaged areas in the film (called tracks), which are subsequently etched with a suitable chemical to create pores with a pre-selected inner diameter (ID). The energetic bombarding particles are nearly identical in size and kinetic energy. Consequently, the tracks produced by each particle are similar under two assumptions: 1) the angles of incidence of the particle beams are similar and 2) prior particle bombardment does not significantly modify the substrate's susceptibility to additional particle impacts. Many materials could potentially be processed via track etching, (e.g., plastic, glass, some minerals), but this technology has only seen commercial use in polymer membranes. The etching process passes the irradiated tracked film through a series of chemical baths. The duration of bath exposure and the chemicals utilized determines the size of the pores. While typical membrane thicknesses are between 10 and 20 μm, particles produced by a cyclotron can be used to make track-etched membranes up to 100 μm thick. Thickness variation in commercial track-etched membranes can usually be controlled to within ± 1 μm. While membranes 100 μm thick would have been most valuable to this thesis due to their large, highly measurable mass transport resistance with respect to other apparatus resistances, thick track-etched samples were not commercially available.
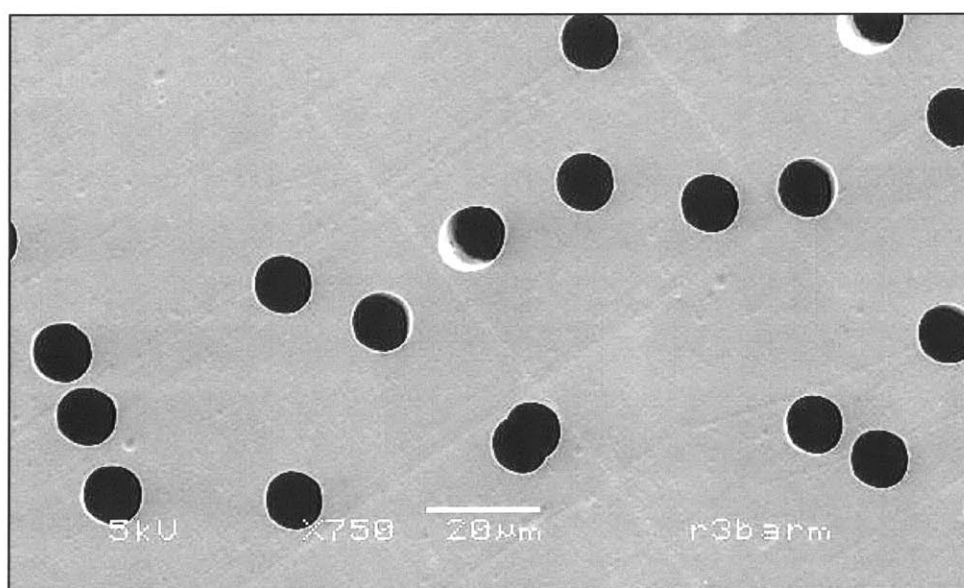
Figure 3.3: Millipore Isopore track-etched membranes contain nearly circular pores.

50

The commercially-available pore size spectrum for this process is 10 nm to 15 μm. There is no theoretical maximum limitation on pore diameter. The fundamental lower limitation on pore size is determined by the etch duration required to dissolve enough material to make through pores. For 5-μm-thick membranes, the lower limit on pore diameter is 10 nm. Manufactures report that variability in pore diameter during production is minimized because it is highly-controlled. However, pore diameter characterization performed for this thesis revealed a variation between -20% and +26% of the pore size stated by the manufacturer for diameters down to 50 nm. A 290% error for 10 nm pore diameter samples was also observed (that is, 39 nm pore diameter was measured in samples which the manufacturer claimed contained 10 nm pores). According to manufactures, the coefficient of variance in pore size from one lot to the next is typically 2 to 3 percent. Pore density (porosity) can also be controlled, and typical pore number density ranges from 1×10^5 to 6×10^8 pores/cm^2, depending on pore size.

3.3   Characterization Tools and Approaches

Membrane average pore size and the pore size distribution were determined through independent characterization studies on all membranes utilized in this thesis. Average and statistical distribution of pore diameter for both DuPont porous membranes and track-etched membranes with pores larger than 220 nm was determined by scanning electron microscopy (SEM). Since the resolution of the SEM at the ISN is about 100 nm, Focused Ion Beam (FIB) was utilized to image track-etched membrane samples with pore diameters below 220 nm. For track-etched membranes, the density of bulk polycarbonate was known, which enabled porosity to be determined gravimetrically. Since polycarbonate is resistive to buckling and tearing when folded, track-etched membrane thickness was determined by folding samples 4 or 5 times and using a micrometer to measure thickness of the sandwiched sample. Hereafter in this thesis, this technique is referred to as the "fold & mic" method. Alternatively, several membranes could have been stacked to measure thickness, avoiding the error associated with measuring a fold crease. However, each membrane had different thickness; so, higher accuracy for individual membrane thickness was obtained by folding a single sample instead of stacking several samples.

For DuPont porous membranes, the density of the bulk materials (DuPont Nucrel® and Hytrel®) was not known at the time characterization was conducted. Therefore, average and statistical distribution of membrane porosity and membrane thickness were determined via SEM.

The DuPont porous membrane samples could not be folded without damage. To obtain membrane thickness, samples were frozen in LN_2 and sliced using a razor or microtome. These samples were them imaged on-edge under SEM to measure membrane thickness. On-edge sample images prepared by the micro-tome also confirmed the straight-through, continuous nature of the DuPont porous membrane channels.

3.3.1 Sample Preparation for SEM and FIB Pore Characterization

Since all membranes under study in this thesis were made of polymer materials that were electrically non-conducting, sample preparation was required for characterization using SEM and FIB. Before imaging, all samples were cut with a sharp razor blade into approximately square sections small enough to fit onto an SEM/FIB stage. Samples were cleaned with dry nitrogen gas for 20 to 30 seconds. The samples were then affixed to the SEM/FIB stage with conducting tape using tweezers and placed in a sputter coater.

For samples with pores larger than 220 nm, a thin layer of gold 20 to 30 nm thick was coated onto each sample within the sputter machine. The sputtered layer uniformly coated the outer face of the membranes but did not penetrate deep into the pores. For samples with pores smaller than 220nm, 3 to 4 nm of palladium was coated onto each sample in the sputter machine. Since sputtered palladium crystals are smaller than sputtered gold crystals, palladium is superior to gold for imaging very small features. Once covered with a conductive film, the samples were ready for SEM or FIB imaging.

3.3.2 SEM/FIB Measurement of Pore Diameter

Pore diameters of both the DuPont porous membranes and the track-etched membranes were determined by image analysis of each sample before mass transport testing on the evaporation experiment. For the DuPont porous membranes, each specimen was divided into a grid with roughly 500 nodes equally spaced from each other. The squares defined by these nodes were systematically examined in a regular continuous tracking pattern (left to right on one row and then right to left along the immediately adjoining row and then repeating this sequence). Between 380 and 500 individual SEMs were required to derive reliable pore size distributions that remained invariant with additional of SEMs above these numbers.

Image analysis was conducted using open source software (ImageJ) from NIH in a manner similar to Hernandez, et al. [Hernandez, et al. (1997)], but developed independently for this research. This software counted individual pixels of an image that were darker than some user-

defined threshold value and compared that pixel count to the total pixels in an image. SEMs of DuPont porous membranes appeared as if the pore openings were black while the solid material was light. The total pore area in an image was obtained by setting the software's grayscale threshold to count dark pixels associated with pores. The software could also calculate how many pores appear in an image by counting the number of dark pixel groupings that contain more dark pixels than some minimum user-defined threshold value. Average pore area for a single image was the quotient of total void area and the number of pores in each image. The mean of average pore areas from all SEM images defined the total mean pore area. Effective pore diameter, d_e, (defined below) was obtained form the total mean pore area.

Effective pore diameters of track-etched membrane samples were determined using the same method as the DuPont porous membranes. However, instead of hundreds of images (as with the DuPont porous membranes), only ten micrographs were utilized to characterize track-etched membrane pore diameters. Calvo, *et al.* [Calvo, *et al.* (2004)], suggested that pore diameters of track-etched membranes could be ascertained from as few as five micrographs due to the high-precision control over pore diameter variability inherent in the manufacturing process. For this thesis, ten unique micrographs were utilized to estimate track-etched membrane pore diameter.

3.3.3 SEM Membrane Thickness Measurements

DuPont porous membrane thicknesses were determined by SEM imaging the edge of razor-sliced membrane samples. Despite imparting severe damage to individual pores, razor slicing returned statistically identical membrane thickness results to micro-toming. Being less labor-intensive than micro-toming, razor slicing was the preferred method in this thesis to extract DuPont porous membrane thickness data.

As with porosity and pore size, high-quality thickness measurements required multiple images to obtain statistically-reliable results. Since DuPont porous membrane thickness was large relative to thickness variability, about 10 SEM thickness measurements were required to obtain repeatable results. The threshold number of images occurred when additional data no longer impacted the average and standard deviation associated with previous measurements.

3.3.4 Gravimetric Measurement for Porosity

Gravimetric determination is an additional method for measuring membrane porosity. Porosity is obtained by accurately measuring the thickness and diameter of samples to ascertain

the total volume. A pycnometer could also be used, but one was not available. Density of the material must also be accurately known. The ratio of the actual membrane mass to the theoretical mass of a non-porous membrane of identical volume gives one minus the void fraction, assuming the mass density is spatially uniform throughout the membrane. Since densities of the particular Nucrel® and Hytrel® materials of the DuPont porous membranes used in this thesis were not provided by DuPont at the time of characterization, gravimetric measurements could not be used to characterize the porosity of these membranes.

DuPont performed an alternative gravimetric study on their porous membranes. These studies relied upon weighing the membranes before pore material was removed and then re-weighing the membranes after the material was removed. These measurements combined with known densities of the membrane and pore materials allowed calculation of membrane porosity without any need to measure the sample volume. DuPont performed the following study to estimate the porosity of the Hytrel® porous membranes utilized in this research [Kapur (2006)]. Five Hytrel® membranes were weighed before and after removal of the pore material. The total weight with pore cores was 1.8135 g, and the total weight without pore cores was 1.2975 g. The density of Hytrel® used in these membranes was 1.17 g/cc, and the density of the core material was 1.07 g/cc; giving a Hytrel® volume of 1.109 cc and a void volume of 0.482 cc. The porosity obtained through these measurements was about 30.3%. According to DuPont, this porosity figure agrees well with complimentary flow rate experiments that determine the membrane porosity at roughly 30 percent.

A Hytrel® membrane from the same lot was also characterized at the ISN using 480 SEM images, representing 40.8 percent of the total membrane surface area. The resulting analysis indicated a membrane porosity of 8.6 ± 2.7 percent. This porosity result is also consistent with experimentally-measured mass transfer rates through the membrane predicted by the transition regime diffusion equation (Equation 2.10). This disagreement between gravimetric and imaging characterization for the DuPont porous membranes was also consistent with the results of the track-etched membrane analysis. It was found that gravimetric measurements consistently gave void fractions for porous membranes that were higher than those determined by SEM. However, it is still unclear why these two characterization approaches did not show closer agreement.

Since the density of polycarbonate was known, gravimetric measurements were conducted to calculate porosity of track-etched membranes. To determine the area of each sample, membranes were placed on a flat, black surface before being instrumented with thermocouples. Each membrane was photographed with a digital camera situated perpendicular to the flat surface. A scale bar of known length was included in each photograph. Membrane areas were determined by counting pixels within each image using ImageJ software from NIH (described in Section 3.3.2). The "fold & mic" method (described in Section 3.3) determined the thickness of each sample. To assure folding did not damage samples prior to evaporation experiments, thickness measurements were taken after experimental tests concluded.

Sample weighing took place on a high-precision Mettler-Toledo AB265-S balance (stated accuracy ± 0.01mg) sitting upon a marble balance table to reduce measurement error arising from vibration. Volume and weight measurements combined to give actual sample density, which was compared to the known density of polycarbonate to obtain membrane porosity. The porosity range stated by Millipore, the manufacturer, was 5% – 20% [Millipore (2007b)]. The measured porosity of the Millipore samples ranged from a low of 5.8% to a high of 32%. In addition, one membrane from General Electric was used with a porosity stated by the manufacturer of 0.047% (based on pore number density) [GE (2007)]. The gravimetrically-measured porosity was 1.4%.

3.3.5 Straight-through Nature of Pores

To represent a desirable micro-truss simulant, membrane pores should run straight-through from one exterior membrane face to another. For this thesis, the straight-through nature of pores was confirmed by imaging samples on-edge to visualize pore paths. However, the membranes had to be sliced and prepared for on-edge imaging without damaging the pores.

DuPont porous membrane samples were prepared by freezing the membranes in LN_2 and slicing with a micro-tome. The freezing process assured that the solid membrane phase was rigid and resilient to tearing during slicing, which kept the pores intact. Figure 3.4 shows that the pores of both Nucrel® and Hytrel® DuPont porous membranes do run continuously straight through the membrane in a direction nominally perpendicular to the surface of the membranes.
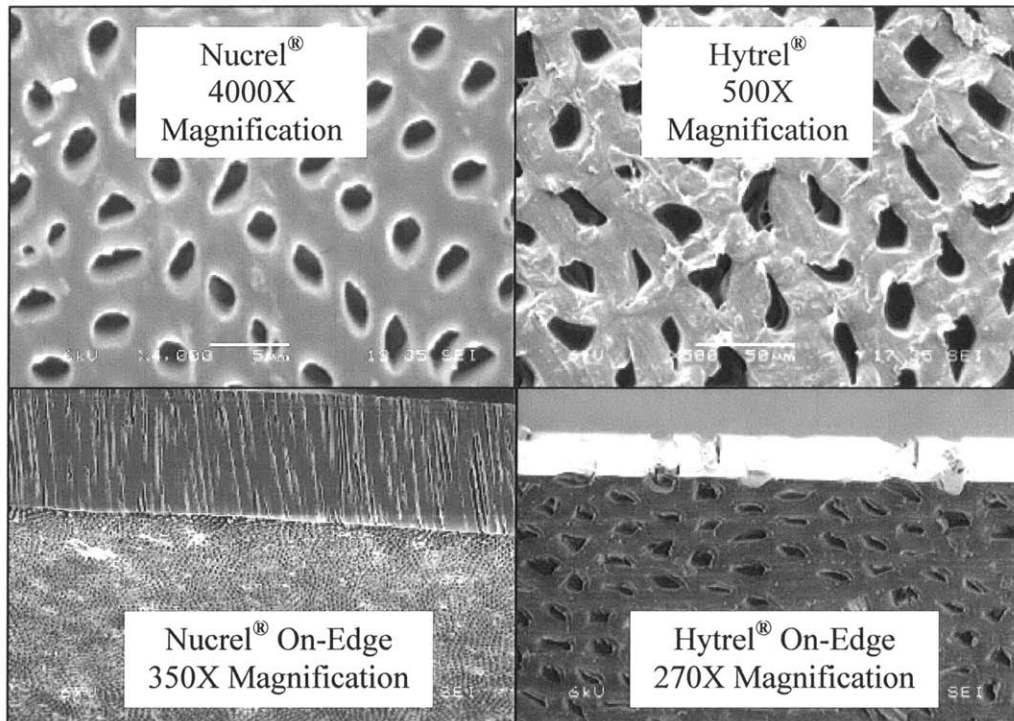
Figure 3.4: Scanning electron micrographs of membrane surfaces (top panels) and edges exposed by microtoming (bottom panels). The straight-through pore geometry is seen in the bottom panels.

Track-etched membranes could not be prepared by freezing and micro-toming because the glass transition temperature of polycarbonate is 150 °C, and freezing these membranes did not induce crystalline rigidity. Instead, these samples were prepared with a JOEL Argon-Ion polisher to reveal sample edges without damaging pores. Figure 3.5 shows pore tracks for a 100nm-pore-diameter track-etched membrane. While the pores ran straight-through from one external membrane face to another, the tracks were not normal to the external faces. Examining several on-edge track-etched membrane images revealed that pore tracks had a preferential angle through the material, which was apparently an artifact of the manufacturing process. This angle was no more than 24 degrees from normal. Thus, the increased diffusion path length arising from the canted pore tracks was no more than 9.5% greater than the membrane thickness. So, the impact on membrane transport resistance arising from non-normal pore path tracks was ignored for this thesis.
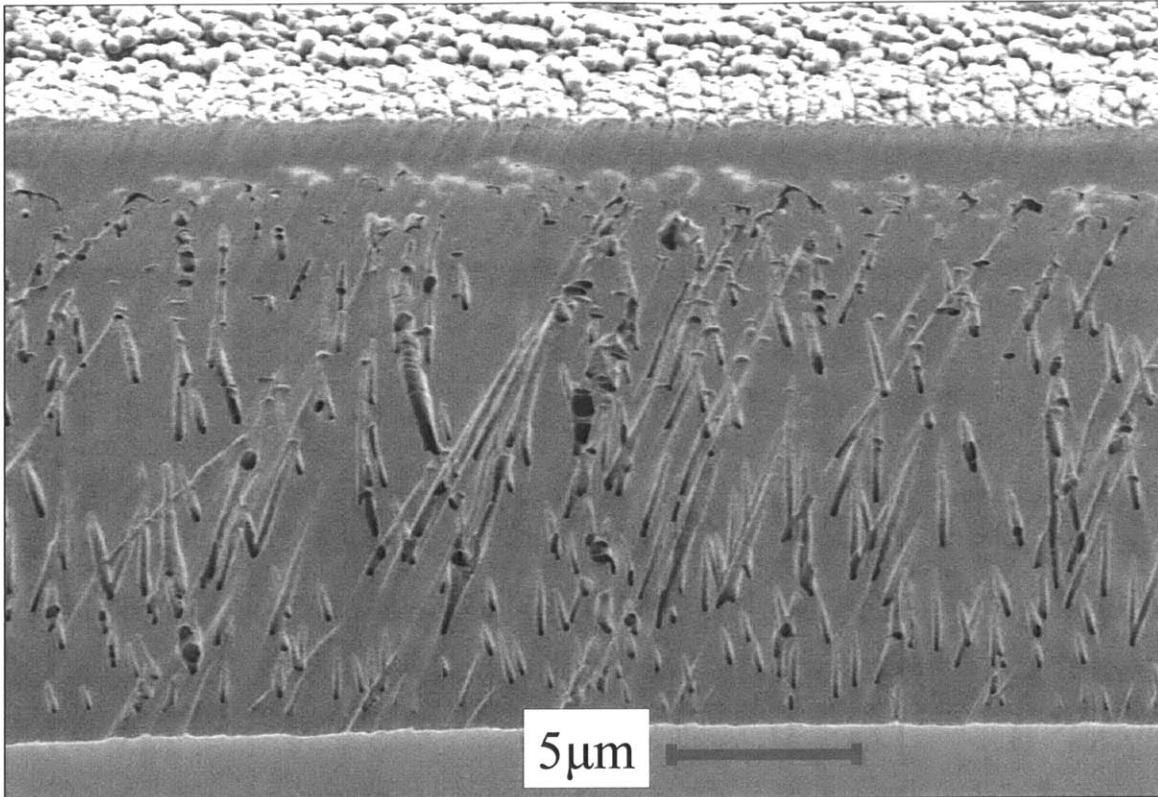
Figure 3.5: 100-nm-pore-diameter track-etched membrane with argon-ion polished edge imaged under FIB. Edge-on image taken with 45° tilt reveals that pores do run straight through between external membrane faces, but the tracks have a characteristic angle of less than 24°. This angle is an artifact of the manufacturing process.

3.4   Characterization Results for DuPont Porous Membranes

Two separate sets of low porosity (7.5-11.2%) DuPont porous membranes made of Nucrel® and Hytrel® were studied for this thesis. Membrane thicknesses pore diameters, and total porosity for four DuPont porous membrane samples is given in Table 3.2. A non-porous latex membrane was utilized as a negative control sample, and the characteristics of this sample are also given in Table 3.2. Based on SEM analysis, the Nucrel® membranes contained pores that were approximately circular in cross section (Figure 3.4), averaging 1.2 μm ID, whereas the membranes of Hytrel had pores of irregular, elongated cross section (Figure 3.4) with an average effective diameter (defined as $d_e = \left(4A/\pi\right)^{0.5}$) of 13.4 μm. Note that d_e differs from the conventional definition of hydraulic diameter, $d_h = \left(4A/p\right)$, where p is the wetted perimeter of the pore. Therefore, $d_e = \left(d_h p/\pi\right)^{0.5}$.

57

Table 3.2: DuPont porous membrane pore size and other geometric properties important for latent heat exchange with underlying surfaces.

Overlay [ ]	Membrane Thickness, L [μm]	Membrane Porosity, ε_v [%]	Ave. Pore Area, A_p [μm^2]	Effective Pore Diameter, d_e [μm]
Nucrel® A	112 ± 3	7.6 ± 2.5	0.8 ± 0.3	1.0 ± 0.2
Nucrel® B	119 ± 4	7.5 ± 3.3	1.6 ± 0.5	1.4 ± 0.2
Hytrel® A	113 ± 3	11.2 ± 3.1	161 ± 36	14.2 ± 1.6
Hytrel® B	123 ± 3	8.6 ± 2.7	126 ± 31	12.6 ± 1.5
Latex$^\alpha$	141 ± 3	0	N/A	N/A

$^\alpha$Negative control for Nucrel® and Hytrel® experiments

3.5   Characterization Results for Track-Etched Membranes

The track-etched membranes contain pores that are almost perfectly circular in cross section (Figure 3.3). Table 3.3 gives membrane thicknesses, pore diameters, and total porosity for all the track-etched membranes studied in this thesis. Non-porous polycarbonate membranes from Goodfellow Corporation were used as negative controls for the track-etched membrane series of runs, and their features are also listed in Table 3.3. Importantly, sample thickness variation (5.9 – 22.0 μm) and porosity variation (1.4% - 32.0%) are constrained to one order of magnitude while a three order of magnitude range in pore diameter (39 nm – 14,400 nm) is available from this set of samples. Thus, these membranes represent promising samples to study the impact of pore diameter on heat and mass transport.

Table 3.3: Track-etched membrane pore size and geometric properties important for latent heat exchange with underlying surfaces.[a]

Overlay [ ]	Pore Diameter [nm]	Thickness [μm]	Porosity [%]
Nonporous Goodfellow[β]	N/A	5.9 ± 0.3	0
Nonporous Goodfellow[β]	N/A	22.0 ± 0.3	0
12,000nm Millipore #1	14,400 ± 1,100	10.6 ± 0.2	17.1 ± 2.2
12,000nm Millipore #2	14,400 ± 1,100	12.2 ± 0.3	12.6 ± 1.1
5,000nm Millipore #1	5,400 ± 500	16.7 ± 0.2	15.4 ± 1.7
5,000nm Millipore #2	5,400 ± 500	16.3 ± 0.3	9.8 ± 1.4
1,200nm Millipore #1	890 ± 30	18.8 ± 0.2	32.0 ± 1.3
1,200nm Millipore #2	890 ± 30	19.1 ± 0.3	6.9 ± 0.9
600nm Millipore #1	700 ± 50	21.3 ± 0.2	22.3 ± 1.3
600nm Millipore #2	700 ± 50	20.9 ± 0.3	8.1 ± 1.2
400nm Millipore	410 ± 20	8.8 ± 0.2	17.3 ± 2.5
220nm Millipore	150 ± 20	19.4 ± 0.2	27.5 ± 1.3
100nm Millipore #1	95 ± 14	18.4 ± 0.2	13.6 ± 1.6
100nm Millipore #2	95 ± 14	18.4 ± 0.3	13.7 ± 1.6
50nm Millipore #1	60 ± 9	19.7 ± 0.2	5.9 ± 1.7
50nm Millipore #2	60 ± 9	21.3 ± 0.3	5.8 ± 1.8
10nm GE	39 ± 13	6.3 ± 0.3	1.4 ± 0.6

[a]Membrane commercial suppliers also shown in Column 1
[β]Negative control for track-etched membrane runs

4 Experimental Apparatuses: Overview and Characterization

Two experimental apparatuses were utilized to take the data presented in this thesis. The first was an exploratory heat and mass transfer measurement device, which was used exclusively to study the DuPont porous membranes described in Chapter 3. Experimentation with this prototype provided expertise in combined heat and mass transfer measurements and built up the physical understanding necessary to create a more sophisticated experimental technique. The second apparatus was a versatile, high-repeatability evaporator for quantitative determination of the rates of latent heat and mass transfer of vapors through nano-engineered porous sheets or plates, including track-etched membranes. It was able to reliably interrogate samples with pore diameters as tiny as 39 nm (and presumably even smaller).

The same types of analysis, modeling, and characterization were required to benchmark both apparatuses. To avoid confusion, the first apparatus will hereafter be referred to as "Heat-And Mass-Transfer Apparatus One" (HAMTA1), and the more sophisticated second apparatus will be referred to as Heat- And Mass-Transfer Apparatus Two" (HAMTA2). Due to their similarity, the analyses for both pieces of equipment are presented in parallel in this chapter.

The research apparatuses were designed to measure rates and extents of surface cooling by liquid evaporation and transport through porous membranes under heat load conditions simulating the heat burden on Soldiers in the Middle East Theater. The apparatuses were sufficiently controlled to allow deduction of quantitative data and illumination of heat transfer processes and mass transport mechanisms within and away from the porous barrier being studied. These apparatuses also allowed complete decoupling of latent heat from conductive heat transfer through the membrane by directly measuring the mass flux of coolant vapor, (i.e., the latent heat carrier) by continuously weighing the apparatus. Apparatus impact on mass transport through the membrane was disaggregated from the experimental mass transfer resistance. This process allowed intrinsic mass transfer resistance for the membrane itself to be quantified, and thus vapor mass transfer characteristics of membranes with different pore sizes could be compared quantitatively. The experimental design assured that an appreciable fraction of the water vapor diffusion resistance in the device occurred across the membrane and that steady state conditions persisted long enough to obtain reliable heat- and mass-transfer data. Existing methods for testing mass transfer through textiles can take several days to return results [Barker (2006)]. HAMTA1 was capable of returning reliable results in about 4 to 5 hours total operating

time, including system and specimen setup. HAMTA2 was capable running four repeat experiments on a single membrane sample in less than 5 hours, and the time for a single run could be reduced to less than 90 minutes.

4.1 Experimental Components and Apparatus Description

Basic descriptions of the components of HAMTA1 and HAMTA2 are provided in this section. The intent is to provide enough detail to allow a reader to exactly reproduce the experiments. Figure 4.1 shows a schematic of HAMTA1 and Figure 4.2 gives a schematic of HAMTA2.
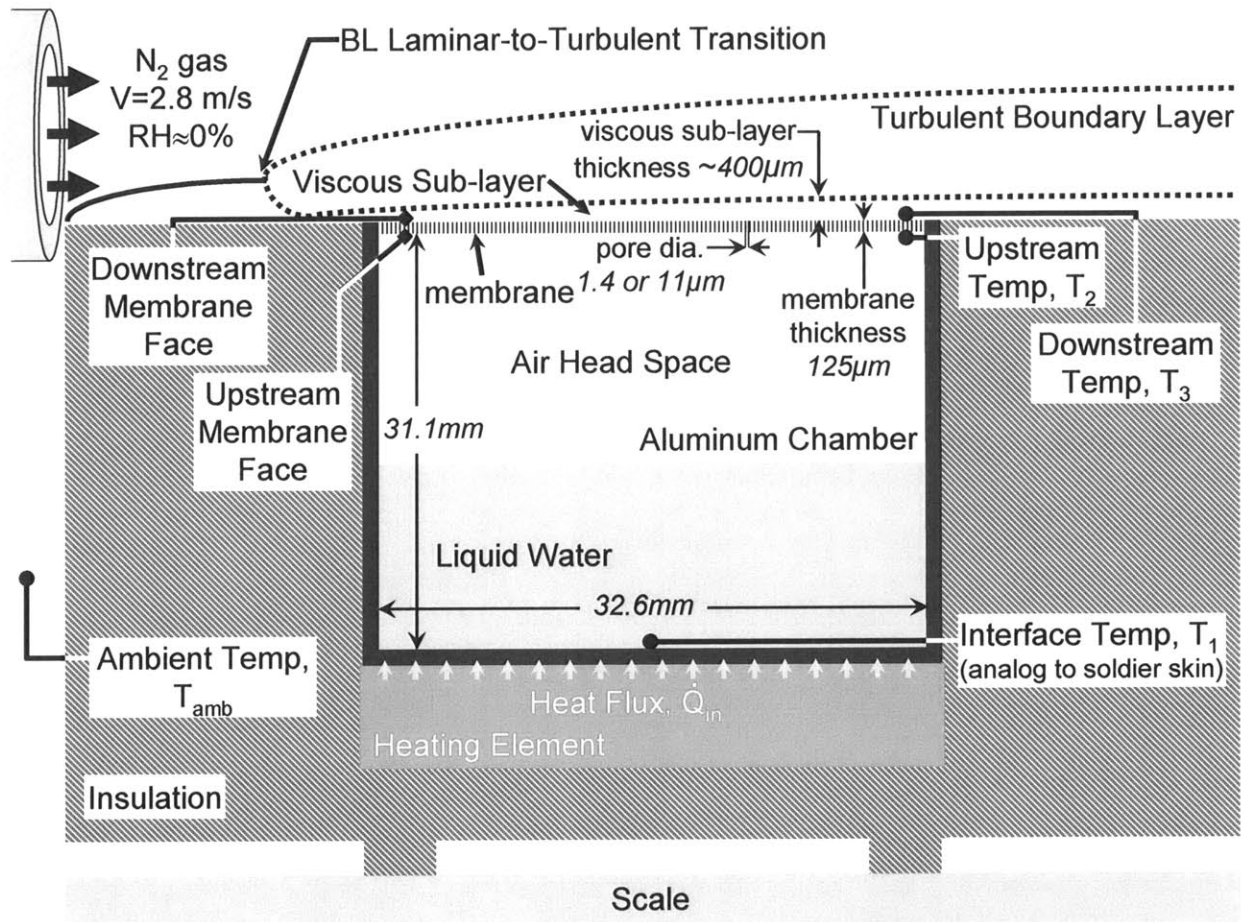
Figure 4.1: Schematic [not to scale] of the HAMTA1 apparatus for quantitative study of evaporative cooling of surfaces using porous overlays. Dotted boundary layers represent average location because turbulence agitates the fluid boundaries.
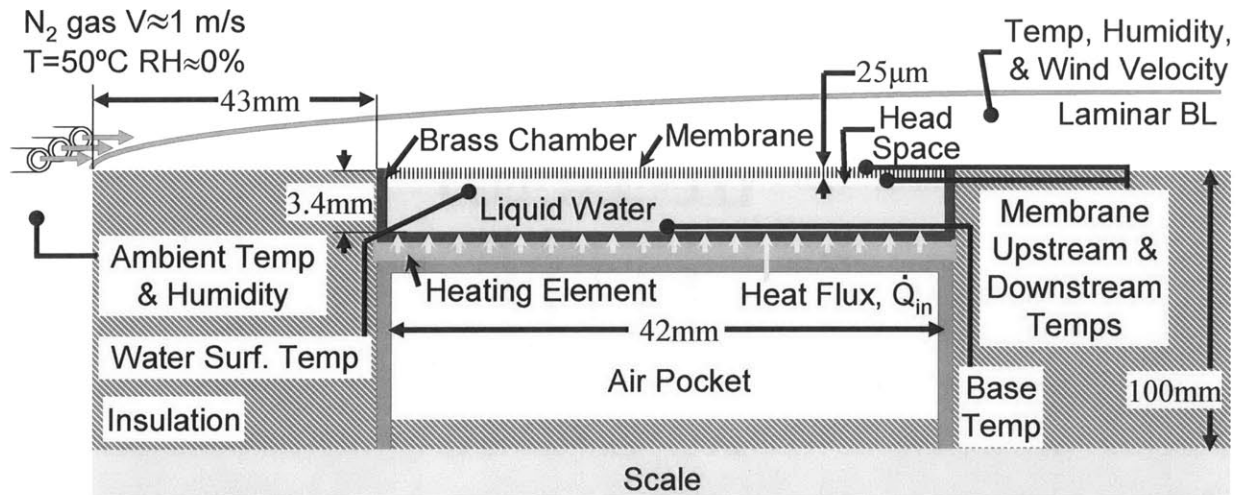
Figure 4.2: Schematic [not to scale] of HAMTA2 apparatus for quantitative study of evaporative cooling of surfaces using porous overlays.

4.1.1 Evaporation Chamber

At the heart of HAMTA1 was a cylindrical aluminum evaporation chamber custom machined to accommodate small porous membrane samples from DuPont. The evaporation chamber held a measured charge of de-ionized water during the experiment and facilitated heat transfer into the total charge of water via natural convection. The aluminum evaporation chamber, pictured in Figure 4.3, had an OD of 33 mm, an ID of 31.7 mm, and stood 32 mm tall. The base was 1 mm thick, and the walls were 0.7 mm thick. The top of the chamber was open so a membrane could be overlaid atop it, allowing water vapor to diffuse through.

The core of HAMTA2 was a cylindrical brass evaporation chamber custom machined to accommodate track-etched membranes, which were commercially available in disks roughly 47 mm in diameter. The brass evaporation chamber, pictured in Figure 4.4, had an OD of 43 mm, an ID of 42 mm, and stood 4.5 mm tall. The base was 1.4 mm thick, and the walls were 0.5 mm thick. The top of the chamber was open so a membrane could be overlaid atop it. The chamber was made to accommodate two integrated thermocouples (to measure base temperature and liquid temperature) and a liquid DI water feed line of 30-guage hypodermic stainless steel tubing. Four threaded holes on the chamber's outside lip accommodated connection of a Kapton heater, and the assembly stood on four nylon legs that provided electrical and thermal insulation.

Figure 4.3: At 33mm in outer diameter, the HAMTA1 evaporation chamber (pictured here with a key for scale) was machined of aluminum to accommodate the DuPont porous membrane samples; 60mm x 45mm was the only size membrane available.

4.1.2 Electric Heater

Input heat flux to HAMTA1 was provided by a commercial-off-the-shelf heater, called the "Cozy-Up Warmer", which was manufactured by ProvoCraft® (Figure 4.5). The hot plate of the heater was about 85 mm in diameter, and it ran on 120 VAC electricity with a stated constant heat flux output of roughly 3600 W/m^2. Inspection of the internal mechanisms revealed no temperature-regulating circuitry; therefore, to control heat flux output to about 1350 w/m^2, the heater was plugged into a Variac, which was plugged into a second Variac to harness two transformer ratios. The second Variac was connected to a 120 VAC wall receptacle. Variac settings were found that reproduced 1350 w/m^2 heat flux accurately to within about $\pm$ 20 w/m^2.
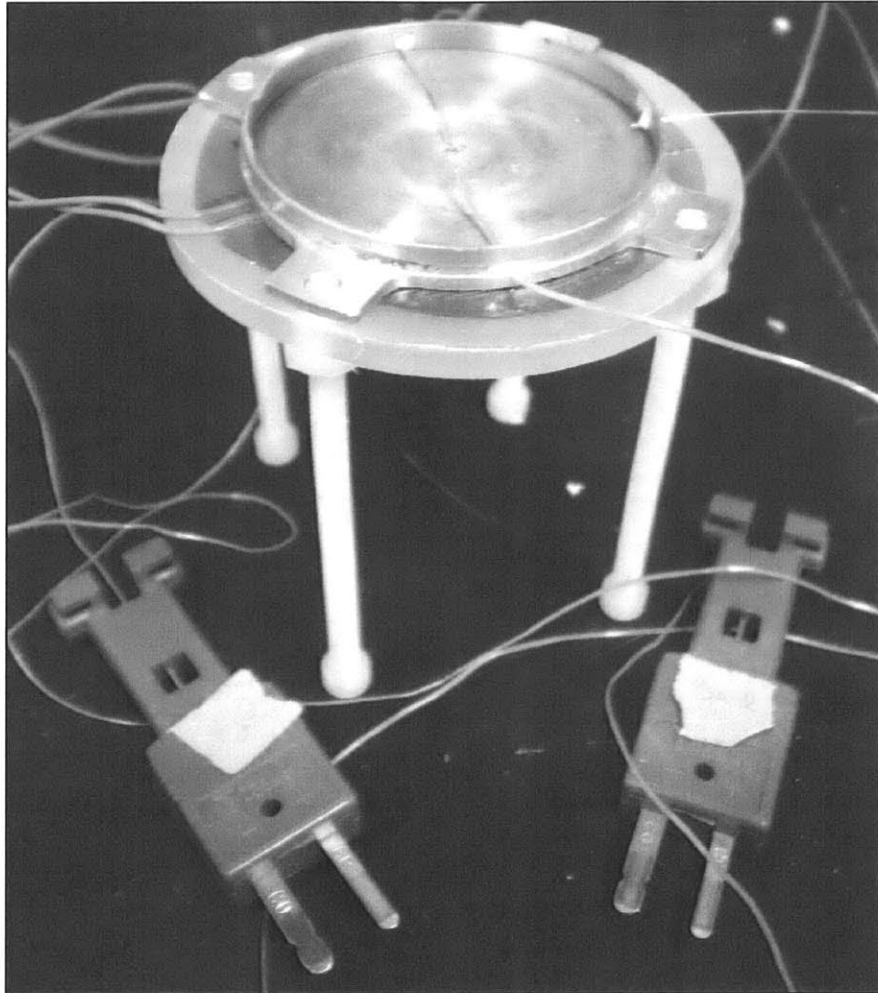
Figure 4.4: The evaporation chamber for HAMTA2 is shown here with its two embedded thermocouples (center of the chamber) and liquid water feed line (top right). This chamber was made to be integrated with a Kapton heater and stand off the lab balance on nylon legs to provide thermal and electrical insulation.

To determine Variac settings required to provide the correct experimental input power flux density, the experiment was set up in closed-chamber mode with no water in the chamber. This arrangement had similar steady-state thermal behavior to the water-filled closed-chamber experiment. However, due to lower thermal mass, it more rapidly settled to new steady-state temperatures arising from changes in heat flux input. In this configuration, the heater was turned on, and the system was allowed to settle to steady state temperature. The RMS voltage, V_{rms}, supplied to the heater was measured by placing a Fluke 114 Electrical Multi-meter [Fluke (2007)] in voltmeter mode across the heater leads. The heater was then momentarily unplugged,

and the internal electrical resistance, $R_{electrical}$, across the leads at elevated temperature was measured. The power input, Π, was estimated from these measurements using

$$\Pi = \frac{V_{rms}^2}{R_{electrical}}$$ (Equation 4.1)

A temperature-resistance relationship for the device was graphed by measuring the resistance across the power leads at various steady-state heater temperatures. A thermocouple in good thermal contact with the center of the heater surface provided temperature data for this calibration (Figure 4.6). The Fluke 114 Electrical Multi-meter in resistance mode that took data was not sensitive enough to measure resistance more precisely than ±1 ohm. However, the heater's resistance was shown to vary by no more than 6 ohms out if about 870 ohms (about 0.7 percent) over the studied operational temperature. Therefore, small variations in the heater's temperature did not dramatically affect the input power at constant voltage. A constant resistance of 875 ohms was assumed in all HAMTA1 power calculations.

Figure 4.5: A commercial candle warmer provided input heat flux for the HAMTA1 evaporation experiments. *Photo by the thesis author.*

There were several benefits to using a ProvoCraft® candle warmer for this experiment. The hot plate of this device was a thin metal sheet, capable of reaching spatially uniform steady-state

temperature after about 25 minutes of warm-up. Spatial uniformity was measured by placing four thermocouples at radial stations 1 cm apart starting from the center of the heating plate. The heater was turned on and the duration required for all four thermocouples to report the same steady-state temperature (within the measurement error of ± 1.1 °C) was recorded. Conventional laboratory heaters took longer to thermally stabilize, due to substantially greater thermal mass, prolonging the duration of each experiment. The heater was self-insulated in a plastic sheath with four small rubber feet that supported it above the scale stage on which it was mounted. These feet eliminated the need to place a layer of thermal protection between the heater and the scale to protect the scale from high temperature. The candle warmer was also extremely lightweight compared to laboratory heaters. Low apparatus weight allowed for additional precision in measuring the weight change of the system (i.e., the mass transport rate) as water evaporated away because the heater was part of the system weighed.
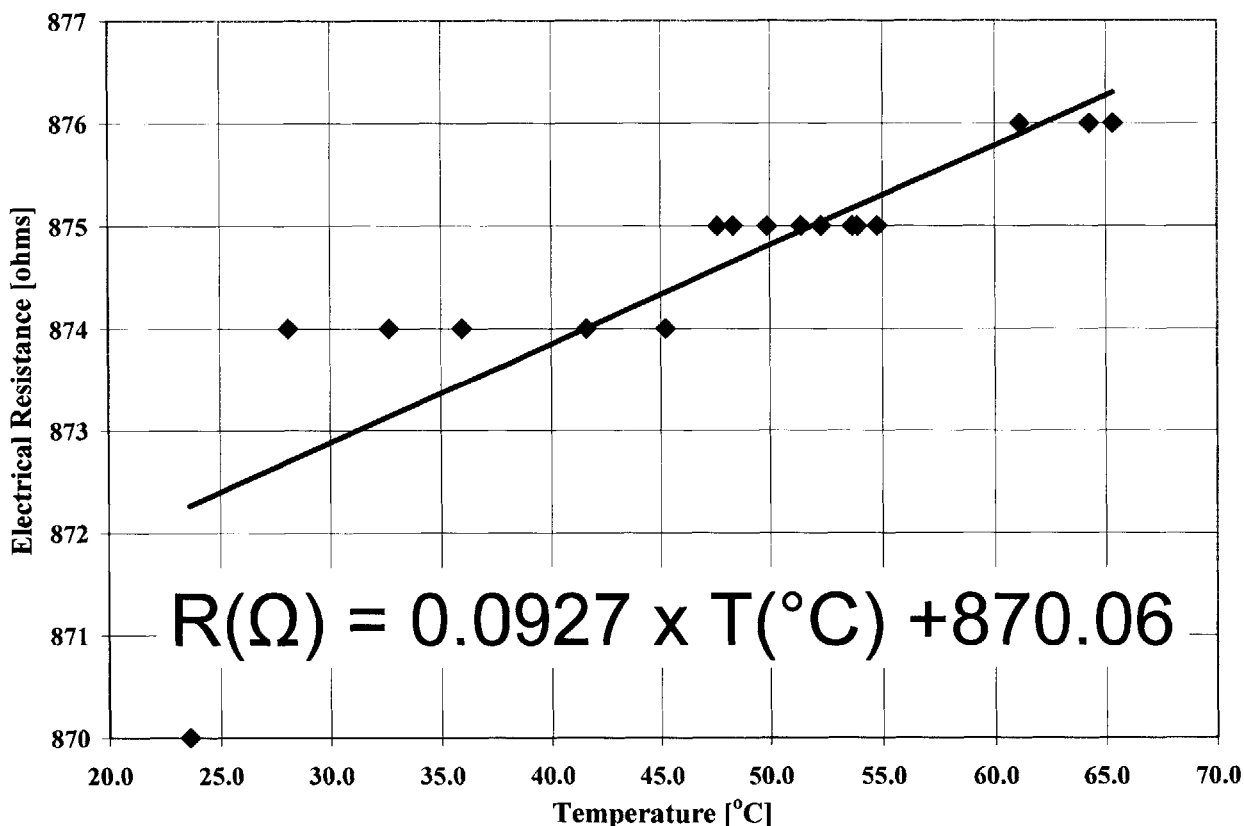

$$R(\Omega) = 0.0927 \times T(°C) + 870.06$$

Figure 4.6: A small dependence of candle heater electrical resistance on temperature was observed for the candle heater over the temperature operating range shown.

The candle warmer surface area was physically much larger than the evaporation chamber base, and required about 8 watts input power to provide 1350 w/m² for HAMTA1. To reduce this power requirement and associated heat leakage, HAMTA2 utilized a 2-inch diameter Kapton heater (McMaster-Carr Part Number 35475K12), which was stuck with adhesive to a small nylon disk. This disk contained four through holes, allowing it to be secured to the under side of the evaporation chamber, which pressed the heater tightly against the bottom face of the evaporation chamber. While the HAMTA2 chamber bottom was 0.0165 m², the heater area was 0.00168 m², and the steady state operating resistance was 453.6 ohms (measured with an Extech 380900 [Extech (2007b)] power meter is resistance mode). Although HAMTA2 was ultimately run with a heat flux of only 400 w/m², as a point of comparison, only 2.35 watts of input power were required to achieve 1350 w/m² in HAMTA2 (versus 8 watts for HAMTA1). The new apparatus included a positive DC adjustable power supply (see details in Section 4.1.3) that actively regulated input voltage across the heater. By measuring HAMTA2 input voltage and current at regular intervals with the Extech 380900 power meter during a run, the need to know the temperature-resistance relationship of the heater was eliminated.

4.1.3 Battery

HAMTA1 obtained power from a wall receptacle, requiring electrical wires that ran off the scale stage to the outlet. Careful experimental protocols reduced the impact of compliance in these wires on the scale measurement. However, the parasitic contribution of compliance in the wires to recorded weight changes could not be completely eliminated with the desired degree of certainty. To eradicate this problem for HAMTA2, a battery supplied the heater with energy, and the battery sat on the scale stage with the rest of the apparatus, eliminating the need for external power lines. A rechargeable 36-volt battery from DeWALT® (model number DC9360) was selected for this duty because 1) the battery's supplied voltage exceeded the 32.6 volts required to drive the heater at 1350 w/m²; 2) the battery used lithium-ion nano-phosphate chemistry [DeWALT (2007)], which was selected because it allowed over 2000 recharges; and 3) the battery was substantially lighter (1.09 kg) than other batteries with the same voltage output and duration between charges. Thus, this battery provided a reliable, lightweight, reusable power source for HAMTA2.

Like all batteries, the available voltage of the DeWALT® 36V decreased as it is discharged (Figure 4.8A), and this decay changed the heat input to the evaporation chamber if left

unchecked. Therefore, a positive DC adjustable power supply circuit (kit number CK403 from Carl's Electronics [Carl's Electronics (2007a)]) was created from a kit (Figure 4.7) to keep the battery output voltage fixed throughout the duration of an experiment (Figure 4.8B). A wireless, infrared switch, made from Carl's Electronics kit number CK1600 [Carl's Electronics (2007b)] was also added into the power circuit in series with the heater. This switch (Figure 4.9) enabled the heater to be turned on and off without touching the experimental apparatus, which eliminated the possibility of upsetting the zero setting on the scale for warm-up and cool-down.

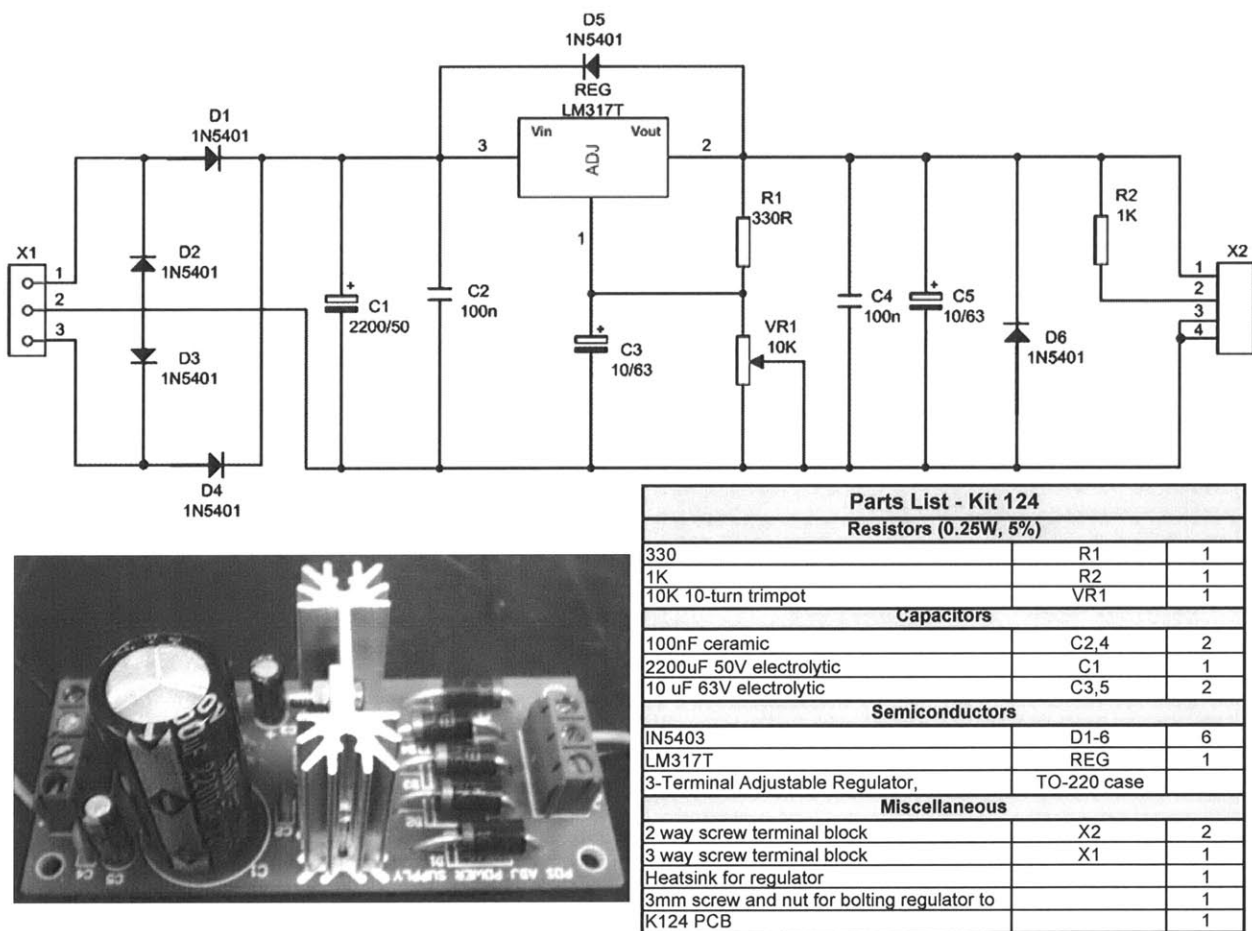| Parts List - Kit 124		
Resistors (0.25W, 5%)		
330	R1	1
1K	R2	1
10K 10-turn trimpot	VR1	1
Capacitors		
100nF ceramic	C2,4	2
2200uF 50V electrolytic	C1	1
10 uF 63V electrolytic	C3,5	2
Semiconductors		
IN5403	D1-6	6
LM317T	REG	1
3-Terminal Adjustable Regulator,	TO-220 case	
Miscellaneous		
2 way screw terminal block	X2	2
3 way screw terminal block	X1	1
Heatsink for regulator		1
3mm screw and nut for bolting regulator to		1
K124 PCB		1

Figure 4.7: Circuit diagram, parts list, and photograph of the DC adjustable power supply circuit [Carl's Electronics (2007a)] used on HAMTA2 to mitigate effects of decay of battery output voltage drop during experiments. The circuit converts the battery to a constant output voltage source. *Circuit diagram and parts list adapted from originals. Photograph by Thesis author.*
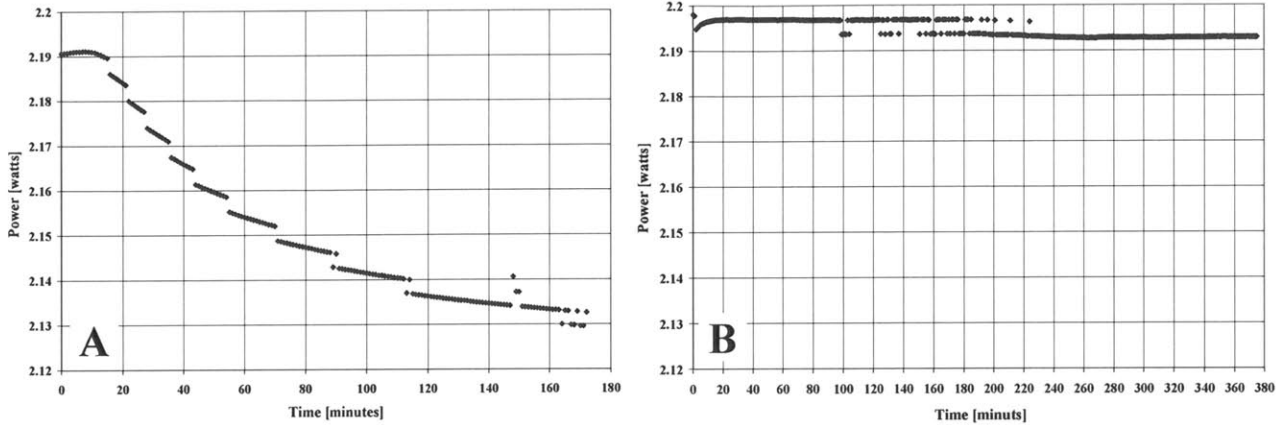
Figure 4.8: Power decay of a DeWALT® 36V battery driving a 465 Ω Kapton heater. (Left) with no power regulation electronics, the battery power decayed rapidly; this changing power output complicated experimental data interpretation. (Right) a simple DC power regulating circuit kept the battery output power constant over the duration of the experiment. Note that step jumps in power on both graphs are artifacts of the resolution in the data collection equipment; without this artifact, the decay would be a continuous function.

ONLY 1 OF THE D FLIP FLOPS HAS BEEN USED.
INPUTS TIED.

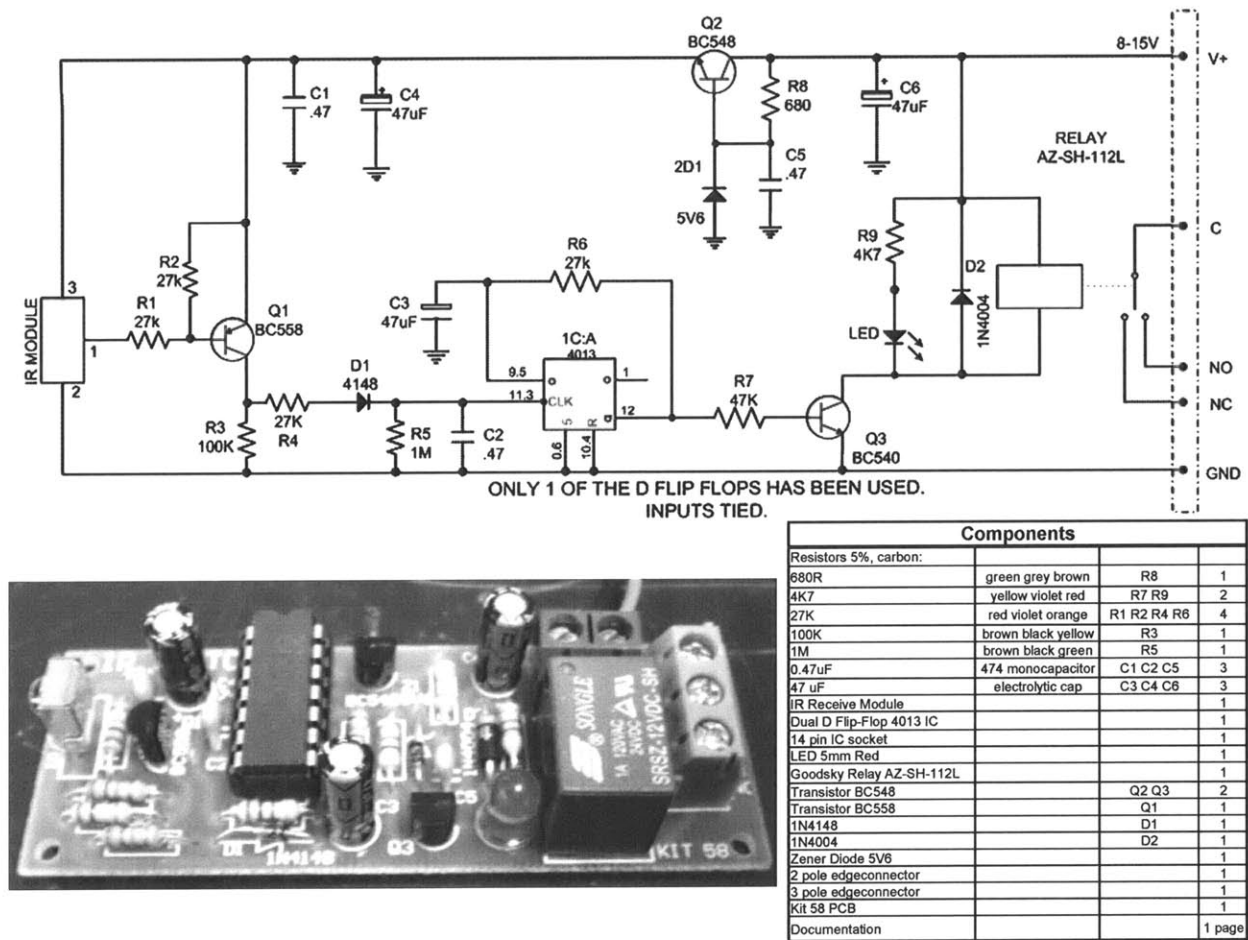| Components			
Resistors 5%, carbon:			
680R	green grey brown	R8	1
4K7	yellow violet red	R7 R9	2
27K	red violet orange	R1 R2 R4 R6	4
100K	brown black yellow	R3	1
1M	brown black green	R5	1
0.47uF	474 monocapacitor	C1 C2 C5	3
47 uF	electrolytic cap	C3 C4 C6	3
IR Receive Module			1
Dual D Flip-Flop 4013 IC			1
14 pin IC socket			1
LED 5mm Red			1
Goodsky Relay AZ-SH-112L			1
Transistor BC548		Q2 Q3	2
Transistor BC558		Q1	1
1N4148		D1	1
1N4004		D2	1
Zener Diode 5V6			1
2 pole edgeconnector			1
3 pole edgeconnector			1
Kit 58 PCB			1
Documentation			1 page

Figure 4.9: Circuit diagram, components list, and photograph of the infrared switch used on HAMTA2 to turn power to the heater on and off without touching the apparatus [Carl's Electronics (2007)]. *Circuit diagram and components list adapted from originals. Photograph by Thesis author.*

4.1.4 Radial Insulation Collar

To reduce radial heat leak from the walls of the evaporation chamber, an annular insulation collar was fashioned from hard Styrofoam used in packing containers for solvent bottles. This method was used to insulate both HAMTA1 and HAMTA2. This material was ideal because it provided a very high thermal resistance across the temperature range of interest compared to other system components and it could operate up to up to 93°C without decomposing. For HAMTA1, the insulating ring was sized to be 33 mm tall, just like the evaporation chamber. The center hole in the ring was just less than 33mm in diameter to assure a press fit over the evaporation chamber. The thickness of the insulation collar was designed to assure radial conduction through the collar was miniscule compared to axial conduction in the water. This criterion was achieved by designing to obtain a large value of the following ratio:

$$\frac{R_{radial}}{R_{axial}} = \frac{\left[\dfrac{\ln\left(\dfrac{r_2}{r_1}\right)}{2\pi L k_{styrofoam}}\right]}{\left[\dfrac{L}{A_{water} k_{water}}\right]} = \frac{\ln\left(\dfrac{r_2}{r_1}\right) r_1^2 k_{water}}{2L^2 k_{styrofoam}} \qquad \text{(Equation 4.2)}$$

where r_1 and r_2 are the internal and external radii of the insulation collar, L is the height of the insulation ring (and consequently the evaporation chamber), k_{water} is the thermal conductivity of water, and $k_{styrofoam}$ is the thermal conductivity of Styrofoam. Setting an acceptable value for Equation 4.2 at 10 (i.e. radial resistance exceeds axial resistance by 10 times), and using k_{water} = 0.611 w/m-K, $k_{styrofoam}$ = 0.032 w/m-K, L = 0.03 m, and r_1 = 0.031 m, the resulting value for r_2 is 0.043 m.

It will later be shown in Section 4.4.1.1 that for HAMTA1 heat transfer in the water was dominated by natural convection; so sizing the insulation ring using a comparison to conduction in the water was extremely conservative. In addition, this analysis did not include the contact resistance between the outside walls of the evaporation chamber and the insulation. Given the conservative nature of this calculation, the similarity between the insulation ring outer diameter (0.086 m), and the diameter of the heating plate (0.080 m), the insulation ring was fabricated with an outer diameter of 0.080 m. This dimension allowed the insulation collar to fit snuggly

atop the heating plate of HAMTA1 and inside the heater's insulating plastic molding, making a continuous layer of insulation between the hot heating element and the ambient environment.

For HAMTA2, the insulation collar included a 43mm-diameter Styrofoam well into which the evaporation chamber assembly fit snuggly. Four tiny holes were drilled in the bottom face of the insulation to allow the Nylon legs of the evaporation assembly to protrude. The outer diameter of the collar was 121 mm, which provided a ratio of radial to axial thermal resistance of 419 (Equation 4.2), whereas HAMTA1 had a ratio of 10.

4.1.5 Gravimetric Balance

The weights of the evaporation research apparatuses were monitored in real time while experiments were being conducted. For HAMTA1, an SR8001 electronic balance manufactured by Mettler-Toledo [Mettler-Toledo (2007b)] was utilized to take these data. The balance had a weight range of 0 g to 8100 g, a readability of 0.1 g, and a repeatability of 0.05 g. The scale had automatic internal correction to adjust for temperature changes at the pan, and it had the capability to re-zero itself at a regular time interval that could not be user-controlled. This later mechanism was shut off to take dynamic measurements over a period of several hours without the scale re-zeroing itself. Measurements of the scale stability over time were taken with this re-zero capability shut off by placing a 100g weight in the scale and rechecking the weight about 24 hours later. The scale maintained precision to 0.1 g over at least 24 hours. Since the typical evaporation experiment duration with HAMTA1 was about 5 hours, the scale precision was adequate for accurate measurements of weight change down to 0.1 g over the duration of the experiment. Data were recorded manually by reading the scale display at regular time intervals throughout the experiment, typically about every 120 ± 20 seconds.

For HAMTA2, an XP5003SDR precision balance manufactured by Mettler-Toledo was utilized [Mettler-Toledo (2007a)]. This balance had a weight range of 0 g to 5100 g, a readability of 0.001 g and a repeatability of 0.006 g. With static electricity mitigation measures in place (see Section 4.1.6), the scale was left data-logging overnight with no weight on the stage to determine the long-term drift error. Figure 4.10 shows that the scale drifted about its zero setting, and the maximum extent of this drift was ± 0.03 grams. This value was therefore taken as the maximum error in the measurement over a 4 – 5 hour duration experiment. The XP5003SDR could output data directly to a computer at a rate of one measurement per second; so recording gravimetric data manually was not necessary for HAMTA2.

4.1.6 Avoiding Electrical Interference Effects

When the HAMTA2 apparatus was completely isolated from the lab bench, static charge tended to build up on the scale stage. This buildup caused a measured scale drift as large as 10 grams in 30 minutes. A grounding mechanism was needed that did not impact the accuracy of weight measurement. The experimental assembly therefore sat upon a 6-inch by 6-inch 0.125-inch-thick copper plate, which was grounded to the faucet on the lab bench with AWG 40 (0.07874 mm diameter) copper wire. The copper plate was electrically connected to a sheet of aluminum foil resting atop the Styrofoam insulating collar, which allowed charge built up on the top surface of the experiment to bleed away to ground. The extremely thin ground wire was the only connection between the scale stage and the lab bench and had negligible impact on the weight measurement accuracy.
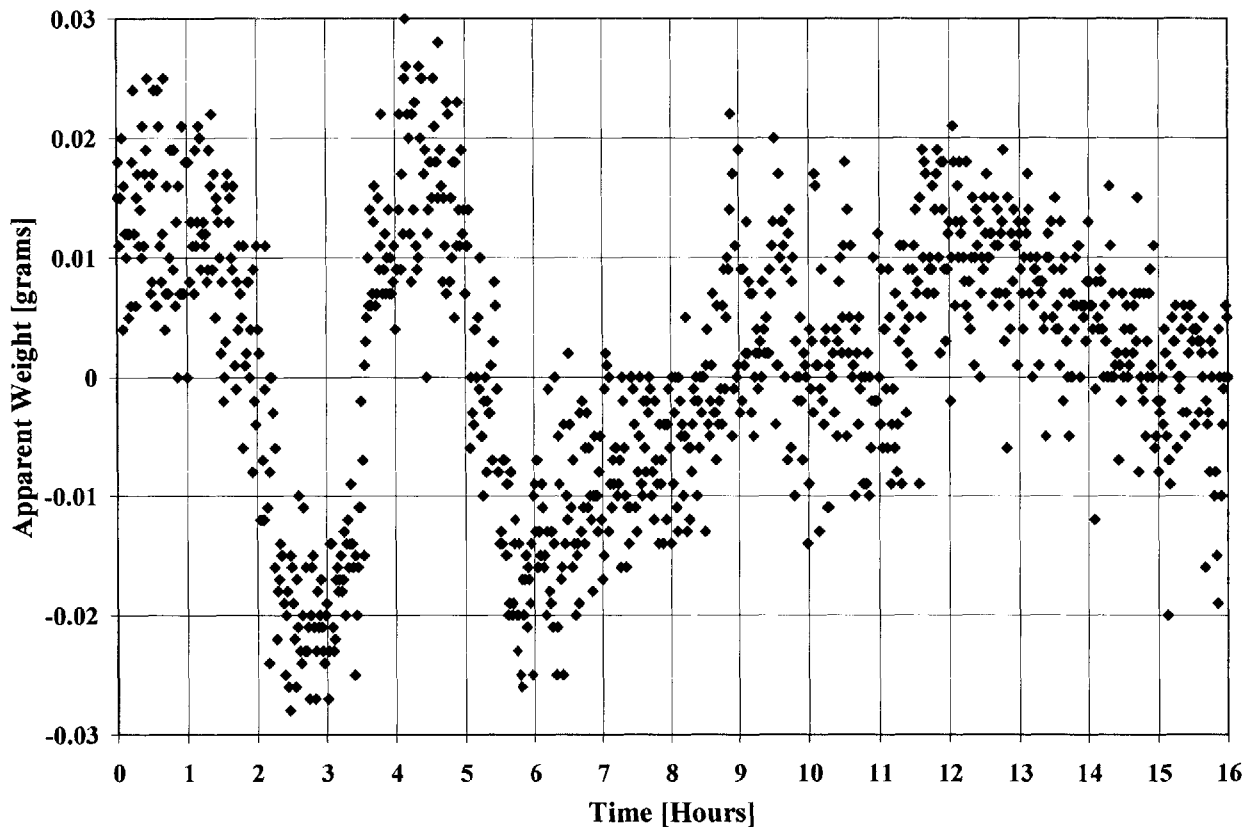

Figure 4.10: The XP5003S scale was left data-logging overnight to ascertain the degree of drift. Over 16 hours, the maximum extent of the drift was ± 0.03 grams.

The degree of grounding wire impact was measured by zeroing the balance with the ground wire not connected and placing on the stage a series of increasingly heavy weights. This procedure was repeated with the ground wire connected. Comparison of results revealed agreement within ± 0.001 g for these two cases. A further test involved connecting the grounding wire and zeroing the balance. The scale stage was then tapped upon repeatedly. After this perturbation, the final weight was always found to be within ± 0.001 g of the original zero. Thus, the grounding wire impact on balance accuracy was less than the stated measurement error of the instrument.

Before each experiment the electrical resistance between the aluminum foil and the lab bench faucet was checked with a Fluke 114 Electrical Multi-meter [Fluke (2007)]. If this resistance measured less than 10 ohms, the apparatus was considered grounded and the experiment could proceed.

4.1.7 Heating and Drying Downstream Boundary Layer Gas

Instead of exhausting water vapor to an ambient temperature boundary layer, HAMTA2 exhausted to a heated downstream boundary layer formed by directing a preheated flow of dry nitrogen over the exterior membrane face. The source of this nitrogen was a 250-liter Airgas Dewar, which was replaced about every two weeks, the typical time for the HAMTA2 runs to exhaust a Dewar of this capacity. House nitrogen was not utilized because pressure changes associated with nitrogen use throughout the building would have caused unacceptable fluctuations in the flow velocity.

After exiting the Dewar, the nitrogen was dried out using a 750cc Supelco moisture trap (model number 23991) capable of reducing water concentration in a gas stream to 15 parts-per-billion [Sigma Aldrich (2007)]. The gas was then warmed through a single-tube heat exchanger, which was heated externally using two Super-High-Temperature (electrical) Heat Ropes (McMaster-Carr part # 3641K27) wired in series and powered by connecting them to a 120VAC wall receptacle. At the nozzle outlet, the gas temperature was 50 °C or 100 °C as measured by an Omega K-Type thermocouple affixed to the aluminum blow-off nozzle (McMaster-Carr part # 5329K65) with Kapton tape. During experiments, this temperature was maintained to ± 1 °C with a Eurotherm 2116 temperature controller [Eurotherm (2007)], running in PID mode, which modulated the power input to the heat exchanger heat ropes by monitoring the nozzle temperature via the thermocouple affixed to it.

4.2 Temperature Measurements

A systematic literature search revealed best practices for surface temperature measurements. This section illustrates how those practices were utilized to positive effect to take high-precision temperature measurements for this research.

In both experimental apparatuses, a thermocouple was anchored to the inside bottom face of the evaporation chamber to measure the temperature at that surface (hereafter called the base temperature). This temperature would be illustrative of the Soldier's skin in the protective garment systems represented through this research. In general, if a thermocouple's thermal contact resistance to the surface being measured is much smaller than its thermal resistance to the surrounding environment, the resulting error in temperature measurement is negligible [Baker, et al. (1953)]. Thus, soldering a thermocouple directly to a metallic surface provided highly-accurate surface temperature measurements.

4.2.1 Connecting Thermocouples to Soft Material Membranes

To obtain temperature measurements at the surface of a porous polymer membrane, soldering a thermocouple to the surface will not work due to the material mismatch and the danger of melting or otherwise damaging the membrane. Some alternate method of attachment must be developed to guarantee good thermal contact between the metal thermocouple tip and soft membrane material. This approach must also assure that thermal resistance to the environment dominates over contact resistance to the membrane. Since this research is concerned with transport through porous media, the method must furthermore block a very small portion of membrane pores (ideally none). Thus, simply affixing thermocouples using pieces of tape or adhesive was ruled out.

Given these considerations, the preferred method of thermocouple attachment was epoxy. A bead of epoxy holds the thermocouple in direct contact with the membrane while also providing thermal protection for the thermocouple from the ambient environment. Thus, the relevant thermal resistance ratio compares the thermocouple-membrane contact resistance against the resistance to heat flow to the environment presented by a mean hemispherical shroud of epoxy covering the thermocouple:

$$\frac{R_{contact}}{R_{shroud}} = \frac{\dfrac{1}{h_{contact}A_{contact}}}{\dfrac{\dfrac{1}{r_1} - \dfrac{1}{r_2}}{2\pi k}} = \frac{2\pi k}{h_{contact}A_{contact}\left(\dfrac{1}{r_1} - \dfrac{1}{r_2}\right)}$$ (Equation 4.3)

where r_1 is the radius of the thermocouple and r_2 is the outer radius of the epoxy shroud, k is the thermal conductivity of epoxy, $A_{contact}$ is the contact area between the thermocouple bead and the soft surface, and $h_{contact}$ is the contact conductance associated with that interface. The epoxy must be selected so as not to chemically or physically damage the membrane. The epoxy must also be water resistant and able to tolerate temperatures of at least 100 °C in air or steam or mixtures thereof.

A two-component, high-thermal-conductivity epoxy manufactured by Omega, OmegaBond® 101 (product number OB-101) [Omega (2007b)], was identified to meet all the needs of the thermocouple-membrane attachment. This material cured at room temperature and was specifically designed to bond permanently to beaded wire thermocouples and a variety of materials, including polymers.

An acceptable engineering value for the contact resistance ratio must be selected, and Equation 4.3, when solved for r_2, determines how thick a shroud of epoxy is required to meet the selected thermal performance metric. Shrouds of smaller radius provide the best connections because they present smaller external surface area to the environment than do larger shrouds.

The acceptable ratio for epoxy shroud thermal resistance to thermal contact resistance was selected to be 100. The contact conductance, $h_{contact}$, was approximated as 1500 W/m²-K, the value given by Mills [Mills (1999a), p. 63] as the minimum contact conductance for metal contacting a non-metal substance. Thermal conductivity for OmegaBond 101 epoxy was k = 0.884 w/m-K, and the diameter of the thermocouple bead was 0.076 mm (r_1 = 0.038 mm). Due to the asymptotic nature of Equation 4.3 with these values input, every shroud radius meets the thermal resistance ratio requirement of 100. Using a 27-gauge syringe needle to manipulate epoxy around thermocouple beads, shrouds measuring 2 mm in diameter or less were made. The membrane area taken up by a 2 mm diameter shroud, 3.1×10^{-6} m², was less than 0.4% of the 8.6×10^{-4} HAMTA1 membrane area and about 0.2% of the 1.5×10^{-3} m² membrane area of HAMTA2.

The measurement effectiveness of the epoxy bead method for thermocouple-membrane attachment was demonstrated experimentally, as shown in Figure 4.11. Thermocouples were affixed to the top and bottom of a thin polystyrene weighing dish. The top thermocouple was shrouded in a 2 mm-diameter epoxy bead while the bottom thermocouple was left bare but located so that is was in good physical contact with the bottom of the thin dish. The dish was floated in water, which was heated from below. The bottom bead was immersed in the water, and the portion of the plastic dish resting below the water line in immediate contact with the water had the same temperature as the water's surface since the plastic was very thin (Biot number < 0.1).
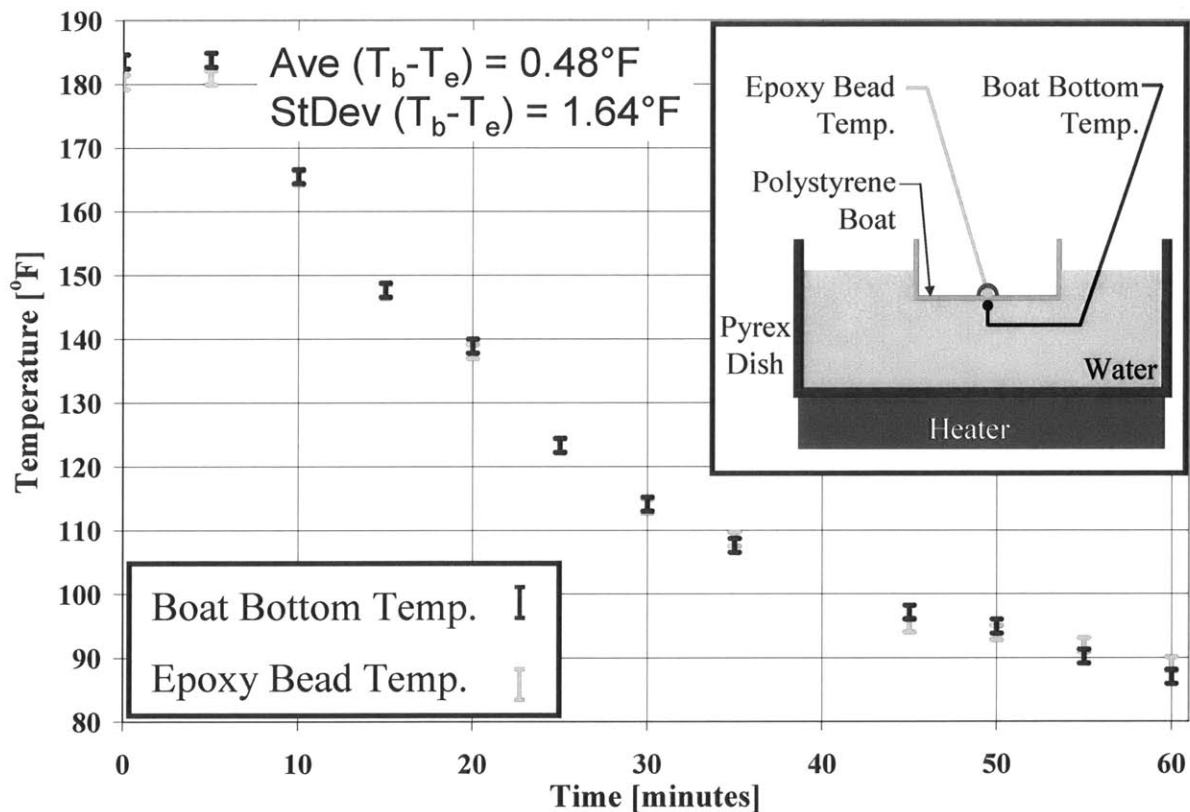

Figure 4.11 The effectiveness of an epoxy-shrouded thermocouple (temperature = T_e) was demonstrated experimentally by tracking the temperature of a bare thermocouple (temperature = T_b) immersed in water in good thermal contact with a very thin layer of polystyrene. As the water cooled, the two thermocouples read essentially the identical temperature within the error of the measurement devices.

As the water cooled from boiling to room temperature, comparison of temperature readings between the two thermocouples indicated how well the shrouded thermocouple tracked the actual plastic surface temperature. The results (Figure 4.11) indicated that, within the uncertainty of the

thermocouple measurements that the temperatures were identical, demonstrating the applicability of the epoxy-shrouded thermocouple for membrane surface temperature measurements. The temperature measurement error was ± 1.1 °C, which arose from the sum of ± 1.0 °C uncertainty arising from T-type thermocouple [Omega (2006)] and ± 0.1 °C uncertainty in the thermocouple reader.

4.3 Experimental Procedure

The typical procedure for HAMTA1 was to thermally equilibrate de-ionized water to ambient temperature by storing it in a covered 10 mL graduated cylinder on the lab bench overnight. The evaporation chamber was weighed and then filled with about 7.0 g of the equilibrated DI water, giving a roughly 11-mm-deep charge. The chamber was then reweighed to determine the exact initial weight of the water. Except in positive control runs (i.e. no membrane covering), the top opening of the evaporation chamber was then completely covered with a membrane sealed taut to the chamber outside wall by an elastic band. The insulation collar was forced over the chamber, and the entire assembly was then placed on the heater and taped down to assure good, repeatable thermal contact between the heater plate and the evaporation chamber bottom. A continuous flow of room-temperature dry nitrogen gas was directed over the top of the apparatus from a tube at an exit velocity of 2.8 ± 0.25 m/s to match the gas rate stipulated by the ASTM Upright Cup Method (see Figure 2.5, top left panel) for determining vapor transmission rates through textiles [ASTM (1999)]. The tube exit velocity was measured using a turbine gas flow meter, a VWR Enviro-Meter digital anemometer (catalog number 46610-028 [VWR (2007)]). The chamber bottom was then heated at 1350 ± 20 W/m^2 (to mimic a typical daytime solar and metabolic heat load on desert Soldiers) by manually adjusting a 120-volt-input, variable transformer (Variac) which powered the 85.55 mm OD ProvoCraft$^{®}$ Candlsense^{tm} electrical hot plate (stated maximum heat flux density 3600 W/m^2), which is described in more detail in Section 4.1.2. The experiments consisted of 4 runs with a non-porous latex membrane (negative control), 4 with no covering (positive control, i.e., maximum evaporative cooling) and 2 each with replicate samples of Nucrel$^{®}$ and Hytrel$^{®}$ from the same lot. Temperature and weight measurements were manually recorded every 120 ± 20 seconds throughout each experiment.

To measure initial conditions, experimental time was started and allowed to run for 10 minutes before electrical power was supplied to the heater. At time = 10 minutes, the electricity was turned on, and the system heated up under a known input heat flux of 1350 ± 20 W/m^2.

After roughly 40 minutes, the system reached steady-state conditions, as defined by two parameters: 1) the apparatus base temperature reading was within 10% of the eventual average steady-state temperature and 2) the liquid water-air interface (the evaporation front) was sufficiently below the entrance face of the membrane to assure enough head space depth for bouncy-driven natural convection to occur spontaneously in the head space (see Section 4.4.1.2).

The key experimental measurements were three surface temperatures and weight as affected by time, for a known heat load. Temperature-time histories were simultaneously recorded for the evaporation chamber base (T_1) and the upstream (T_2) and downstream (T_3) faces of the membrane. Thermocouple T_1 was mounted at the center of the bottom surface of the evaporation chamber and soldered in place with generic rosin core (electrical) solder to provide excellent thermal contact with the bottom of the chamber (see Section 4.2). Thermocouples T_2 and T_3 were respectively affixed to the upstream and downstream faces of the membrane with high-thermal-conductivity epoxy cement, OmegaBond® 101 (see Section 4.2.1). These thermocouples were separated from the metal walls of the evaporation chamber by about 14 mm.

The HAMTA2 start-up procedure was very similar to that for HAMTA1. The apparatus was prepared by placing the evaporation chamber into the well within the Styrofoam insulation collar. A membrane was laid over the top of evaporation chamber and sealed in place by slipping a custom-machined aluminum ring over the membrane into a press-fit with the chamber outer wall. A flat 0.25-inch-thick polycarbonate plate with a hole large enough to accommodate the membrane was placed on top of the insulation collar, creating a very smooth surface for boundary layer development. Testing with a spirit level assured the experiment sat perfectly level with respect to the gravity vector, and brass shims were used to correct slight deviations from level. De-ionized liquid water was taken directly from the tap into a 3 mL syringe. The syringe was weighed before and after filling with water to assure 3.00 ± 0.01 grams of water were used. Precise control of liquid water mass was critical to assuring consistency of the height of the head space between each HAMTA2 experiment. The water-filled syringe was screwed into the hypodermic delivery line protruding from the evaporation chamber, and 3 grams of water were pushed into the evaporation chamber. Flow of heated dry nitrogen gas (50 °C or 100 °C) from the blow-off nozzle at 1.00 ± 0.15 m/s was initiated over the flat plate and the membrane.

The flow velocity of 1.00 ± 0.15 m/s was selected for HAMTA2 (as opposed to 2.8 ± 0.25 m/s, which was used for HAMTA1) to assure the boundary layer formed on the external

membrane face was laminar. Observation of mass flow rates through track-etched membranes subjected to turbulent flows suggested that recurring pressure fluctuations in the turbulent boundary layer caused the very thin track-etched membranes to vibrate. It was observed that all track-etched porous membranes exhibited nearly identical mass transfer rates regardless of pore diameter when subjected to turbulent flow. The DuPont porous membranes were not subject to this turbulence-induced vibration because they were much thicker. It was hypothesized that membrane vibrations caused water vapor to be actively pumped through the membrane, a mechanism completely different than the diffusion transport processes studied in this thesis. To eliminate membrane vibration, laminar flow was utilized over the membrane exterior surface; hence the selection of 1.00 ± 0.15 m/s flow velocity.

Flow velocity, temperature, and relative humidity were measured with a Kestrel$^{®}$ 4000 Pocket Wind Meter [Nielsen-Kellerman (2007)]. The experiment was allowed to heat up under these conditions to an initial steady-state temperature (which took about 15 minutes). After the initial warm-up period, the Kapton electrical heater was turned on via an infrared switch (described in Section 4.1.3) to deliver 400 w/m^2 (to mimic a typical metabolic heat load on jogging desert Soldiers carrying loads of 120+ pounds) through the bottom of the evaporation chamber. Weight measurements were sent through an RS-232 serial computer cable from the Mettler-Toledo XP5003SDR balance to a data-logging computer once per second. Evaporation chamber base and water temperature measurements were automatically logged using an Extech EasyView^{TM} EA15 thermocouple reader [Extech (2007a)], which recorded data once every three seconds. Membrane temperature measurements were automatically logged using a pair of Omega HH2001LTC thermocouple readers [Omega (2007a)], which recorded data once every sixty seconds. Heater input power and current were logged once per minute by an Extech 380900 power meter [Extech (2007b)] in dual channel mode. All logging instruments were portable and sat on the scale to eliminate unnecessary wires running from the scale stage to the lab bench.

In addition to the three temperature measurements described for HAMTA1, a fourth thermocouple was added to HAMTA2, which monitored the temperature of the liquid-air interface inside the evaporation chamber. This probe was a bare 0.076-mm diameter T-type thermocouple bead positioned just slightly submerged under a 3-gram charge of water. This thermocouple was placed so that over the course of an experiment (about 30 – 40 minutes) the water level would not recede (due to evaporation) below the bead.

When each experiment ended, the heated nitrogen, electrical heater, and data-logging instruments were left running. The exact loss of mass due to evaporation of liquid water was noted. The 3 mL syringe was removed from the experiment and filled with a mass of DI liquid water matching the exact weight that had evaporated away. The syringe was then re-attached to the fill line leading into the evaporation chamber, and the makeup water was pushed in to replenish the charge to exactly 3 grams to begin the next experiment. Up to four 60-minute experiments (warm-up, steady state, injection of fresh liquid) could be conducted for each membrane while data logging membrane temperatures at 1-minute intervals. This limit was set by the Omega HH2001LTC thermocouple readers, which only had enough memory to accommodate 250 data points.

4.4 Apparatus Design and Data Interpretation

To obtain apparatus-independent transport resistances for each membrane it was necessary to disaggregate the effects of mass transfer resistances upstream and downstream of the membrane.

For HAMTA1, the following effects were disaggregated: 1) thermal buoyancy in the air-water vapor head space between the top surface of the liquid water and the upstream face of the membrane; 2) radial concentration gradients of water vapor at the membrane entrance; 3) mass transfer resistances within and beneath (i.e., in the viscous sub-layer) the turbulent boundary layer between the downstream face of the membrane and the ambient air; and 4) radial dependence of mass transport resistance in the boundary layer on the upstream membrane face. HAMTA1 water vapor mass concentrations at the upstream face of the membrane were calculated from corresponding membrane surface temperatures using data on the saturation pressure of steam [Mills (1999a), pp. 931-933], the assumption of 100% relative humidity at the upstream face of the membrane, and the Ideal Gas Law:

$$\rho_{H_2O} = \frac{m}{\forall} = \frac{M \cdot P_{H_2O}}{R_U \cdot T}$$

(Equation 4.4)

The assumption of 100% RH at the upstream face of the membrane follows from the temperature of this surface intentionally being kept below the temperature of the liquid water-air interface (the evaporation front) within the chamber, necessitating some condensation. In addition, the evaporation chamber walls were kept above the temperature of the liquid water-air interface to prevent condensation of water out of the air in the vicinity of the chamber walls.

Thus the relative humidity (RH) of the surviving air-water vapor mixture at the entrance to the membrane inside the chamber must be 100%.

For HAMTA2, the water vapor mass concentration was calculated at the liquid-air interface (the evaporation front) within the evaporation chamber. By definition of this type of interface, the RH in the air boundary directly above the liquid must be 100%. Using the temperature measurement from the thermocouple situated at this location, the water vapor mass concentration was obtained using data on the saturation pressure of steam [Mills (1999a), pp. 931-933] and the Ideal Gas Law (Equation 4.4).

For both apparatuses, the assumption of 0% RH at the downstream membrane face was checked by measuring the RH of the sweep gas at 2.8 m/s and 27.5 °C (and 1.0 m/s and 50.0 °C for HAMTA2) with the RH meter module of a Kestrel® 4000 Pocket Wind Meter. This instrument showed actual readings of 1.4% to 4.6% RH (the stated accuracy of the instrument is ± 3.0% RH with a specified range of 5.0% to 95.0% RH), indicating that the nitrogen was so dry that it was below the RH meter's ability to measure moisture content.

While there might have been a trace of water vapor in the sweep gas, the extremely low RH at this location warranted an engineering approximation of 0% RH since the actual sweep gas humidity was not measured during the experiment. This approximation was valid because mass flux rate depended upon the mass concentration gradient between a very wet region and a very dry region. For example, the water vapor concentration of air inside the HAMTA1 chamber at 43 °C and 100% RH was 0.0588 kg/m^3 and inside the HAMTA2 chamber at 35 °C and 100% RH was 0.0392 kg/m^3. Assuming the highest measured RH, 4.6%, plus the measurement error of +3%, the sweep gas at 27.5 °C might have had a water vapor concentration as high as 0.00194 kg/m^3. The difference between the upstream and downstream values for HAMTA1 was 0.0568 kg/m^3, representing at most a 3.4% discrepancy from the 0% RH assumption. The difference between the upstream and downstream values for HAMTA2 was 0.0373 kg/m^3, representing at most a 4.9% discrepancy from the 0% RH assumption.

4.4.1 Buoyancy-Driven Natural Convection

The use of natural convection currents was critical to the correct function of HAMTA1. Natural convection was utilized for two purposes. In the water charge, it assured effective heat transfer from the base of the evaporation chamber deep into the water charge. In the head space defined in Section 4.4 (i.e., the air-water vapor mixture above the liquid-air interface), natural

convection assured the delivery of water-vapor-saturated air to the upstream face of the membrane. Accounting quantitatively for the mass transport resistance of the head space natural-convection-driven flow enabled disaggregation of the intrinsic mass transfer resistance of the membrane itself.

4.4.1.1 Natural Convection in the Water Charge Owing to Thermal Buoyancy

The Rayleigh Number for the liquid water was calculated from data taken during a HAMTA1 experiment with the chamber uncovered. Rayleigh Number is defined as

$$Ra_L = \frac{gL^3\beta\Delta T}{v\alpha}$$
(Equation 4.5)

where g is the gravitational acceleration, L is a characteristic length of the system, β is the fluid's thermal expansion coefficient, ΔT is the temperature gradient across the liquid, α is the fluid's thermal diffusivity and v is the fluid's kinematic viscosity. The L for this system is the depth of the water, measured experimentally based on weight of the water and knowledge of the apparatus geometry and evaporation chamber inner diameter. For liquid heated from the bottom between a solid surface and a free boundary, the *critical* Rayleigh Number for the onset of thermally driven free convection is 1101; [Deen (1998), p. 493].

A steady state temperature difference of about 10.6 °C was measured between the chamber bottom and the water-air interface using Omega 5SC-TT-T-40-36 T-type thermocouples. In addition to the thermocouple soldered to the base of the chamber, a second thermocouple was dipped into the water 26.5 mm above the floor of the chamber, but visibly below the water charge surface by a few millimeters. When the chamber had an initial 7.0-gram water charge, the calculated water Rayleigh Number was about 1.4 x 10^6. So, buoyancy-driven natural convection occurred in the liquid under these conditions.

As an additional confirmation of buoyancy-driven natural convection, a tracer study introduced tiny drops of food dye into the water with a toothpick after steady-state conditions were achieved in an open chamber run. Circulation of the drops visually confirmed thermal buoyancy driven flow and indicated the flow chirality (circulation direction) of the flow cells (Figure 4.12); it took between 5 to 10 seconds for a dye filament to make a complete loop. The filaments traveled down the center axis of the water charge, traversed along the bottom of the dish, made their way upwards to the surface of the water along the walls, and then flowed back

towards the center axis to complete the "loop". The filaments were dissipated and mixed into the water after about two such loop circulations.

While the Rayleigh Number in the liquid charge started above the critical value of 1101, liquid water evaporated away as the experiment proceeded. The resulting reduction in water depth, L, decreased the water Rayleigh Number. Assuming L was the only parameter changing during evaporation, the Rayleigh Number in the water charge was calculated to remain above the critical value until the water weight dropped below 0.6 grams.
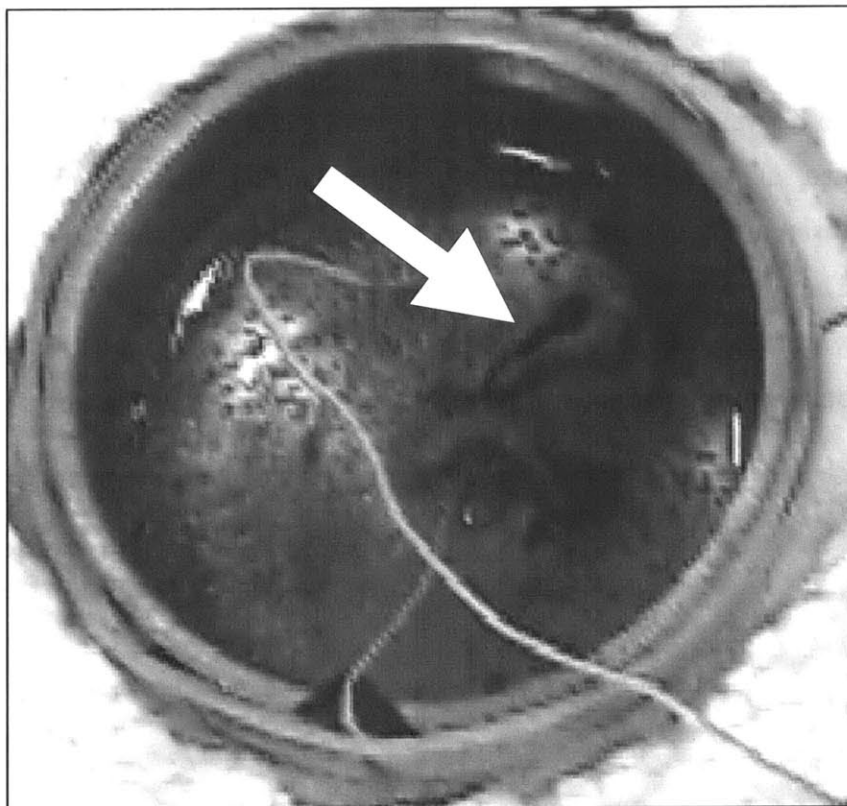
Figure 4.12 Buoyancy-driven natural convection was confirmed using a food dye tracer that illustrated the flow chirality. Dye filaments traveled down the center axis of the water charge, traversed along the bottom of the dish, made their way upwards to the surface of the water along the walls, and then flowed back towards the center axis to complete the "loop".

4.4.1.2 Natural Convection Caused by Thermal Buoyancy in the Head Space

The Rayleigh Number in the head space air atop the water was defined as in Equation 4.5 above, except the thermal-physical properties of water were replaced by those for air. Characteristic driving temperature difference was measured between the air-water interface (by dipping a thermocouple approximately 1 mm into the water) and the upstream membrane face

(via a second thermocouple epoxied to the inside face of the membrane, T_2) during a closed-chamber run to determine the Rayleigh Number for a typical evaporation chamber arrangement and experimental conditions. For gas heated from the bottom between two solid surfaces, the critical Rayleigh Number is 1708; [Deen (1998), p. 493].

At the beginning of a HAMTA1 experiment, head space Rayleigh Number was 1384, somewhat below the critical value of 1708. However, as water evaporated, the head space grew deeper. The Rayleigh Number increased to over 11,000 by the time the water was exhausted. The evaporation chamber was sized to assure head space Rayleigh Number surpassed the critical value before the steady-state conditions used to measure mass transfer rates were achieved.

Head space buoyancy drove water vapor toward the chamber walls, parallel to the liquid water-air interface, and then up the inside walls of the chamber. This flow chirality was observed experimentally using a fog of condensed water vapor as a tracer in an open-chamber experiment (Figure 4.13). The fog was created by placing a small (roughly 10 mg) chip of dry ice into the center of the evaporation chamber. The resulting sublimation effluent carried condensed water vapor, which could be observed under bright illumination, along with the flow.
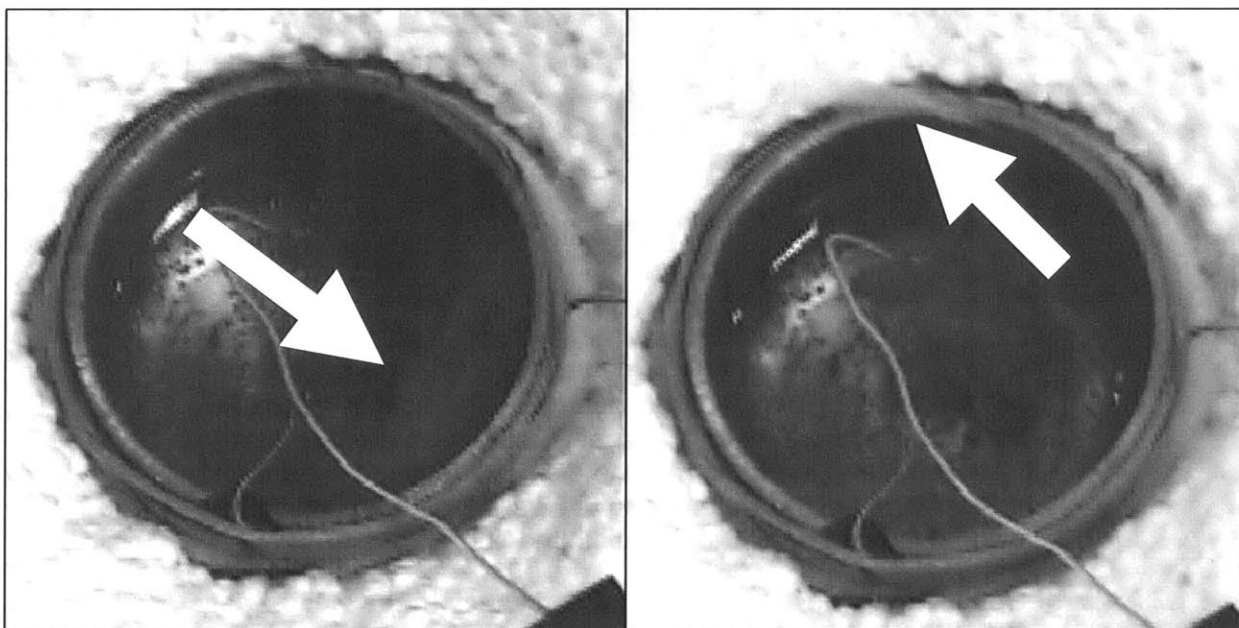

Figure 4.13 Head space buoyancy was observed experimentally using a fog of condensed water vapor as a tracer in an open-chamber experiment. Fog was generated by introducing small (~10 mg) chip of dry ice into the heated liquid. Resulting wisps of airborne water droplets traversed along the liquid, up the chamber walls, and out into the ambient; indicating the chirality of this flow. At least two different convection cells were observed. Depending on where the dry ice chip was dropped, the water vapor wisp was entrained to the bottom of the evaporation chamber (left) or the top (right).

The small amount of water vapor mixed with the air was negligible in the head space, i.e., less than 10% mass concentration. Therefore, the contribution of water vapor to the natural convection process was ignored. The stability analysis for buoyancy-driven flow in the head space assumed mass continuity of the convecting fluid, i.e., no loss of fluid or change of molar density owing to chemical reactions or to escape from the chamber. However, because mass did, in fact, leave the experimental system continuously owing to diffusion of water vapor through the membrane, the density of the air-water mixture near the chamber top was lower than the value assumed when calculating the driving density gradient for the Rayleigh Number. This density difference could potentially have changed the stability analysis upsetting the onset of circulation. However, at 43 °C and 1 atmosphere, typical operating conditions at the upstream membrane face, dry air density is 1.12 kg/m^3 while saturated air density is 1.09 kg/m^3; a difference of only 2.7 percent [Mills (1999a), p. 958]. Even if all water vapor in the head space near the membrane were lost by transport through the membrane, the impact on density at that location could not have exceeded 2.7 percent. Thus, the contribution of water vapor to the density of air in the head space could be ignored in the critical Rayleigh Number calculations.

4.4.1.3 Natural Convection Imposed Operational Envelope

Since buoyancy-driven convective flow was critical to the proper function of the HAMTA1 evaporation chamber, the Rayleigh Number for the charge of liquid water (which decreased as water evaporated) and the head space Rayleigh Number (which increased as water evaporated) defined the operating envelope for the apparatus, Figure 4.14. Provided the apparatus was functioning at steady-state temperature within this envelope, the mass flux through the membrane remained constant. Due to buoyancy-driven convection, the diffusion resistance to water vapor mass transport in the head space was negligible while operating in this range.

Examination of the Sherwood Number clarifies this point. The Sherwood Number represents a ratio of a characteristic convective flux rate to a characteristic diffusive flux rate,

$$Sh = \frac{U_b \cdot d}{D_{H_2O,Air}}$$
(Equation 4.6)

where $D_{H2O,Air}$ is the diffusion coefficient of water vapor in air, d is the diameter of the evaporation chamber, and U_b is the characteristic velocity of buoyancy-driven natural convection [Deen (1998), p. 949]:

$$U_b = (gL\beta\Delta T)^{0.5}$$
(Equation 4.7)

A lower bound on the Sherwood Number for HAMTA1 was obtained using experimental operating values (L, β, ΔT, and U_b = 0.095 m/s) consistent with the beginning of the steady-state operating period. This condition gave a lower bound because L increased as liquid water evaporated away, causing the characteristic convective velocity, U_b, to rise. The chamber diameter, d, was about 31.7 mm (0.0317 meters). Under the conditions within the evaporation chamber, a typical value for $D_{H2O,Air}$ was 2.6 x 10^{-5} m^2/s. Thus, the Sherwood Number was at least 120 for HAMTA1. This result is important because it demonstrates the dominance of convective over diffusive processes for mass transport in the head space. As a practical consequence, the experiment was unaffected by changes in water depth over the steady-state operating range indicated in Fig. 4.14.
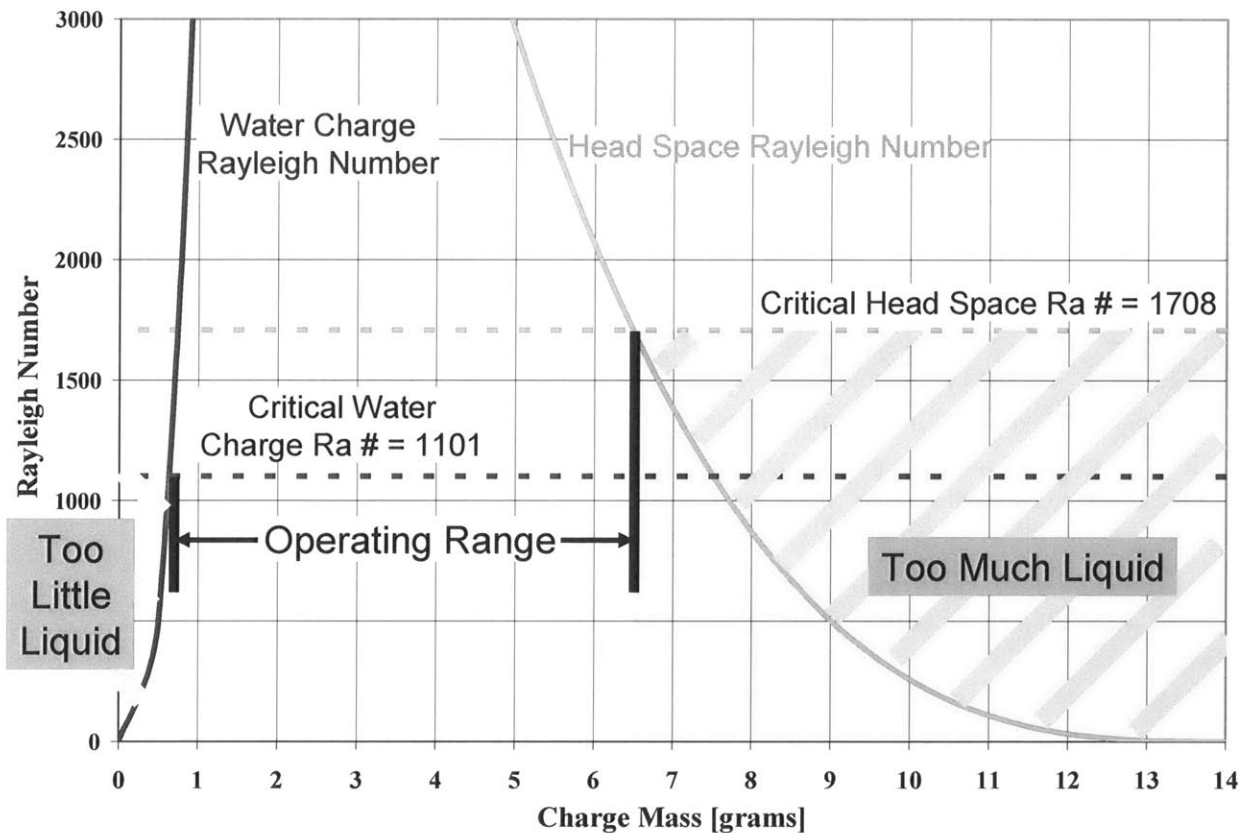

Figure 4.14: The Rayleigh Numbers in the water charge and in the head space must both be above their respective critical values to assure natural convection occurs in both regions. These two requirements define a range of values for the mass of liquid water in the evaporation chamber over which the apparatus will operate properly.

4.5 Apparatus Thermal Validation

Applying the First Law of Thermodynamics to a control volume representative of the experimental apparatus (Figure 4.15) yielded

$$\frac{d(C_P \cdot M \cdot T_1)}{dt} = \dot{Q}_{in} - \dot{Q}_{lost} - Ah(T_1 - T_{amb}) - \dot{m} \cdot \Delta H_{fg} \qquad \text{(Equation 4.8)}$$

where C_p is the overall average specific heat of the apparatus; M is the instantaneous mass of the apparatus; T_1 is the instantaneous temperature of the apparatus, taken via thermocouple at the base of the evaporation chamber; t is time; $\dot{Q}_{in}$ is the energy input to the system by an electric heater; $\dot{Q}_{lost}$ represents heat leakage unaccounted for by the other terms (ideally $\dot{Q}_{lost}$ should be zero); $\dot{m}$ is the rate of mass leaving the control volume as water vapor diffuses through the porous membrane; ΔH_{fg} is the latent heat of evaporation for water; h is a lumped natural convection coefficient; A is the surface area of the membrane atop the dish; and T_{amb} is instantaneous environmental temperature near the downstream membrane face.
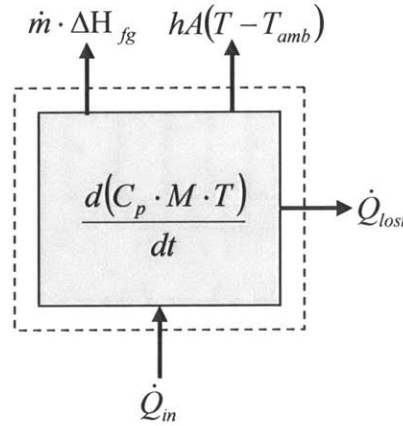

Figure 4.15: Control volume for overall heat balance on the evaporation apparatus.

The overall average specific heat of the apparatus, C_p, which is dominated by the liquid water, changes by less than 0.9% over the operating range of interest for these experiments (273 K to 373 K). Therefore, it was assumed to be independent of temperature (and therefore time) for this thermal model.

Table 4.1 lists the steps and modeling assumptions leading to experimental determination of $C_p \cdot M$ and h for both experimental apparatuses. The overall lumped thermal mass of the apparatus, $C_p \cdot M$, was obtained from the slope of the early stage heat-up curve (Figure 4.16) for closed chamber (latex or non-porous polycarbonate membrane) runs where evaporative transport was prevented (i.e., $\dot{m} = 0$) and it was a reasonable approximation to neglect convective cooling (i.e., $T_1 - T_{amb} \approx 0$). Using this $C_p \cdot M$ value, the overall convective heat transfer coefficient, h,

was determined by fitting a Newtonian lumped cooling model to the cool-down curve for closed chamber runs, recognizing that $\dot{Q}_{in} = 0$ (heater off).

Table 4.1: Equations and simplifying assumptions used to calculate unknown thermal quantities and an overall heat balance for the evaporative cooling apparatuses used in this thesis.

	Equation	Assumptions
Overall Balance	$\dfrac{d\left(C_p \cdot M \cdot T\right)}{dt} = \dot{Q}_{in} - \dot{Q}_{lost} - \dot{m} \cdot \Delta H_{fg} - hA(T - T_{amb})$	T spatially uniform
Warm Up	$C_p M \dfrac{dT}{dt} = \dot{Q}_{in}$	Lumped mass of uniform T No water transport $\quad T \approx T_{inf} \quad \dot{Q}_{lost} \approx 0$
Cool Down	$C_p M \dfrac{dT}{dt} = -hA(T - T_{amb})$	Lumped mass of uniform T No water transport $\quad \dot{Q}_{lost} \approx 0$ No heating
Cool Down	$\ln\left(\dfrac{T - T_{inf}}{T_o - T_{inf}}\right) = -\dfrac{hA}{C_p M} t$	Lumped mass of uniform T No water transport $\quad \dot{Q}_{lost} \approx 0$ No heating

For HAMTA1, the repeatability of the $C_p \cdot M$ and h determinations over the 4 runs was within the uncertainty estimated by propagation of error analysis. The experimentally derived h (192 w/m^2-K) was within the accepted range for forced convective cooling with air, 10 - 200 W/m^2-K [Mills (1999a), p. 22]. The $C_p \cdot M$ value (131 ± 19 J/K) was within 15% of a value estimated from known masses and tabulated heat capacities of apparatus components. Using these experimentally-derived parameters in a steady state, closed chamber heat balance [i.e., $d(M \cdot T_1)/dt = 0$ and $\dot{m} \cdot \Delta H_{fg} = 0$ in Eq (4.8)], the first and third terms on the RHS of Equation 4.8 accounted for all thermal flows within +8.7% to -0.1% (Table 4.2). For a steady state heat balance with these $C_p \cdot M$ and h values for the porous membrane runs (evaporation enabled), the first, third, and fourth terms on the RHS of Equation 4.8 accounted for all thermal flows within +12.4% to +3.3%. For these heat balance calculations, $\dot{m}$ was obtained from the weight loss measurements as described in Section 4.1.5, and ΔH_{fg} was taken as the latent heat of vaporization of liquid water at 320 K, These heat balances were satisfying given the use of lumped thermal physical parameters deduced from the transient heat-up and cool-down phase of the experiments. The heat balances were also excellent given the small size of the apparatus because the surface to volume ratio was higher than for larger set-ups, providing greater relative area for parasitic heat loss.
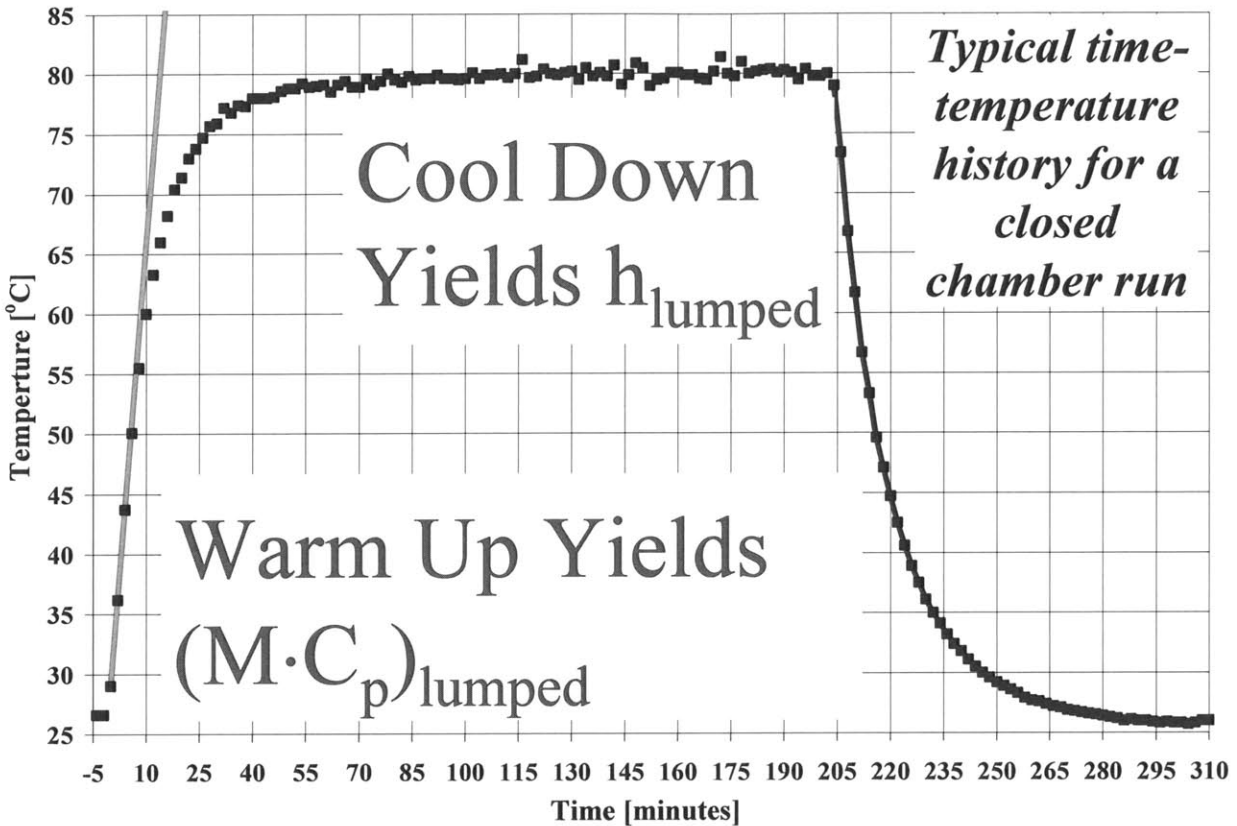
Figure 4.16: Fitting model curves to the measured temperature-time history for the evaporation chamber base during heat up and cool down, with the chamber covered to prevent escape of water vapor, allows estimates of the apparatus thermal mass and an overall lumped heat transfer coefficient for apparatus heat loss respectively.

For HAMTA2, the values of the $C_p \cdot M$ and h were determined from 4 closed chamber runs. The experimentally derived average h (115.3 w/m²-K) was within the accepted range for forced convective cooling, 10 - 200 w/m²-K [Mills (1999a), p. 22]; in addition this value was less than 192 w/m²-K for HAMTA1, which was consistent with lower velocity of sweep gas over the membrane (2.8 m/s for HAMTA1 versus 1.0 m/s for HAMTA2). The experimentally determined $C_p \cdot M$ was 35.59 ± 4.78 J/K, which was consistent with 41.17 J/K estimated from known masses and tabulated heat capacities of apparatus components. Using these experimentally-derived parameters in a steady state, closed chamber heat balance [i.e., $d(M \cdot T_1)/dt = 0$ and $\dot{m} \cdot \Delta H_{fg} = 0$ in Eq (4.8)], the first and third terms on the RHS of Equation 4.8 accounted for all thermal flows within +4.5% to -13.1% (Table 4.3). For a steady state heat balance with these $C_p \cdot M$ and h values for the porous membrane runs (evaporation enabled), the first, third, and fourth terms on the RHS of Equation 4.8 accounted for all thermal flows within +8.5% to -5.2%.; where, as with

HAMTA1, $\dot{m}$ was determined from weight loss measurements (Section 4.1.5) and ΔH_{fg} was taken as the latent heat of evaporation of water at the air-liquid water interface temperature inside the evaporation chamber for each individual run (between 300 °C and 305 °C depending on the magnitude of $\dot{m}$).

Table 4.2: Heat balance results for four closed chamber experiments using HAMTA1

Closed Chamber Run Number	Average M·C$_p$	Average h	$\dot{Q}_{in}$	h$_{lumped\_ave}$A(T$_1$-T$_{amb}$)	$\dot{Q}_{lost}$	$\dot{Q}_{lost} / \dot{Q}_{in}$
[ ]	[J/K]	[w/m^2-K]	[w]	[w]	[w]	[%]
Experiment 1	132.58 ± 18.62	189.36 ± 23.73	8.03	8.04	-0.01	-0.1
Experiment 2	132.52 ± 15.39	188.16 ± 25.48	7.90	7.69	0.21	2.6
Experiment 3	129.21 ± 19.13	196.01 ± 23.88	8.06	7.36	0.70	8.7
Experiment 4	131.17 ± 14.75	193.91 ± 23.34	8.06	7.48	0.58	7.2

Table 4.3: Heat balance results for four closed chamber experiments using HAMTA2

Closed Chamber Run Number	Average M·C$_p$	Average h	$\dot{Q}_{in}$	h$_{lumped\_ave}$A(T$_1$-T$_{amb}$)	$\dot{Q}_{lost}$	$\dot{Q}_{lost} / \dot{Q}_{in}$
[ ]	[J/K]	[w/m^2-K]	[w]	[w]	[w]	[%]
Experiment 1	39.54 ± 5.81	106 ± 8.8	0.668	0.580	-0.088	-13.1
Experiment 2	28.63 ± 4.22	120 ± 8.8	0.669	0.626	-0.043	-6.4
Experiment 3	37.16 ± 3.16	110 ± 8.8	0.669	0.671	0.002	0.3
Experiment 4	37.02 ± 6.14	125 ± 8.8	0.668	0.698	0.030	4.5

4.6 Heat Leak and Heat Balance Error

The most substantial heat leak in HAMTA1 was radiation emanating from the bottom of the heater to the surface of the scale upon which the apparatus sat. To quantify this heat leak, thermocouples were affixed to the bottom surface of the heater and to the scale surface. The heater was allowed to settle to a standard steady-state operating temperature. Temperature data were taken at the thermocouples for 65 minutes, and these data were averaged to obtain a mean temperature difference between the two surfaces.

An upper bound on the radiative heat leak was obtained by assuming both surfaces behave as black body radiators. While the scale stage was metal and probably had an emittance between 0.30 and 0.70, the black body assumption (emittance = 1.0) assured an upper bound on radiative heat leak was calculated. The view factor from the heater to the scale surface was taken as roughly 1, which was an accurate approximation because the distance between the heater and the scale (1 mm) was much smaller than the critical heater dimension (diameter ~ 120mm). Under

these assumptions, a one-dimensional radiation resistor model yielded maximum thermal leakage of 0.76 watts. Compared to the 8.0 watt input required to simulate 1350 w/m^2, the radiation leakage represented no more than 9.5 percent of the total input power.

While this radiation mechanism existed for the apparatus under steady state operating conditions, it was much reduced during warm-up and cool-down because the temperature gradient between the heater and scale was less severe during these transient processes. It was hypothesized, therefore, that this radiation term accounted for a substantial portion of the incomplete heat balance closure. Radial heat leakage and radiation from other apparatus surfaces probably represented the remaining leaked thermal energy.

The use of a well in the insulation for HAMTA2 (see Figure 4.2) attempted to improve upon HAMTA1 by reducing the radiative heat leak from the base of the heater to the scale. Within this well, the hot (heater) surface was above the cold (insulation) surface with respect to the gravity vector; therefore, buoyancy-driven natural convection could not occur in the insulation well. Thus, heat could leak only by conduction and radiation. An experimental heat transfer study estimated the axial heat leak into the insulation collar. A pair of thermocouples, one placed at the bottom of well and the other placed on the downward face of the evaporation assembly, was used to measure the axial temperature gradient across the pocket. On the downward face of the heater, the average temperature under steady state conditions was 51.0 ± 0.1 °C, and on the bottom of the well, the temperature was 38.1 ± 0.1 °C in steady state. Under assumptions of black body radiation and view factor of unity, the radiative heat leak into the bottom of the insulation collar could not exceed 0.086 watts. This heat leak path represented no more than 12.8% of the 0.67 watts of input power required for HAMTA2. Under the model assumptions, the insulation well seems to provide no benefit for reduced radiation from the bottom side of the heater. As with HAMTA1, the similarity between the magnitude of incomplete heat balance closure (+4.5% to -13.1%) and radiative heat loss from the bottom of the evaporation chamber (12.8%) suggests that radiation losses represented a substantial portion of the unaccounted for heat leak.

5 Mathematical Modeling of Apparatus Operation

This chapter describes the mathematical modeling techniques, assumptions, and methods as well as associated experimental validations utilized to probe and understand intricate functions of the experimental apparatuses. These approaches provide mass transport models for both HATMA1 and HAMTA2, which enable disaggregation of intrinsic (apparatus independent) mass transport coefficients for each membrane studied. A major contribution of this research is connecting intrinsic membrane mass transport coefficients to membrane cooling efficacy to inform design of systems employing latent heat transport through porous media for surface cooling.

5.1 Dominant Transport Mechanisms

Several possible mechanisms may have enabled or hindered mass transfer through the porous membranes including diffusion, transpiration, Stefan Flow (convection owing to diffusion), and choked flow. Also, multiple mechanisms working together could have been responsible for transport processes. For these experiments, transpiration, Stefan Flow, and choked flow were negligible with respect to diffusion, which was the dominant mass transport mechanism under the concentrations and length scales of interest in this research. Calculated mass flow via transpiration was about eight orders of magnitude smaller than the diffusion mass flow rate. Choked flow could not occur unless the pressure ratio across the membrane exceeded 1.89, but the largest pressure ratio obtained for any experiment was less than 1.28. Stefan Flow contributed a calculated mass flow rate enhancement of no more than 12.9% (for the DuPont porous membranes) and 3.9% (for the track-etched membranes), consistent across all pore diameters under study. The Stefan Flow mechanism did not impact the diffusion coefficient itself, and its contribution was ignored in apparatus modeling calculations. Validation calculations detailing the negligible impact of these various mechanisms are provided in Appendix 1.

5.1.1 Diffusion

Fick's Law for diffusion provides the appropriate model for mass transport through porous membranes. When written in terms of mass flux, $\dot{m}_{H_2O}$, Fick's Law in one dimension through a porous medium is

$$\dot{m}_{H_2O} = \frac{D_{H_2O,air} \cdot A \cdot \varepsilon_v}{\tau \cdot L} \left(\rho_{H_2O,2} - \rho_{H_2O,3} \right)$$

(Equation 5.1)

92

where $D_{H2O,air}$ is the diffusion coefficient of water vapor in air, A is the membrane area normal to diffusion, ε_v is the membrane porosity (also called void fraction), τ is the membrane tortuosity, L is the membrane thickness, and $\rho_{H2O,2}$ and $\rho_{H2O,3}$ are the mass concentrations of water vapor on either side of the membrane, stations 2 and 3 (Figure 4.1).

Porosity and thickness of each sample were measured using the membrane characterization techniques outlined in Chapter 3. Tortuosity was taken as unity because pores on both the DuPont porous membranes and the track-etched membranes ran essentially straight-through from one exterior face to the other and were of essentially uniform cross section in the axial direction (Section 3.3.5).

5.2 Membrane Downstream Apparatus Mass Transport Resistances

The downstream membrane faces of both HAMTA1 and HAMTA2 (i.e., the upward facing surfaces exposed to the ambient environment) were maintained at constant temperature and near-zero relative humidity by dry nitrogen sweep gas. This gas formed a boundary layer on the membrane surface, which contributed to the apparatus-imposed mass transport resistance experienced by water vapor diffusing from inside the evaporation chamber to ambient.

5.2.1 HAMTA1 Viscous Sub-layer Mass Transport Resistance

Nitrogen sweep gas in HAMTA1 originated from a 6.67 mm inner diameter tube and flowed over the membrane at 2.8 ± 0.25 m/s and 27.5 °C. The Reynolds Number (based on diameter) for internal flow in the tube was 1201, below the Re_D of 1700 – 2300 generally associated with onset of turbulence. However, no diffuser was used at the tube's end, and sharp transition between tube flow and jet flow may have generated some flow instability. Upon jetting from the nozzle, tracer studies revealed that the flow developed along the Styrofoam insulation collar for about 43 mm before reaching the membrane. The Styrofoam collar was extremely rough, with beads on the order of a half a millimeter protruding from the surface in a vaguely hexagonal pattern. Surface roughness probably contributed to the early onset of turbulent flow.

This system was mathematically modeled as flow over a flat plate. Had the plate been smooth, Re_L at the membrane's leading edge would have been 12,200, below the transition threshold for turbulent flow, $Re_{L,tr}$ = 50,000 – 200,000. Nonetheless, the sharp transition from pipe flow to jet flow at the outlet tube coupled with the surface roughness of the Styrofoam collar induced a turbulent boundary layer, as observed via experimental tracer studies. Balachandar and Patel [Balachandar and Patel (2002)] showed that turbulence could be induced

at low Reynolds Numbers when surface roughness height was a significant proportion of the boundary layer thickness. Tracer studies of flow over the Styrofoam collar, conducted with water vapor as the visualization medium (Figure 5.1), confirmed transition to turbulence along the Styrofoam collar upstream of the membrane.
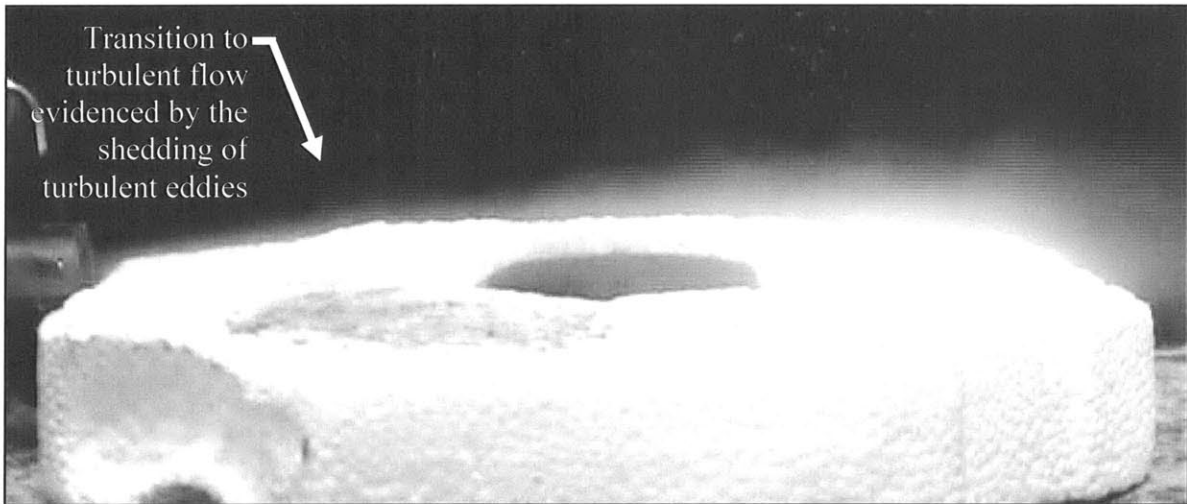

Figure 5.1: Transition to turbulence in the dry nitrogen jet flowing over HAMTA1 was observed to occur in advance of the membrane via a tracer in the flow.

The tracer particles were drops of condensed water vapor generated by passing nitrogen (N_2) gas though a flask of boiling liquid water. Small pieces of dry ice were added to the flask. The resulting cold CO_2 gas, which sublimed from the dry ice, lowered the dew point in the flask sufficiently to condense liquid droplets small enough to be entrained in the gas flow. For tracer studies, the fog was directed over the evaporation chamber from a 6.67 mm inner diameter tube located at the same position with respect to the membrane as the dry nitrogen sweep gas nozzle in normal experiments.

The Sherwood Number model for mass transport in a turbulent boundary layer over-predicted the mass transport resistance of the sweep gas because the transition between the Styrofoam (where no water diffuses into the boundary layer) and the membrane (were water does diffuse into the boundary layer) was not accounted for. This transition created a mass concentration boundary layer starting from the leading edge of the membrane, a different location than the momentum boundary layer, which was initiated at the leading edge of the Styrofoam collar. The diffusion resistance of the viscous sub-layer represented a better model for the mass transfer resistance at the external membrane face.

Figure 5.2 shows in schematic a turbulent boundary layer, including a very thin region in the vicinity of the wall representing the viscous sub-layer. In the viscous sub-layer, flow is dominated by viscous forces, and turbulent mixing and convection do not occur. This region is therefore capable of supporting a water vapor concentration gradient between the external face of the membrane and the bulk turbulent boundary layer.
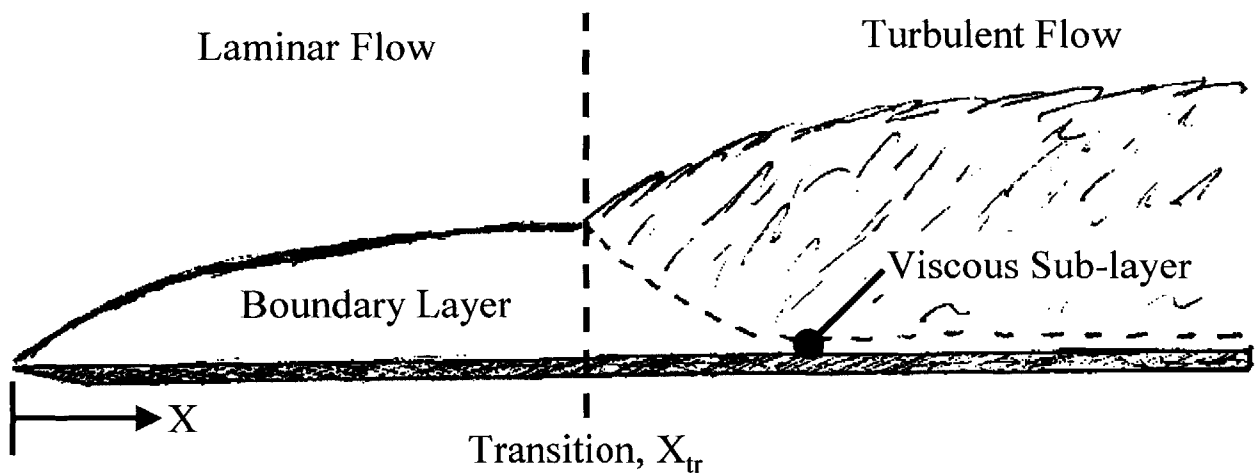

Figure 5.2: Schematic representation of development of a turbulent boundary layer over a flat plate. The turbulent portion of the boundary layer includes a viscous sub-layer, which is responsible for a majority of the mass transport resistance in the boundary layer. While the viscous sub-layer does grow in thickness with increased distance along the flat plate, this growth is too small to be discerned on an image at this scale. *Figure based on original in Mills [Mills (1999a)], page 281.*

Due to the extreme thinness of this layer (on the order of 0.5 mm) and the linear nature of the velocity profile within it, it was assumed that the water vapor concentration gradient in the viscous sub-layer was linear. The "Law of the Wall" from turbulent flow theory [Mills (1999b), pp. 465-471] was utilized to calculate viscous sub-layer thickness. Figure 5.3 shows the empirical velocity profile in a turbulent boundary layer, inclusive of the region near the wall. According to the law of the wall, within the region near a solid surface, the velocity profile of any turbulent boundary layer can be described by a dimensionless linear expression

$$u^+(x) = \frac{U}{u_\tau(x)} = \frac{\delta(x) \cdot u_\tau(x)}{\upsilon} = y^+(x)$$ (Equation 5.2)

where $u^+(x)$ and $y^+(x)$ are dimensionless velocity and dimensionless boundary layer thickness respectively at station x, U is the free stream velocity, $\delta(x)$ is the actual boundary layer thickness

at station x, ν is the fluid's kinematic viscosity, and $u_\tau(x)$ is the "friction velocity" determined from the sheer stress on the wall [Mills (1999b), p. 466; Tritton (1977), pp. 275-281]. The formula for $u_\tau(x)$ is

$$u_\tau(x) = U\left(\frac{C_{f,x}}{\rho}\right)^{\frac{1}{2}}$$

(Equation 5.3)

where $C_{f,x}$ is the local skin friction at station x at the wall and ρ is the density of the fluid. The skin friction, $C_{f,x}$, must be calculated to determine the boundary layer thickness.
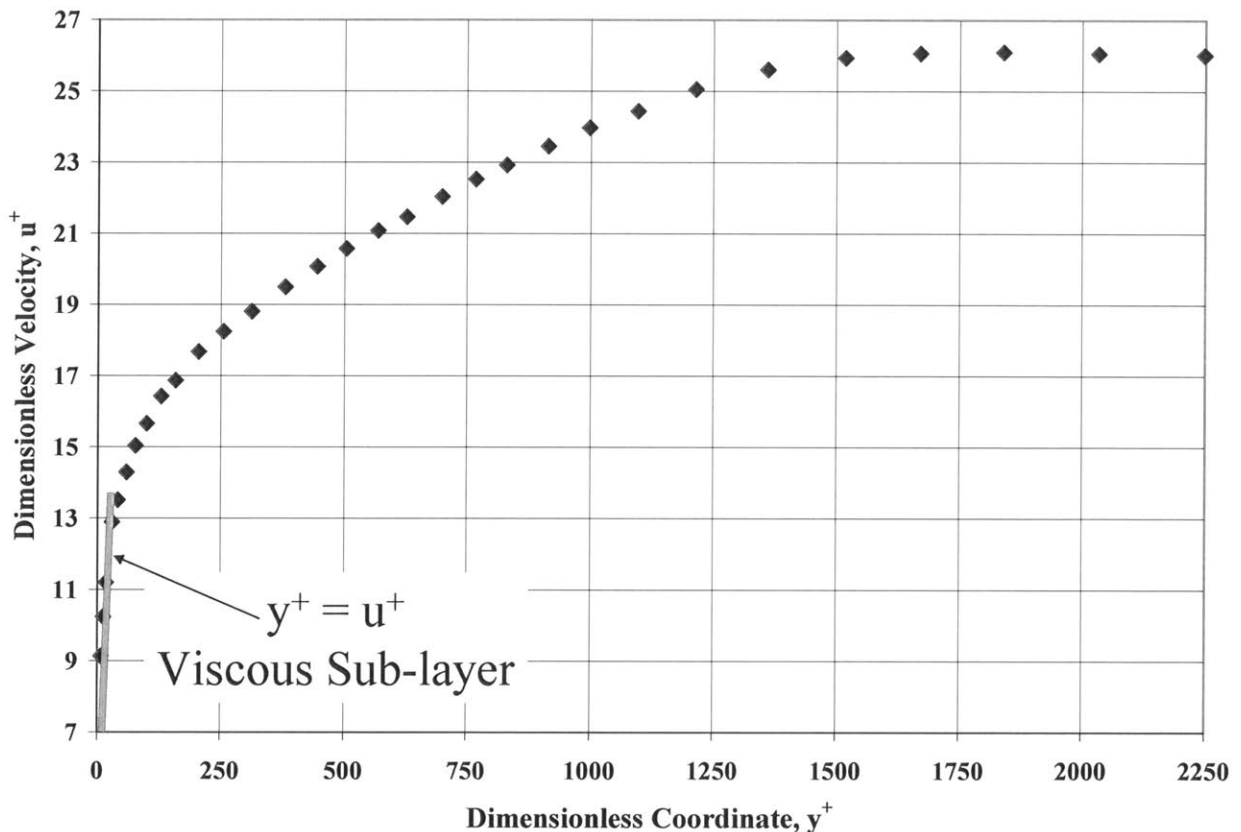
Figure 5.3: The "Law of the Wall" suggests that a linear velocity profile characterizes the viscous sub-layer region of a turbulent boundary layer owing to the eddy damping impact of the wall. *This figure was developed from hot-wire anemometer raw data for turbulent flow over a flat plate, Re_Θ = 4981 [Smith (1994)].*

There are three regimes of wall skin friction: 1) smooth surface, which depends only on Reynolds Number; 2) rough surface, which depends only on the ratio of surface roughness to plate length; and 3) transition, which depends on both Reynolds Number and surface roughness.

Since the DuPont porous membranes tested with HAMTA1 had smooth surfaces (i.e., no features protruding up from the surface that might interrupt the flow), the smooth surface model

was selected. For turbulent flow over smooth flat surfaces, Mills [Mills (1999a), p. 282] suggests the empirical correlation

$$C_{f,x,smooth} = 0.0592 \cdot \mathrm{Re}^{\frac{-1}{5}}$$ (Equation 5.4)

which is valid for $10^5 < \mathrm{Re} < 10^7$, while in this situation $\mathrm{Re} = 1.6 \times 10^4$. Nonetheless, this correlation was selected to represent the turbulent nature of the flow as evidenced by experimental tracer studies.

Equation 5.2 only applies within the viscous sub-layer. Beyond this region, the relationship between $u^+(x)$ and $y^+(x)$ is no longer linear. The linear viscous sub-layer region exists between 0 $< y^+ < \delta^+$ where the value of δ^+ is between 5 [Mills (1999b), p. 467] and 8 [Tritton (1977), pages 275-281].

For this calculation, $\delta^+ = 5$ was utilized since it is the more prevalent value in the literature. Using Equations 5.3 and 5.4 in Equation 5.2 and re-arranging for $\delta(x)$ gave:

$$\delta(x)_{smooth} = \frac{5\upsilon}{U\left(\dfrac{0.0592 \cdot \mathrm{Re}^{\frac{-1}{5}}}{\rho}\right)^{\frac{1}{2}}}$$ (Equation 5.5)

Since there was a gap between the Styrofoam collar and the membrane too large to be traversed by an intact boundary layer (see Figure 5.1), it was assumed that the turbulent boundary layer reformed at the leading edge of the membrane. Average viscous sub-layer thickness over the membrane was found via integration over the membrane diameter

$$\overline{\delta} = \frac{1}{2r_o}\int_0^{2r_o} \frac{5\upsilon}{U\left(\dfrac{0.0592 \cdot \mathrm{Re}_x^{-\frac{1}{5}}}{\rho}\right)^{\frac{1}{2}}}dx$$ (Equation 5.6)

where r_0 is the outer radius of the membrane. Dividing the average viscous sub-layer height by the diffusion coefficient of water vapor in air (from Equation 2.8) resulted in a mass transfer resistance with units [s/m]. For nitrogen at 27.5 °C at 2.8 m/s, $\overline{\delta}_{smooth} = 4.0 \times 10^{-4}$ m, and the associated diffusion resistance was $R_{VSL} = 15.6$ s/m. This result quantified the membrane downstream resistance to mass transport for HAMTA1.

5.2.2 HAMTA2 Laminar Boundary Mass Transport Resistance

To enable better characterization of the downstream membrane face boundary layer, HAMTA2 was designed to allow the exposed membrane face to poke through a hole machined into a 0.125-inch thick sheet of polycarbonate (Figure 5.4). Seamless transition from smooth plate to smooth membrane assured that mass transport models arising from correlations for flow over a flat plate would be highly representative.
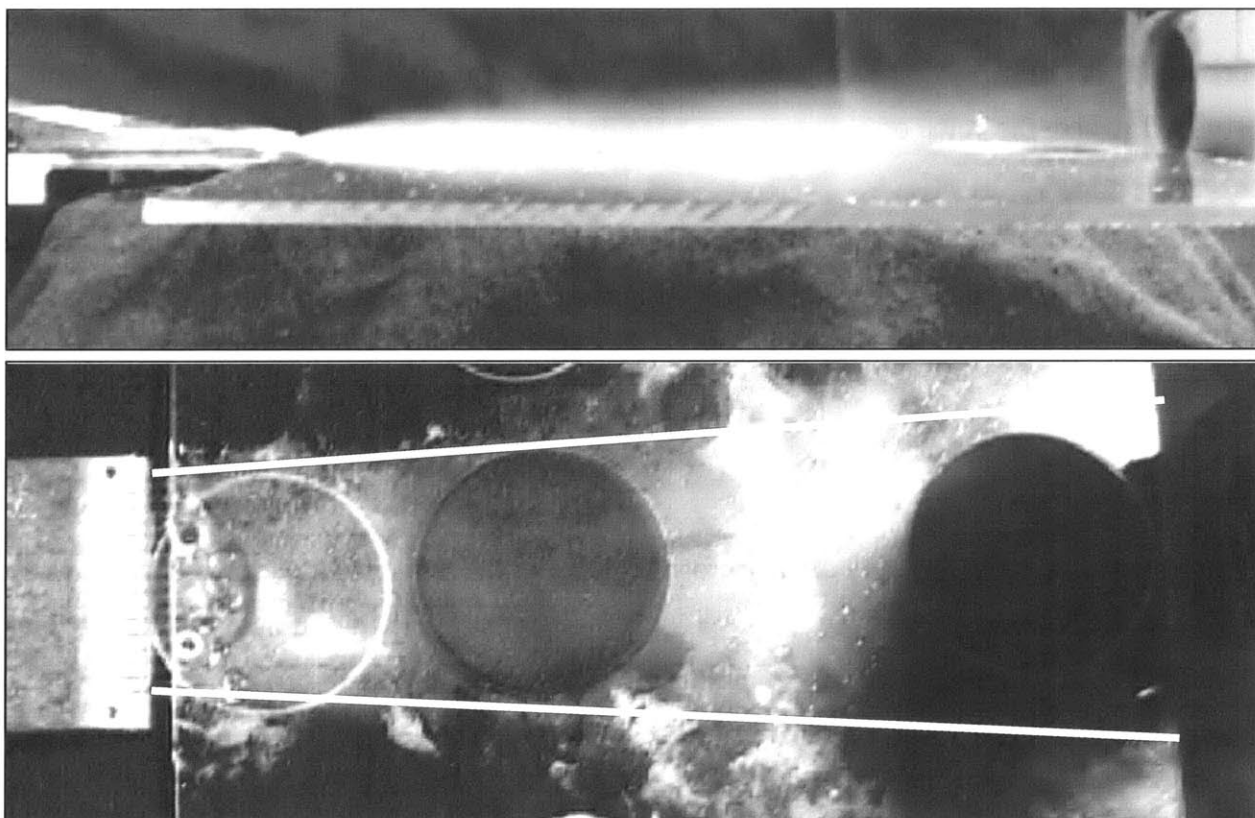

Figure 5.4: (Top) Laminar boundary layer formation induced by flow at 1 m/s emanating from a flat nozzle. The flow develops over a smooth, flat plate with a flush embedded membrane. (Bottom) The nozzle is wider than the membrane [i.e., the black circle near the center of the image] and the resulting flow field [denoted within the two superimposed straight white lines] completely covers the membrane surface. Additional circles in the image are shims used to assure the flat plat rests perfectly horizontally.

Nitrogen sweeping over the membrane in HAMTA2 originated from a flat aluminum blow-off nozzle, about 5 cm wide. The nozzle contained twenty 1 mm ID, round jet holes aligned next to one another to generate a flat sheet of fluid. Dry nitrogen left these jets at 1.0 ± 0.15 m/s at 50.0 °C. Under these conditions, the Reynolds Number based on nozzle diameter for each jet was

98

56, below $Re_D < (1700 - 2300)$ for the onset of turbulence. Flow disturbances arising due to transition from pipe flow to jet flow were damped out as the fluid encountered the smooth, flat polycarbonate sheet. The nitrogen flowed 43 mm over this flat surface before reaching the membrane, which was seamlessly integrated into the plastic sheet. The membrane was 42 mm in diameter, and the Reynolds Number (based on plate length) at the leading point of the membrane was 2400 and at the trailing point was 4750. These values were much smaller than the transition Reynolds Number (50,000 to 200,000) for onset of turbulence. Flow over the membrane was laminar, and tracer studies similar to those described in Section 5.2.1 confirmed the laminar nature of the flow (Figure 5.4).

An excellent representation of this system was a heat transfer model for laminar flow over a smooth, flat plate insulated on its leading edge and heated starting at some downstream location, ξ, (Figure 5.5).
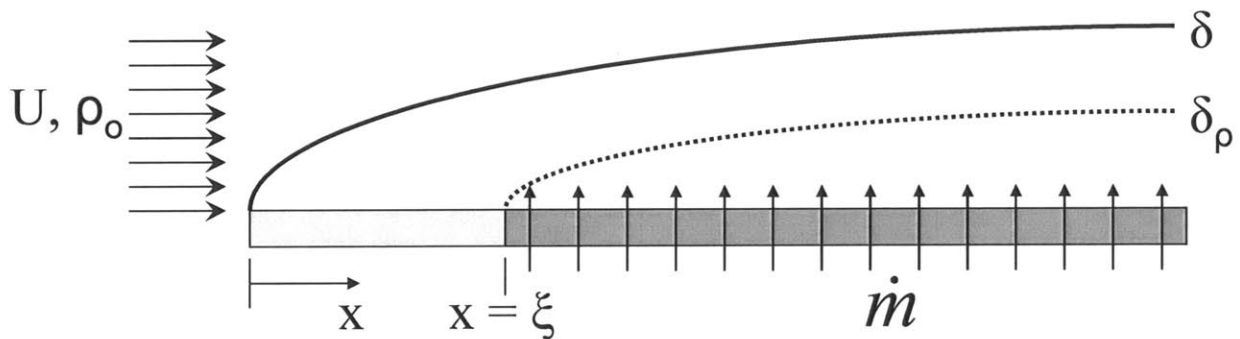
Figure 5.5: The momentum boundary layer, δ, and mass concentration boundary layer, $δ_ρ$, develop from different locations for laminar flow over a smooth flat plate in which the leading plate section is not permeable to mass transport. At downstream station ξ the membrane allows permeation of water vapor into the flow, creating a mass concentration boundary layer. *Adapted from original in Mills (1999) page 411.*

The correlation for this arrangement, developed from first principles by Mills [Mills (1999a), pp. 409-412], was modified to generate a mass transfer correlation by substituting the Schmidt Number for the Prandtl Number to relate Nusselt Number to Sherwood Number as per Mills [Mills (1999a), p. 782],

$$Sh_x = \frac{Nu_x \cdot Sc^{\frac{1}{3}}}{Pr^{\frac{1}{3}}}$$

(Equation 5.7)

The Mills model elegantly accounts for the growth of the laminar boundary layer from the leading edge of the polycarbonate plate and the subsequent growth of the mass concentration boundary layer over the porous membrane. The insulated (non-heating) leading edge of the plate in the model was analogous to the polycarbonate sheet, through which no water vapor is transported. Heating at downstream location ξ in the model was analogous to water vapor diffusing through the membrane into the flow, generating a mass concentration boundary layer. With Sc substituting for Pr, the Mills correlation became

$$Sh_x = \frac{0.331 \mathrm{Re}_x^{\frac{1}{2}} Sc^{\frac{1}{3}}}{\left[1-\left(\frac{\xi}{x}\right)^{\frac{3}{4}}\right]^{\frac{1}{3}}}$$ (Equation 5.8)

where Re_x was the Reynolds Number of the flow based from the leading edge of the impervious plate, and ξ was the downstream station representing the leading edge of the water-permeable membrane. Integrating Equation 5.8 over the membrane diameter gave an average Sherwood Number representing mass transport in the boundary layer over the membrane;

$$\overline{Sh}_L = \frac{1}{L_f - L_o} \int_{L_o}^{L_f} \frac{0.331 \mathrm{Re}_x^{\frac{1}{2}} Sc^{\frac{1}{2}}}{\left[1-\left(\frac{\xi}{x}\right)^{\frac{3}{4}}\right]^{\frac{1}{3}}} dx$$ (Equation 5.9)

where L_o and L_f were the leading and trailing edges of the membrane respectively. The average mass transport coefficient for the boundary layer on the downstream membrane face, $\overline{h}_{BL}$, was obtained from the definition of Sherwood Number,

$$\overline{Sh}_L = \frac{\overline{h}_{BL} L}{D_{H_2O,Air}}$$ (Equation 5.10)

where L was the membrane diameter and $D_{H2O,Air}$ was the diffusion coefficient of water vapor in nitrogen obtained from Equation 2.8 for temperature and pressure conditions at the downstream membrane face. For typical HAMTA2 experiments, the range of $\overline{h}_{BL}$ was 45.4 to 61.6 m/s, depending on the exact velocity and flow temperature conditions measured during a particular experiment.

5.3 Membrane Upstream Apparatus Mass Transport Resistances

The upstream face of the DuPont porous membrane on HAMTA1 (i.e., the downward facing surface exposed to the inside of the evaporation chamber) was subjected to buoyancy-induced convective flow arising from the intentional design of the deep evaporation chamber. The resulting boundary layer modified water vapor transport and had to be properly accounted for to disaggregate the intrinsic experimental membrane mass transport resistance. There was no convective flow inside the HAMTA2 evaporation chamber due to its shallow design. However, water vapor transport through the quiescent air in the HAMTA2 head space introduced mass transport resistance that had to be accounted for to calculate the intrinsic mass transport resistance of the membrane using experimental data.

5.3.1 HAMTA1 Buoyancy-Driven Head Space Concentration Gradient

While substantial functional benefit was derived from buoyancy-driven flows in the HAMTA1 evaporation chamber, the head space flow created a complicating factor: a boundary layer and associated radial concentration gradient along the upstream membrane face.

Deen [Deen (1998), p. 494] derived the characteristic velocity for buoyancy-driven natural convection inside a chamber,

$$U_b = \left(gL\beta\Delta T\right)^{0.5}$$ (Equation 5.11)

which arose from scaling terms in the buoyancy-driven flow momentum equation. Here, g is the gravitational constant, L is the characteristic length over which flow occurred, β is the fluid's thermal expansion coefficient, and ΔT is the temperature difference driving the convective flow. Substituting HAMTA1 apparatus values for these variables at the beginning of the steady-state period, U_b = 0.095 m/s. As the liquid water in the evaporation chamber was depleted and the head space grew, the characteristic velocity increased to 0.128 m/s by the time the experiment lost enough water to leave the steady-state operating envelope. Therefore, an average value of U_b = 0.112 m/s was utilized for calculations in this thesis.

As an experimental check on the calculated value of U_b, videos were taken during an open-chamber experiment using a dry-ice tracer to visualize the movement of convective cells inside the evaporation chamber (Figure 4.13). The tracer moved from the center of the liquid water, along the water's surface, up the evaporation chamber wall, and away from the system in approximately one-half second. The distance traveled was roughly 0.025 meters, indicating an

approximate tracer velocity of 0.05 m/s. This very rough result was about 50 percent of the calculated characteristic velocity, providing additional confirmation of the validity of this model. Buoyant flow impact on transport was modeled by considering a characteristic control volume, hollow and cylindrical, at radius r from the center of the upstream membrane face; it had an infinitesimal thickness of Δr, and a height, $\delta(r)$ (Figure 5.6). As the fluid element traveled along the membrane, mass left the top of the element through the area dA via diffusion.
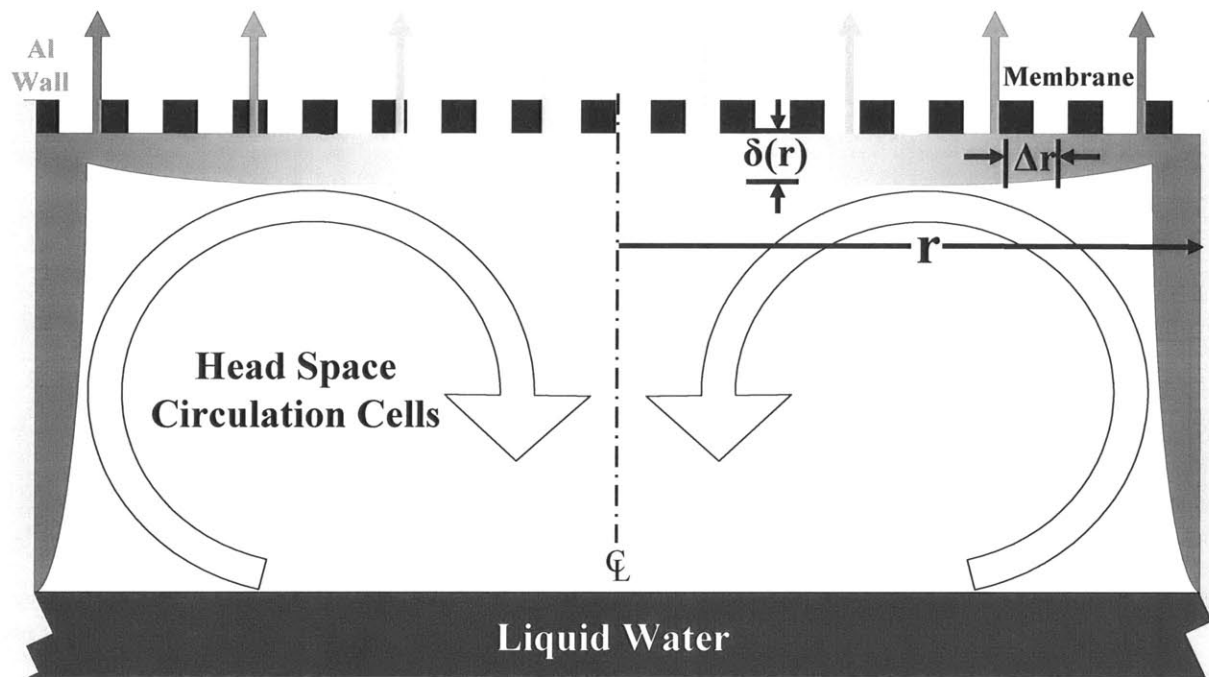
Figure 5.6: Head space natural convection generated concentration gradients along the upstream membrane face. In this figure, darker colors indicate higher water vapor concentration. In the finite difference model, characteristic fluid volumes had width Δr and height $\delta(r)$, dimensions which are represented in this figure.

The boundaries of the characteristic fluid volume were the membrane on the top and a boundary on the bottom through which only limited mass could travel. This approximation was well-represented by a viscous boundary layer where the viscous properties of the fluid dominated convection, impeding convectively-driven transport. As shown in Turner [Turner (1973), pp. 222-225], natural convection cells move with rapid circulation that increases towards the center of the cells. Inside the evaporation chamber, mixing within the circulation cells assured that most of the air in the head space was saturated with water vapor. However this water-vapor-rich air could not convect into the boundary layer near the membrane due to the viscous dominance

there. The only way water vapor could readily pass through the boundary layer was by diffusion driven by a concentration gradient (Fick's Law). The concentration gradient across the upstream membrane boundary layer was small compared with the concentration gradient across the membrane. The rate of water vapor diffusion into the boundary layer was only about 13.1% of the water lost through the membrane (which will be verified in Section 5.4.2). Therefore, for the purposes of modeling, the boundary layer thickness provided an estimate for the characteristic fluid particle height. The characteristic fluid volume was therefore the product of differential area, dA, and a characteristic height, $\delta(r)$, represented by a boundary layer thickness.

Since the Rayleigh Number in the head space never exceeded 10^9, the transition Rayleigh Number for onset of turbulent flow, the boundary layer on the upstream face of the membrane was assumed to begin as laminar. Although the upstream membrane face boundary layer originated due to natural convection, upon reaching the membrane, the fluid could no longer move upward under buoyant forces. Therefore, a Rayleigh Number correlation was not appropriate to determine the boundary layer thickness. A Reynolds Number was needed.

The characteristic velocity of flow up the chamber walls, U_b, was known (Equation 5.11). Considering mass continuity in the radial direction, flow velocity increased as the fluid approached the center of the membrane as a result of the reduced cylindrical confinement. Solving the continuity equation yielded

$$A_1 V_1 = A_2 V_2 \rightarrow 2\pi r_1 L V_1 = 2\pi r_2 L V_2 \rightarrow r_1 V_1 = r_2 V_2 \qquad \text{(Equation 5.12)}$$

where V_1 and V_2 were the velocities at radial stations r_1 and r_2. Within the evaporation chamber, the flow velocity at radial location, r, was calculated via

$$V(r) = \frac{U_b r_o}{r} \qquad \text{(Equation 5.13)}$$

where U_b was the characteristic flow velocity at the outer radius if the evaporation chamber, r_o.

The thermodynamic properties of air remained almost constant over the membrane face, changing only slightly due to loss of water vapor (the maximum possible density change was only 3.3 percent at 316K [Cravalho and Smith (1981)]. Therefore, a Reynolds Number could be calculated using the fixed density of air at 316 K. The radial position, r, appeared in the Reynolds Number both as a pure variable and through its influence on velocity

$$\text{Re}_r = \frac{\rho_{air} \cdot V(r) \cdot r}{\upsilon} \qquad \text{(Equation 5.14)}$$

103

When combined, Equation 5.13 and Equation 5.14 caused cancellation of the radial coordinate to produce a Reynolds Number characteristic of the flow along the upstream membrane face.

$$Re = \frac{\rho_{air} \cdot U_b r_o}{\upsilon}$$ (Equation 5.15)

While the geometry and conditions of this boundary layer flow were not identical to those under which the Blasius solution was derived [Blasius (1908)], the Blasius solution velocity profile represented a computationally inexpensive means to estimate the boundary layer height to the correct order or magnitude. A numerical model (outlined in Section 5.4) illustrated that the water vapor concentration at the membrane center, $\rho(r=0)$, which was the point most sensitive to changes to boundary layer height changes, increased by only 17.1% for an over-predication of 10 times (one order of magnitude) in the boundary layer thickness. Therefore, the Blasius solution was adequate to obtain accurate results with this model:

$$\delta(r) = \frac{5r}{Re^{\frac{1}{2}}}$$ (Equation 5.16)

5.3.2 HAMTA2 Head Space Mass Transport Resistance

The evaporation chamber was filled with an identical mass of liquid water between each experiment, but the available volume was not filled completely. A very shallow head space air gap was intentionally left to prevent liquid water from physically contacting the membrane to eliminate wicking into the pores. Comparing the evaporation chamber volume to the volume of the liquid charge, 1.49 mm of air separated the evaporation front from the membrane at the beginning of each experiment. The mass transport resistance associated with this air gap was

$$R_{headspace} = \frac{L}{D_{H_2O,Air}}$$ (Equation 5.17)

where L was the height of the gap and $D_{H2O,Air}$ was the diffusion coefficient of water vapor in air (from Equation 2.8). Typical experimental values for $R_{headspace}$ ranged between 35.4 and 60.9 s/m depending on exactly how much makeup water was injected into the apparatus between experiments.

As each experiment proceeded, liquid water evaporated away. The head space distance, L, increased and the resistance to mass transport also rose. The maximum experimental mass transport rate measured through a track-etched membrane was 4.3 x 10^{-7} kg/s. At this evaporation rate, the head space height increased at a rate of 3.1 x 10^{-7} m/s (0.019 mm/minute),

or about 1.4% per minute compared to the original 1.49 mm height. HAMTA2 steady state data were collected over 20 minutes. In this time, the head space height increased from 1.49 mm to 1.87 mm, and the transport resistance changed from about 50 to 60 s/m, about 20%. Since the total apparatus mass transport resistance presented by the membrane and boundary layers was at least 100 s/m, this change in resistance was barely perceptible in the data and was ignored for purposes of intrinsic mass transport resistance calculation.

5.4   Complete Mass Transfer Resistance Models for the Evaporation Apparatuses

Diffusion resistances encountered by the water vapor as it transported from the evaporation chamber were modeled to predict vapor mass flux from the apparatus. This result was compared with observed rates of apparatus weight loss to allow the intrinsic mass transfer resistance of the membrane itself to be deduced. The evaporation apparatuses described in Chapter 4 presented three significant resistances to transport of water vapor: the porous membrane itself and the upstream and downstream boundary layers created at the membrane surfaces by forced flows (downstream) and thermal buoyancy induced flows or quiescent air (upstream). Because the flows were spatially continuous, the effects of these three resistances on steady state water vapor mass transfer could be modeled by analogy to the flow of electrical current in a circuit containing three resistors in series. Summing the membrane resistance with the boundary-layer-based diffusion resistances yielded a complete mass transfer expression,

$$\dot{m}_{ave} = \frac{A\left(\rho_o - \rho_{amb}\right)}{R_{mem} + R_{US} + R_{DS}}$$

(Equation 5.18)

where R_{US} and R_{DS} are the apparatus mass transport resistances on the upstream and downstream membrane faces, as described in Sections 5.2 and 5.3 above). Owing to the simplicity of the HAMTA2 design, Equation 5.18 was an accurate representation of the mass transport processes of that apparatus. By plugging in experimentally measured values of $\dot{m}_{ave}$, and the mass transport resistance values obtained from the above analyses, Equation 5.18 was solved for the intrinsic mass transport resistance of the membrane, R_{mem}. This solution represents a core contribution of this thesis.

The intrinsic (apparatus independent) diffusion coefficient for transport through the membrane pores was obtained from the disaggregated membrane mass transfer resistance in Equation 5.18 as follows:

$$D_{H_2O,air} = \frac{L}{\varepsilon_v \cdot R_{mem}}$$ (Equation 5.19)

where the membrane thickness, L, and the membrane porosity (void fraction), ε_v, were determined using the membrane characterization techniques outlined in Chapter 3.

5.4.1 HAMTA1 Canonical Model

Despite the simple form of Equation 5.18, refinements were needed to correct for buoyancy-driven circulation of air-water vapor mixture within the deep evaporation chamber headspace for HAMTA1.

A canonical model for steady-state mass transfer in HAMTA1 was defined using transport models outlined in the above sections. The apparatus-specific overall average mass transfer rate, $\dot{m}_{ave}$, was modeled by applying Fick's Law over the area of the membrane where the concentration gradient also changed in the radial direction for reasons discussed in Section 5.3.1:

$$\dot{m}_{ave} = \int_{r_o}^{r=0} \frac{2\pi \cdot r}{R_{BL,downstream} + R_{mem}} \left[\rho(r) - \rho_{ambient} \right] dr$$ (Equation 5.20)

where $\rho_{ambient} \approx 0$ for all r due to the dry nitrogen cross flow on the upstream membrane face. The concentration of water vapor in a characteristic fluid volume as a function of radial location, $\rho(r)$, arose from analysis of the flow over the upstream membrane face (Section 5.3.1).

The value of the term $\rho(r)$ in Equation 5.20 at $r = r_o$ was the mass concentration of water vapor at the outer radius of the evaporation chamber, obtained from the upstream membrane surface temperature (T_2), the Ideal Gas Law, and the properties of steam assuming saturation, as described in Section 4.4.

To obtain an expression for the radial concentration gradient at the upstream membrane face, a mass continuity balance was applied on a fluid element in the vicinity of the upstream membrane face. The element was a cylindrical shell of radius r, width Δr, and height $\delta(r)$, approximated as the boundary layer thickness (as described in 5.3.1). The top surface of the element was the upstream membrane face, and the element followed the fluid flow from the outer radius of the evaporation chamber, r_o, towards the chamber center, $r = 0$ (as demonstrated by tracer studies), through incremental reductions in its radius represented in the model as Δr. By mass continuity, the water vapor contained within the characteristic fluid element must equal the mass entering minus the mass leaving the element:

$$\frac{d\rho(r)}{dt} dA(r)\delta(r) = \frac{dm_{in}}{dt} - \frac{dm_{out}}{dt}$$ (Equation 5.21)

By expanding the left hand side of Equation 5.21 in a Taylor Series and cancelling like terms,

$$\frac{d\rho(r)}{dr} \Delta r dA(r)\delta(r) = \frac{dm_{in}}{dt}\Delta t - \frac{dm_{out}}{dt}\Delta t$$ (Equation 5.22)

To put the fluid element in a La Grangian reference frame, a substitution is made for Δt to give:

$$\frac{d\rho(r)}{dr} \Delta r dA(r)\delta(r) = \frac{dm_{in}}{dt}\frac{\Delta r}{v(r)} - \frac{dm_{out}}{dt}\frac{\Delta r}{v(r)}$$ (Equation 5.23)

Recognizing that the mass flows in and out of the fluid element are governed respectively by diffusion (in) through the boundary layer on the upstream membrane face and diffusion (out) through the membrane and downstream boundary layer, the following substitutions are made,

$$\frac{dm_{in}}{dt} = \frac{\rho_{chamber} - \rho(r)}{R_{BL,upstream}} dA(r) \quad \text{and} \quad \frac{dm_{out}}{dt} = \frac{\rho(r) - \rho_{ambient}}{R_{mem} + R_{BL,downstream}} dA(r)$$ (Equation 5.24)

where $\rho_{ambient} \approx 0$ due to cross flow of dry nitrogen. Finally, substituting the expressions of Equation 5.24 into Equation 5.23 and cancelling like terms, the desired result, Equation 5.25, is obtained:

$$\frac{d\rho(r)}{dr} = \frac{1}{\delta(r)v(r)}\left[\frac{\rho_{chamber} - \rho(r)}{R_{BL,upstream}} - \frac{\rho(r) - \rho_{ambient}}{R_{mem} + R_{BL,downstream}}\right]$$ (Equation 5.25)

Both boundary layer resistances are calculated as described above, and Equation 5.25 is combined with Equation 5.20 to create the following canonical equation representative of mass transport out of the experimental apparatus and sensitive to all mass transfer resistances:

$$\dot{m}_{ave} = \int_{r_o}^{r=0}\frac{2\pi \cdot r}{R_{BL,downstream} + R_{mem}}\left\{\int_{r_o}^{r=0}\frac{1}{\delta(r)v(r)}\left[\frac{\rho_{chamber} - \rho(r)}{R_{BL,upstream}} - \frac{\rho(r)}{R_{mem} + R_{BL,downstream}}\right]dr - \rho_{ambient}\right\}dr$$ (Eq. 5.26)

Equation 5.26 was solved numerically via MATLAB for the unique combination of R_{mem} and $\rho(r)$ that satisfied the boundary conditions. The water vapor mass concentration at Step 0 ($r = r_o$) was known: it was the concentration of water vapor in a representative fluid particle as the chamber circulation cell reached the membrane. By selecting a very small step in r, Δr, the radius-dependant variables impacting the species concentration were solved at each new index. The change in water vapor mass concentration in the characteristic fluid element was calculated using Equation 5.25, and density at Step 1 was established. The process was iterated until r reached the center of the membrane, resulting in a precise species concentration profile, $\rho(r)$,

which was a function of radial position. The correct step length, Δr, was determined by first guessing an adequate value of Δr and obtaining the resulting function ρ(r). The value of Δr was then halved and a new ρ(r) calculated. This process was repeated until decreasing the size of Δr had no appreciable impact on ρ(r). This halving method is a standard approach in finite element modeling [Noels (2006)].

As with the more simple expression above, Equation 5.18, experimentally measured values of $\dot{m}_{ave}$ and the apparatus mass transport resistance values were plugged into Equation 5.26 to solve for the intrinsic mass transport resistance of the membrane, R_{mem}.

5.4.2 Verification of Canonical Model Assumptions

The canonical model enabled verification that the viscous boundary layer on the upstream membrane face represented a virtual boundary to mass transfer as compared with the mass flux through the membrane. Fick's Law was applied between the bulk air in the head space (assumed to be saturated) and the boundary layer, using a representative boundary layer thickness as the diffusion resistance length (Figure 5.7).

$$\frac{dm_{out}(r)}{dt}$$

$$\delta(r) \quad \rightarrow \Delta r \leftarrow$$

$$\frac{dm_{in}(r)}{dt}$$
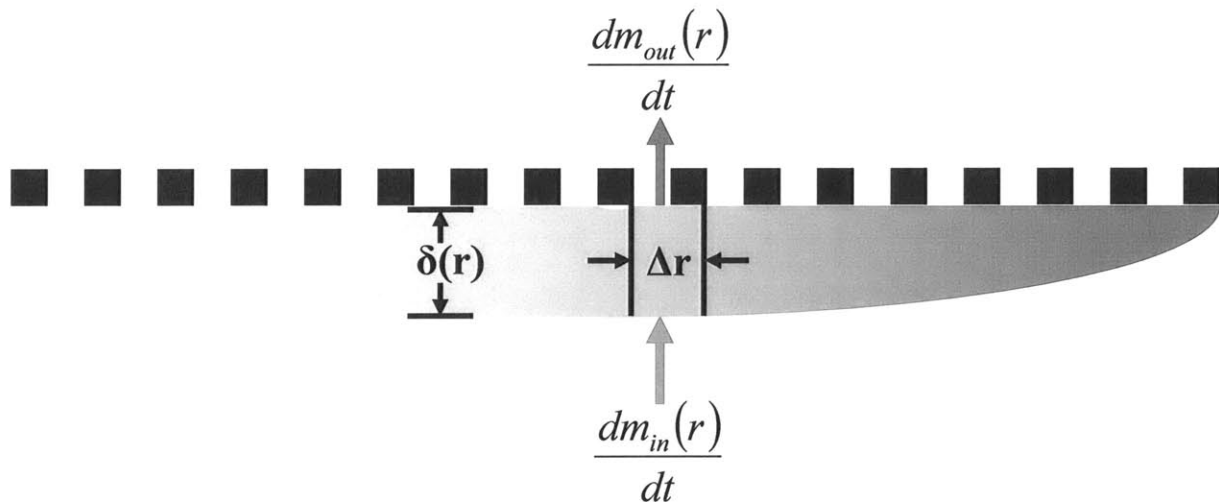
Figure 5.7 Schematic representation of mass transport rates into and out of a characteristic fluid volume in the boundary layer on the upstream membrane face. Calculations in Section 5.4.2 show that inward mass flux is only 13.1% of outward mass flux, confirming the modeling assumption of radial concentration gradient in the membrane upstream boundary layer.

For this representative case, 8.6×10^{-8} kg/s of water vapor diffused into the boundary layer from the head space while 6.5×10^{-7} kg/s diffused out of the boundary layer across the

membrane. The source term was only 13.1 percent of the sink term. The duration a characteristic fluid volume was in membrane contact was about 0.128 seconds (calculated from r_o/U_b); in this time 8.32 x 10^{-8} kg of water vapor left the volume while only 1.1 x 10^{-8} kg entered. This result validated the assumption that the viscous boundary layer could be used as a representative characteristic fluid particle height.

5.5 Impact of Membrane Water Droplet Formation on Transport

The design of HAMTA2 prevented liquid water from condensing on the membrane because the membrane was intentionally kept above the water condensation temperature. No liquid was seen condensing on the track-etched membranes during any experiments. However, the temperature gradients required to induce buoyancy-driven natural convection cells in HAMTA1 also caused liquid water droplets to condense on the upstream DuPont porous membrane face (Figure 5.8). Cooling efficacy could have been impacted if liquid wicked into the pores and was deposited on the downstream membrane surface, blocking the pores. An experiment was conducted to check for the presence of wicked liquid through the pores.

A small piece of Whatman cellulose filter paper [Whatman (2007)] was hung on a support within the laboratory 24 hours prior to the experiment to allow weight equilibration with the humidity of the room. The weight of the filter paper was established by weighing with a scale accurate to ± 1 mg. The experimental evaporation apparatus was turned on and allowed to reach steady state, forming droplets on the upstream membrane face. The apparatus was then allowed to cool to room temperature to minimize the vapor diffusion rate through the membrane. The pre-weighed filter paper was raked across the downstream side of the membrane over the spots where water droplets were visible on the upstream face. The paper was then quickly re-weighed, and the weight was found to not have changed within the sensitivity of the scale. This experiment demonstrated that liquid water was not wicking up through the membrane pores, eliminating wicking transport as a parasitic heat transfer mechanism. This result is consistent with contact angle measurements (Appendix 2) that suggest Nucrel® and Hytrel® are moderately hydrophobic. Hydrophobic pore walls impede the entry of liquid and prevent wicking.

Despite lack of wicking, liquid water might still form within the membrane pores via condensation from the water-saturated air contacting membrane surfaces that are below the dew point temperature. On first glance, internal droplet condensation might seem to decrease the system's effective cooling by reducing the apparent open volume of the membrane through

which water vapor could diffuse. However, liquid could not plug the pores in this manner because access to the ambient environment through the external opening of the pores would cause the liquid to evaporate. In fact, since the vapor in the "plugged" pores directly above the liquid was at 100% RH at the membrane surface temperature, water vapor would diffuse at exactly the same rate as if there were no liquid covering the pore. The Kelvin effect in which curvature of a liquid surface changes the vapor pressure above that surface is extremely small in the micron pore diameter regime, and has a vapor pressure impact of only a 0.2% and a 0.02% on 1 micron and 10 micron pores respectively.

Figure 5.8 Liquid water droplets forming on the upstream membrane face during HAMTA1 steady-state operation result from use of buoyancy-driven natural convection, which was employed intentionally to eliminate complications associate with the moving evaporation front.

The most serious implication of liquid droplet formation to the model presented here was interruption of the boundary layer on the upstream membrane face. This boundary layer had a retarding effect on mass transport because it supported a radial concentration gradient and it

imposed a diffusion resistance impeding the ability of water vapor in the head space from reaching the membrane. By plugging pores with liquid water, the mass transfer retarding effect of the upstream boundary layer was eliminated in the liquid-filled pores. This effect would have increased the rate of vapor transport through the membrane, and it is detailed in Section 7.1.3.

6   Results

This chapter presents modeled and experimental results from the porous membrane studies described in this thesis. Both mass transport and associated surface cooling efficacy results are presented. Implications pertaining to the modeling processes and experimental apparatus designs described in this thesis are also discussed. However, detailed analysis of these results and their implications for basic transport theory and engineering design is reserved for Chapter 7. Mass and heat transfer results for the HAMTA1 experiments with DuPont porous membranes will be presented first, followed by results for the HAMTA2 experiments with track-etched membranes.

6.1   HAMTA1 Mass Transfer Results

Cumulative weight loss from the HAMTA1 evaporation chamber with respect to time is shown in Figure 6.1. On the abscissa is time in minutes; here time = 0 denotes the moment at which the evaporation chamber first attained steady-state operation. On the ordinate is mass lost from the evaporation chamber, where zero coincides with the onset of steady-state conditions. The derivative of each curve denotes the instantaneous rate of water evaporation at that time.

There are two limiting cases. The "Open Chamber" case represents an experiment where the evaporation chamber was run with no membrane in place, leaving the chamber open to the environment. Otherwise, the experimental conditions are identical to runs with the membrane in place. In this configuration water leaves at the maximum possible rate, as evidenced by the large data slope, since there is no membrane in place to impede transport. The second extreme case is the "Closed Chamber" in which a non-porous latex membrane about the same thickness as the DuPont porous membranes (141 μm) is sealed over the evaporation chamber. Water can not penetrate this nonporous membrane in the time scale relevant to the experiment (6 hours), and evaporative cooling is therefore not possible. The mass transport rate is zero for this experiment, as indicated by the zero data slope.

Between these extreme cases lay two pairs of replicate DuPont porous membrane experiments. For the porous membranes, linear data correlation indicates that the experimental water vapor diffusion rate out of the evaporation chamber is constant. This result confirms that buoyancy-driven convection cells induced by temperature gradients inherent in the deep evaporation chamber design eliminate the moving evaporation front complication.
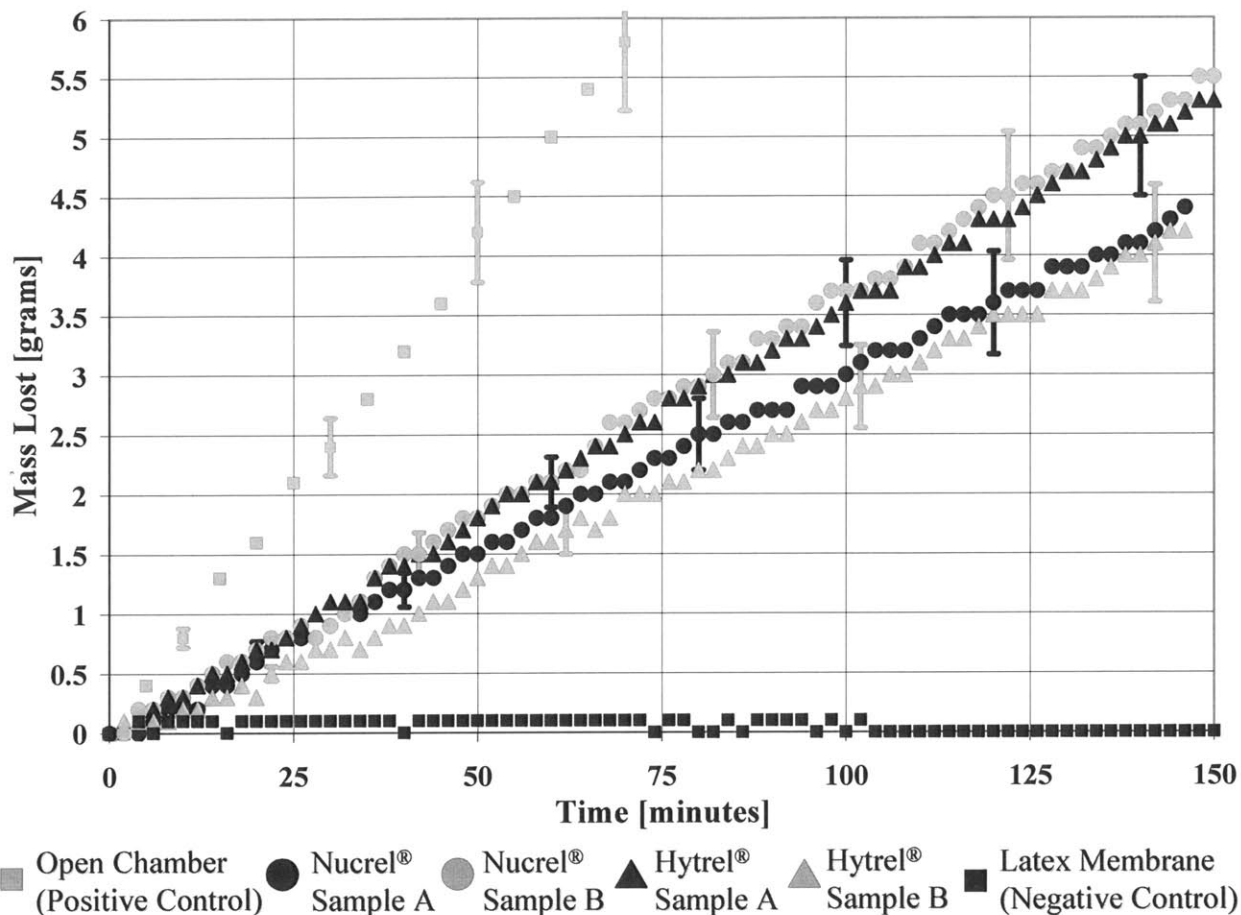
Figure 6.1: Cumulative mass of water vapor transported from the evaporation chamber as affected by time. Experimental rates of mass change in the evaporation chamber (derivatives of the curves shown) denote the flux of coolant vapor through the membrane pores. The implied mass flux rates were time-independent for all four porous membrane samples, indicating that steady-state diffusion occurred.

If mass transport occurred by pure diffusion through the head space air, constant mass transfer rate would not have been observed. Instead, this rate would have decreased as water evaporated, increasing the diffusion path length between the evaporation front and the membrane and slowing down the diffusion process. While the magnitude of water vapor mass concentration gradient across the porous membrane ultimately drove transport through the pores, the magnitude of that gradient may be impacted by other mass transfer resistances of the particular apparatus. In the case of HAMTA1, the mass transfer resistances associated with the upstream and the downstream boundary layers impacted the mass concentration gradient across the porous membrane.

The average rate of water vapor mass transfer from the apparatus, $\dot{m}_{ave}$, is the quotient of the cumulative steady-state weight loss and the cumulative time over which that weight loss occurred. The uncertainly in this quantity for HAMTA1 is approximately $\pm$ 2.2 x 10^{-8} kg/s, estimated from the propagation of error in the weight measurement (5.5 $\pm$ 0.2 g – scale readability, plus drift measured over 9000 seconds) and uncertainty in time measurement (9000 $\pm$ 30 seconds) multiplied by the largest measured $\dot{m}_{ave}$ (about 6.0 x 10^{-7} kg/s). Mean values of $\dot{m}_{ave}$ for all four membrane experiments agree to within $\pm15\%$ despite a 10-fold difference in average effective pore diameter between Nucrel$^{®}$ (d_e = 1.2 μm) and Hytrel$^{®}$ (d_e = 13.4 μm). This observation is consistent with the similar porosities and thickness of all four membranes and minimal, if any, impacts of pore width detectable with the HAMTA1 apparatus. Disagreement between the four slopes is attributed to slight differences in thickness and porosity between the membranes. Error bars plotted in Figure 6.1 account for the uncertainty of the experimental measurement. Within the experimental uncertainty of HAMTA1, the mass transfer rates associated with the four porous membranes were identical.

Perspiring, a natural form of evaporative cooling, is the principle mechanism for thermal regulation of the human body when ambient temperature exceeds internal body temperature. Schmidt-Nielsen [Schmidt-Nielsen (1979)] reports typical desert perspiration rates for human males in the range between 0.5 and 1.5 liters/m^2-hr of liquid water. Based on the slopes (i.e., the mass transfer rates) for the DuPont porous membranes in Figure 6.1, the average liquid water volume transfer rate for these experiments is 2.1 liters/m^2-hr. This result indicates that the evaporative cooling technique described in this thesis can be employed to create protective garments with integrated self-cooling abilities for humans that will not saturate under normal perspiration rates. It also shows that measured experimental conductances reliably mimicked human perspiration rates.

6.1.1 Comparison of HAMTA1 Experimental & Mass Transfer Modeling Results

There are two methods to compare experimental mass transport rates to the canonical model for HAMTA1 outlined in Section 5.4.1. Equation 5.26 has two unknowns, the apparatus-dependant mass transport rate, $\dot{m}_{ave}$, and the intrinsic mass transport resistance of the membrane, R_{mem}. When solved using experimentally obtained values for $\dot{m}_{ave}$, Equation 5.26 yields R_{mem}. From this result, the intrinsic diffusion coefficient for transport through the pores, $D_{H_2O,air}$, is

deduced using equation 5.19. As shown in Table 6.1, experimentally-derived $D_{H_2O,air}$ values for the DuPont porous membranes compare well with each other and are within +9 to -40 percent of theoretical predications for $D_{H_2O,air}$ from the transition diffusion regime model (Equation 2.10).

Table 6.1: Comparison of intrinsic coefficients for diffusion of dilute water vapor in air (total pressure, about 1 atm) through membrane pores, with values predicted for mutual diffusion of water vapor in air, for continuum conditions and with correction for the onset of fluid rarefaction.

Overlay	Knudsen Number	Continuum Theory $D_{H2O,Air}{}^{\alpha}$	Rarified Theory $D_{H2O,Air}{}^{\beta}$	Apparatus-ind. Experimental $D_{H2O,Air}$	% Difference Rarified vs. Experiment
[ ]	[ ]	[m²/s]	[m²/s]	[m²/s]	[%]
Nucrel®, Sample A	0.099	2.37E-05	2.12E-05	1.95E-05	-9
Nucrel®, Sample B	0.071	2.36E-05	2.18E-05	2.68E-05	19
Hytrel®, Sample A	0.007	2.35E-05	2.33E-05	1.68E-05	-38
Hytrel®, Sample B	0.008	2.39E-05	2.36E-05	1.68E-05	-40

$^{\alpha}$Equation 2.8; $^{\beta}$Equation 2.10

The alternate solution method is to predict $\dot{m}_{ave}$ for each membrane using $\rho(r)$ based on measured temperatures from within the evaporation chamber (Chapter 4), and R_{mem} values obtained through characterization techniques (Chapter 3) using Equation 2.12. The diffusion coefficient, $D_{H2O,Air}$, can be approximated via Equation 2.10 using measured temperatures within the evaporation chamber.

Figure 6.2 shows how the predicted $\dot{m}_{ave}$ values became successively better as the predictive model assumptions evolve from simple 1-D continuum diffusion (Equation 5.1) to a more precise description including Knudsen diffusion, radial concentration gradient, upstream boundary layer resistance, and downstream boundary layer resistance (i.e., Equation 5.26). The most sophisticated model predicts $\dot{m}_{ave}$ values to within +13.8% to -20.8% of the experimental measurements, building confidence in the reliability of the experimental approach and the steady state transport analysis.
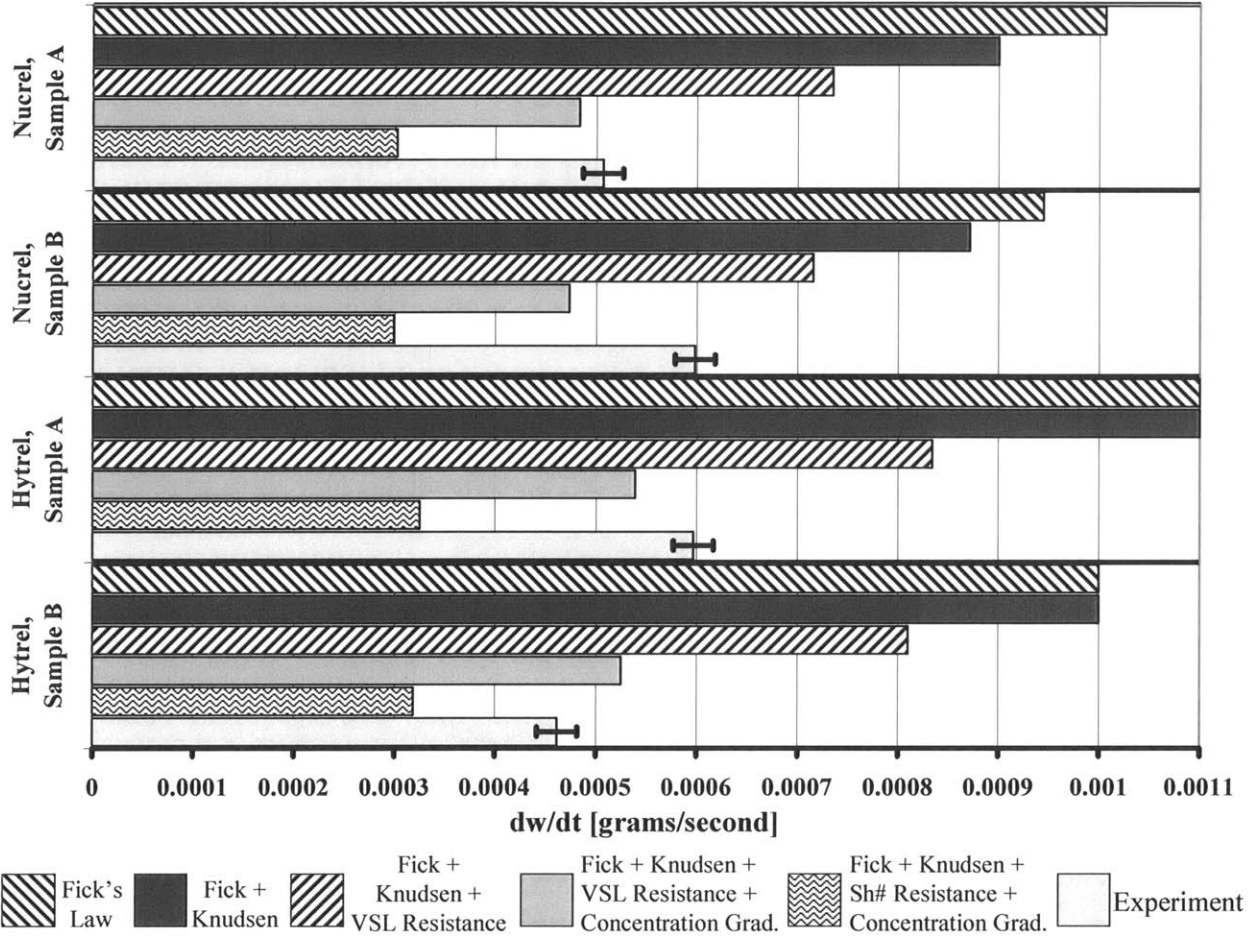
Figure 6.2: Comparison of experimental (light grey with uncertainty bars) and theoretical (patterned or darker filling) mass transport rates for the four porous membrane experiments. As model sophistication improved through introduction of additional terms, the ability to accurately predict experimental mass transfer rates got better. This convergence builds confidence in the validity of the assumptions within this thesis regarding dominant apparatus mass transport resistances at steady state.

6.2 HAMTA1 Cooling Efficacy Results

Figure 6.3 shows typical temperature-time histories for the Hytrel® and Nucrel® DuPont porous membranes and the negative (closed chamber - Latex) and positive (open chamber) control experiments. The abscissa denotes time in minutes, and the ordinate shows the temperature of the base of the evaporation chamber with ambient temperature subtracted out. Instead of showing just steady-sate data, Figure 6.3 provides the complete history of experimental warm up (large increase in temperature from t=0), steady state (long plateau in temperature), and cool down (exponential temperature drop-off after the steady state period, i.e.,

from the time of heater shut off) processes utilized to perform the apparatus thermal validation outlined in section 4.5[1].
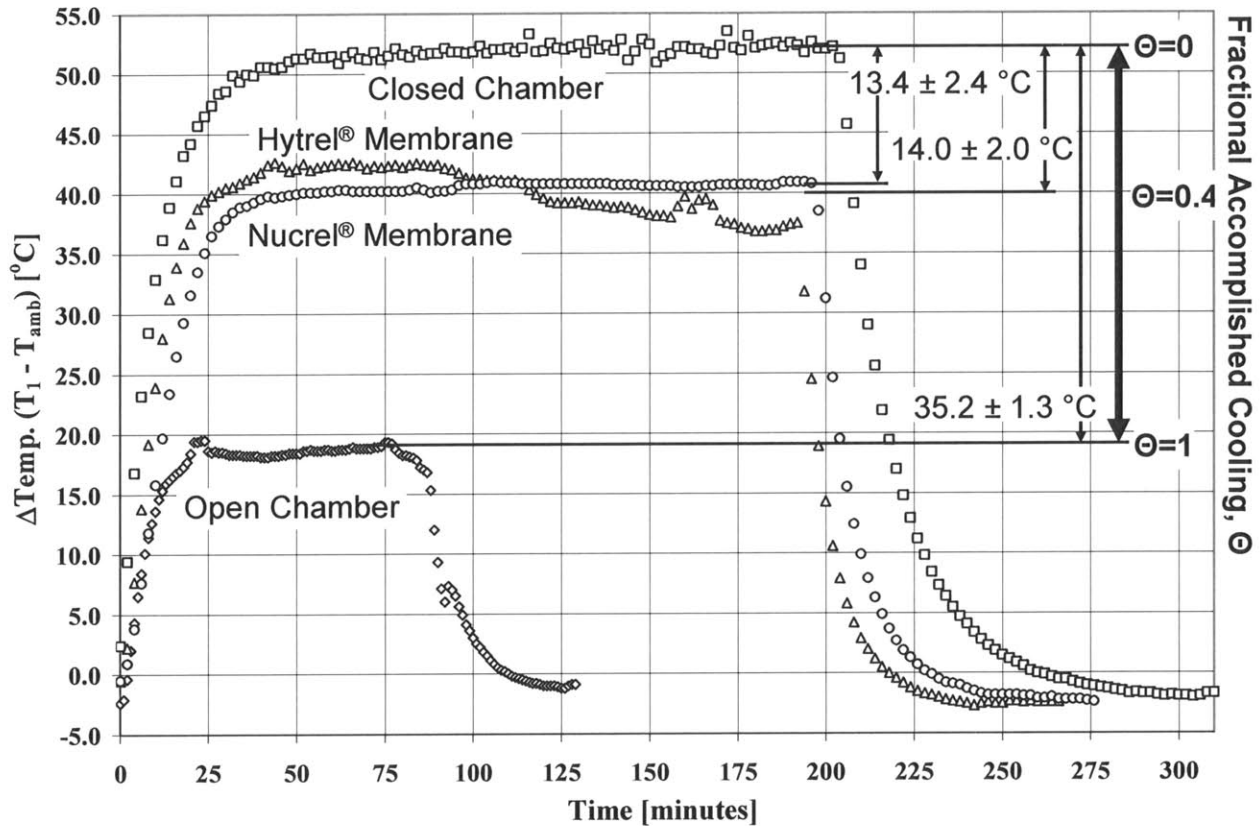
Figure 6.3: Typical temperature-time histories (corrected for ambient temperature) for evaporative cooling of an aluminum surface through Hytrel® and Nucrel® membranes and for negative (closed chamber) and positive (open chamber, maximum cooling) controls. The Cooling Index and Fractional Accomplished Cooling, Θ, both defined in the text, are also shown.

Membrane cooling efficacy is quantified by the difference between the average steady state chamber base temperature (T_1) for the closed chamber versus the Hytrel®, Nucrel®, or open chamber base temperatures. This difference is called the *Cooling Index*. Evaporative cooling through Nucrel® (d_e = 1.2 μm) creates 14.0 ± 2.0 °C temperature reduction below the closed chamber case while Hytrel® (d_e = 13.4 μm) creates a 13.4 ± 2.4 °C surface temperature reduction. These temperature reductions are substantial fractions (about 40%) of the maximum possible cooling (35.2 ± 1.3 °C) obtained in the open chamber case where resistance to water vapor transport is smallest.

---

[1] These data also provide valuable information on apparatus performance, mass transfer rates, and membrane cooling efficacy during transient heating and cooling events. Other than using these data to illuminate parameters for the apparatus heat balance, transient processes were not further analyzed in this thesis.

To quantify cooling efficacy using a universal, dimensionless quantity, the *Fractional Accomplished Cooling*, Θ, is defined as follows:

$$\Theta = \frac{\left(T_{1,closed} - T_{1,mem}\right)}{\left(T_{1,closed} - T_{1,open}\right)}$$

(Equation 6.1)

where $T_{1,closed}$ is the surface temperature of the experiment in closed chamber mode, $T_{1,open}$ is the surface temperature of the experiment in open chamber mode and $T_{1,mem}$ is the surface temperature of the experiment with a porous membrane covering the evaporation chamber. Thus, $\Theta = 1$ implies maximum possible evaporative cooling while $\Theta = 0$ implies no evaporative cooling.

Table 6.2 summarizes the Fractional Accomplished Cooling and steady-state temperatures for all HAMTA1 experiments. Both DuPont porous membrane types support appreciable Fractional Accomplished Cooling, 0.4 for Nucrel® (and 0.38 for Hytrel®), despite their tiny pore IDs and small total porosity, 7.5-7.6% (8.6-11.2%). Moreover each membrane provides substantial solid material that can be nano-engineered to incorporate other capabilities, e.g., high mechanical strength.

Table 6.2: Cooling indices and steady state temperatures for evaporative cooling of underlying surfaces with DuPont porous membranes

Membrane {Number of Runs}	Ave T_{amb} [°C]	Ave T_1 [°C]	Fractional Accomplished Cooling [ ]	Cooling Index [°C]
Closed Chamber {4}	27.2 ± 0.2	80.1 ± 0.7	0.00	N/A
Open Chamber {4}	26.9 ± 0.2	44.6 ± 0.4	1.00	35.2 ± 1.3
Nucrel® {2}	27.5 ± 0.2	66.4 ± 1.0	0.40 ± 0.06	14.0 ± 2.0
Hytrel® {2}	27.5 ± 0.2	67.0±1.4	0.38 ± 0.07	13.4 ± 2.4

6.3 HAMTA2 Mass Transfer Results

Cumulative weight loss from the HAMTA2 evaporation chamber with respect to time is shown in Figure 6.4. As with Figure 6.1 the abscissa denotes time in minutes with time = 0 denoting when steady-state operation was first obtained, and the ordinate is mass lost from the evaporation chamber, beginning with the onset of steady-state. The slopes of these mass transfer data correspond to the instantaneous rate of water evaporation. As with HAMTA1, there are two

extreme bounding situations: the open chamber case where the slope represents the largest possible mass transport rate and the closed chamber case where the slope is essentially zero. For the closed chamber experiments, a 20 μm thick nonporous polycarbonate membrane from Goodfellow Corporation (Goodfellow item # CT301210, [Goodfellow (2007)]) was utilized.

The track-etched membranes studied using HAMTA2 had a wide range of porosity and thickness, and it was therefore not advantageous to compare the apparatus-specific mass transport rates represented by the slopes in Figure 6.4. Nonetheless, linear mass transport data confirmed that short duration runs (i.e., about 20 minutes) using a shallow chamber mitigated impact of the moving air-liquid evaporation front (as described in Section 5.3.2) on the mass transport rate. If increasing diffusion resistance associated with the growing head space were significant, the mass transport rate would drop during the experiments instead of remaining essentially linear.

Membrane[a]	Ave Mass Loss Rate
[ ]	[g/s]
Non Porous	1.8E-05
12 μm Millipore	3.6E-04
5 μm Millipore	3.6E-04
1.2 μm Millipore	3.4E-04
600 nm Millipore	3.6E-04
100 nm Millipore	2.5E-04
50 nm Millipore	2.4E-04
10 nm GE	1.7E-04
Open Chamber	7.8E-04

[a]manufacturer-reported pore widths. Actual pore widths reported in Table 3.3
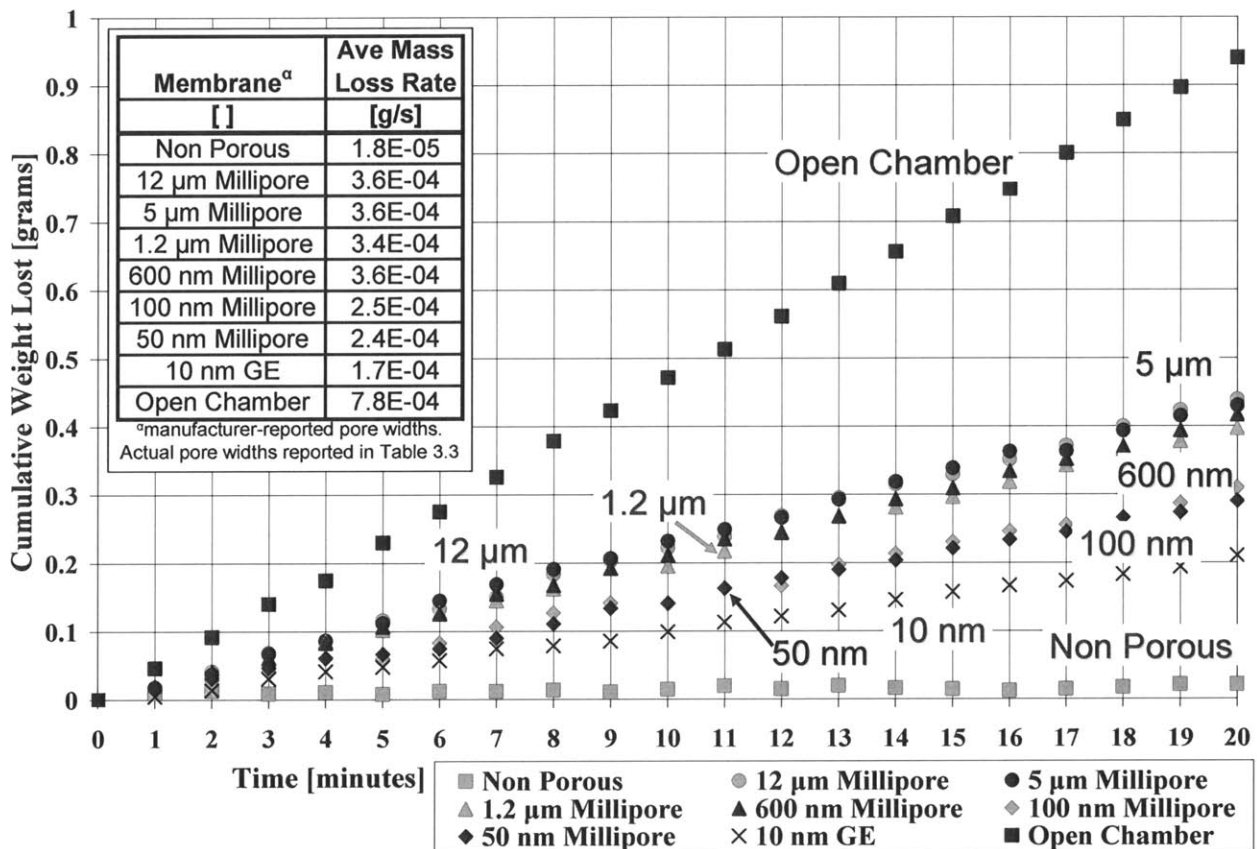
Figure 6.4: Cumulative mass of water vapor transported through track-etched membranes from the HAMTA2 evaporation chamber as affected by time. Experimental rates of mass change in the evaporation chamber (derivatives of the curves shown) denote the flux of coolant vapor through the membrane pores. The implied mass flux rates were time-independent for all porous membrane samples, indicating that steady-state diffusion occurred.

The uncertainly in $\dot{m}_{ave}$ for HAMTA2 was approximately $\pm$ 2.52 x 10^{-8} kg/s. This error was estimated via propagation of uncertainty in the weight measurement (0.0005 $\pm$ 0.00003 kg – error arising from scale drift: Figure 4.10) and the time measurement (1200 $\pm$ 1 second – the stated error in the data logging temperature readers) multiplied by the largest measured $\dot{m}_{ave}$, about 4.2 x 10^{-7} kg/s.

Instead of analyzing apparatus-dependant mass transport rate, a more informative mass transport comparison is to plot the intrinsic (apparatus-independent) mass transport coefficient, $D_{H2O,Air}$, as a function of the Knudsen Number (Figure 6.5). $D_{H2O,Air}$ was obtained by using the experimentally-measured value of $\dot{m}_{ave}$ to solve Equation 5.18 to attain R_{mem}. Equation 5.19 was then applied to solve for the intrinsic mass transport coefficient. Recall that $R_{BL,upstream}$ and $R_{downstream}$ were calculated using the methods outlined in Section 5.2.2 and Section 5.3.2 respectively.

Figure 6.5 serves both to compare the transport efficacy of the membranes to each other as well as benchmark the results against transition regime diffusion theory, Equation 2.10. In Figure 6.5, the top abscissa denotes the Knudsen Number for each membrane based on pore diameter (the bottom abscissa provides 1/Kn), and the ordinate represents the intrinsic mass transport coefficient, $D_{H2O,Air}$ for each sample, derived from the experimental data.

The abscissa uncertainty in Figure 6.5 arises from uncertainly in the pore diameter measurement technique (Chapter 3), and the uncertainty bars are about the size of the data points themselves. The ordinate uncertainty bars in Figure 6.5 are calculated through propagation of three sources of measurement error: 1) experimental determination of $\dot{m}_{ave}$, 2) the membrane porosity by gravimetric measurement, and 3) determination of membrane thickness by the fold & mic method. Not included in this analysis was error arising from the upstream and downstream boundary layers. With pore diameter above 1 micron, the membrane represents a minor resistance to mass transport (about 5 – 15% of the total resistance). As the pore width is decreased at constant pressure and the diffusion process transitions to an increasingly rarified regime, the mass transport resistance of the membrane becomes increasingly dominant over the upstream and downstream boundary layer resistances. Thus, the accuracy of the $D_{H2O,Air}$ measurement increases as the pores become smaller.

At Knudsen Numbers less than 0.1, (i.e. pores above 1 micron in diameter at about 1 atmosphere), there are several outlying data points that do not fall within the boundaries of the Figure 6.5 chart. For example, both data points at Kn = 0.05 (d ~ 12 μm) are too low (0.43 x 10^{-5} and -1.41 x 10^{-5} m^2/s) and one data point at Kn = 0.1 (d ~ 1.2 μm) is also too low (-2.89 x 10^{-5} m^2/s). The expected $D_{H2O,Air}$ value for both these pore diameters is about 2.6 x 10^{-5} m^2/s. These severe deviations are attributed to the calculated error in the boundary layer exceeding the value of $D_{H2O,Air}$ for larger pore diameters.
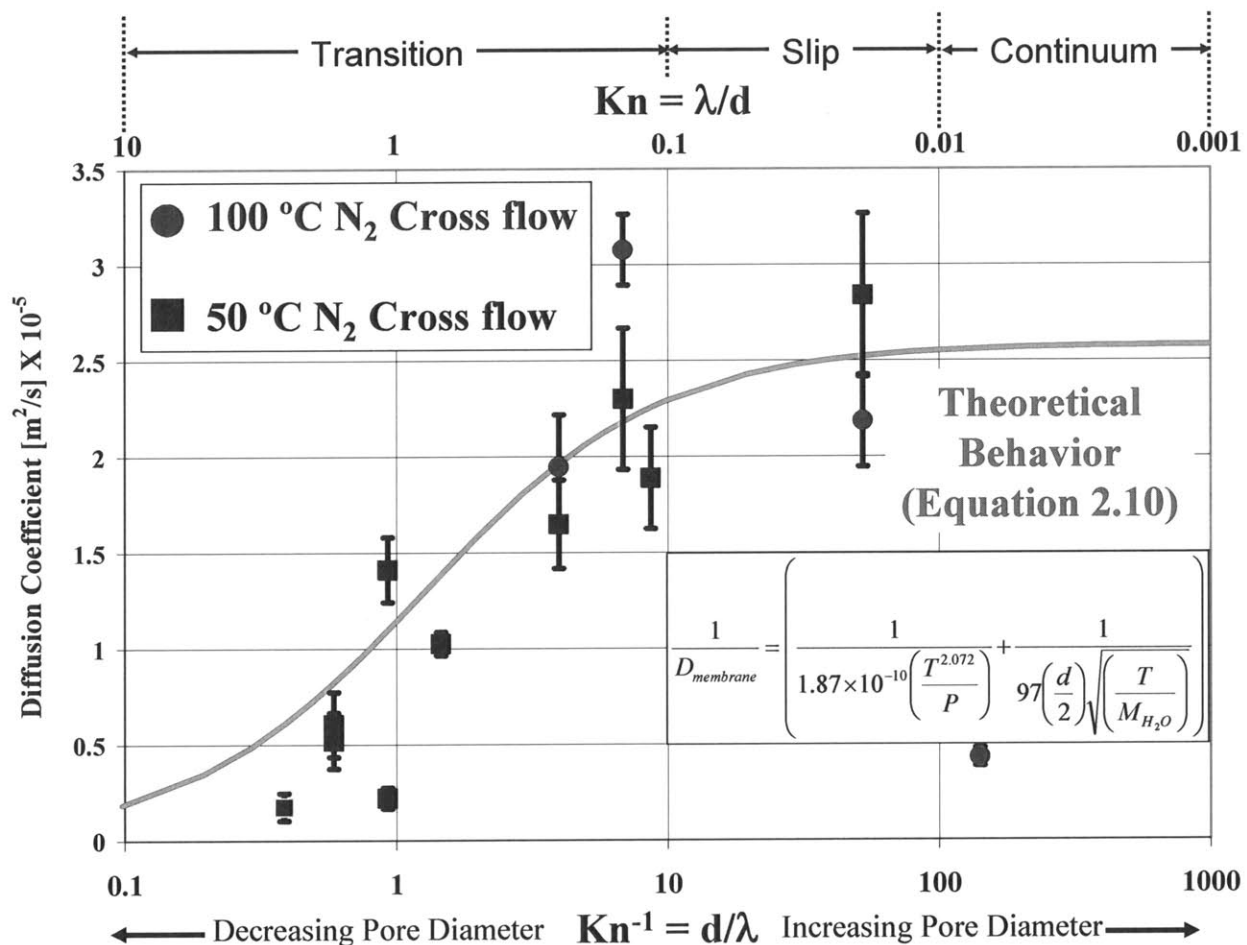
Figure 6.5: Intrinsic pore mass transfer diffusion coefficients for water vapor in air in track-etched membranes as a function of Knudsen Number. The diffusion coefficients were calculated from experimental measurement of mass transport rate (Equation 5.18 and 5.19). Apparatus-independent mass transfer coefficients show strong correspondence to transition regime diffusion theory (Equation 2.10). By manipulating pore diameter instead of pressure (mean free path), the onset of Knudsen diffusion was confirmed in a manner different from classical studies.

6.4 HAMTA2 Cooling Efficacy Results

To facilitate cooling efficacy comparison of the HAMTA2 track-etched membrane experiments, the Fractional Accomplished Cooling, Θ, for each membrane is given in Table 6.3 and plotted in Figure 6.6 as a function of membrane number, ζ. The membrane number is a dimensionless term representing physical attributes of porous membranes significant to mass transport,

$$\zeta = \frac{d\varepsilon_v}{L\tau}$$ (Equation 6.2)

where d is the pore diameter, ε_v is the membrane porosity (void fraction), L is the membrane thickness, and τ is the tortuosity. For this thesis, membrane numbers for samples of interest ranged from about 8.6 x 10^{-5} to 0.23. Tortuosity was taken as unity for all track-etched membranes based on micrograph evidence that the pores ran straight-through (Section 3.3.5).

Table 6.3: Fractional Accomplished Cooling and associated steady state temperatures for evaporative cooling with track-etched membranes.

Membrane (Nozzle Temperature) [ ]	Measured Pore Diameter [nm]	Ave T_{amb} [°C]	Ave T_1 [°C]	Fractional Accomplished Cooling [ ]
Closed Chamber (100°C Nozzle)	N/A	45.0 ± 0.4	47.3 ± 0.2	1.00
Closed Chamber (50°C Nozzle)	N/A	32.5 ± 0.2	36.0 ± 0.3	1.00
12 μm Millipore (100°C Nozzle)	14,400 ± 1,100	42.2 ± 0.3	33.3 ± 0.4	0.593 ± 0.040
12 μm Millipore (50°C Nozzle)	14,400 ± 1,100	32.1 ± 0.1[a]	27.0 ± 0.2	0.513 ± 0.043
5 μm Millipore (100°C Nozzle)	5,400 ± 500	39.0 ± 1.2	33.1 ± 0.3	0.601 ± 0.037
5 μm Millipore (50°C Nozzle)	5,400 ± 500	33.1 ± 0.1[a]	26.4 ± 0.2	0.543 ± 0.044
1.2 μm Millipore (100°C Nozzle)	890 ± 30	41.3 ± 0.3	31.9 ± 0.3	0.653 ± 0.039
1.2 μm Millipore (50°C Nozzle)	890 ± 30	32.9 ± 0.1[a]	26.9 ± 0.2	0.515 ± 0.043
600 nm Millipore (100°C Nozzle)	700 ± 50	43.3 ± 0.5	32.9 ± 0.3	0.608 ± 0.038
600 nm Millipore (50°C Nozzle)	700 ± 50	32.5 ± 0.1[a]	27.0 ± 0.2	0.512 ± 0.042
400 nm Millipore (100°C Nozzle)	410 ± 20	45.7 ± 0.5	33.1 ± 0.3	0.599 ± 0.038
400 nm Millipore (50°C Nozzle)	410 ± 20	31.9 ± 0.2[a]	28.0 ± 0.1	0.452 ± 0.038
220 nm Millipore (100°C Nozzle)	150 ± 20	44.5 ± 0.6	33.5 ± 0.3	0.582 ± 0.038
100 nm Millipore (50°C Nozzle)	95 ± 14	31.2 ± 0.2	28.2 ± 0.1	0.440 ± 0.039
100 nm Millipore (50°C Nozzle)	95 ± 14	32.9 ± 0.1[a]	28.9 ± 0.2	0.404 ± 0.039
50 nm Millipore (50°C Nozzle)	60 ± 9	31.4 ± 0.1	30.4 ± 0.1	0.315 ± 0.033
50 nm Millipore (50°C Nozzle)	60 ± 9	32.8 ± 0.1[a]	29.8 ± 0.1	0.349 ± 0.037
10 nm GE (50°C Nozzle)	39 ± 13	32.9 ± 0.1[a]	32.3 ± 0.1	0.207 ± 0.032
Open Chamber (100°C Nozzle)	N/A	34.4 ± 0.2[a]	23.6 ± 0.3	0.00
Open Chamber (50°C Nozzle)	N/A	27.8 ± 0.2[a]	18.4 ± 0.2	0.00

[a]These temperatures were not directly measured. They were extrapolated from a sweep gas temperature measurement taken at a station 42mm downstream of the external membrane face.

Figure 6.6 reveals a regime of membrane numbers for which cooling efficacy is not impacted by pore diameter. In this regime, Fractional Accomplished Cooling is as high as 0.6, demonstrating that substantial evaporative cooling can be obtained from membranes with relatively small void fractions (less than 32%).
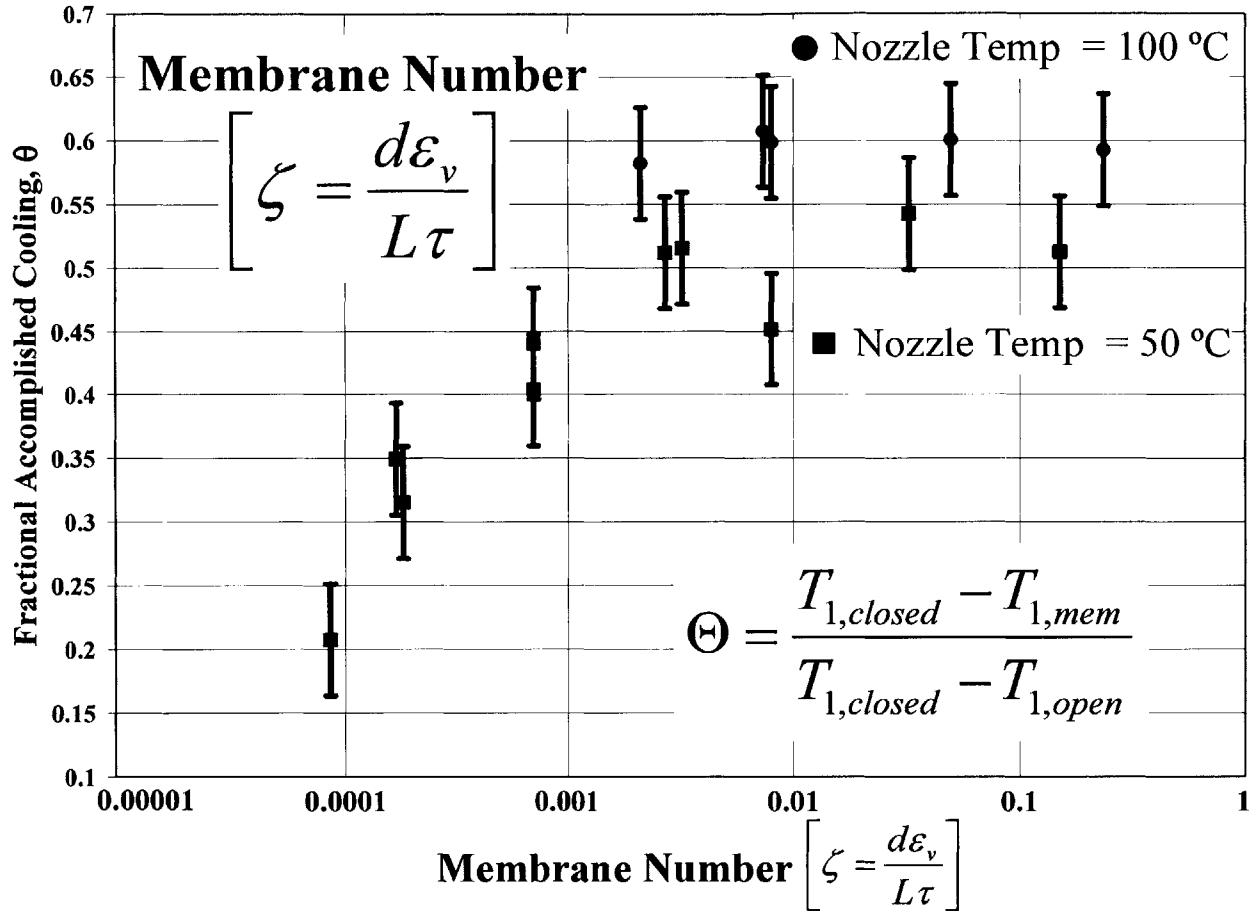
Figure 6.6: Fractional Accomplished Cooling of each track-etched membrane with respect to membrane number. For a range of membrane numbers from 0.005 to 1.0, Θ is essentially unaffected, ranging from 0.45 to 0.61. For membrane number smaller than 0.005, cooling efficacy begins to drop, reaching Θ = 0.21 at ζ = 0.00009. This observation is consistent with smaller membrane number representing larger membrane mass transport resistance and hence less evaporative cooling.

At about ζ = 5.0 x 10^{-3}, Fractional Accomplished Cooling begins to become dependant upon membrane number. This shift is coincident with onset of the transition diffusion regime as pore size drops. At higher Knudsen Number (i.e. smaller diameter pores), less mass evaporates through the membrane and Fractional Accomplished Cooling drops to as low as 0.2. However, even at 39 nm pore diameter and 1.4% porosity, evaporative cooling is not entirely extinguished.

Here, $\Theta = 0.2$ is achieved, indicating that the evaporative cooling approach illustrated in this thesis can impact a wide range of pore diameters, down to the nanometer scale, and can be used to provide cooling to, and in concert with integrated MEMS and nano-scale components.

7　Discussion

This chapter provides technical discussion and assessment of the experimental and modeling results presented in Chapter 6. It also describes a correlation, developed from first principles, useful for design of cooling systems based on the techniques of this thesis. Finally, brief descriptions of potential engineering applications beyond Soldier cooling are provided.

The porous membranes studied in this thesis permitted water vapor mass transport rates between 1.3×10^{-7} and 6.0×10^{-7} kg/s, corresponding to a latent heat transfer lift between 0.31 and 1.35 watts, roughly 215 to 1350 w/m^2. Cooling was realized utilizing non-boiling phase change of water in a system competent for integration with other protective capabilities. If used in protective raiment, the techniques presented in this thesis could provide substantial improvement in human thermal comfort and efficient water management compared to modern body armor or chemical-biological protection suits, which afford almost no evaporative cooling ability. While the techniques herein have potential to provide appreciable cooling for humans in the desert, they could also be extended to electronics thermal management as well as other products and processes.

7.1　DuPont Porous Membrane Performance

As shown in Figure 6.3, the average DuPont porous membrane surface cooling, 14.0 ± 2.0 °C for Nucrel® ($d_e = 1.2$ μm) and 13.4 ± 2.4 °C for Hytrel® ($d_e = 13.4$ μm), are substantial fractions of the maximum possible cooling. This cooling efficacy is represented by the Fractional Accomplishing Cooling: $\Theta = 0.40 \pm 0.6$ for Nucrel® and $\Theta = 0.38 \pm 0.7$ for Hytrel® (Table 6.2). Thus, both membranes supported appreciable cooling despite their tiny pore IDs and small total porosity (7.5-11.2%). Moreover, each membrane provided substantial solid material that could be nano-engineered to incorporate other capabilities, e.g., high mechanical strength. Nonetheless, no significant difference in cooling efficacy was observed in the 1.0 – 15 μm pore diameter range.

Consistent with the indistinguishable cooling result, the average mass flow rates for the four membrane experiments agreed to within ±15% of their mean value, and there was no significant difference between the average values for Nucrel® ($d_e = 1.2$ μm) and Hytrel® ($d_e = 13.4$ μm). This observation was consistent with the intentional selection of similar porosities and thickness for all four test specimen membranes. However, this result also implied that for this range of pore IDs (1 – 15 μm) size effects on diffusion were insignificant and/or too small to be

detected with the HAMTA1 apparatus and technique. Transition regime diffusion theory (Equation 2.10) indicated that the diffusion coefficient should decrease from the continuum diffusion regime value (Equation 2.8) by about 6.1% for pore ID of about 1.0 - 1.4 μm and should decrease by about 0.7% for pore ID of about 12.6-14.2 μm. Given the 3.7 % measurement error in HAMTA1, the possible 12.9% transport enhancement arising from Stefan Flow (Section 5.1), and the potential uncertainties in boundary layer mass transport resistances, the presence of a 0.7% or 6.1% effect could not have been detected with a high level of confidence.

7.1.1 Pore Shape Effect Impedes Transport Performance

When solved for R_{mem} with experimental values of $\dot{m}_{ave}$, Equation 5.26 accurately predicted $D_{H2O,air}$ within +19% to -40% of theoretical values (Table 6.1). Predictive ability for the nominally 1.2 μm Nucrel® pores was more precise than for the larger pores, indicating that Equation 5.26 tended to over-predict the transport efficacy of the Hytrel® membranes. While chemical differences between these materials might have impacted transport efficacy (i.e., Hytrel® absorbs small amounts of water while Nucrel® does not), it was hypothesized that over-prediction associated with samples containing larger pores arose from a shape effect. The Hytrel® pores were not cylindrical (Figure 3.4), but appeared as squished triangles whose corners were highly acute. A water molecule moving axially down the center of such a pore had little wall interaction, and it would experience a low local Knudsen Number consistent with a pore diameter much greater than its mean free path. However, a water molecule in the vicinity of the pore corners would undergo frequent wall interactions, and it would therefore experience a relatively large local Knudsen Number. In actuality, as water molecules experienced the random walk of the diffusion process, they would drift between these two regions, sometimes experiencing low local Knudsen Number and sometimes experiencing high.

These dissimilar transport regime regions are shown schematically in Figure 7.1. Since the portion of the pore near the corners impeded mass transport due to locally high Knudsen Number, these crushed triangular pores presented a larger mass transport resistance than would a perfectly circular pore with the same cross sectional area. Equation 5.26 included no correcting factors for pore shape; it assumed that pores have circular cross section.

An analysis of this hypothesized triangular pore shape effect model is presented in Appendix 4. It was found that rarefaction near the pore corners would only account for a reduction of about 1.7% in the intrinsic membrane diffusion coefficient, far short of the 40%

difference between theoretical and experimental results. However, it was also found that if the corner area associated with rarefaction (i.e., about 39.5% of the total pore area) were completely blocked, the diffusion coefficient would appear to drop 40.2%, almost exactly the reduction measured experimentally. It is possible that liquid water condensed in the corners and was somehow held there and prevented from rapid evaporation by surface effects. However, it is not clear whether the pore corners were truly blocked nor is there a mechanistic explanation for this blockage. So, it remains unclear why the Hytrel® experimental diffusion coefficient was so low.

Figure 7.1: A schematic representation of a micron-scale pore with triangular cross section shows the presence of two dissimilar transport regions. Far from the corners in the center of the pore (light grey region), local Knudsen Number is low, facilitating continuum transport. However, near the corners (dark grey region), molecule-wall interactions are prevalent, and local Knudsen Number is high, retarding transport. Due to high local Knudsen Number regions, the overall transport rate of this pore will be less than a circular pore with the same total cross sectional area.

To ensure maximum vapor mass transport rate, the ideal pore shape would have no corners where water molecules might encounter a region of locally high Knudsen Number or a liquid blockage. Therefore, pores of circular cross section are expected to provide the best vapor

127

transport with respect to this particular shape effect. Unfortunately, each pore in the Hytrel®️ membranes studied in this thesis had markedly different pore shape, and there were about 120 million unique pores in a single membrane sample. Therefore, it was difficult to more specifically quantify the cause and impact of this shape effect from the data of this thesis. As a follow-on study, it would be interesting to utilize interference lithography or some other parallel nanofabrication technique to create large arrays of identical pores of different shape. Several samples containing pores of various shapes could be studied to quantify the transport implications of this shape effect.

7.1.2 Accuracy of Mass Transport Modeling

Figure 6.2 depicts the results of various mass transport models of increasing complexity for transport through DuPont porous membranes using HAMTA1. In each case, R_{mem}, based on the membrane characterization techniques in Chapter 3, was utilized to predict $\dot{m}_{ave}$. The models utilized included: 1) continuum 1-D Fick's Law; 2) 1-D Fick's Law with correction for rarified transport; 3) 1-D Fick's Law with correction for rarified transport plus contribution of the viscous sub-layer [VSL] on the downstream membrane face, 4) Fick's Law with rarified transport, VSL, an upstream boundary layer, and radial concentration gradient on the upstream membrane face; and 5) Fick's Law with rarified transport, a boundary layer and radial concentration gradient on the upstream membrane face, and a Sherwood Number analysis for the transport resistance on the downstream membrane face [instead of a VSL].

As indicated in Chapter 6, Model (4), which included all of the critical mass transport resistance terms, provided the closest $\dot{m}_{ave}$ prediction to experiment for the four DuPont porous membrane experimental measurements. The Sherwood Number correlation over-predicted mass transport resistance of the membrane downstream sweep gas due to the dissimilarity between the momentum boundary layer, which was initiated at the leading edge of the Styrofoam collar, and the mass transport boundary layer, which starts at the membrane leading edge.

7.1.3 Water Droplet Formation and Mass Transport

Three of the four experimental results displayed in Figure 6.2 fell between the $\dot{m}_{ave}$ values predicted by Model (4) and Model (3). These models were differentiated by introduction of the viscous sub layer and radial concentration gradient on the upstream face of the membrane. In effect, Model (4) represented a completely dry membrane without water droplet formation. Model (3) represented a completely wet membrane because the mass transfer retarding effect of

128

the upstream boundary layer was not considered, increasing the rate of vapor transport through the membrane (as explained in Section 5.5).

It was experimentally observed that a portion of the membrane upstream face was covered by liquid condensate during the steady-state period (Figure 5.8). Since liquid water did not wick up the pores (Section 5.5) evaporation occurred from the bottom opening of liquid-saturated pores. The air at these openings was 100% water vapor saturated at the temperature of the upstream membrane face. So, these pores behaved as if there was no membrane upstream boundary layer, explaining why most of the experimental HAMTA1 mass transport rates actually fell between two model results: one that included and one that neglected the boundary layer on the upstream membrane face.

It is not certain why one of the two Hytrel$^{\circledR}$ mass transport results (Hytrel$^{\circledR}$ B) was even lower than the $\dot{m}_{ave}$ value predicted by Model (4). Great care was taken to assure the two Hytrel$^{\circledR}$ tests were as similar as possible. There was nothing remarkable about the geometry of this sample to differentiate it from the Hytrel$^{\circledR}$ A sample or to suggest different mass transport properties.

7.2 HATMA2 Track-Etched Membrane Performance

Figure 6.5 depicts the intrinsic mass transport coefficients of the track-etched membranes as a function of Knudsen Number. These results are compared against transition regime diffusion theory (Equation 2.10). As pore diameter decreased at constant pressure, Knudsen Number increased, and the experimental mass transport resistance of the membranes increased in a manner consistent with theoretically-predicted behavior. The result indicated in Figure 6.5 was one of the major contributions of this thesis because previous research in capillary diffusion modulated the Knudsen Number utilizing a tube of fixed diameter by changing the pressure of the diffusing species to impact mean free path [Knudsen (1952)]. While Figure 6.5 is in line with well-established theory for $0 < Kn < 3$ [Pollard and Present (1948); Kärger and Ruthven (1992); Mills (1999a), pp. 810-812], a novel means to manipulate Knudsen Number was used to obtain the result: modulating pore diameter in regular increments over a range from 15 µm to 39 nm.

The present data do not show evidence of the Knudsen minimum, experimentally observed by others at about $Kn = 3$ [Knudsen (1952); Karniadakis and Beskök (2002)] and derived by Chen [Chen (2005), pp. 308-313]. Beyond this minimum, larger Knudsen Numbers give rise to increased mass transport. One of the hypotheses of this thesis was that enhanced transport at high

129

Knudsen Numbers through tiny pores could be utilized to increase cooling efficacy above levels achieved at small Knudsen Number (larger pores) for the same membrane porosity and thickness. Since no enhancement was observed in this research up to Knudsen Number of about 5, it was concluded that various transport-enhancing mechanisms such as specular reflection, two-dimensional gas flow, nano-scale thermal recuperation, or some unforeseen (and as of yet unobserved) nano-scale effect are not significant under the experimental conditions outlined in this thesis. Confirmation in this thesis of transition regime diffusion theory (Equation 2.10) up to a Knudsen Number of 5 was disappointing in this respect. However, it confirmed that none of the enhanced transport effects recently observed by other researchers at slightly higher Knudsen Numbers [Roy, *et al.* (2005); Holt, *et al.* (2006)] were significant in the transition regime up to Kn = 5.

While following the anticipated trend, the experimental membrane mass transport coefficients were lower than predicated by theory as Knudsen Number approached 5 for a majority of the data points (Figure 6.5): between 10% and 35% on average too low between 60 nm and 400 nm diameter pores and 71% too low at 39 nm. Pore tortuosity may have been a partial cause for apparent experimental underperformance. The model (Equation 2.10) assumed tortuosity of unity, straight through pores. However, FIB-imaged cross sections of the smaller pore diameter membranes showed pore track deviation as large as 24 degrees from normal (Section 3.3.5), which equated to a 9.5% increase in diffusion distance through the membrane. A corresponding 9.5% reduction in diffusion coefficient would be expected. In addition, the smaller-diameter pores may not have had uniform cross section at every axial station due to channel necking induced by the etching steps in the manufacturing process. However, the existence of non-uniform cross section would be very difficult to detect via SEM or FIB cross section imaging.

Since FIB cross section imaging via argon-ion polishing was labor-intensive, only 100 nm and 400 nm samples were imaged using this technique. This process was destructive; so, the exact samples used in experiments were not imaged; instead samples from the same lot were analyzed to determine pore track path. Results from these two samples were assumed to extend to the other track-etched membranes. It is possible that samples used in the evaporation experiments had pore tracks with tilts greater than 24 degrees from normal, inducing larger

membrane transport resistance than the anticipated 9.5% reduction. However, it is unlikely that the entire underperformance effect arose from this single mechanism.

7.2.1 Importance of Membrane Sherwood Number

The Sherwood Number is utilized to model and quantify mass transport processes. One interpretation of Sherwood Number is as a dimensionless comparison of the mass transport resistances of a diffusive transport process and a convective transport process. Thus, for the experiments presented in this thesis, it is valuable to compare the mass transport resistance in the upstream and downstream boundary layers with the resistance of the membrane itself,

$$Sh_{L,membrane} = \frac{R_{mem}}{R_{headspace} + R_{BL,downstream}}$$
(Equation 7.1)

where, R_{mem} , $R_{headpace}$, and $R_{BL,downstream}$ are mass transport resistances of the membrane, head space, and downstream boundary layer respectively. Hereafter in this thesis, the quantity in Equation 7.1 will be referred to as the "membrane Sherwood Number". Calculation of apparatus mass transport resistances is discussed in Chapter 5. The membrane mass transport resistance includes membrane thickness (L), porosity (ε_v), and the mass transport coefficient for diffusion of water vapor though the membrane pores, as given in Equation 5.19,

$$D_{H_2O,air} = \frac{L}{\varepsilon_v \cdot R_{membrane}}$$
(Equation 5.19)

7.2.2 Membrane Sherwood Number Relationship to Fractional Accomplished Cooling

Defined in Section 6.2, the Fractional Accomplished Cooling, Θ, is a generic dimensionless parameter that can be broadly applied to characterize many non-boiling evaporative cooling systems of interest:

$$\Theta = \frac{\left(T_{1,closed} - T_{1,mem}\right)}{\left(T_{1,closed} - T_{1,open}\right)}$$
(Equation 6.1)

The engineering value of Θ resides in the critical physical relationship between $Sh_{L,membrane}$ and Θ. To derive this relationship, the apparatus heat balance, Equation 4.8,

$$\frac{d\left(C_p \cdot M \cdot T_1\right)}{dt} = \dot{Q}_{in} - \dot{Q}_{lost} - Ah\left(T_1 - T_{amb}\right) - \dot{m} \cdot \Delta H_{fg}$$
(Equation 4.8)

was idealized using the following assumptions: 1) steady state operation, 2) no parasitic leakage, and 3) identical convective cooling, h, for both closed chamber and porous membrane

experiments. Equation 4.8 was recast to give base temperatures for the closed chamber case, $T_{1,closed}$ and for an arbitrary porous membrane case, $T_{1,mem}$.

$$\dot{Q}_{in} = Ah\left(T_{1,closed} - T_{amb}\right) \qquad \text{(Equation 7.2)}$$

$$\dot{Q}_{in} - \dot{m} \cdot \Delta H_{fg} = Ah\left(T_{1,mem} - T_{amb}\right) \qquad \text{(Equation 7.3)}$$

A temperature ratio related to the input power was expressed as a ratio of Equation 7.3 and 7.2

$$\frac{\dot{Q}_{in} - \dot{m} \cdot \Delta H_{fg}}{\dot{Q}_{in}} = \frac{Ah\left(T_{1,mem} - T_{amb}\right)}{Ah\left(T_{1,closed} - T_{amb}\right)} = \frac{\left(T_{1,mem} - T_{amb}\right)}{\left(T_{1,closed} - T_{amb}\right)} \qquad \text{(Equation 7.4)}$$

It was noted that Equation 7.4 could be rewritten

$$\frac{\dot{Q}_{in} - \dot{m} \cdot \Delta H_{fg}}{\dot{Q}_{in}} = 1 - \frac{\dot{m} \cdot \Delta H_{fg}}{\dot{Q}_{in}} = \frac{\left(T_{1,mem} - T_{amb}\right)}{\left(T_{1,closed} - T_{amb}\right)} \qquad \text{(Equation 7.5)}$$

and with some algebra,

$$\frac{\dot{m} \cdot \Delta H_{fg}}{\dot{Q}_{in}} = 1 - \frac{\left(T_{1,mem} - T_{amb}\right)}{\left(T_{1,closed} - T_{amb}\right)} \qquad \text{(Equation 7.6)}$$

With some additional algebra, the dimensionless temperature ratio, Φ_M, was obtained

$$1 - \frac{\left(T_{1,mem} - T_{amb}\right)}{\left(T_{1,closed} - T_{amb}\right)} = \frac{\left(T_{1,closed} - T_{amb}\right) - \left(T_{1,mem} - T_{amb}\right)}{\left(T_{1,closed} - T_{amb}\right)} = \frac{\left(T_{1,closed} - T_{1,mem}\right)}{\left(T_{1,closed} - T_{amb}\right)} = \Phi_M \qquad \text{(Equation 7.7)}$$

and therefore,

$$\frac{\dot{m} \cdot \Delta H_{fg}}{\dot{Q}_{in}} = \Phi_M \qquad \text{(Equation 7.8)}$$

A special case of Φ_M was obtained for the experiment running in open chamber mode. This special case was denoted Φ_o, where

$$\Phi_o = \frac{\left(T_{1,closed} - T_{1,open}\right)}{\left(T_{1,closed} - T_{amb}\right)} \qquad \text{(Equation 7.9)}$$

The terms Φ_M and Φ_o provide a relationship between the temperature ratio resulting from the closed chamber and porous membrane runs (Equation 7.4) and Fractional Accomplished Cooling. Equation 7.10 verified that $\Phi_M / \Phi_o = \Theta$

$$\frac{\Phi_M}{\Phi_o} = \frac{\left(T_{1,closed} - T_{1,mem}\right)}{\left(T_{1,closed} - T_{amb}\right)} \frac{\left(T_{1,closed} - T_{amb}\right)}{\left(T_{1,closed} - T_{1,open}\right)} = \frac{\left(T_{1,closed} - T_{1,mem}\right)}{\left(T_{1,closed} - T_{1,open}\right)} = \Theta \qquad \text{(Equation 7.10)}$$

Therefore

$$\Theta \cdot \Phi_o = \Phi_M = \frac{\dot{m} \cdot \Delta H_{fg}}{\dot{Q}_{in}} \quad \text{and} \quad \Theta \cdot = \frac{\dot{m} \cdot \Delta H_{fg}}{\Phi_o \cdot \dot{Q}_{in}} \qquad \text{(Equation 7.11)}$$

132

Equation 2.11 provides an explicit, general expression for mass transport rate, $\dot{m}$, based on apparatus and membrane parameters.

$$\dot{m} = \frac{A(\rho_0 - \rho_{amb})}{\sum R_{mass\_transport}}$$ (Equation 2.11)

Thus, Equation 7.11 can be recast as

$$\Theta = \frac{A(\rho_0 - \rho_{amb})}{\sum R_{mass\_transport}} \frac{\Delta H_{fg}}{\Phi_o \cdot \dot{Q}_{in}}$$ (Equation 7.12)

The summation of mass transport resistances in the denominator can be broken into intrinsic membrane resistance and apparatus resistances,

$$\sum R_{mass\_transport} = R_{headspace} + R_{BL,upstream} + R_{mem}$$ (Equation 7.13)

Utilizing the expression for membrane Sherwood Number (Equation 7.1) and some algebra, the summation of mass transfer resistances (Equation 7.13) can be recast into two important expressions:

$$\sum R_{mass\_transport} = \left(R_{headspace} + R_{BL,upstream}\right) \cdot \left(1 + Sh_{L,membrane}\right)$$ (Equation 7.14)

or

$$\sum R_{mass\_transport} = R_{mem}\left(\frac{Sh_{L,membrane}}{Sh_{L,membrane} + 1}\right)$$ (Equation 7.15)

Utilizing Equation 7.14 in Equation 7.12 gives a relationship for Fractional Accomplished Cooling and membrane Sherwood Number important for engineering design of systems utilizing evaporative cooling through porous membranes:

$$\Theta = \frac{A(\rho_0 - \rho_{amb})}{\left(R_{headspace} + R_{BL,upstream}\right) \cdot \left(1 + Sh_{L,membrane}\right)} \frac{\Delta H_{fg}}{\Phi_o \cdot \dot{Q}_{in}}$$ (Equation 7.16)

Equation 7.16 is useful because every variable (with one exception) within this expression can be easily measured or estimated for any evaporation apparatus for which Equation 7.4 is valid. These terms can also be held constant for one experiment to the next. Most importantly, the impact of various membrane Sherwood Numbers (i.e. membrane mass transport resistances) can be estimated without need to run an experiment using a porous membrane.

The only variable that cannot be determined without a membrane in place on the experiment is the water vapor mass concentration at the liquid-air interface within the evaporation chamber, ρ_0. This parameter is dependant upon the temperature of the evaporation

chamber for each individual membrane. However, it can be bounded by measuring the temperature at the liquid-air interface for open chamber and closed chamber experiments. The integrated form of the Clausius-Clapeyron relation can be utilized to estimate bounding mass concentration from these limiting temperature measurements.

$$\rho_o \approx \frac{P_1 \cdot e^{\frac{\Delta H_{fg}}{R}\left(\frac{1}{T_1} - \frac{1}{T_{boil}}\right)}}{RT_1}$$

(Equation 7.17)

Figure 7.2 gives the upper bound and lower bound estimates for the HAMTA2 closed and open evaporation chamber temperatures at a nozzle temperature of 50 °C. Experimental data for various track-etched membranes run under the same ambient conditions are also given for comparison. Figure 7.2 shows that as the membrane Sherwood Number increases, the two bounding cases converge to nearly identical values. Thus, this engineering estimation technique can be a powerful tool for predicting the thermal performance of membranes that yield a membrane Sherwood Number of 5 or greater.

Equation 7.16 can also reasonably approximate porous membrane cooling efficacy if the average mass concentration of the two extreme bounding cases is utilized for ρ_o. Figure 7.2 shows how Equation 7.16 based on the average ρ_o value compares to the bounding cases and track-etched membrane data.

Returning to the alternate derivation for mass transport resistance, Equation 7.15 used within Equation 7.12 gives a Fractional Accomplished Cooling to membrane Sherwood Number relationship numerically identical to Equation 7.16. However, this incarnation provides additional physical insight into the importance of R_{mem} to cooling efficacy and mass transport

$$\Theta = \frac{A(\rho_0 - \rho_{amb})}{R_{mem}} \frac{\Delta H_{fg}}{\Phi_o \cdot \dot{Q}_{in}}\left(\frac{Sh_{L,membrane} + 1}{Sh_{L,membrane}}\right)$$

(Equation 7.18)

Applying the bounds of large and small membrane Sherwood Number to Equation 7.18 illustrates how the magnitude of R_{mem} impacts the Fractional Accomplished Cooling:

$$\frac{Lim \cdot \Theta}{Sh_{L,membrane} \to 0} = \frac{A(\rho_0 - \rho_{amb})}{R_{mem}} \frac{\Delta H_{fg}}{\Phi_o \cdot \dot{Q}_{in}}\left(\frac{0 + 1}{Sh_{L,membrane}}\right) = A(\rho_0 - \rho_{amb})\frac{\Delta H_{fg}}{\Phi_o \cdot \dot{Q}_{in}}\left(\frac{1}{R_{headspace} + R_{BL,upstream}}\right)$$

(Eq 7.19)

For small membrane Sherwood Number, the membrane mass transport resistance is insignificant, and the limit expressed in Equation 7.19 shows that in this case the Fractional Accomplished

Cooling is not at all dependent upon R_{mem}. Conversely, for large membrane Sherwood Number, the membrane mass transport resistance dominates:

$$\frac{Lim \cdot \Theta}{Sh_{L,membrane} \to \infty} = \frac{A(\rho_0 - \rho_{amb})}{R_{membrane}} \frac{\Delta H_{fg}}{\Phi_o \cdot \dot{Q}_{in}} \left(\frac{Sh_{L,membrane}}{Sh_{L,membrane}} \right) = \frac{A(\rho_0 - \rho_{amb})}{R_{membrane}} \frac{\Delta H_{fg}}{\Phi_o \cdot \dot{Q}_{in}} \quad \text{(Equation 7.20)}$$

The limit expressed in Equation 7.20 shows that for large $Sh_{L.membrane}$, Fractional Accomplished Cooling is not dependent upon the apparatus mass transport resistances and is determined only by R_{mem}.
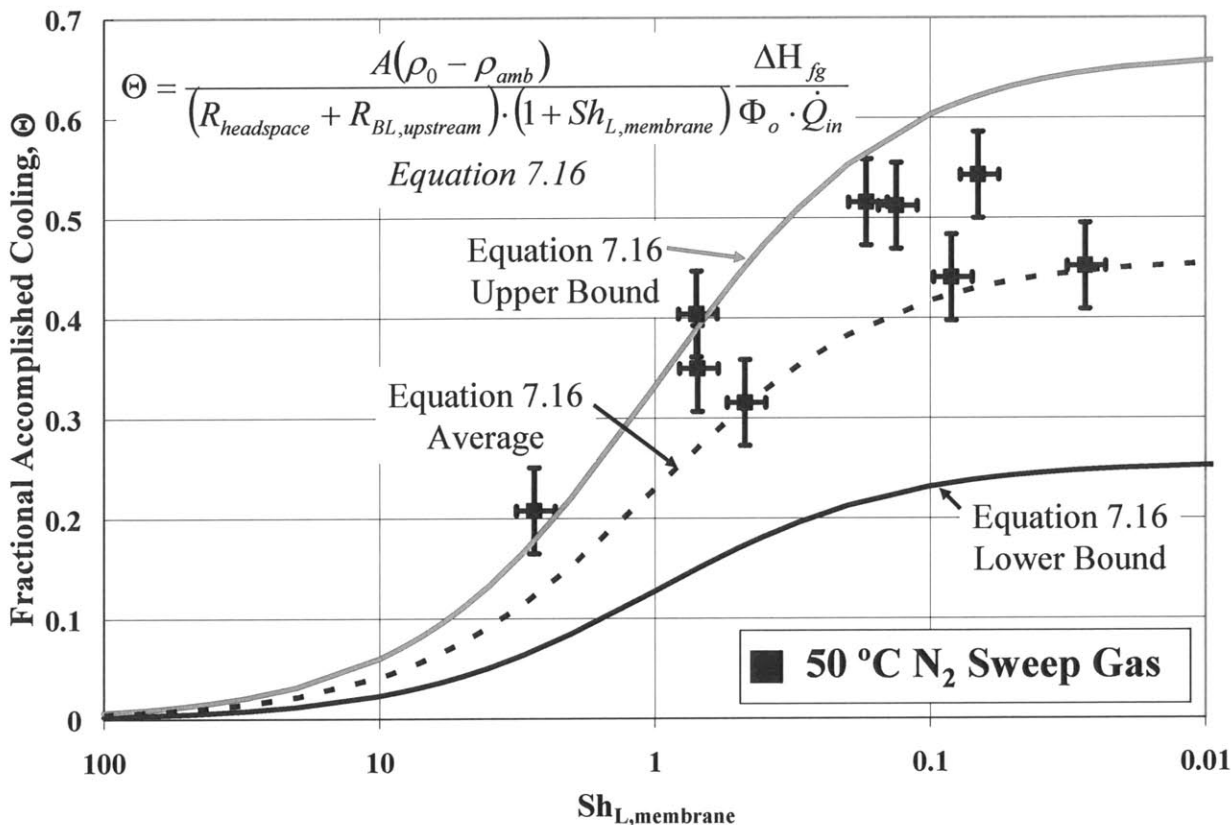
Figure 7.2: Fractional Accomplished Cooling, Θ, expressed as a function of membrane Sherwood Number, $Sh_{L,membrane}$. The upper bound (solid gray line) and lower bound (solid black line) are given based on the recorded temperatures in the evaporation chamber for open- and closed-chamber runs. Equation 7.16 provides a powerful, predictive engineering design tool to evaluate the cooling efficacy of various porous membranes without the need for experiments. The curve for an average value of apparatus mass concentration (dotted black line) is compared against HAMTA2 experimental data to provide a sense of the accuracy of this modeling method.

Further value in the arrangement of the Equation 7.18 is obtained through the expression of this equation in terms on an intrinsic mass transfer coefficient. If the mass transport from the evaporation apparatus depended solely upon the membrane (and not the upstream and downstream mass transport resistances), an intrinsic mass flux could be expressed as

$$\dot{m}_{membrane} = \frac{(\rho_o - \rho_{amb})}{R_{mem}}$$

(Equation 7.21)

Equation 7.21 combined with Equation 7.18 gives Fractional Accomplished Cooling as a function of membrane Sherwood Number with respect the intrinsic mass flux rate.

$$\Theta = \frac{A \cdot \dot{m}_{membrane} \cdot \Delta H_{fg}}{\Phi_o \cdot \dot{Q}_{in}} \left(\frac{Sh_{L,membrane} + 1}{Sh_{L,membrane}} \right)$$

(Equation 7.22)

The quantity $A \cdot \dot{m}_{membrane} \cdot \Delta H_{fg}$ is the rate of latent heat transport out of the evaporation chamber in the idealized situation that resistances to mass transport presented by the boundary layers on either side of the membrane are zero. This quantity can be used as an upper bound to predict the latent heat transport efficacy of any evaporative cooling system employing transport across porous membranes. Importantly, the ratio $A \cdot \dot{m}_{membrane} \cdot \Delta H_{fg} / \dot{Q}_{in}$ is a dimensionless power relating rate at which energy is carried away by transport of latent heat to the rate of energy input into the evaporation chamber. This dimensionless power ratio is denoted Λ. Thus, Equation 7.18 can be expressed in terms of only dimensionless numbers

$$\Theta = \frac{\Lambda}{\Phi_o} \left(\frac{Sh_{L,membrane} + 1}{Sh_{L,membrane}} \right)$$

(Equation 7.23)

where Λ represents the flow of energy through the system, Φ_o represents the range of temperatures the experimental apparatus can experience, and $Sh_{L,membrane}$ represents the various membrane and apparatus mass transport parameters.

$$\Theta = \frac{\Lambda}{\Phi_o}\left(\frac{Sh_{L,membrane}+1}{Sh_{L,membrane}}\right)$$

Equation 7.23

Θ (100°C Nozzle)
Equation 7.23

Θ (50°C Nozzle)
Equation 7.23

● **100 °C N$_2$ Sweep Gas**

■ **50 °C N$_2$ Sweep Gas**
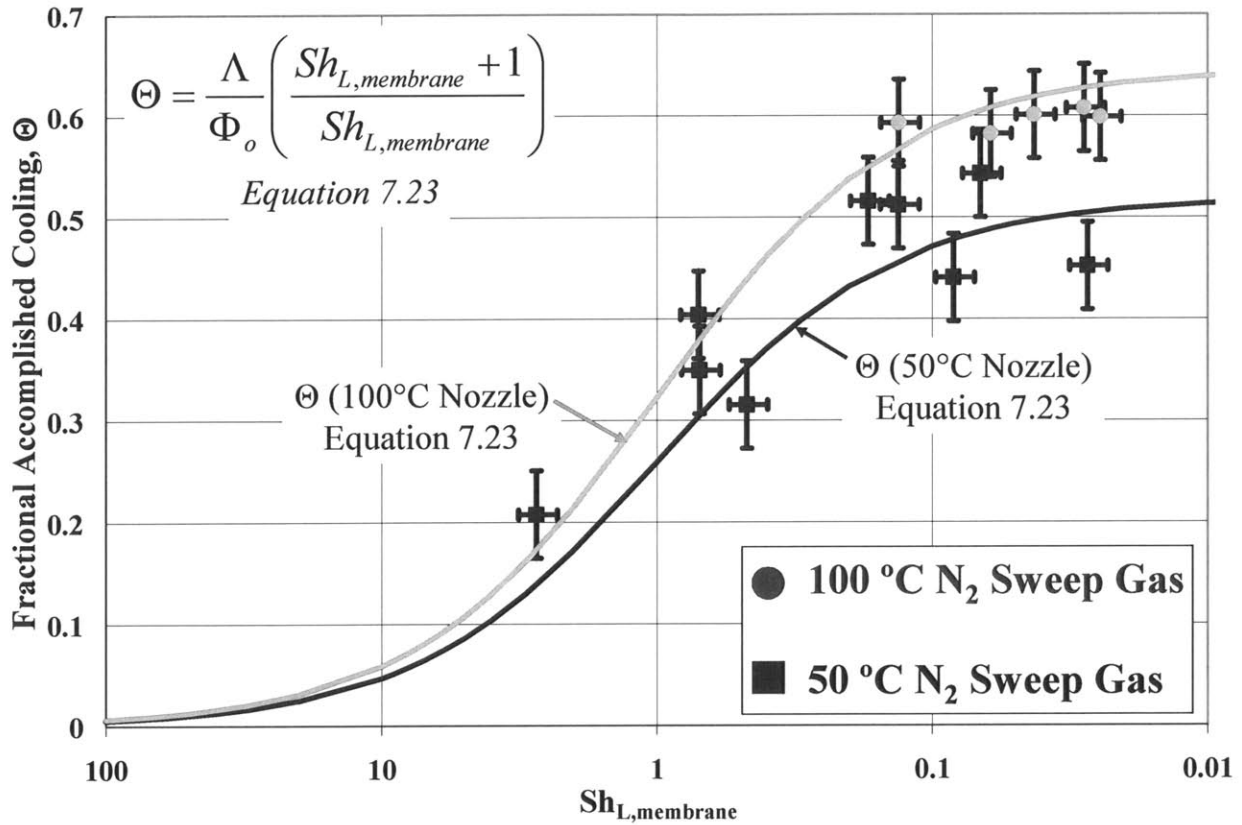
FIGURE 7.3: Fractional Accomplished Cooling, Θ, expressed as a function of membrane Sherwood Number, $Sh_{L,membrane}$. Equation 7.23 was solved for the conditions of the evaporation chamber at 100 °C (solid gray line) and 50 °C (solid black line) nozzle temperature. The model is compared to HAMTA2 experimental data from the track-etched membranes for these two operating conditions.

7.2.3 Physical Significant of the Membrane Sherwood Number

Great effort was expended in designing and implementing the experiments reported in this thesis to assure that $R_{headspace}$ and $R_{BL,downstream}$ were very similar for all HAMTA2 runs. Membranes with large pores (low Knudsen Number, low membrane Sherwood Number) provided very minor contribution to mass transport resistance. Hence, the similarity in $R_{headspace}$ and $R_{BL,downstream}$ across all experiments generated similar Fractional Accomplished Cooling for the large-pore-diameter membranes, as evidenced by the asymptotic tendency of the experimental data and models in Figures 7.2 and 7.3 for low membrane Sherwood Number.

Since $Sh_{L,membrane}$ represents a ratio of the (fixed) apparatus mass transport resistance and the (variable) membrane mass transport resistance, some fundamental change in the transport process is expected to happen around $Sh_{L,membrane} \sim 0.1$. This is the threshold at which the

membrane transport resistance becomes a non-negligible (i.e., greater than 10%) contributor to the total apparatus mass transport resistance. This fundamental shift in the transport process around $Sh_{L,membrane} \sim 0.1$ is observed in the data of Figure 7.3 and in the model (Equation 7.23). The Fractional Accomplished Cooling begins to become impacted by decreasing membrane pore diameter. Above $Sh_{L,membrane} \sim 0.1$, Θ becomes a strong function of $Sh_{L,membrane}$ whereas below this value, the dependence grows weak.

The most interesting portion of the Figure 7.3 data occurs when $Sh_{L,membrane} > 0.1$. As $Sh_{L,membrane}$ increases, membrane mass transfer resistance becomes large with respect to the total mass transfer resistance, and the membrane itself becomes the bottleneck to latent heat transport. The entire system responds by increasing in temperature. Equilibrium is re-established when the temperature inside the evaporation chamber is high enough to generate large enough water vapor concentration gradient to force the proper amount of latent heat through the membrane. The resulting measured Fractional Accomplished Cooling for the system drops accordingly. Experiments confirm that the relationship between membrane Sherwood Number and Fractional Accomplished Cooling nearly identically follows the trend predicted by Equation 7.23.

This behavior mirrors the DuPont porous membrane results from HAMTA1 with an additional component. For HAMTA1, pore size did not impact transport rate or cooling efficacy because the pores were too large for transition regime transport to be important. For HAMTA2, continuum diffusion is maintained for pore diameters down to 1 μm; for this pore size and up, pore diameter does not matter. However, $Sh_{L,membrane} \sim 0.1$ corresponds roughly to pore diameter of 500 nm (Kn $\sim$ 0.4). Transition regime theory (Equation 2.10) indicates that at this pore diameter, a 13.1% drop in $D_{H_2O,Air}$ should be expected. While this reduction in mass transport coefficient is apparent in Figure 6.5, the reduced membrane mass transport coefficient has negligible impact on Fractional Accomplished Cooling at this pore size. Despite the increase in mass transport resistance owing to smaller pore diameter, the membrane resistance in this regime is not large enough to exceed the $Sh_{L,membrane} \sim 0.1$ threshold. So, impact of smaller pore size and onset of rarefaction at this diameter (~500 nm) does not significantly impact the mass transport rate or cooling efficacy.

Importantly, there are two regimes in which pore diameter does not impact cooling efficacy. First, for pore diameter above 1 μm, transport through the pores occurs in the continuum regime where pore size does not matter; only membrane thickness, porosity (void

fraction), and tortuosity matter above 1 μm. Second, despite the transition to more rarefied diffusion in pores smaller than 1 μm, pore diameter still does not significantly impact cooling efficacy until rarified flow induced by small pores increases the mass transport resistance of the membrane to an appreciable fraction of the total transport resistance for the system under study. Understanding these regimes is critical to engineering design of evaporative cooling systems based on the techniques highlighted in this thesis.

One important interpretation of the membrane Sherwood Number for mass transport experiments is to illustrate when the mass transport resistance of the membrane is significant. If the membrane resistance is relatively small compared to the upstream and downstream boundary layer resistances, the membrane Sherwood Number is small, and the rate of cooling via latent heat transport is governed entirely by the upstream and downstream BL resistances. However, it is not true in this regime to say that the membrane does not matter at all. Even if membrane resistance approaches 0, the membrane still defines the boundary that differentiates the upstream and downstream boundary layers and provides the surface over which these two flows form and develop.

7.2.4 Determining Diffusion Coefficient Through the Membrane

Using Equation 7.16, researchers can design experiments to determine $D_{H2O,Air}$ for any porous membrane sample of interest by tuning $R_{headspace}$ and $R_{BL,downstream}$ appropriately through control of experimental parameters. No membrane characterizations using SEM/FIB (Chapter 3) are necessary nor are careful studies of highly accurate mass transport rates (Chapter 4). With equation 7.16, only three experimental temperature measurements are required to obtain R_{mem}, and simple techniques like fold & mic (Section 3.3) and gravimetric measurements (Section 3.3.4) can be applied to calculate $D_{H2O,Air}$ from R_{mem} using Equation 5.19.

Under a fixed sweep gas temperature, T_{amb}, three steady-state temperatures must be measured using an experimental apparatus for which Equation 7.4 is valid: $T_{1,closed}$, $T_{1,open}$, and $T_{1,mem}$. These values can be obtained via a single thermocouple temperature measurement of the apparatus base temperature in three successive experiments. The Fractional Accomplished Cooling, Θ, is calculated from these results (Equation 6.1), and the resultant Θ value is utilized to solve Equation 7.16 for membrane Sherwood Number. The water vapor mass concentration at the air-liquid interface, ρ_o, can be estimated from $T_{1,mem}$ using the Clausius-Clapeyron relation and Ideal Gas Law (Equation 7.17). The boundary layer transport resistances, $R_{headspace}$ and

$R_{BL,downstream}$ are obtained from conventional mass transfer correlations (as described in Sections 5.3.2 and 5.2.2 respectively for HAMTA2), leaving R_{mem} as the only unknown.

7.2.5 Determining Surface Temperature and Concentration Gradients

Working in reverse, a researcher who has determined theoretical R_{mem} for the membrane using SEM/FIB techniques in Section 3.3, could utilize equation 7.16 to perform thermal modeling without the need for experiments with porous membranes. However, two experimental temperature measurements on the system of interest, $T_{1,closed}$ and $T_{1,open}$, are required to solve for $T_{1,mem}$. By calculating $R_{headspace}$ and $R_{BL,downstream}$ for an engineering design of interest, the membrane Sherwood Number is calculated from R_{mem}. Using the Clausius-Clapeyron relation (Equation 7.17) and Ideal Gas Law (Equation 4.4) to solve for ρ_o Equation 7.16 gives the Fractional Accomplished Cooling, Θ, for this configuration. Since $T_{1,mem}$ appears both in Θ and in ρ_o, Equation 7.16 written in this manner is a transcendental equation that must be solved iteratively to converge to the correct $T_{1,mem}$ result,

$$\frac{\left(T_{1,closed} - T_{1,mem}\right)}{\left(T_{1,closed} - T_{1,open}\right)} = \frac{A \cdot \left(\frac{P_1 \cdot e^{\frac{\Delta H_{fg}}{R}\left(\frac{1}{T_{1,mem}} - \frac{1}{T_{boil}}\right)}}{RT_{1,mem}} - \rho_{amb}\right)}{\left(R_{headspace} + R_{BL,upstream}\right) \cdot \left(1 + Sh_{L,membrane}\right)} \cdot \frac{\Delta H_{fg}}{\Phi_o \cdot \dot{Q}_{in}}$$

(Equation 7.24)

The cooling efficacy of several different membrane types could be gauged through this process without running any evaporative cooling experiments on the membranes themselves. Furthermore, based on the calculated $T_{1,mem}$ result, the concentration gradient of water vapor across the membrane can also be estimated using steam tables. This additional result will be valuable for design of humidity control devices utilizing membranes akin to those highlighted in this thesis.

7.3   Applications Beyond Human-Portable Cooling

This thesis has focused on the impact of porous media on heat and mass transport of water vapor for evaporative cooling of humans wearing protective garments. However, the concepts herein can be expanded more generally to encompass any solid barrier material with pores or channels that simultaneously: (a) protect a substance from an adverse environmental impact, e.g., damage from ballistic fragments or blast waves, corrosive or hazardous agents, etc.; and (b) manipulate the rate of transformation of a substance protected by the barrier from one

thermodynamic state to another. The later occurs though influence of transport rate of a fluid between the enclosed/protected substance and the environment from which the substance is separated by the porous barrier material. Examples of processes to which the concepts of this thesis apply include: evaporation of a liquid to a gas, sublimation of a solid to its vapor, melting of a solid to form a liquid, decomposition of a chemical compound to produce or remove at least one liquid or gaseous substance. The reverse of all of these processes are also applicable, for example, condensation of a gas to a liquid. Various manifestations of how thermodynamic state could be modulated through mass transport are shown in Figure 7.4.
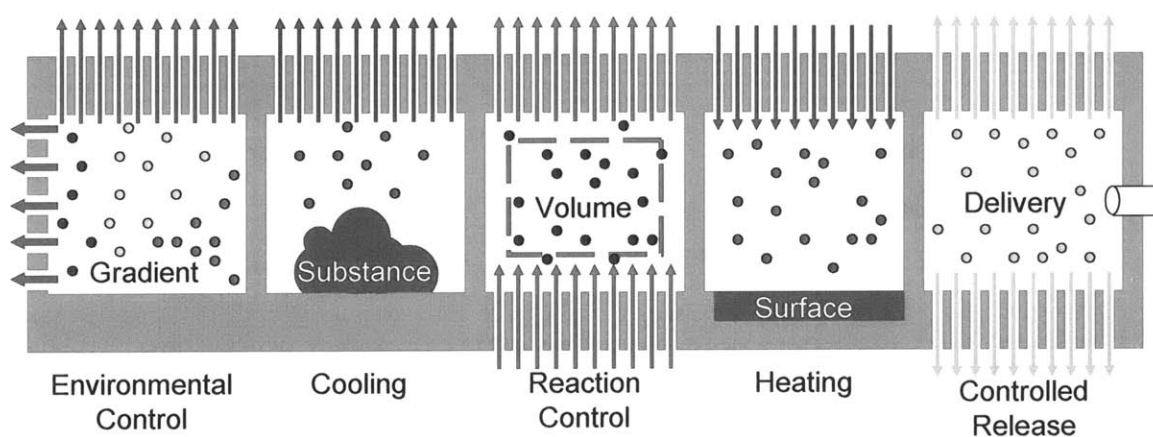
FIGURE 7.4: A schematic representation of potential applications of overlays with tiny pores to control mass transfer. The figure illustrates several potential configuration and application combinations.

In addition to providing cooling for Soldiers in combat, garments of porous media could provide Soldiers and first responders simultaneous cooling and chemical/biological protection (e.g. chem-bio suits with pores or channels nano-engineered to allow water vapor escape while preventing influx of adverse substances). Simultaneous cooling and protection of thermally sensitive electronics from ballistic shock is an application for inanimate objects. Other examples include mechanical and thermal protection of enclosures designed to hold and preserve temperature- or humidity-sensitive specimens e.g., biological samples, works of art, archeological samples, perishable food, and the like during transit, storage, display, and/or use.

A related application would be maintenance of a specified partial pressure of a particular gaseous substance inside a porous container. By designing the porous walls of a container with the correct pore diameter to regulate the diffusion flux out of the container, the molecular concentration of a gaseous substance inside the container can be controlled. By manipulating the

rate of transport of vapor or liquid through the porous barrier, porous media can be used to adjust the concentration of vapor or liquid produced by an endothermic transformation (e.g., phase change, chemical reaction) in the vicinity of a substance (i.e., a surface, volume, or material) or process. In this manner a porous enclosure can be used to maintain, increase, or decrease the concentration of a particular chemical species within or at the substance. This approach would be useful to manipulate the rates and extents of phase changes and chemical reactions that consume or produce at least one fluid product.

Porous media can also be used in filtration and separation procedures, where pore size and shape as well as surface texture and surface functionality are separately or collectively adjusted to promote or impede chemical or physical processes, (i.e., nucleation and phase changes such as vaporization and condensation in flowing fluids within the nano-engineered channels).

7.4 Future Directions for This Research

The research and results presented in this thesis suggest four major avenues for continued study of heat and mass transport through porous membranes for surface cooling.

7.4.1 Enhanced Mass Transport and Cooling Beyond the Knudsen Minimum

As outlined in Section 7.2, one of the original hypotheses of this thesis was that enhanced mass transport observed experimentally by other researchers beyond the Knudsen minimum (roughly $Kn = 3$) could be harnessed to obtain enhanced cooling at small pore diameters. This enhancement might provide superior transport through an array of nano-pores as compared against an array of macro-pores of the same open area. Superior mass transport would provide better cooling of underlying surfaces.

The range of Knudsen Numbers studied in this thesis reached the Knudsen minimum regime, but did not achieve high enough Knudsen Number for enhanced transport to be observed. Future research should utilize membranes with smaller pores than the tiniest used here (39 nm) to ascertain whether enhanced mass transport and cooling can be realized at higher Knudsen Numbers. Track-etched membranes are available with pore widths down to 10 nm, [SPI (2007)] which will give $Kn \sim 10$. Critical dimensions on the straight-through pores in zeolites are typically 0.3 to 1.4 nm [Satterfield (1991), p. 228, Table 7.3], and anodized aluminum can self-assemble into straight-through channels 15 nm in diameter [Sadasivan, *et al.* (2005)] and potentially much smaller. The promise for zeolite and anodized aluminum to provide straight-

through pores with sub-nanometer diameter makes these materials very promising candidates for further study of vapor transport at high Knudsen Number at ambient pressure and temperature.

7.4.2 Confirm the Fractional Accomplished Cooling – Membrane Sherwood Number Relationship with Non-nano Pores

Equation 7.23 is a dimensionless expression that relates Fractional Accomplished Cooling to the membrane Sherwood Number. The predictive ability of this equation was demonstrated in this thesis by modulating membrane Sherwood Number utilizing thin membranes (6 – 141 μm) and a range of pore diameters from 14,400 nm down to 39 nm. However, because Equation 7.23 is dimensionless, the same Fractional Accomplished Cooling result should be obtained by varying membrane Sherwood Number over the identical range (0.05 to 5) through different means. For example, membrane thickness or porosity could be systematically varied to modulate mass transport resistance, or the membrane upstream mass transport resistance could be modulated using different head space heights. Note that the downstream mass transport resistance should not be varied because the derivation of Fractional Accomplished Cooling relies upon the assumption of constant convective heat transfer coefficient, h, on downstream membrane face. Changing the downstream boundary layer resistance between experiments (i.e., by changing the velocity of the sweep gas) would invalidate the assumption of constant h.

Varying the membrane Sherwood Number by modulating the membrane thickness (i.e. using a series of progressively thicker membranes) would allow more accurate measurement of the temperature gradient across the membrane and provide insight into how the thermal conductance of the membrane solid phase impacts cooling efficacy. Thicker membranes with the same membrane numbers used in this thesis (0.0001 – 1) would also allow accurate measurement of the Bowen Ratio [Lewis (1995)], the ratio of latent to conductive heat transport across the membrane. This research would also highlight how energy can be moved against a thermal gradient using a concentration gradient of the latent heat carrier in the direction opposed to the thermal gradient.

7.4.3 Input Power as a Variable Parameter in Fractional Accomplished Cooling

Experimental results reported in this thesis for HAMTA1 were all conducted at a constant heat input of 1350 W/m^2 while the results of HAMTA2 were all at a constant 400 W/m^2. However, Equation 7.16 and Equation 7.23 include input power among their variable parameters, suggesting that the relationship between Fractional Accomplished Cooling and membrane

Sherwood Number is not just a two-dimensional curve (Figures 7.2 and 7.3) but a three-dimensional surface containing as a principle variable input power (or dimensionless power, Λ, in the case of Equation 7.23).

Experimental studies are needed consisting of a spectrum of membrane Sherwood Numbers and a variety of input powers to confirm the validity of Equations 7.16 and 7.23 across various important ranges of principle variables important to engineering design $Sh_{L,membrane}$ and $\dot{Q}_{in}$.

7.4.4 Study Impacts of Pore Shape on Mass Transport and Cooling Efficacy

Section 7.1.1 illustrates a possible pore shape effect: non-circular pores in the Hytrel DuPont membranes may have caused reduced mass transport owing to rarefaction effects or blockage near the acute corners of these pores. However, the extent of transport retardation cannot be fully explained by the model presented in Section 7.1.1, and further study is necessary.

A particularly insightful study would fabricate a series of membranes of the same material with identical thickness and porosity and run experiments at 1 atmosphere pressure. The membrane pores of the various samples would run straight through normal to the external faces and have the same effective diameter (defined in Section 3.4). However, the pores of each sample would have a different cross-sectional shape (i.e. circles, ovals, squares, triangles, stars, etc.)

With circular pores as the baseline control case, pores of various other shapes could be studied for shape effects that modify the mass transport rate across the membrane. The changeover from the continuum diffusion regime into the transition diffusion regime could be utilized to great advantage by designing the pores with effective diameter of roughly 1.5 μm, right on the division between the two transport regimes. Any pore shape effect impeding mass flux would push the transport into the transition regime, magnifying the shape effect and making it very easy to detect with a simple weighing apparatus like HAMTA2.

8 Conclusions

To address the questions proposed in Chapter 1 of this thesis, two experimental apparatuses were developed to quantify latent heat flux rates and major mass transport mechanisms for surface cooling by evaporation of water vapor through nano-engineered porous membranes. These apparatuses reproduced practically relevant conditions to Soldiers operating in the desert: continuous depletion of cooling liquid (water), realistic heat loads, air space between the surface being cooled and the protective membrane (i.e., stand-off body armor), and latent heat absorption through non-boiling evaporation.

Both apparatus where thermally validated using a heat balance technique that compared transient to steady state performance. All steady-state thermal flows were accounted for in membrane transport mode to +12.4% to +3.3% for Heat and Mass Transfer Apparatus 1 (HAMTA1 – deep dish, Figure 4.1) and +8.5% to -5.2% for Heat and Mass Transfer Apparatus 2 (HAMTA2 – shallow dish, Figure 4.2). The experimentally measured thermal mass of these apparatuses agreed to better than 15% of the estimated values based on calculated thermal masses of individual components. The experimentally determined convection coefficients for both experiments were within the accepted range for forced convective cooling with air, $10 - 200$ w/m^2-K [Mills (1999a), p. 22].

Two kinds of porous membranes were studied: DuPont porous membranes and track-etched membranes. Both membrane types represented good heat and mass transport simulants for nano-truss (Section 3.1, Figure 3.1). Importantly, the availability of samples with nearly straight-through pores provided a unique opportunity to study transport process without the added complication of tortuosity. Tortuosity has been defined as the ratio of the bulk path length a molecule takes between two exterior faces of a barrier to the shortest distance between those faces [Yu and Li (2004)]. This parameter is often used as an empirical fitting coefficient to match experimental and model results for transport through membranes whose pores do not run straight through the sample or vary in cross-sectional area. Since all the samples studied herein had straight-through pores of constant cross-sectional area, tortuosity approached unity, and this parameter was assumed to be 1.

This thesis provides an important experimental study for designers of future protective systems that exploit porous materials for evaporative cooling. First, it was confirmed experimentally that a protective barrier material with pores in as small as 1 micron in diameter

did not adversely impact latent heat carrier transport rate owing to the onset of transition regime diffusion. Second, designers must also be conscious of internal and external boundary layer diffusion resistances that may manifest in their systems. If these resistances are much larger than the membrane mass transport resistance, the membrane's presence is inconsequential to mass transport processes. Finally, two key dimensionless parameters, the membrane Sherwood Number and the Fractional Accomplished Cooling were introduced herein and shown to be general metrics for evaluation of porous membrane mass transport and cooling efficacy. Theoretical correlations between these two terms were developed from first principles (Equations 7.16 and 7.23) as tools for engineering design to facilitate creation of future cooling systems based on latent heat transport through porous membranes.

In summary, the following ten major conclusions arise from the concepts, models, experiments, and analysis presented within this thesis:

1. In the range of larger pore diameters (Kn < 0.01 at 1 atmosphere), continuum expressions for the membrane diffusion coefficient provide an adequate mass transfer model. Mass transfer rate and cooling efficacy are therefore only affected by membrane porosity (void fraction) and thickness in this regime, not pore diameter. Boundary layers on either side of the membrane also impact mass transport and cooling efficacy in this regime, provided the membrane Sherwood Number is less than 0.1.

2. A pair of experimental research apparatuses were developed that enabled measurement of intrinsic diffusion coefficients of a practical working fluid (water vapor) for membranes with pore diameters from 14,400 nm to 39 nm under realistic environmental pressure, temperature, and heat load simulating desert conditions.

3. To detect the impact of porous membranes on heat- and mass-transfer for typical, practical applications, the transport resistance of the membrane must be an appreciable portion of the total resistance encountered by the diffusing species (at least 10% of the total for the apparatus). As the membrane resistance increases, the magnitude of error associated with the boundary layers becomes less significant in calculation of R_{mem}. Therefore, the experimental intrinsic diffusion

coefficient measurement becomes less uncertain as pore diameters decrease due to the associated increase in membrane mass transport resistance.

4. A transition regime correlation for Knudsen Number (rarefaction effects) on the diffusion coefficient of water vapor in air (Equation 2.10) predicts experimentally-observed membrane mass transport coefficients to between +10% and +35% on average for pore diameters between 60 nm and 400 nm (0.01 < Kn < 3). Pore tracks were observed running up to 24 degrees from normal with respect to the exterior membrane faces. The resulting increased diffusion distance reduces the transport coefficient by about 9.5%, which partially explains membrane under-performance. The Equation 2.10 prediction is 71% too high at 39 nm pore diameter (Kn ~ 5). Increased tortuosity in tiny pores owing to manufacturing processes may represent a partial cause for the apparent over prediction, but there is no firm explanation for this membrane underperformance.

5. In contrast to classical experimental studies where capillary ID was fixed and pressure was reduced to attain high Knudsen Number [Knudsen (1952)], in this research, Knudsen Number was systematically varied by changing pore diameter while pressure and temperature remained nearly constant. Therefore, the predictive ability of the transition diffusion regime equation (Equation 2.10) was confirmed using a unique approach to obtain Kn > 1.

6. Substantial Fractional Accomplished Cooling (up to 60% of the operational maximum) was demonstrated using the latent heat transport techniques developed in this research, despite relatively low membrane porosity with no attempt at optimization. The absolute magnitude of achieved surface cooling was at least 3.7 K for every pore diameter studied from 39 nm to 14,000 nm. In some cases the absolute magnitude of achieved surface exceeded 14.0 K.

7. Pore diameter did not significantly impact cooling efficacy in the range between 400 nm and 14,400 nm. Theory suggests that the threshold of measurable pore diameter impact should be just below 1 μm as the onset of rarified diffusion begins to reduce pore transport efficacy. However, as stated in (3), there is a second regime in which pore diameter does not significantly impact transport: when the mass transport resistance of the membrane is less than 10% of the total mass

transport resistance presented by the apparatus. This threshold is achieved at a pore diameter of 400 nm.

8. Consistent with the calculated Reynolds Number for flow over a smooth, flat plate under experimentally-imposed conditions, tracer studies demonstrated laminar flow over the membrane downstream face from the supply of heated, dry nitrogen for Heat and Mass Transfer Apparatus 2 (HAMTA2 – shallow dish). In Heat and Mass Transfer Apparatus 1 (HAMTA1 – deep dish), due to surface roughness and a gap between the insulation collar and membrane, empirical correlations were inadequate to estimate the mass transport efficacy of this boundary layer. Tracer studies showed that the flow over the membrane was turbulent, which led to use of a viscous sub-layer model to estimate mass transport associated with that boundary layer. In general, it is essential to tightly control the experimentally-imposed membrane upstream and downstream mass transfer resistances and the associated boundary layer flow regimes to obtain high-precision measurements of membrane mass transfer resistance.

9. Several non-labor-intensive techniques (gravimetric weighing and fold & mic) were proven to provide membrane porosity and thickness data consistent with more labor-intensive, technology-dependent techniques (porosimetry & SEM imaging).

10. Mass flux rates of water vapor through porous membranes measured via experiments highlighted in this thesis exceed human perspiration rates. Therefore, the validity of multi-functionality (evaporative cooling, mechanical energy absorption, and light-weight material) for human protection applications using nano-enabled components has been successfully demonstrated in a practically relevant bench-top prototype.

Appendix 1: Neglecting Transpiration, Stefan Flow, and Choked Flow

This section provides calculations demonstrating that Transpiration, Stefan Flow, and choked flow can be ignored as transport enriching or retarding mechanisms for the research within this thesis.

Transpiration

Thermal transpiration describes the pressure drop that develops across a capillary tube between two reservoirs at different temperatures. This phenomenon has been demonstrated experimentally in capillary tubes at very high Knudsen Numbers. It might provide an enhancement to transport of water vapor through the tiny pores studied in this thesis due to the temperature gradient imposed across the membrane. Karniadakis and Beskök [Karniadakis and Beskök (2002), pp. 139-141] integrate the velocity profile for pressure driven tube flow with transpiration to give a mass flow expression. However, their expression is incorrect due to an integration error. The correct mass flow formula is

$$\dot{m} = -\frac{d^3 P}{12\mu R_u T}\frac{dP}{dx}\left[1 + 6\frac{2-\sigma_v}{\sigma_v}\left(Kn - Kn^2\right)\right] + \frac{3\pi}{16}\frac{\mu d^2}{T}\frac{dT}{dx} \quad \text{(Equation A1.1)}$$

where d is the tube diameter, P is pressure, μ is the fluid dynamic viscosity, R_u is the universal gas constant, T is temperature, σ_v is the tangential momentum accommodation coefficient, Kn is the Knudsen Number, and x is the axial coordinate down the tube. The term on the far right hand side represents the transpiration component of the flow,

$$\dot{m} = \frac{3\pi}{16}\frac{\mu d^2}{T}\frac{dT}{dx} \quad \text{(Equation A1.2)}$$

By inputting characteristic values into Equation A1.2, the magnitude of thermal transpiration contribution to mass transport across the membrane can be estimated.

$$\dot{m} = \frac{3\pi}{16}\frac{18.43\times10^{-6}\frac{kg}{m\cdot s}\left(1\times10^{-6}m\right)^2}{330K}\frac{(360K - 300K)}{1.25\times10^{-4}m} = 7.9\times10^{-15}\frac{kg}{s}$$

Comparing this result against the minimum measured transport rate for the DuPont porous membranes, 4.62×10^{-7} kg/s, the impact of thermal transpiration on mass transport is at least eight orders of magnitude less than pure diffusion. Therefore, this mechanism can be ignored.

Stefan Flow

Stefan Flow is convective flow induced by diffusion, which occurs to some extent in every two-species diffusion process. This mechanism can be ignored if the diffusing component is very dilute, but it begins to dominate over pure diffusive transport as the molar concentration of the diffusing species becomes a significant portion of the mixture. Figure A1.1 provides a schematic representation of a single capillary pore separating a liquid reservoir from ambient and through which Stefan Flow is occurring.
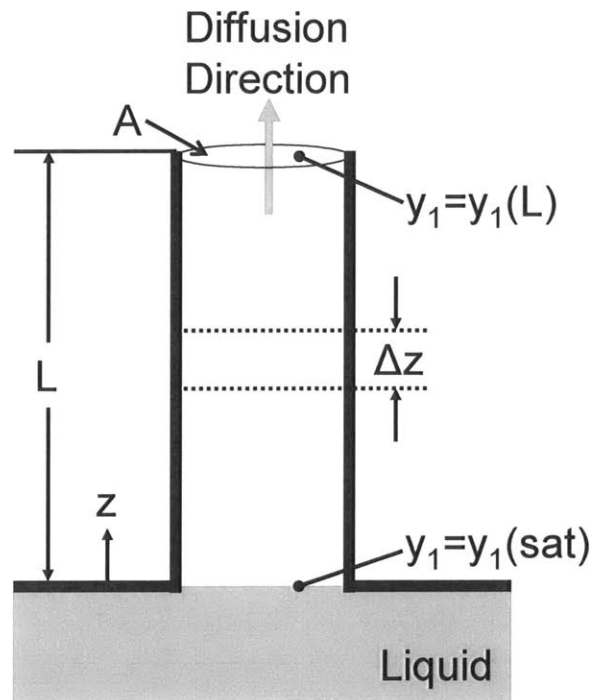
Figure A1.1: Schematic of a single capillary tube of length L through which Stefan Flow is occurring. *Figure adapted from original in Cussler [Cussler (1997)].*

Following the derivation provided by Cussler [Cussler (1997), p. 59] for the control volume defined by the capillary walls and the differential slice, Δz, the molar concentration balance is

$$\frac{\partial}{\partial t}\left(A\Delta z \cdot C_1\right) = Aw_1\big|_z - Aw_1\big|_{z+\Delta z} \qquad \text{(Equation A1.3)}$$

where w_1 is the molar flux of species 1 (the substance that exists as liquid at the bottom of the capillary [Figure A1.1]), A is the cross sectional area of the capillary tube, and C_1 is the molar

concentration of species 1. Dividing both sides by $A\Delta z$ and taking the limit as Δz approaches zero gives the expression

$$\frac{\partial C_1}{\partial t} = \frac{\partial w_1}{\partial z}$$ (Equation A1.4)

For steady-state operation, the molar concentration in the control volume remains unchanged. Incorporating steady-state operation into Equation A1.4 gives the governing equation for time-invariant molar flux in the capillary tube,

$$\frac{\partial w_1}{\partial z} = 0$$ (Equation A1.5)

Integrating Equation A1.5 gives the anticipated result that molecular flux of species 1 is constant and identical at all axial stations along the capillary tube.

Rate of molecular flux can be expressed as

$$w_1 = j_1 + C_1\left(C_1\overline{V}_1 v_1 + C_1\overline{V}_2 v_2\right)$$ (Equation A1.6)

where j_1 is the diffusion flux of species 1, $\overline{V}_i$ is the partial molar volume of species i, and v_i is the bulk velocity of species i. Fick's Law for diffusion provides and expression for j_1, the diffusion flux

$$j_1 = -D_{1,2}\frac{dC_1}{dz}$$ (Equation A1.7)

where $D_{1,2}$ is the diffusion coefficient for species 1 in species 2. By definition, $w_1 = C_1 v_1$ and $w_2 = C_2 V_2$. However, v_2 must equal zero because species 2 (the host gas within the capillary) cannot penetrate into the liquid water, and therefore its bulk velocity must remain zero. Under these additional considerations Equation A1.6 becomes

$$w_1 = -D_{1,2}\frac{dC_1}{dz} + C_1\overline{V}_1 w_1$$ (Equation A1.8)

Assuming that the evaporating species (species 1) behaves as an ideal gas in the vapor phase

$$C_1\overline{V}_1 = C_1\frac{R_u T}{P} = \frac{C_1}{C} = y_1$$ (Equation A1.9)

where R_u is the universal gas constant, T is temperature, P is pressure, C is the total concentration (species 1 and species 2 combined), and y_1 is the mole fraction of species 1. Combining Equation A1.9 with Equation A1.8 gives

$$w_1 = -D_{1,2} \frac{dy_1 C}{dz} + y_1 w_1 \qquad \text{or} \qquad w_1(1 - y_1) = -D_{1,2} C \frac{dy_1}{dz} \qquad \text{(Equation A1.10)}$$

This expression is the differential equation describing transport through the capillary tube. The boundary condition on Equation A1.10 is the mole fraction of species 1 at z = 0. In Figure A1.1 $y_1(z=0) = y_{sat}$. However, in the experimental apparatuses, the mole fraction is determined by the partial pressure of water vapor at the entrance of the membrane. This quantity is estimated by the Clausius-Clapeyron relation and Ideal Gas Law based on measured membrane temperature, T_2. Integrating Equation A1.10 once, manipulating with some algebra, and utilizing the boundary condition gives

$$w_{1,total} = \frac{D_{1,2} C}{L} \ln\left[\frac{1 - y_1(L)}{1 - y_1(0)}\right] \qquad \text{(Equation A1.11)}$$

This expression for the total flux of species 1 (including diffusion and Stefan components, can be compared against the expression for pure diffusion to determine the magnitude of Stefan Flow contribution to the transport process. The pure diffusion expression in terms of molar flux is

$$w_{1,diffusion} = \frac{DC}{L}[y_1(0) - y_1(L)] \qquad \text{(Equation A1.12)}$$

Taking the ratio of Equation A1.11 to Equation A1.12 gives

$$\frac{w_{1,total}}{w_{1,diffusion}} = \frac{\left(\frac{D_{1,2} C}{L} \ln\left[\frac{1 - y_1(L)}{1 - y_1(0)}\right]\right)}{\frac{D_{1,2} C}{L}[y_1(0) - y_1(L)]} = \frac{\ln\left[\frac{1 - y_1(L)}{1 - y_1(0)}\right]}{[y_1(0) - y_1(L)]} \qquad \text{(Equation A1.13)}$$

To bound the Equation A1.13 expression, it was assumed that $y_1(L) = 0$ due to the sweep gas on the downstream membrane face (which presumes the mass transport resistance in the boundary layer on the external membrane face is zero). At the membrane inlet, the largest possible $y_1(0)$ value encountered in the research in this thesis was about 0.219, based on a membrane temperature of 67 °C (340 K) for the DuPont porous membranes running on HAMTA1. For the track-etched membranes running on HAMTA2, the largest possible $y_1(0)$ value was about 0.075, based on a membrane temperature of 40 °C (313 K).

For the DuPont porous membranes, $\ln\left[\frac{1-0}{1-0.219}\right]\Big/[0.219 - 0] = 1.129$ was the largest possible total transport-to-diffusion transport ratio. For the track-etched membranes, the largest possible

transport-to-diffusion ratio was $\ln\left[\dfrac{1-0}{1-0.075}\right]\bigg/[0.075-0] = 1.039$. Thus up to a 12.9% and 3.9%

increase in transport rate may have occurred for the DuPont and track-etched membranes respectively owing to convection. Since these values represented upper bounds and small increases over the transport rates for pure diffusion, the engineering approximation was made to ignore Stefan Flow for modeling in this thesis.

Choked Flow

The upper rate at which fluid can flow through an orifice is when the velocity of the flow at the orifice choke point reaches the speed of sound in that fluid, a. This condition is called choked flow. If flow velocities through membrane pores approached choked flow conditions, the rate of mass transport would be limited. The pressure gradient across the membrane required to induce sonic velocity in the pores is obtained from the definition of the speed of sound:

$$a = \frac{\partial P}{\partial \rho}\bigg|_{s} \qquad \text{(Equation A1.14)}$$

From the definition of isentropic processes

$$P = F\rho^{\gamma} \qquad \text{(Equation A1.15)}$$

where F is a constant and γ is the ratio of specific heats ($\gamma = C_p/C_v$). Using Equation A1.15 in Equation A1.14 gives

$$\frac{\partial P}{\partial \rho}\bigg|_{s} = \gamma \cdot F\rho^{\gamma-1} = \gamma \cdot F\rho^{\gamma}\rho^{-1} = \gamma \cdot \frac{F\rho^{\gamma}}{\rho} = \gamma \cdot \frac{P}{\rho} \qquad \text{(Equation A1.16)}$$

From the Ideal Gas Law, $P = \rho R_u T$,

$$\frac{\partial P}{\partial \rho}\bigg|_{s} = \gamma \frac{\rho R_u T}{\rho} = \gamma R_u T = a^2 \qquad \text{and} \qquad a = \sqrt{\gamma R_u T} \qquad \text{(Equation A1.17)}$$

For isentropic flow between two stations (1 and 2) along a flow channel,

$$\frac{P_1}{\rho_1^{\gamma}} = \frac{P_2}{\rho_2^{\gamma}} \qquad \text{(Equation A1.18)}$$

Applying the Ideal Gas Law,

$$\frac{P_1 P_2^{\gamma}}{R^{\gamma}T_2^{\gamma}} = \frac{P_2 P_1^{\gamma}}{R^{\gamma}T_1^{\gamma}} \rightarrow \frac{P_1 P_2^{\gamma}}{T_2^{\gamma}} = \frac{P_2 P_1^{\gamma}}{T_1^{\gamma}} \qquad \text{(Equation A1.19)}$$

giving the classical relationship for isentropic flows

$$\left(\frac{P_1}{P_2}\right)^{\gamma-1} = \left(\frac{T_1}{T_2}\right)^{\gamma} \qquad \text{or} \qquad \frac{P_1}{P_2} = \left(\frac{T_1}{T_2}\right)^{\frac{\gamma}{\gamma-1}} \qquad \text{(Equation A1.20)}$$

The exponent in Equation A1.7 can be expressed as

$$\frac{\gamma}{\gamma-1} = \frac{C_p}{R_u} \qquad \text{(Equation A1.21)}$$

and the internal energy of the flow at Station 2 is a function of its temperature

$$C_p T_2 = \frac{\gamma R_u T_2}{\gamma-1} \qquad \text{(Equation A1.22)}$$

Using the definition of the speed of sound obtained in Equation A1.17 in Equation A1.22 gives

$$C_p T_2 = \frac{a^2}{\gamma-1} \qquad \text{and} \qquad C_p = \frac{a^2}{T_2(\gamma-1)} \qquad \text{(Equation A1.23)}$$

The total energy of the flow at Station 2 is the sum of the internal energy and the flow energy

$$C_p T_{2,total} = C_p T_2 + \frac{U_2^2}{2} \qquad \text{and} \qquad T_{2,total} = T_2 + \frac{U_2^2}{2 \cdot C_p} \qquad \text{(Equation A1.24)}$$

where U_2 is the flow velocity at Station 2. Using the definition of C_p from Equation A1.23,

$$T_{2,total} = T_2 + \frac{U_2^2}{2 \cdot \dfrac{a^2}{T_2(\gamma-1)}} = T_2 + \frac{U_2^2 \cdot T_2 \cdot (\gamma-1)}{2 \cdot a^2} = T_2 + Ma_2^2 \frac{T_2 \cdot (\gamma-1)}{2} \qquad \text{(Equation A1.25)}$$

where Ma_2 is the Mach number at Station 2. Since no energy is added to the flow between Station 1 and Station 2

$$T_2\left[1 + Ma_2^2 \frac{(\gamma-1)}{2}\right] = T_{2,total} = T_{1,total} = T_1\left[1 + Ma_2^2 \frac{(\gamma-1)}{2}\right] \qquad \text{(Equation A1.26)}$$

However, within the evaporation chamber, the flow has no bulk velocity. So, $T_{1,total} = T_1$. If the flow is choked (sonic) at Station 2, $Ma_2 = 1$. Station 2 can be at any axial location along a membrane pore channel

$$T_1 = T_2\left[\frac{(\gamma+1)}{2}\right] \qquad \text{(Equation A1.27)}$$

Using Equation A1.27 in Equation A1.20 gives and expression for the pressure ratio required to attain sonic velocity within the membrane pore

154

$$\frac{P_1}{P_2} = \left(\frac{2}{\gamma+1}\right)^{\frac{\gamma}{\gamma-1}}$$

(Equation A1.28)

Approximating $\gamma = 1.4$ (which is the value typically used for air), Equation A1.28 required

$$\frac{P_1}{P_2} = \left(\frac{2}{2.4}\right)^{3.5} = 0.5283 \qquad \text{or} \qquad \frac{P_2}{P_1} = \left(\frac{2}{2.4}\right)^{-3.5} = 1.893$$

Thus, the pressure inside the evaporation chamber must exceed the ambient pressure by at least 1.893 times before conditions exist that may induce choked flow. This result is a lower bound on required pressure ratio because it assumes isentropic (lossless) flow through the membrane pores. Owing to the small pore diameter and large Reynolds Number within the pores, viscous losses will dissipate energy from the flow, forcing a much higher pressure ratio than calculated to attain sonic velocity in the pores.

The Clausius-Clapeyron relation can be used to estimate the water vapor pressure inside the evaporation chamber based on the highest measured temperature for a porous membrane experiment in this thesis, 67 °C (about 340 K).

$$P \approx P_1 \cdot e^{-\frac{\Delta H_{fg}}{R}\left(\frac{1}{T_1} - \frac{1}{T_{boil}}\right)}$$

(Equation A1.29)

Summing this vapor pressure with atmospheric pressure gives the maximum total pressure obtained in the evaporation chamber, 129,697 Pa. The ratio of this pressure to atmospheric pressure is 1.28, which is short of the 1.893 minimum bounding pressure ratio required to achieve choked (sonic) flow in the pores. Therefore, the flow across the membrane through the pores was never choked during experiments, and choked flow can be ignored as a retarding mechanism to transport.

Appendix 2: Contact Angle Measurements

As illustrated by the inspirational model of camel fur for evaporative cooling (Section 1.9), control of the liquid-vapor evaporation front within pores is critical for optimal cooling efficacy. Wicking of liquid through membrane pores must be avoided to assure evaporation occurs behind the protective thermal resistance of the membrane. A head space air gap was employed to prevent wicking in both experimental apparatuses described in this thesis; this gap separated the liquid water charge from the membranes. However, liquid condensation on the membranes was observed in HAMTA1. Condensation was a necessary side effect of the buoyancy-driven convection mechanism in the head space that kept the evaporation chamber operating at steady state despite depletion of water. In HAMTA2, no liquid water could condense on the membrane due to the intentional temperature gradient design within the evaporation chamber.

Section 5.5 describes experimental evidence indicating that no liquid water condensing on the upstream membrane face was able to wick through the pores to the downstream face. This behavior was indirectly confirmed by measuring the contact angles of liquid water in air on samples of the DuPont porous membranes. These measurements showed the DuPont membranes to be slightly hydrophobic, which is consistent with the observation that the liquid water did not enter the membrane pores via wicking in HAMTA1. Contact angles of liquid water in air on the track-etched polycarbonate membranes used on HAMTA2 were also measured. These membranes, in general, were hydrophilic. All contact angle data is given in Table A2.1. Contact angles for a porous Teflon membrane were also taken as a control measurement. Teflon is known to be very hydrophobic, which was confirmed by these measurements.

Importantly, all of the samples listed in Table A2.1 were porous (with the exception of one non-porous polycarbonate membrane from Goodfellow), and the pores were filled with air during the contact angle measurements. The porosity of these samples certainly interfered with the liquid-membrane contact and probably resulted in measurements departing from the true contact angle for the bulk materials. Nonetheless, nonporous samples of DuPont Nucrel® and Hytrel® were not available for contact angle testing.

156

Table A2.1: Contact angles of liquid water in air measured on various porous and non-porous membrane samples. The DuPont porous membranes were slightly hydrophobic while the polycarbonate track-etched membranes were (in general) hydrophilic.

Material	Pore size	Manufacturer	Advancing Contact Angle	Receding Contact Angle
[ ]	[µm]	[ ]	[degrees]	[degrees]
Nucrel®	1	DuPont	95.5 ± 0.1	87.2 ± 1.4
Hytrel®	10	DuPont	93.9 ± 0.7	56.8 ± 2.2
Polycarbonate	N/A	Goodfellow	95.5 ± 0.4	88 ± 0.1
Polycarbonate	12	Millipore	70.9 ± 0.8	51.3 ± 0.1
Polycarbonate	1.2	Millipore	106.2 ± 0.3	108.2 ± 0.5
Polycarbonate	0.1	Millipore	55.4 ± 1.5	55.6 ± 0.4
Polycarbonate - PVPF	10	GE	105.6 ± 0.7	84.5 ± 0.7
Polycarbonate - PVPF	1	GE	94.5 ± 0.7	83.3 ± 0.2
Polycarbonate - PVPF	0.1	GE	86.9 ± 1.7	57.9 ± 1.3
Teflon	10	Millipore	141 ± 0.4	146.6 ± 0.4

The contact angle measurement apparatus, which belongs to the Rubner Laboratory at MIT, is pictured in Figure A2.1. This device was used to generate the data of Table A2.1. An example contact angle image is given in Figure A2.2. The apparatus includes a computerized image analysis tool that calculates the water droplet contact angle of a sample by fitting a partial circle to the outline of the drop and estimating the angle between the circle perimeter and the underlying surface at the triple contact point (see Figure A2.2).
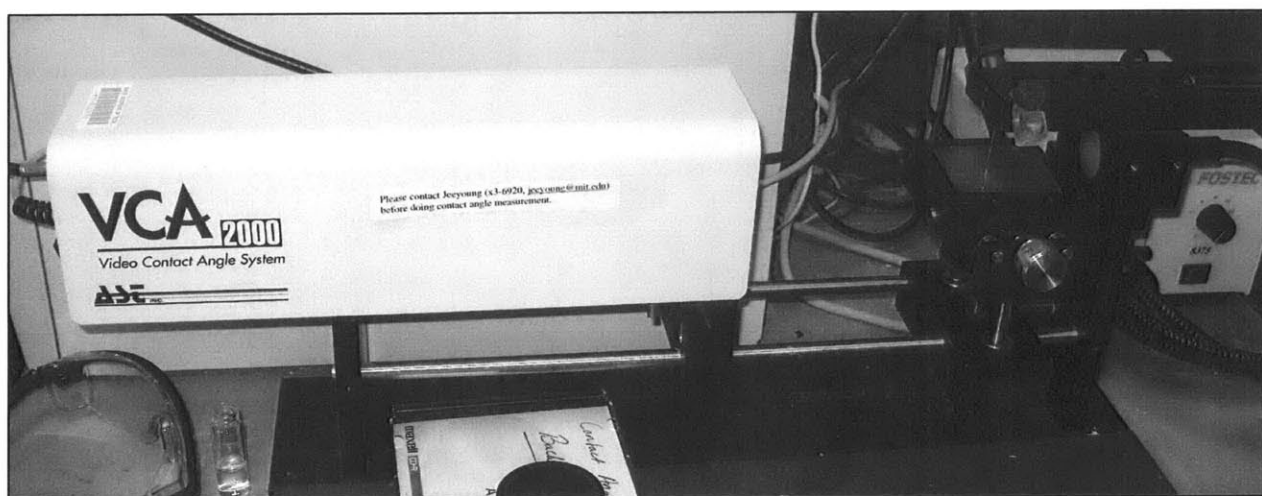
Figure A2.1: Contact angle measurement apparatus in the Rubner Laboratory at MIT.
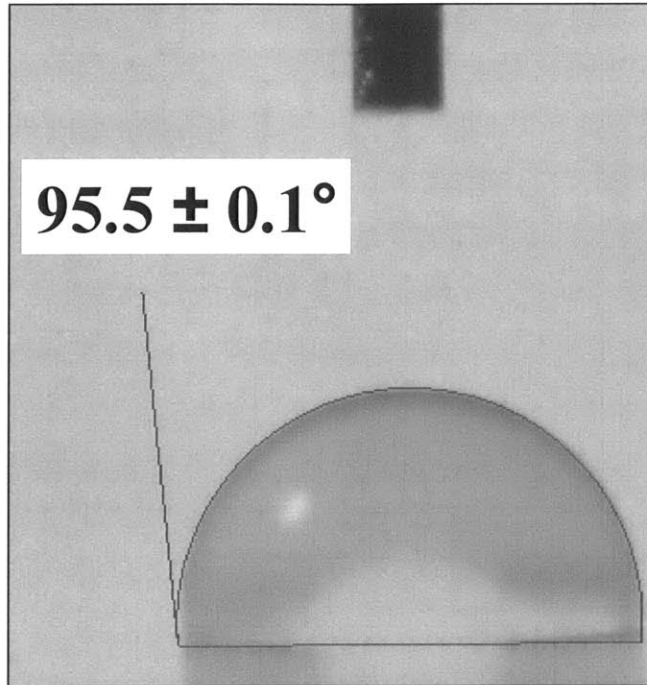
Figure A2.2: Measurement of contact angle for liquid water in air on porous Nucrel® membrane from DuPont. The nominal pore diameter of this sample was 1.0 µm.

Appendix 3: Down-selection of Candidate Cooling Techniques for Dismounted Soldiers

In Section 1.8, results of an analysis of several potential Soldier cooling approaches are presented. This appendix contains details of that analysis, leading to the result that evaporation of water from the Soldier system is the preferred way to effect cooling.

Several potential Soldier cooling techniques were brainstormed, and this list of candidate approaches was analyzed using the climate and loads of the design point: 50 °C ambient environment, 1000 w/m^2 insolation, and 350-400 w/m^2 metabolic heat generation. A skin temperature target of 37 °C (98.6 °F) was selected because this temperature can be comfortably endured by the human body. It was assumed that no metabolic regulation (no sweating) occurred unless the technique under scrutiny specifically enabled it. Convection was assumed to occur only from buoyant effects – no wind was blowing on the Soldier. Finally, it was assumed that the Soldier used no additional thermal management coping mechanisms (such as standing in the shade) to mitigate heat. This analysis therefore represented an upper bound on the heat load that the Soldier must dissipate to maintain comfortable thermal equilibrium. Under these assumptions, the following potential cooling techniques were analyzed: 1) Evaporating Perspiration, 2) Evaporation of Exotic Materials, 3) Cryogenic Thermal Energy Storage, 4) Cryogenic Thermal Energy Storage Plus Fuel, 5) Mechanical Refrigeration, 6) Super Insulators and Reflectors, and 7) Endothermic Chemical Reactions.

Each cooling approach was evaluated using five metrics: 1) was the approach physically possible, 2) what weight and bulk was required to meet 1 hour of peak heat load, 3) how much power was required for implementation 4) how easily could an approach be integrated into the Soldier battle suit and the Army supply chain, and 5) how amenable was the approach to improvements by nanotechnology research. Evaluations were applied in order. If an approach failed a test, the analysis was terminated, i.e., the remaining figures of merit were not applied. It was found that of the candidate cooling techniques, evaporating perspiration best met all of the metrics.

Evaporating Perspiration

At 1 liter per hour (1 kg/hr) the perspiring Soldier can mitigate almost half of the total peak heating load. At 2.25 liters per hour, which is within the realm of realistic peak perspiration rates [Schmidt-Nielsen (1979)], the entire heat load is mitigated. The only additional weight required to enable sweating is a porous material to transport the water vapor away from the Soldier or a

water-absorbing material to promote evaporation and collection. No additional mechanical weight is required. However to avoid serious or potentially fatal dehydration, the Soldier must have access to sufficient liquid water to timely replenish that lost by perspiration.

Water is already part of Army supply chain, and water can also be found in and utilized from the surrounding environment. To a limited extent, the Soldier can "store" excess water by super-hydrating himself before going on patrol, and excess water can be easily carried in simple containers. However, if water is carried as part of the logistic chain onboard the Soldier, this extra weight must be accounted for as a penalty for this approach. A further benefit of sweat-enhancing techniques is that the human perspiration rate is regulated by homeostatic mechanisms in the human body. Homeostasis is the ability or tendency of an organism or cell to maintain internal equilibrium by adjusting its physiological processes – sweating is a mammalian homeostatic mechanism to cope with increased heat to maintain constant body temperature. So long as the porous covering permitting water vapor to escape can handle any realistic human perspiration rate without saturation, no active control is required. The Soldier sweats just as much as is required to effect adequate cooling.

Given the substantial interest in the literature concerning enhanced transport of energy and mass through tiny structures, it is logical to consider means to exploit nano-engineering of structures to achieve efficacious cooling of the Soldier by evaporative cooling.

Evaporation of Exotic Materials

No materials currently exist that compare with water for its safety for human use and the amount of energy that it can absorb per unit weight when evaporated. Developing a comparable or better anthropogenic substitute (e.g., a "designer" latent heat transfer fluid) or discovering one in nature is beyond the scope of the present thesis, but in light of the encouraging findings of the current research, this approach does merit serious consideration for future work.

Cryogenic Thermal Energy Storage

Twelve kg of LN_2 or seven kg of solid CO_2 per hour would be required to affect adequate peak load cooling. A substantial additional weight penalty would be incurred for the storage of low-temperature liquid/solid in a Dewar. For example, one commercially available Dewar capable of holding 5.6 kg of liquid nitrogen (about 30 minutes of peak cooling) weighs 6.6 kg when empty [Tristan Technologies (2006)]. A heat exchanger would also be required to enable

160

cooling at 37 °C and keep the Soldier protected from cold burns. The total weight requirement of any inert cryogenic system would be too large to make it feasible.

Cryogenic Thermal Energy Storage Plus Fuel

The weight of liquid hydrogen required for one hour of peak load cooling, 1.1 kg, is superior to water. Once used for cooling, the H_2 could be routed into a fuel cell to generate electricity. Thus, this concept would receive additional credit for the eliminated weight of batteries and other energy sources. Nonetheless, safe storage of liquid hydrogen at 20.4 K would impose a severe weight penalty. For example, Bunger and Zittel [Bunger and Zittel (2001)] calculated that 5 kg of LH_2 (about 4.5 hours of peak cooling) could be safely stored with a container weighing 36 kg.

Hydrogen is not part of the current Army supply chain, and the Soldier would need to be re-supplied from a central source each time the hydrogen ran out. In addition, the cryogenic storage system would need to evaporate off hydrogen to maintain the supply reservoir at 20.4 K. Thus, for 24 to 72 hours of autonomous operation, the weight of such a system would be substantial. Chemically-bound hydrogen atoms are abundant on Earth, e.g., in water, but naturally occurring molecular hydrogen is rare and essentially un-harvestable, i.e., in volcanic emissions. Molecular hydrogen can be manufactured by various processes, but these are expensive and of relatively low efficiency in small scale systems. As a benchmark, the thermal efficiency of manufacturing molecular hydrogen in a large petroleum refinery by steam reforming natural gas, is roughly 62% including all parasitics [Gary and Handwerk (1984)]. The equipment required to compress and cool hydrogen to liquid in the field would be prohibitively heavy to carry.

Nano-enabled storage of hydrogen is an active field of scientific research and technology development. So, this concept would be amenable to a nano-science thesis. However, hydrogen also has safety challenges: wide flammability limits with air, a virtually invisible flame, and a very low Joule-Thompson inversion temperature. At room temperature, hydrogen heats up on expansion, creating potential for hydrogen jetting from a pin-hole leak to burst into flame. These safety issues demand great care in practical use of hydrogen and in its use in scientific research, even in small scale laboratory experiments.

Mechanical Refrigeration

Mechanical refrigeration is a well-developed technology. Ignoring the weight of the mechanical components, only 0.36 kg of battery weight is needed per hour to enable peak cooling (based on idealized COP). Thus, on a power-weight basis, mechanical refrigeration is the lightest of the cooling techniques examined. However, to provide substantial, efficient Soldier cooling, the mechanical weight would be prohibitive. For example, one commercially available portable refrigerator capable of cooling 15 liters of volume to 11 °C in 46 °C ambient conditions weighs 18.2 kg [Fridge Freeze (2007)].

The batteries required to run these coolers are part of the Army's supply chain. Nonetheless, there are several barriers to Soldier suit integration. First, conventional cooling cycles with moving parts would generate noise, making it difficult for Soldiers to hide their acoustic signatures from the enemy. Second, mechanical breakdowns of complex miniaturized refrigerators would be challenging to repair in the field and such could be exacerbated by adverse climate or terrain, e.g., the unusually fine sand encountered in Iraq. Third, some significant area of the Soldier uniform would be required to reject thermal energy at a higher temperature than the ambient environment. This rejection site would probably be hot enough to burn the soldier and would give off a significant thermal signature.

Conventional refrigeration cycles are well-developed and not conducive to nanotechnology research. More exotic Carnot-limited cooling techniques with nano-enabled components (e.g. thermoelectrics) are extensively studied, but these systems are less efficient than conventional refrigeration cycles. To be viable, these exotic systems would need to address the increased weight of batteries required to operate them.

Super Insulators and Reflectors

It would be relatively easy to incorporate insulators and reflectors into the Soldier uniform, with little or no added weight, to mitigate exposure to insolation and reduce the peak heating load requirement. The development of super-reflectors and super-insulating materials is also amenable to study for nanotechnology research. It is possible that the Soldier of the future will employ nano-enabled reflectors and insulators to reduce his or her heat load. Nonetheless, this approach fails to simultaneously address both the solar and metabolic loads. Insulation might worsen the accumulation of metabolic heat without synergistic integration of some other cooling

strategy. In addition, reflection of sunlight would create a large thermal and optical signature, which would need to be eliminated for this technique to be useful to the Soldier.

Endothermic Chemicals

Endothermic chemical reactions may be able to provide Soldier cooling with little additional weight. The chemicals would need to be safe to handle, and they would ideally generate a product of further use to the Soldier or function reversibly. The ideal endothermic reaction would be reversible at night (when the temperature dropped), enabling regeneration with no need for input power or re-supply. This combination of chemicals is not likely a part of the current Army supply chain and could probably not be easily obtained form the environment. Nanotechnology could be employed to control surface area to modulate the reaction rate or to develop and/or package new designer chemistries capable of endothermic reactions. While the Soldier of the future might employ endothermic chemical cooling in his battle suit, development of these chemicals is beyond the scope of this thesis.

Appendix 4: Triangular Pore Shape Effect Rarefaction Model

Equation 5.26 tended to over-predict the transport efficacy of the Hytrel® membranes, and it was hypothesized that over-prediction arose from a shape effect that retarded transport through the membrane pores;

$$\dot{m}_{ave} = \int_{r_o}^{r=0} \frac{2\pi \cdot r}{R_{BL,downstream} + R_{mem}} \left\{ \int_{r_o}^{r=0} \frac{1}{\delta(r)v(r)} \left[\frac{\rho_{chamber} - \rho(r)}{R_{BL,upstream}} - \frac{\rho(r)}{R_{mem} + R_{BL,downstream}} \right] dr - \rho_{ambient} \right\} dr \quad \text{(Eq. 5.26)}$$

The Hytrel® pores (Figure 3.4) were not cylindrical, but appeared as squished triangles whose corners were highly acute. A water molecule moving axially down the center of such a pore would have little wall interaction, and it would experience a low local Knudsen Number consistent with a pore diameter much greater than its mean free path. However, a water molecule in the vicinity of the pore corners would undergo frequent wall interactions, and it would therefore experience a relatively large local Knudsen Number. These crushed triangular pores therefore presented a larger mass transport resistance than would a perfectly circular pore with the same cross sectional area. Equation 5.26 included no correcting factors for pore shape; it assumed that pores have circular cross section.

To develop a simple representative model, an equilateral triangle was assumed as a characteristic membrane pore shape. The area of the characteristic triangular pore was estimated by averaging SEM image data of the pores in the membrane samples (see Section 3.4). This averaged pore area was 143.5 μm^2. As shown in Figure 7.1, a circular area was inscribed within the triangular pore and treated as a region far from the pore's corners with relatively low Knudsen Number. The area outside the circle within the corners was treated as the zone with relatively high Knudsen Number.

Applying geometry (Figure A4.1) to relate the circle diameter, d, to the triangle edge length, X, it was noted that three obtuse isosceles triangles (one is denoted in Figure A4.1 by dotted lines) with side length $\sqrt{3}X/2$ make up the area of the larger triangle. The height of the smaller obtuse isosceles triangle is d/2. Equating these areas provides a relationship between d and X:

$$\frac{3}{2}(d \cdot 2X) = \sqrt{3}X^2 \qquad \text{and} \qquad d = \frac{2\sqrt{3}}{3}X \qquad \text{(Equation A4.1)}$$
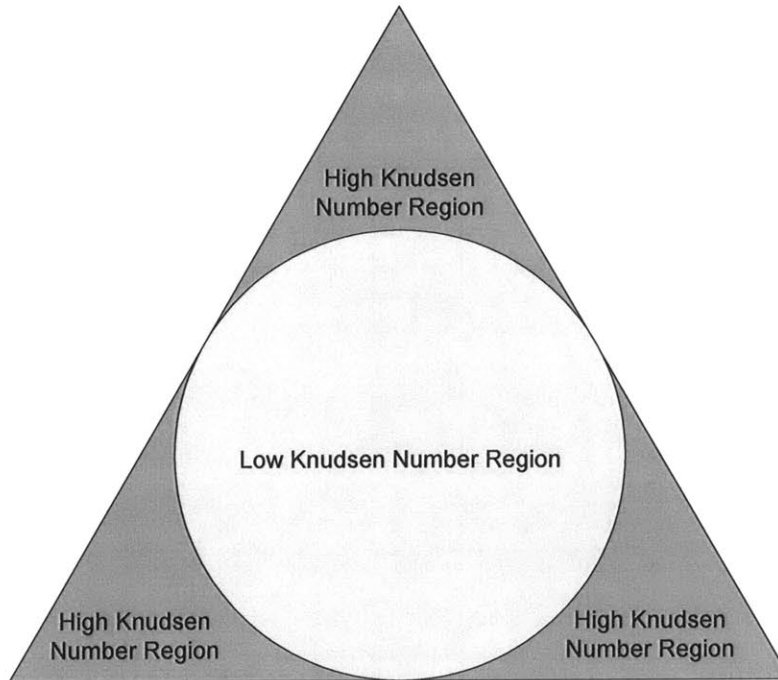
Figure 7.1: A schematic representation of a micron-scale pore with triangular cross section shows the presence of two dissimilar transport regions. Far from the corners in the center of the pore (light grey region), local Knudsen Number is low, facilitating continuum transport. However, near the corners (dark grey region), molecule-wall interactions are prevalent, and local Knudsen Number is high, retarding transport. Due to high local Knudsen Number regions, the overall transport rate of this pore will be less than a circular pore with the same total cross sectional area.

From the total triangular pore area, 143.5 μm^2, and Equation A4.1, X and d were calculated: X = 9.1 μm and d = 10.5 μm. Based on d, the inscribed circular area with relatively low Knudsen Number is 86.76 μm^2. The remaining area, 56.74 μm^2, was then broken up into three smaller circles, each with an area of 18.91 μm^2 and a diameter of 4.91 μm. This equivalent area arrangement is shown in Figure A4.2,

Equation 2.10 was then applied to the four channels in Figure A4.2, which have an area equivalent to the original characteristic triangular pore in Figure 7.1. The continuum regime diffusion coefficient for the temperature and pressure conditions encountered by the pores is about 2.45 x 10^{-5} m^2/s (from Equation 2.8). With correction for Knudsen Number, the 10.51 μm diameter pore in Figure A4.2 gives a 2.42 x 10^{-5} m^2/s diffusion coefficient while the 4.91 μm diameter pores in Figure A4.2 provides a 2.39 x 10^{-5} m^2/s diffusion coefficient.
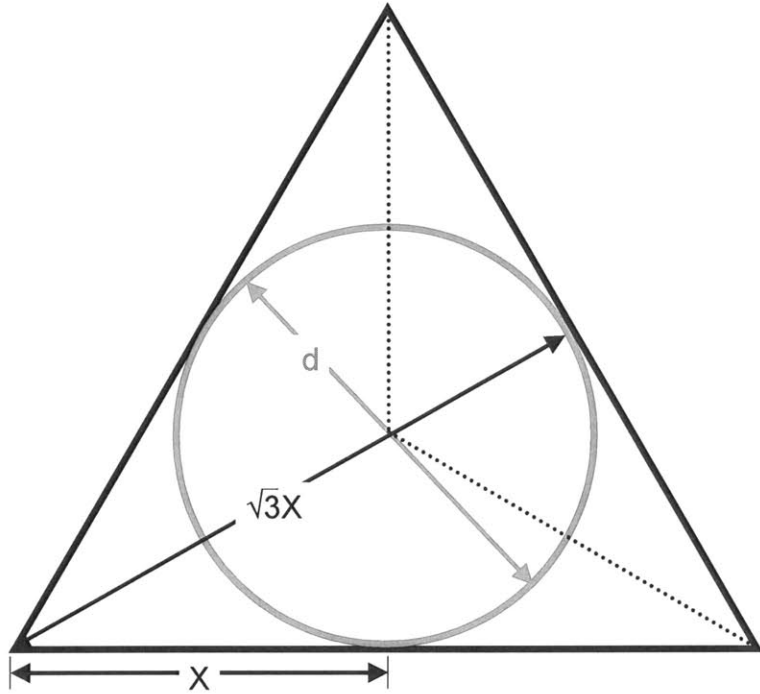
Figure A4.1: Pore with triangular cross section of side length 2X. Inscribed within this pore is a circular region with diameter d.
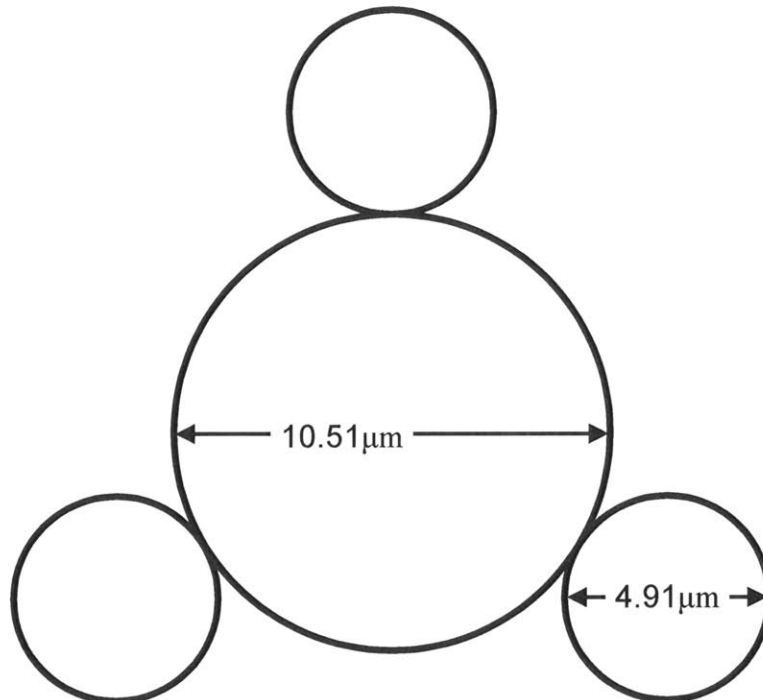
Figure A4.2: Rarefaction effects were estimated by modeling the triangular pore using four circular pores with the same combined total area as the triangle. One large central pore is surrounded be three smaller pores. The transition regime diffusion equation was applied to this arrangement to estimate a diffusion coefficient based on the pore shape effect.

To compare the total transport coefficient of the equivalent arrangement in Figure A4.2 to a circular pore with the same cross sectional area (and an effective diameter, d_e = 13.52 μm), the diffusion coefficients were weighted by the areas of their respective pores to determine an equivalent diffusion coefficient,

$$\frac{A_1 \cdot D_{H_2O,Air}\big|_{pore1} + A_2 \cdot D_{H_2O,Air}\big|_{pore2}}{A_{total}} = D_{H_2O,Air}\big|_{equivalent} \quad \text{(Equation A4.2)}$$

The resulting value, 2.41 x 10^{-5} m^2/s was about 1.7% less than the 2.45 x 10^{-5} m^2/s diffusion coefficient for a circular pore of the same area (d_e = 13.52 μm). This diffusion coefficient reduction mechanism does not account for the experimentally measured diffusion transport coefficient of about 1.68 x 10^{-5} m^2/s.

It was also found that if the corner area associated with larger Knudsen Number (i.e., about 39.5% of the total pore area) were completely blocked, the diffusion coefficient would appear to drop 40.2%, almost exactly the reduction measured experimentally. It is possible that liquid water condensed in the corners, was somehow held there, and prevented from rapid evaporation by surface effects. However, it is not clear whether the pore corners were truly blocked nor is there a mechanistic explanation for this blockage. So, it remains unclear why the Hytrel® experimental diffusion coefficient was so low.

Appendix 5: Experimental Data

Location of Original Data: research notebooks and original data, stored electronically, are archived at MIT.

The following figures show the temperature data from all the experiments conducted to complete this thesis.

Figures A4.1 through A4.8 represent temperature and weight data for Heat and Mass Transfer Apparatus 1 (HAMTA1) running in open chamber mode. Figures A4.9 through A4.16 represent temperature and weight data for HAMTA1 running in closed chamber mode. Figures A4.17 through A4.20 represent temperature and weight data for HAMTA1 running with DuPont Hytrel® porous membranes (d_e = 14.2 μm and 12.6 μm respectively). Figures A4.21 through A4.24 represent temperature and weight data for HAMTA1 running with DuPont Nucrel® porous membranes (d_e = 1.4 μm and 1.0 μm respectively).

Figures A4.25 through A4.28 represent temperature and weight data for Heat and Mass Transfer Apparatus 2 (HAMTA2) running in open chamber mode. Figures A4.29 through A4.32 represent temperature and weight data for HAMTA2 running in closed chamber mode. Figures A4.33 through A4.64 represent temperature and weight data for HAMTA2 running with various polycarbonate track-etched porous membranes ranging in pore diameter from 14,400 nm down to 39 nm.
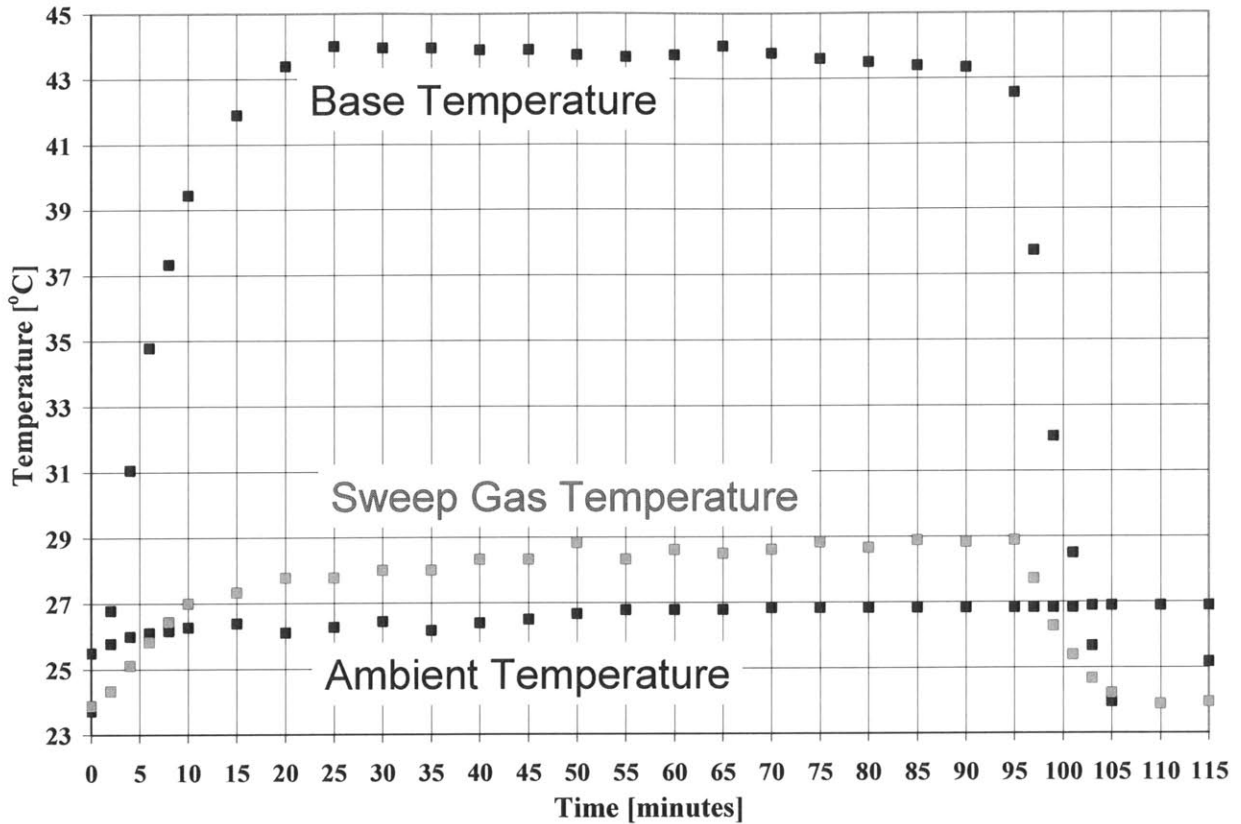
Figure A4.1: Temperature-time history for HAMTA1 running open chamber on 2006-01-20 (Run A).
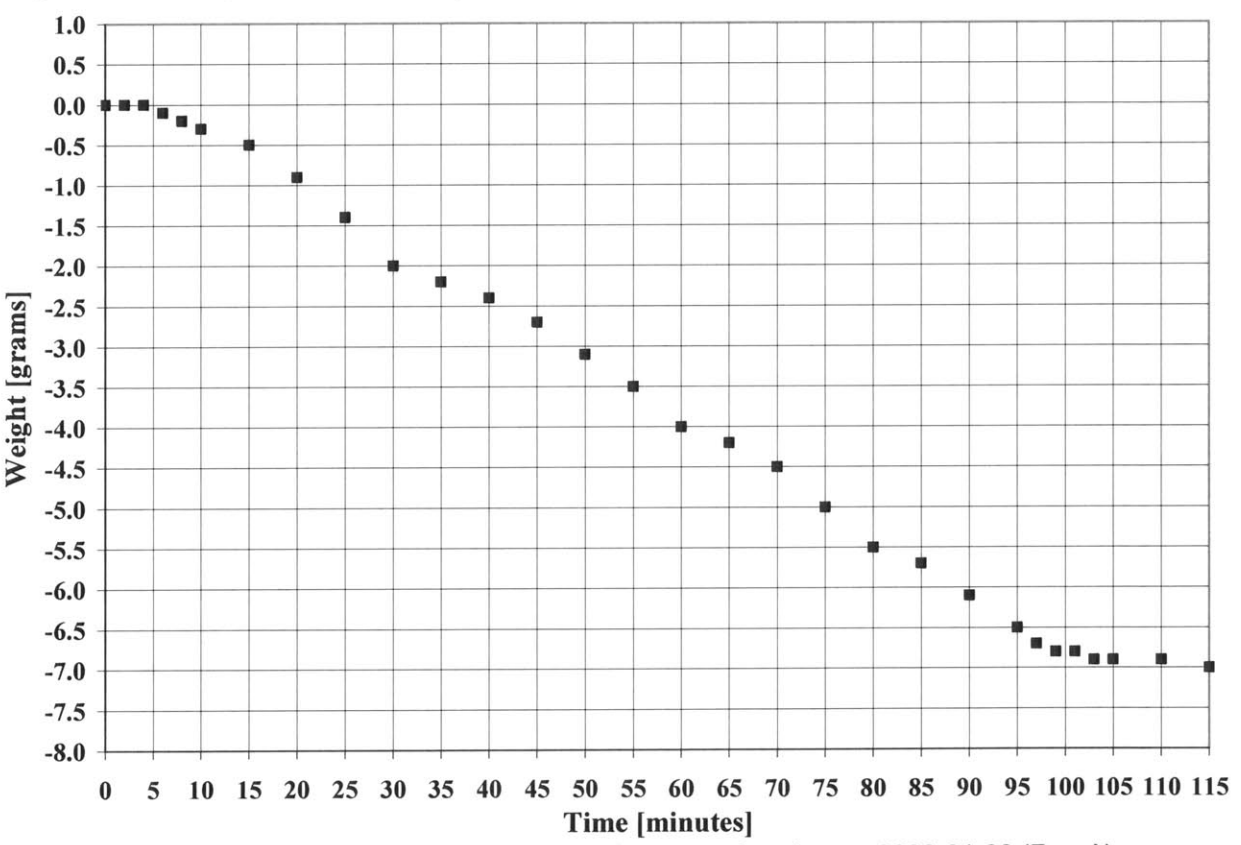
Figure A4.2: Weight-time history for HAMTA1 running open chamber on 2006-01-20 (Run A).

169
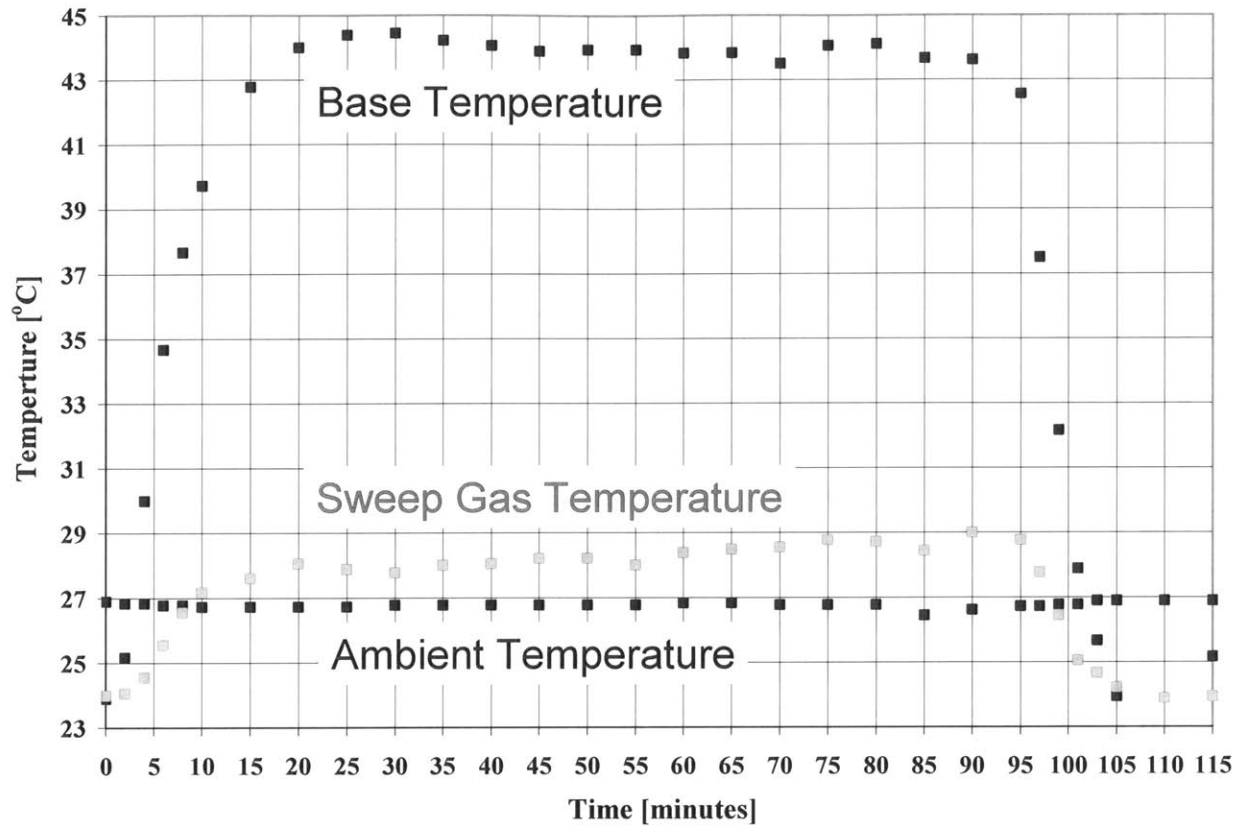
Figure A4.3: Temperature-time history for HAMTA1 running open chamber on 2006-01-20 (Run B).
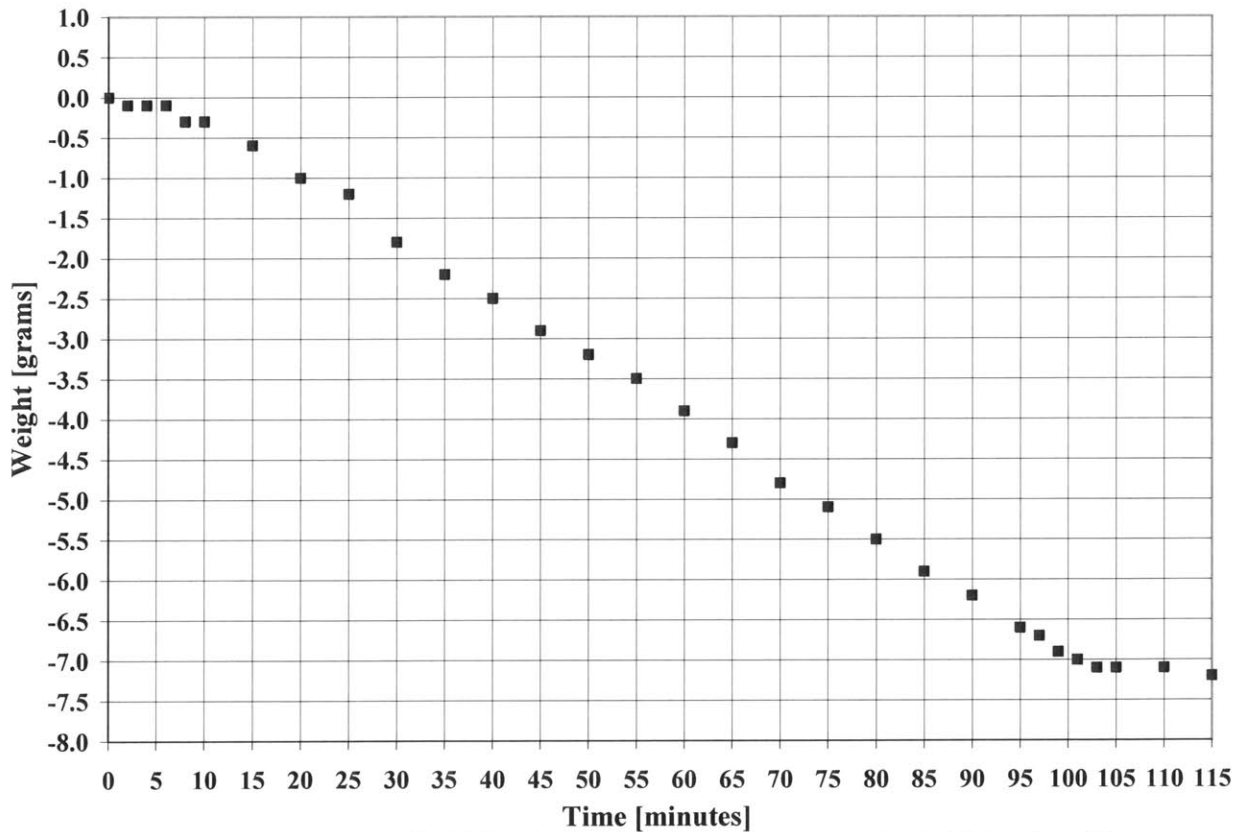
Figure A4.4: Weight-time history for HAMTA1 running open chamber on 2006-01-20 (Run B).
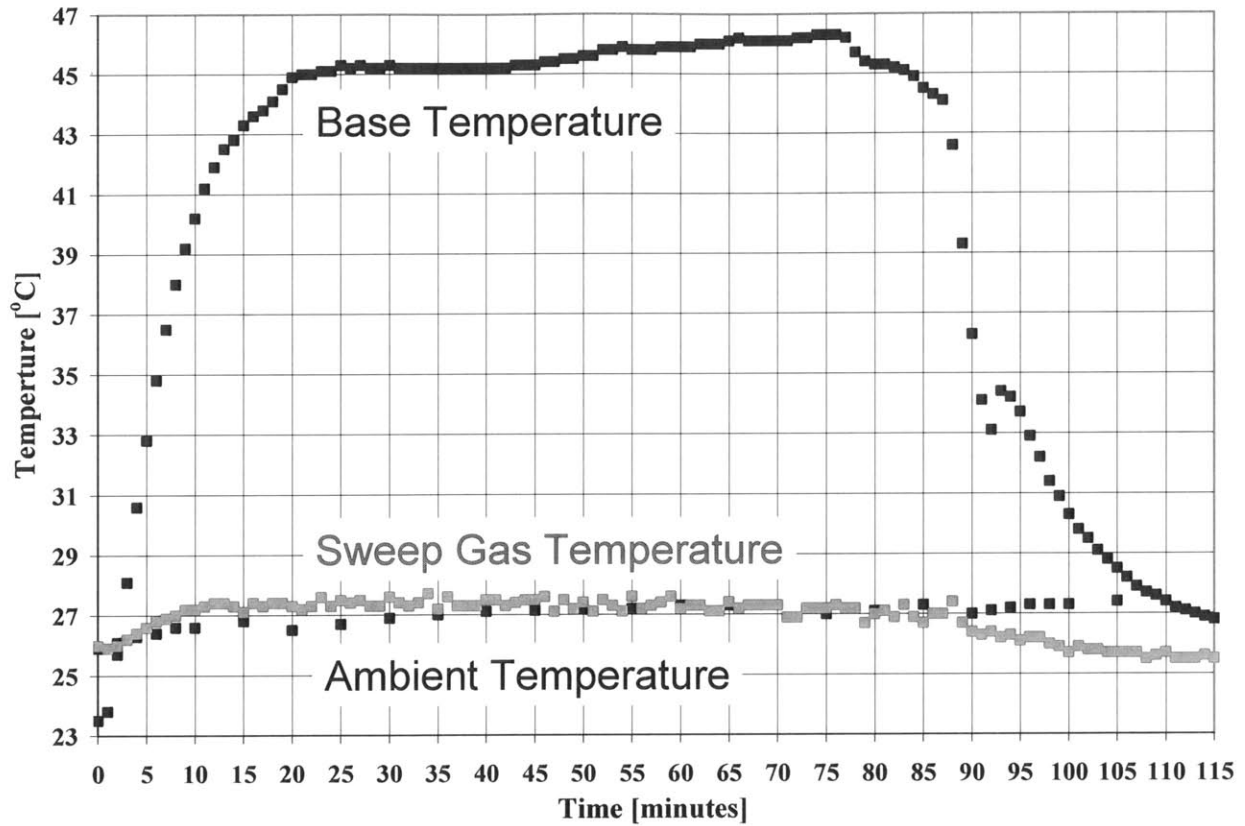
Figure A4.5: Temperature-time history for HAMTA1 running open chamber on 2006-01-28.
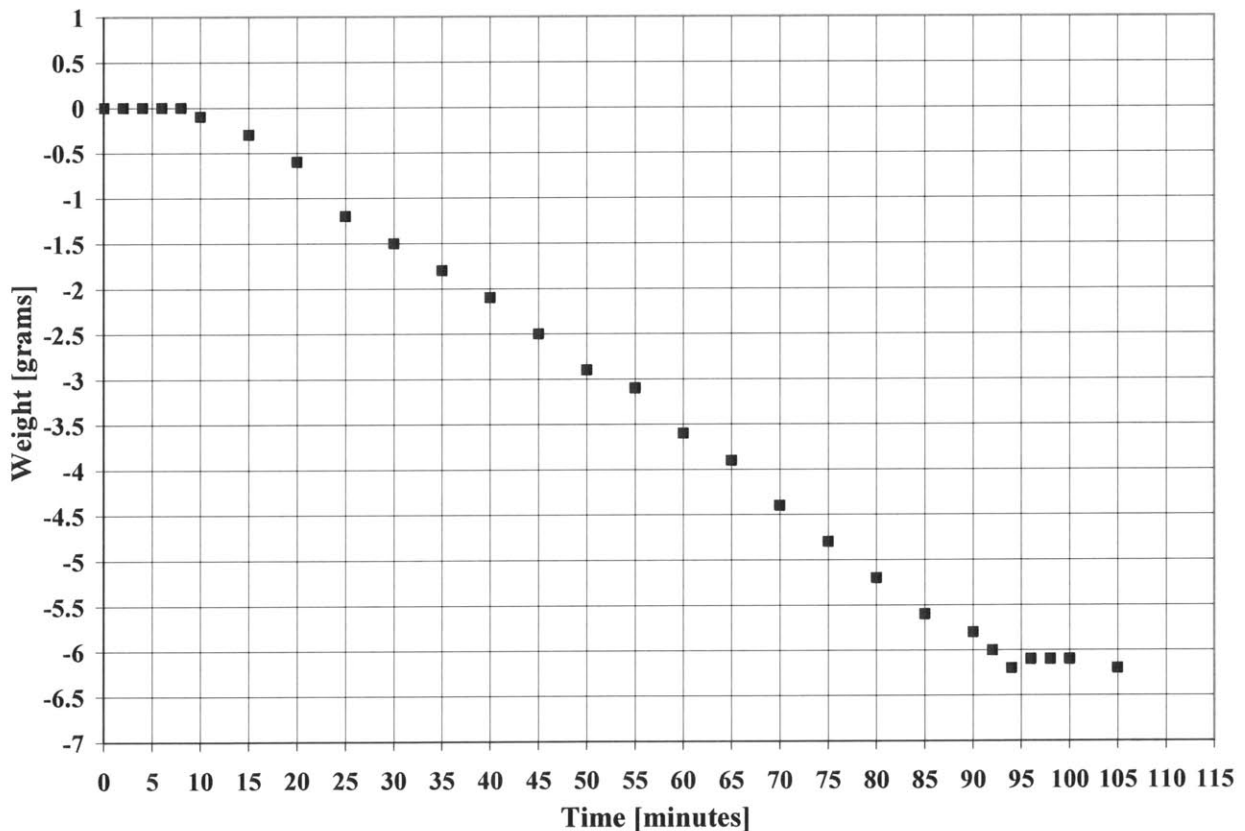
Figure A4.6: Weight-time history for HAMTA1 running open chamber on 2006-01-28.

171
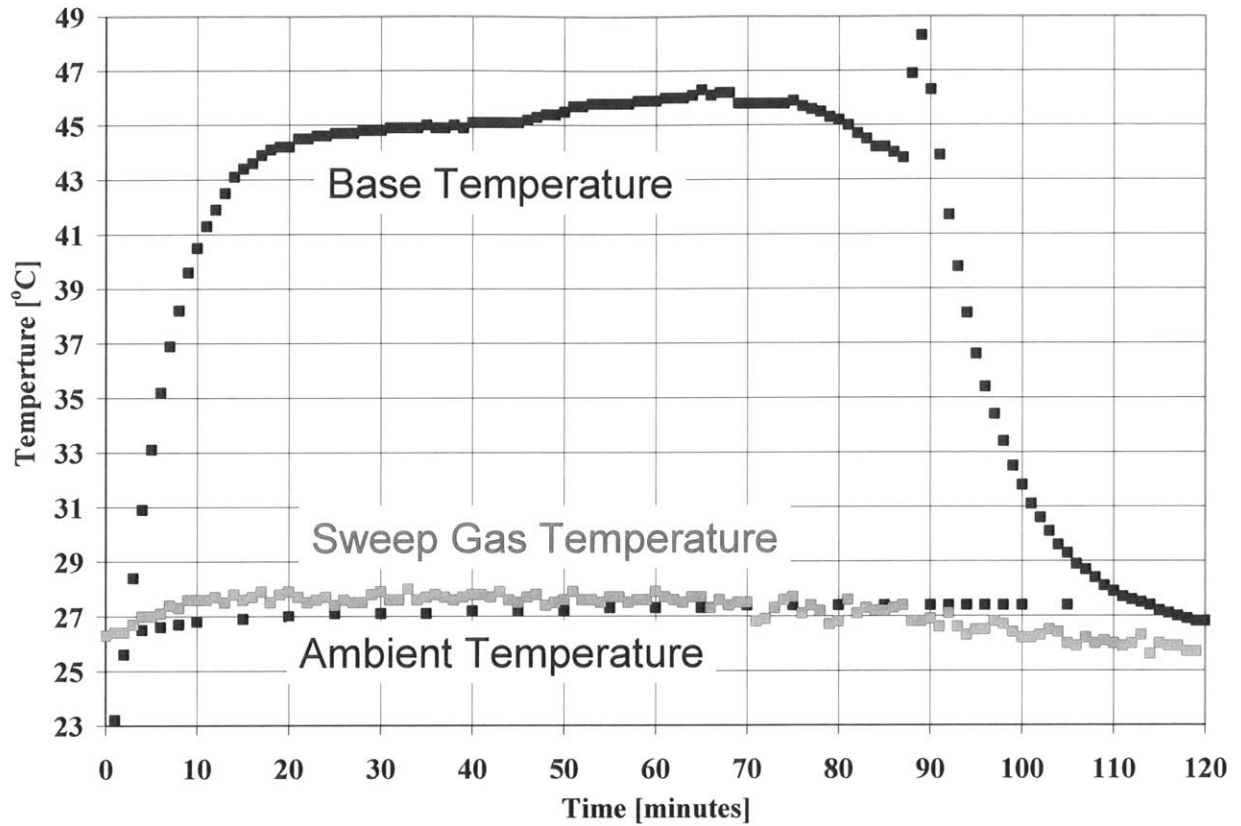
Figure A4.7: Temperature-time history for HAMTA1 running open chamber on 2006-01-29.
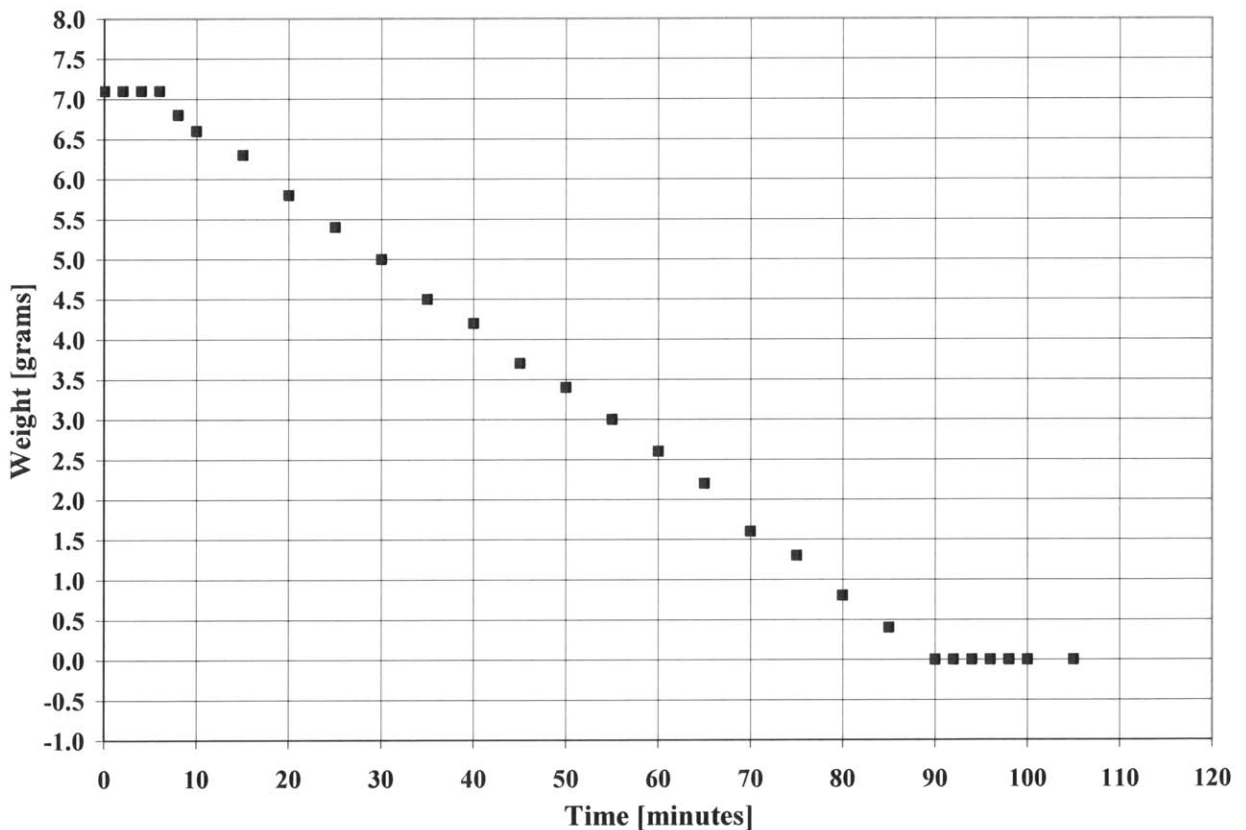
Figure A4.8: Weight-time history for HAMTA1 running open chamber on 2006-01-29.

172
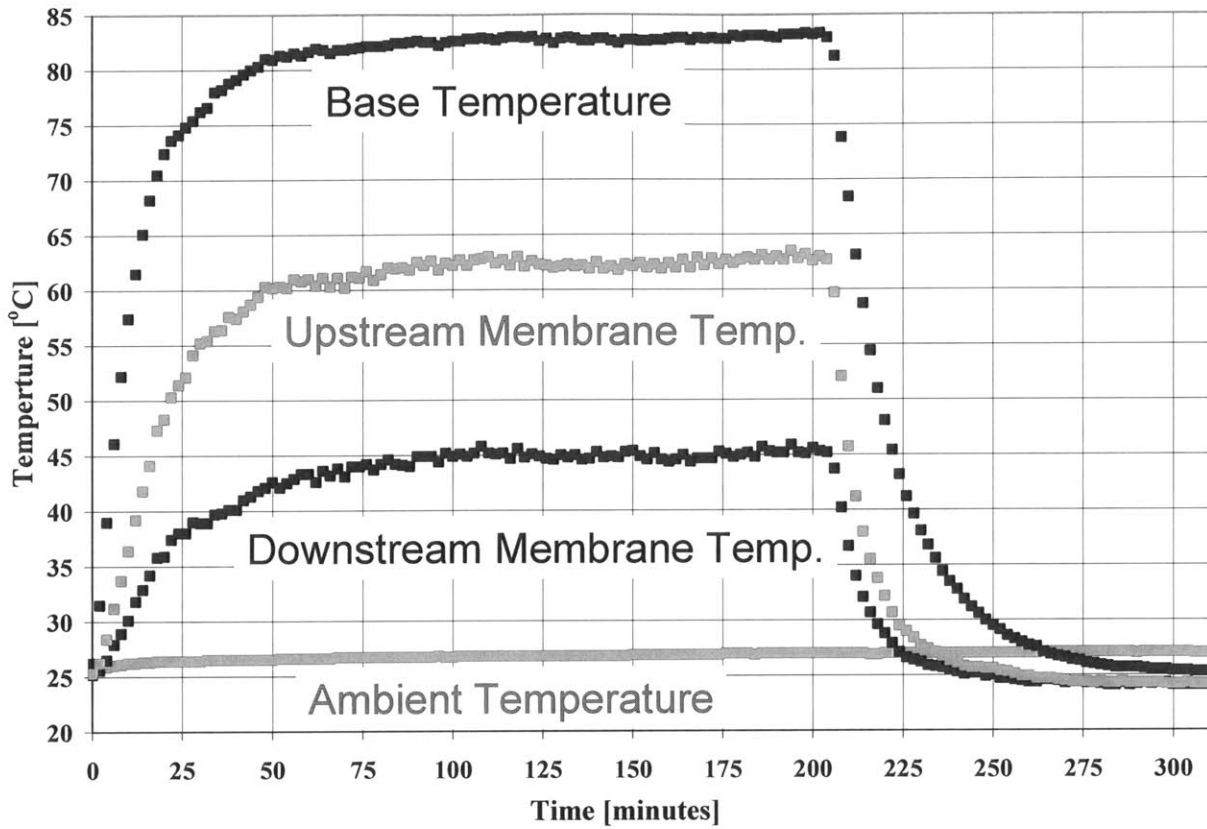
Figure A4.9: Temperature-time history for HAMTA1 running closed chamber on 2006-01-31.
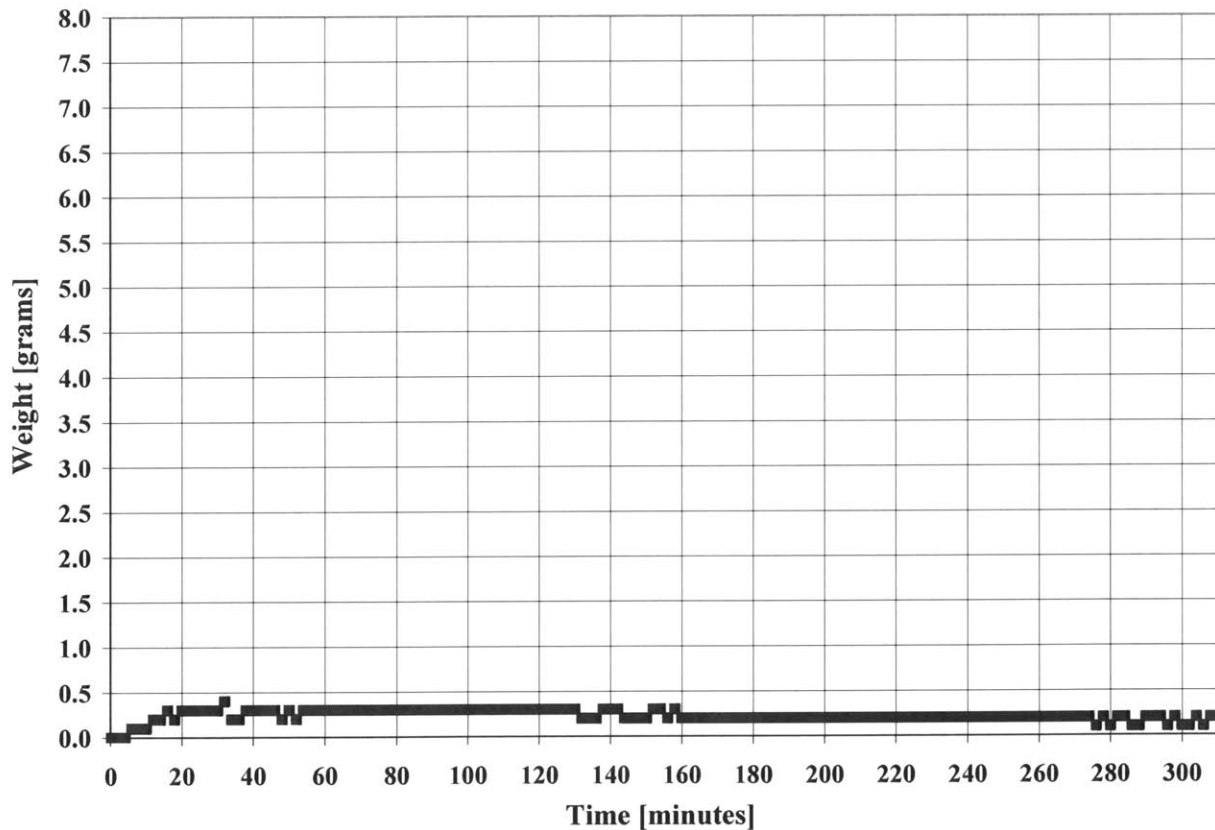
Figure A4.10: Weight-time history for HAMTA1 running closed chamber on 2006-01-31.

173
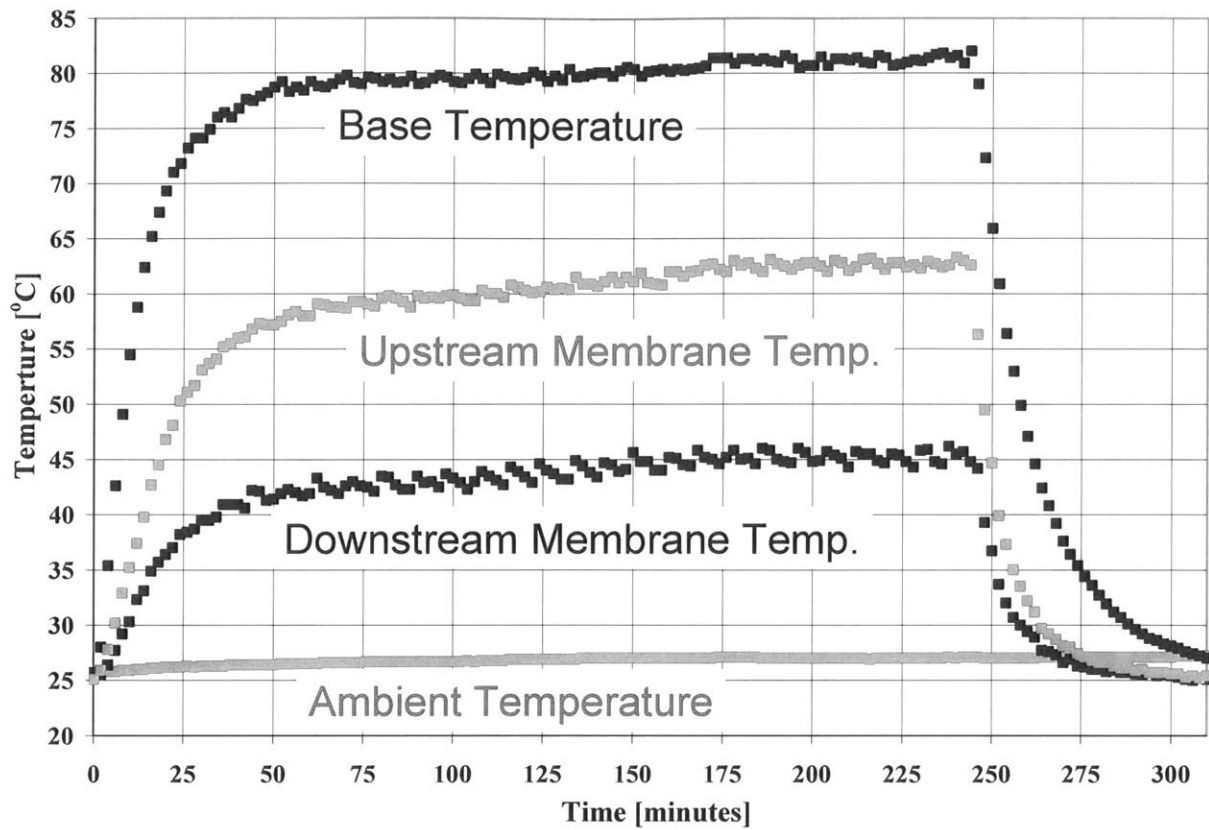
Figure A4.11: Temperature-time history for HAMTA1 running closed chamber on 2006-02-01.
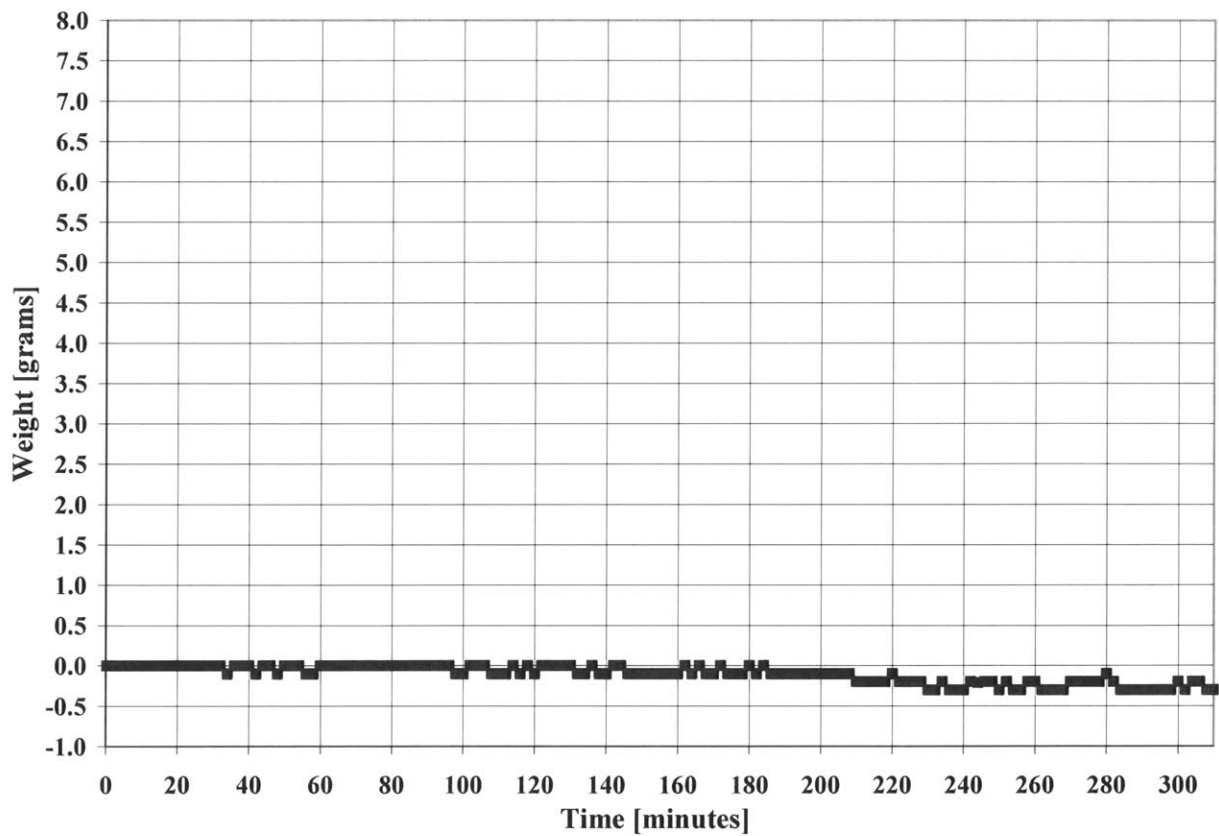
Figure A4.12: Weight-time history for HAMTA1 running closed chamber on 2006-02-01.

174
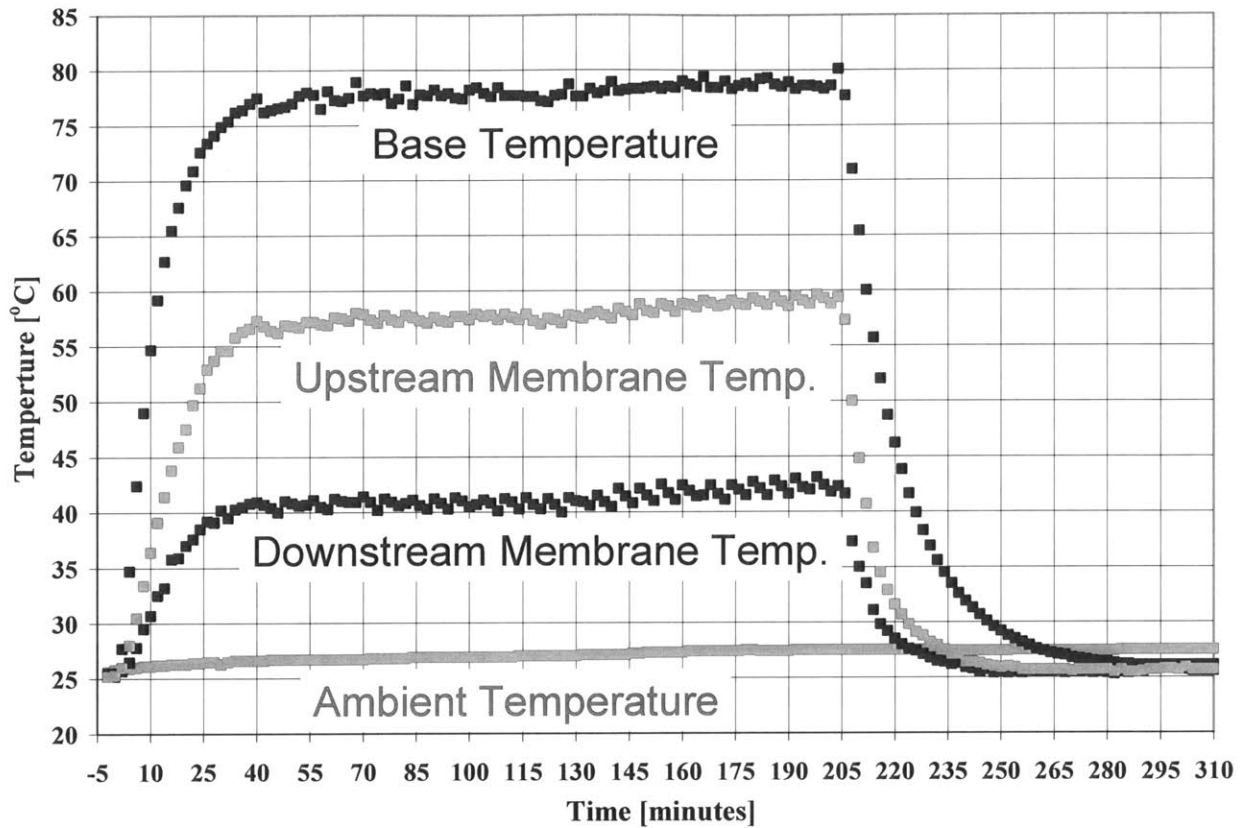
Figure A4.13: Temperature-time history for HAMTA1 running closed chamber on 2006-02-02 (Run A).
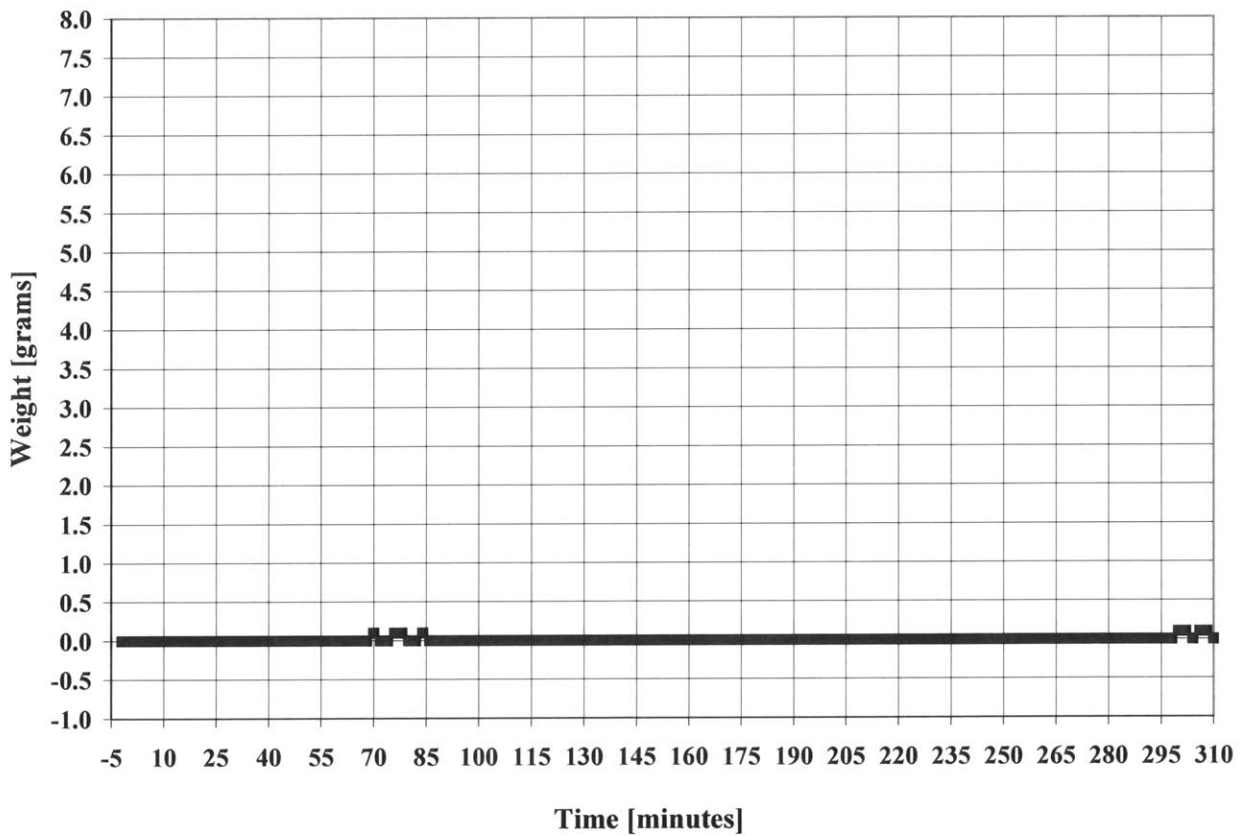
Figure A4.14: Weight-time history for HAMTA1 running closed chamber on 2006-02-02 (Run A).

175
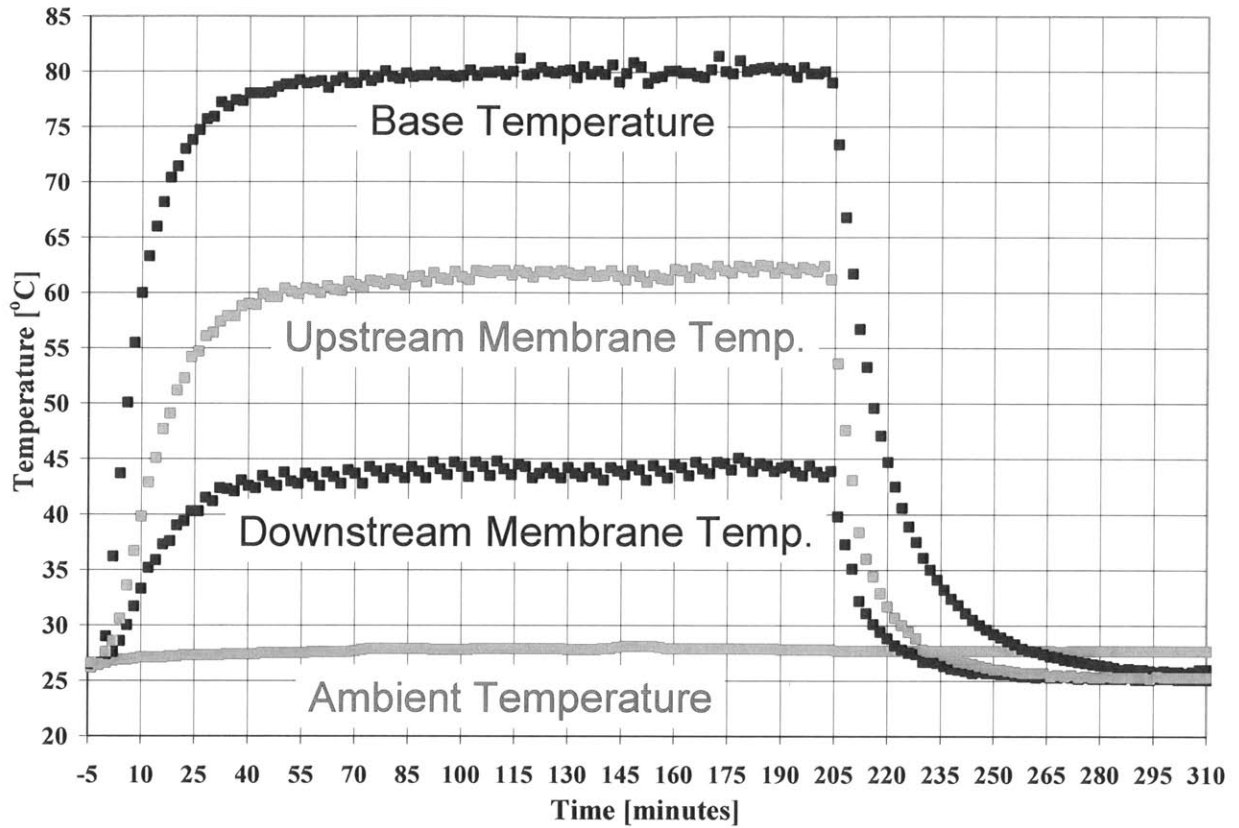
Figure A4.15: Temperature-time history for HAMTA1 running closed chamber on 2006-02-02 (Run B).
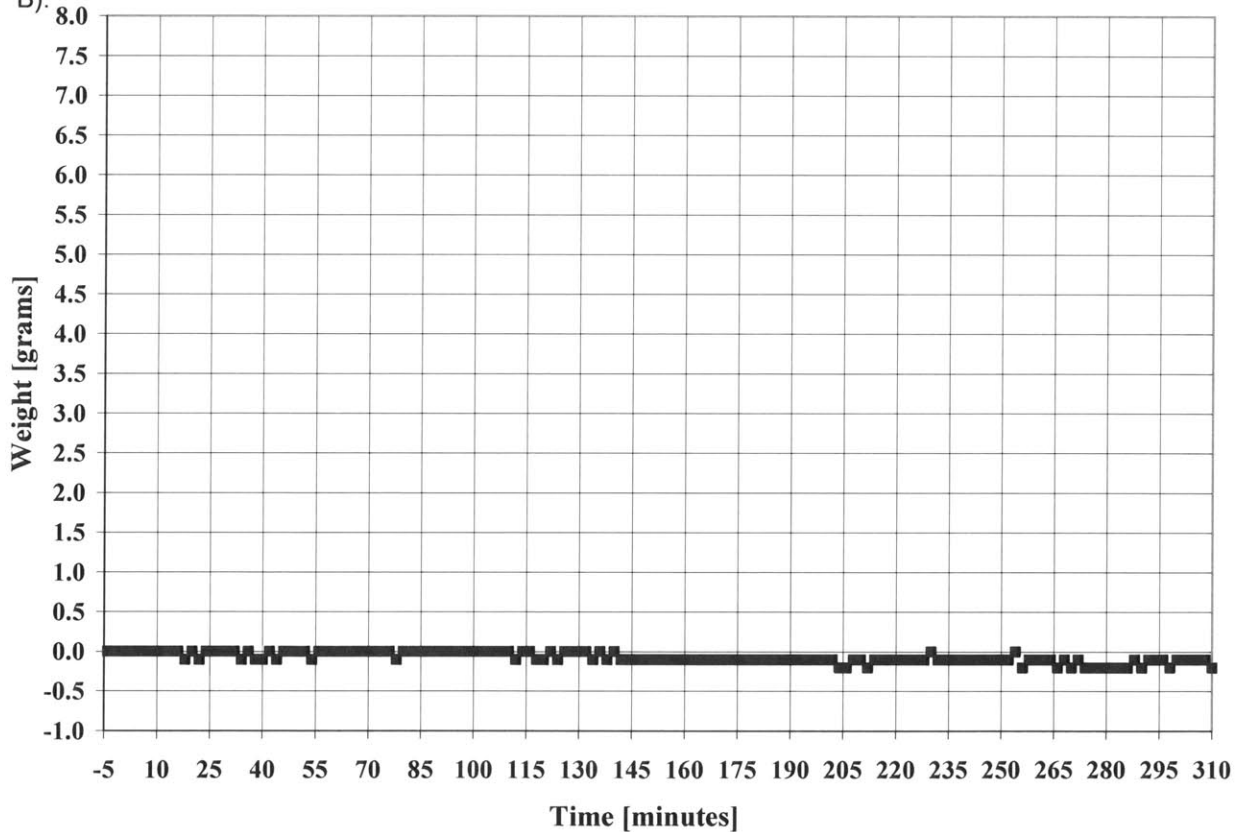
Figure A4.16: Weight-time history for HAMTA1 running closed chamber on 2006-02-02 (Run B).

176
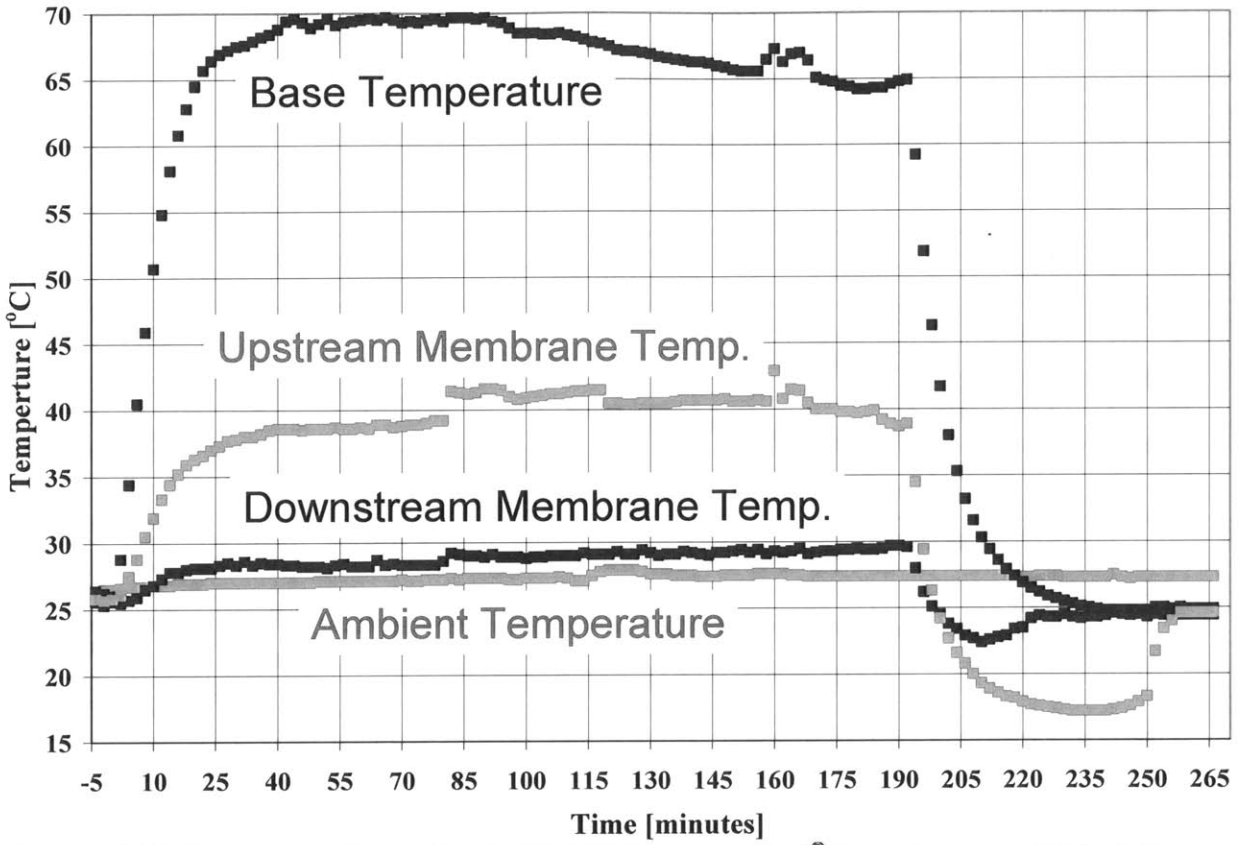
Figure A4.17: Temperature-time history for HAMTA1 running Hytrel® A membrane on 2006-02-05.
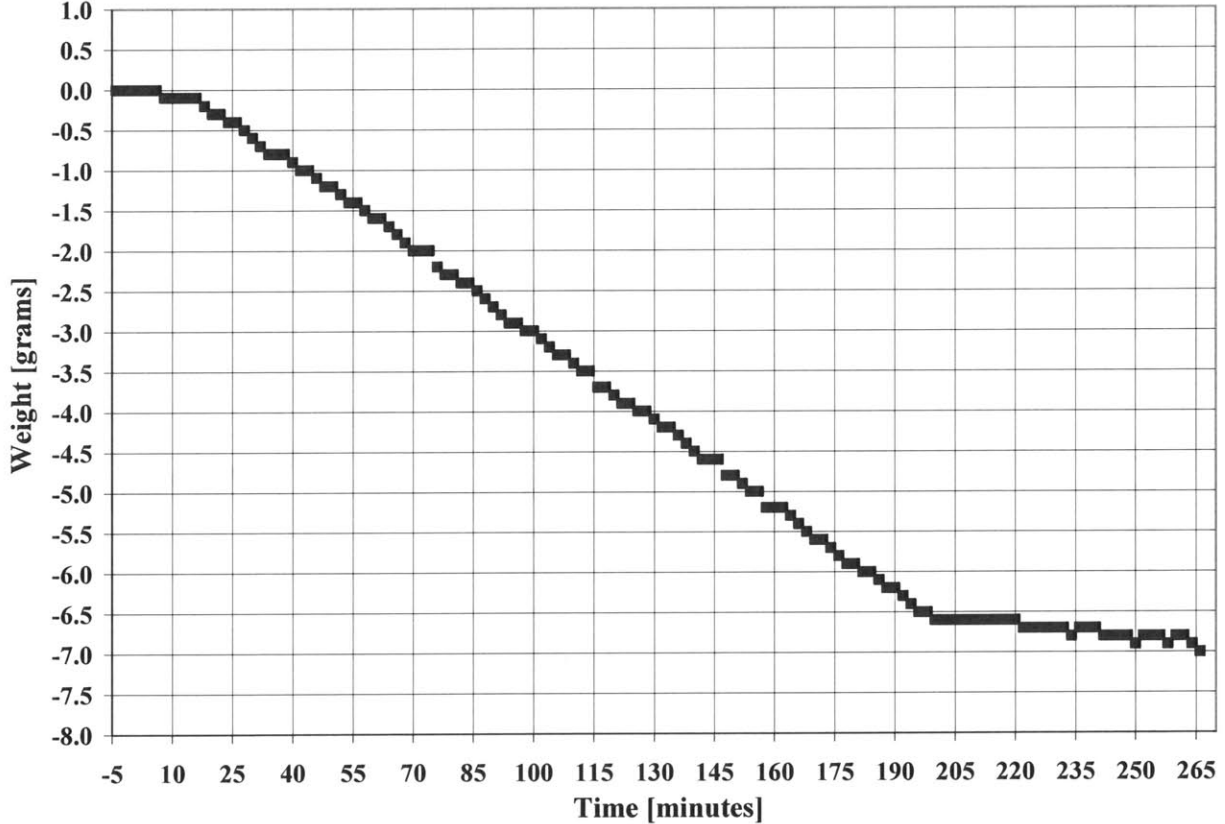
Figure A4.18: Weight-time history for HAMTA1 running Hytrel® A membrane on 2006-02-05.

177
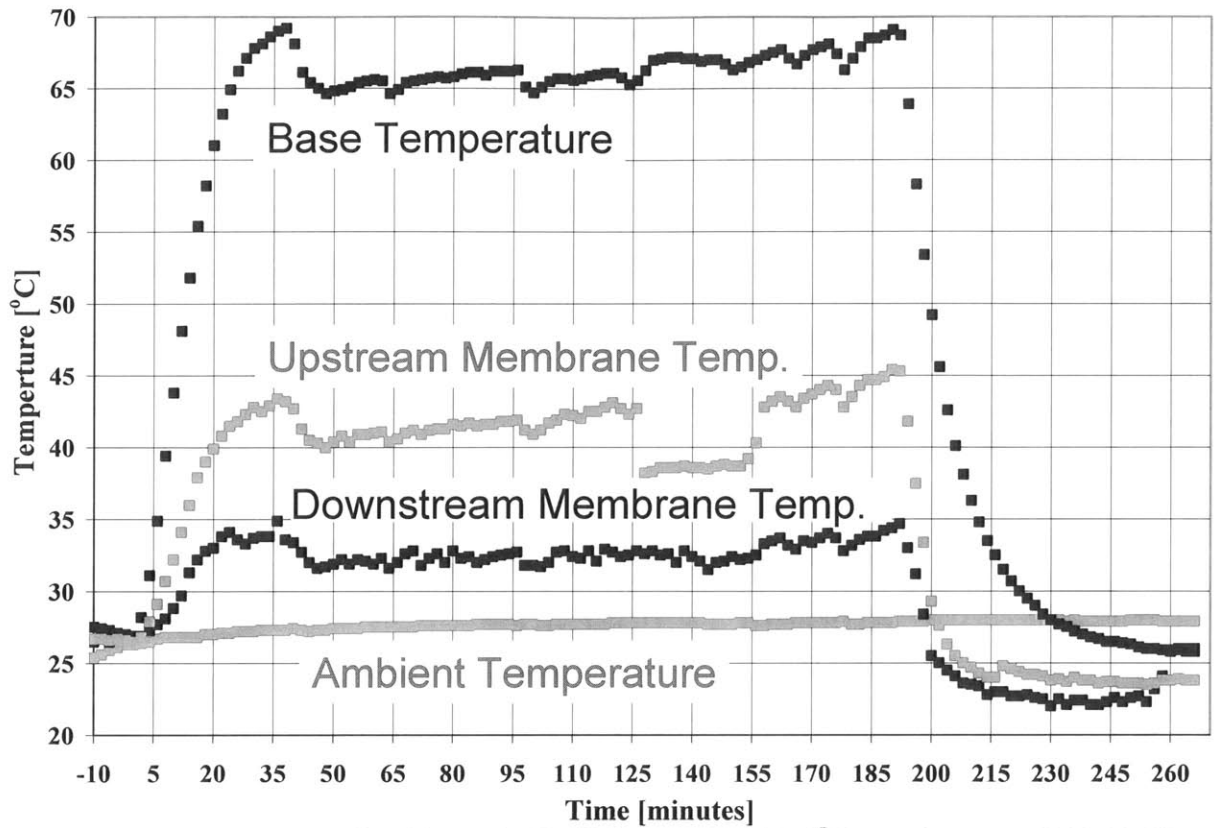
Figure A4.19: Temperature-time history for HAMTA1 running Hytrel® B membrane on 2006-02-14.
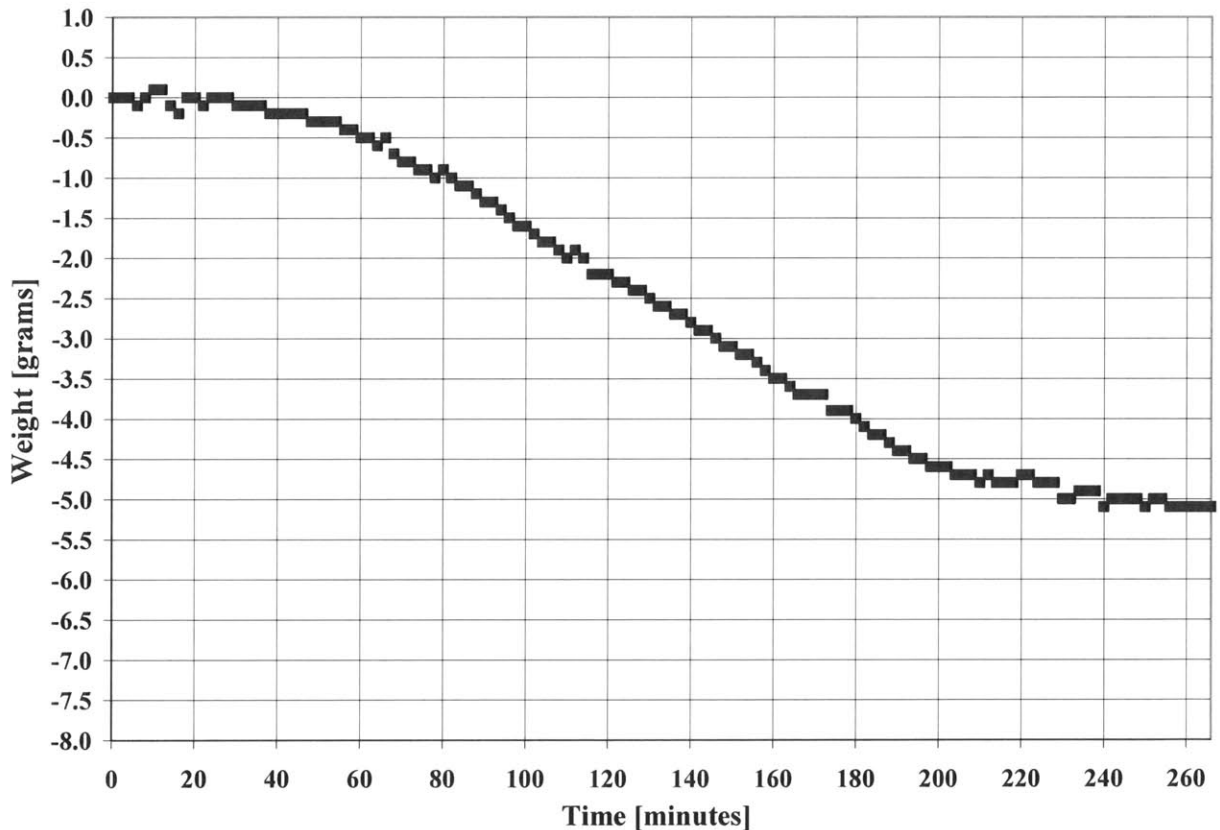
Figure A4.20: Weight-time history for HAMTA1 running Hytrel® B membrane on 2006-02-14.

178
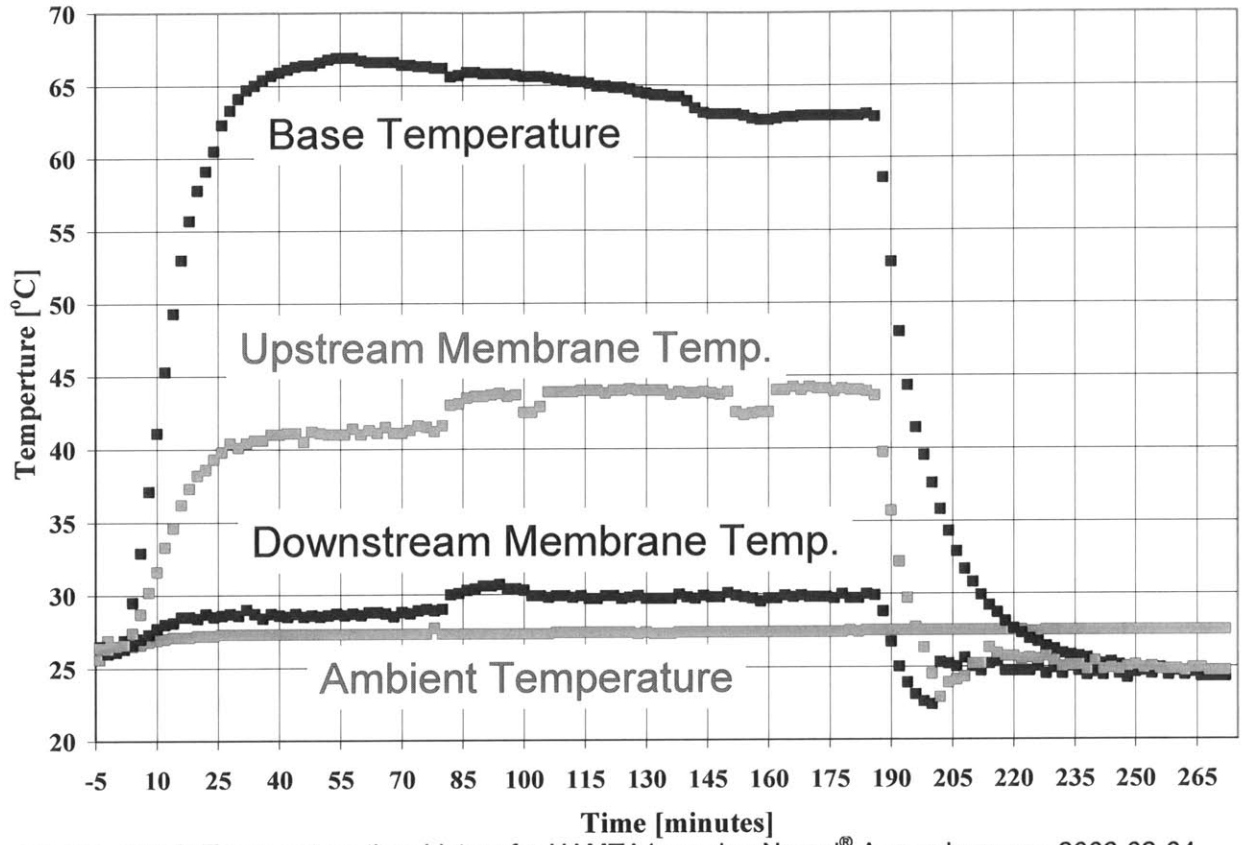
Figure A4.21: Temperature-time history for HAMTA1 running Nucrel® A membrane on 2006-02-04.
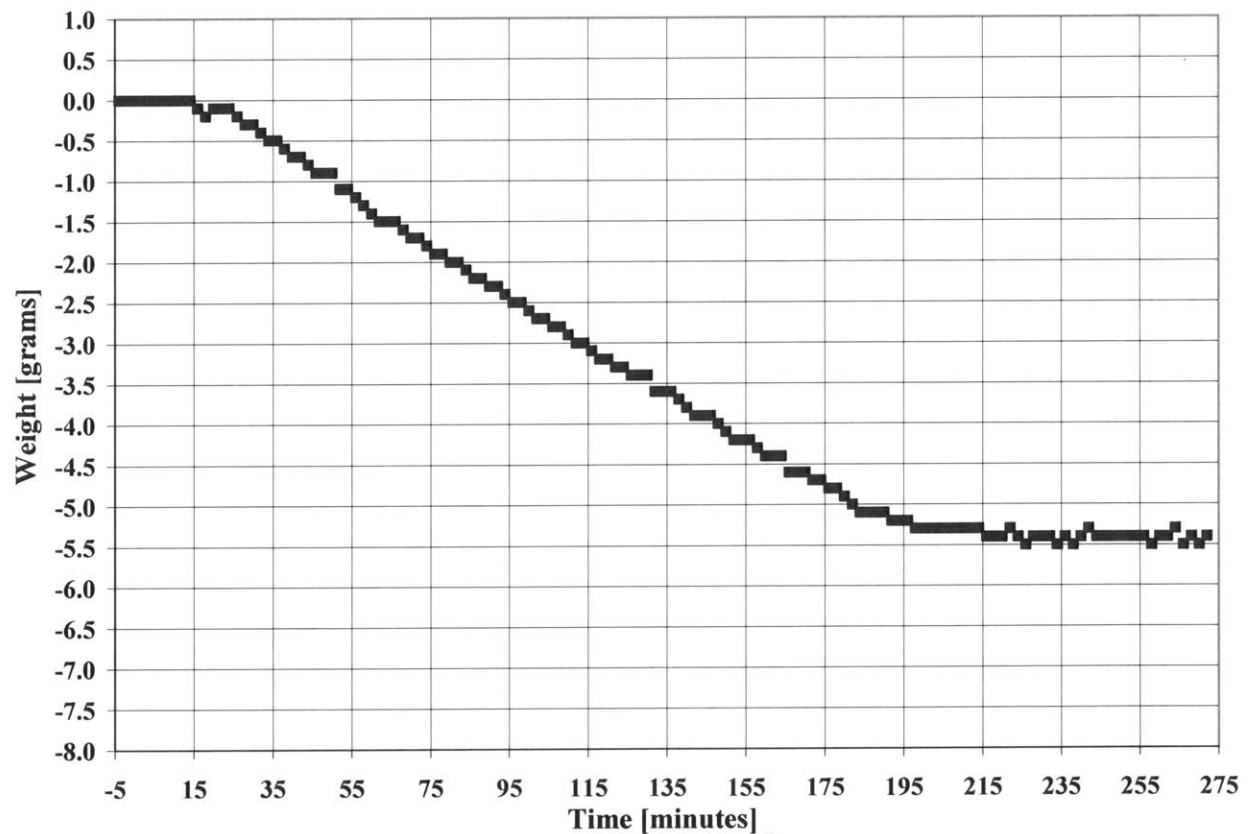
Figure A4.22: Weight-time history for HAMTA1 running Nucrel® A membrane on 2006-02-04.

179
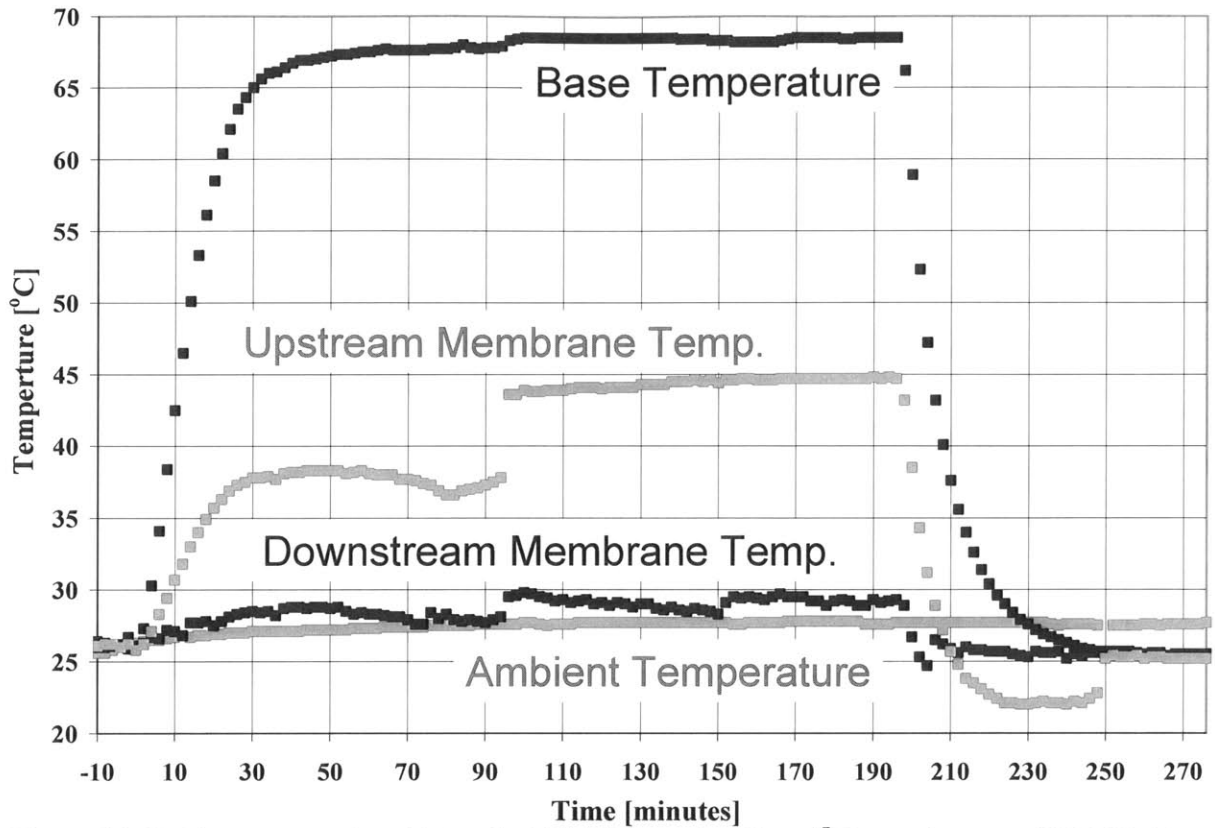
Figure A4.23: Temperature-time history for HAMTA1 running Nucrel® B membrane on 2006-02-15.
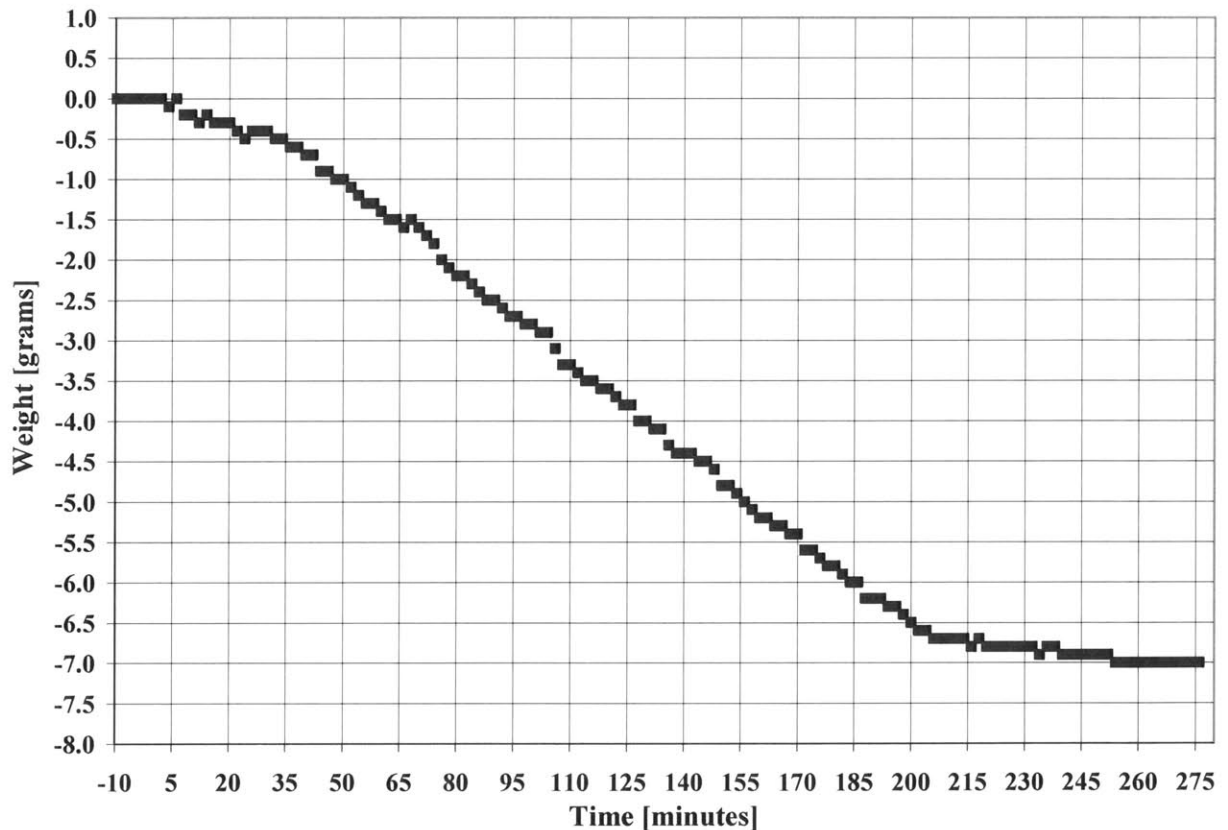
Figure A4.24: Weight-time history for HAMTA1 running Nucrel® B membrane on 2006-02-15.

180
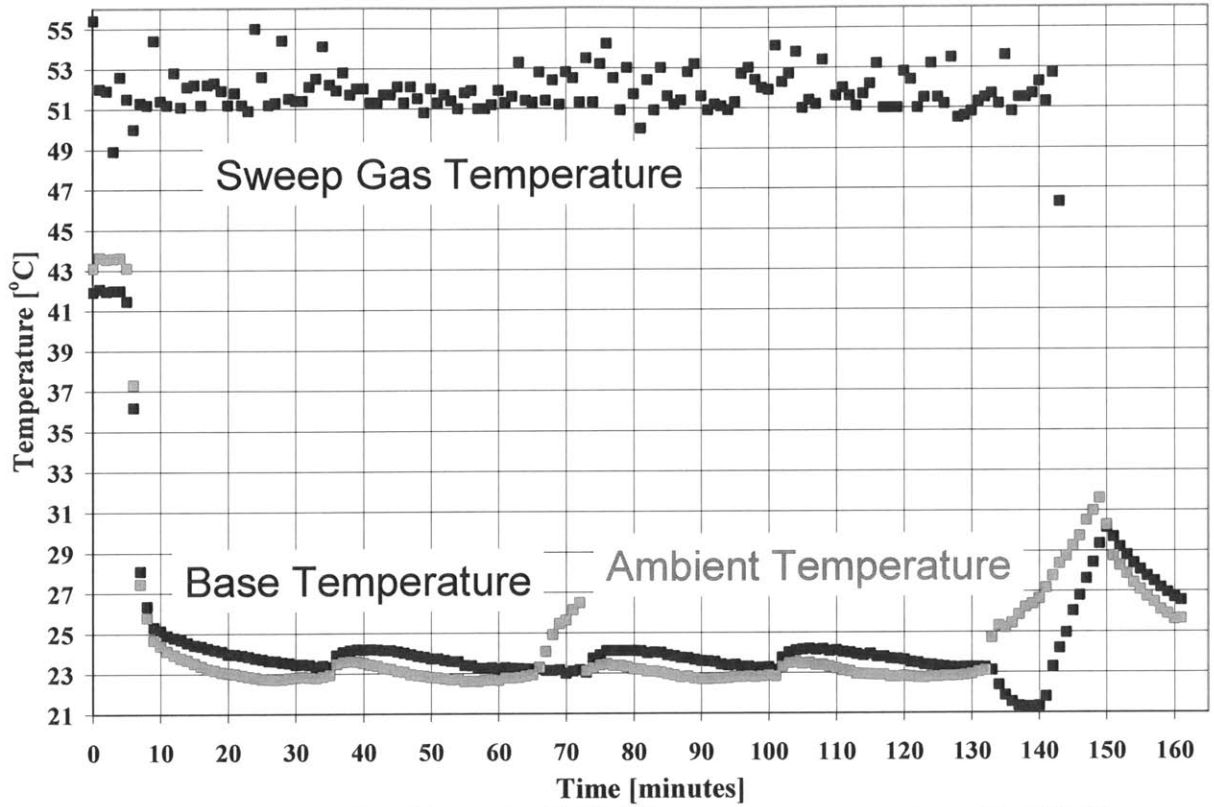
Figure A4.25: Temperature-time history for HAMTA2 running open chamber with 100 °C nozzle temperature on 2007-02-01.
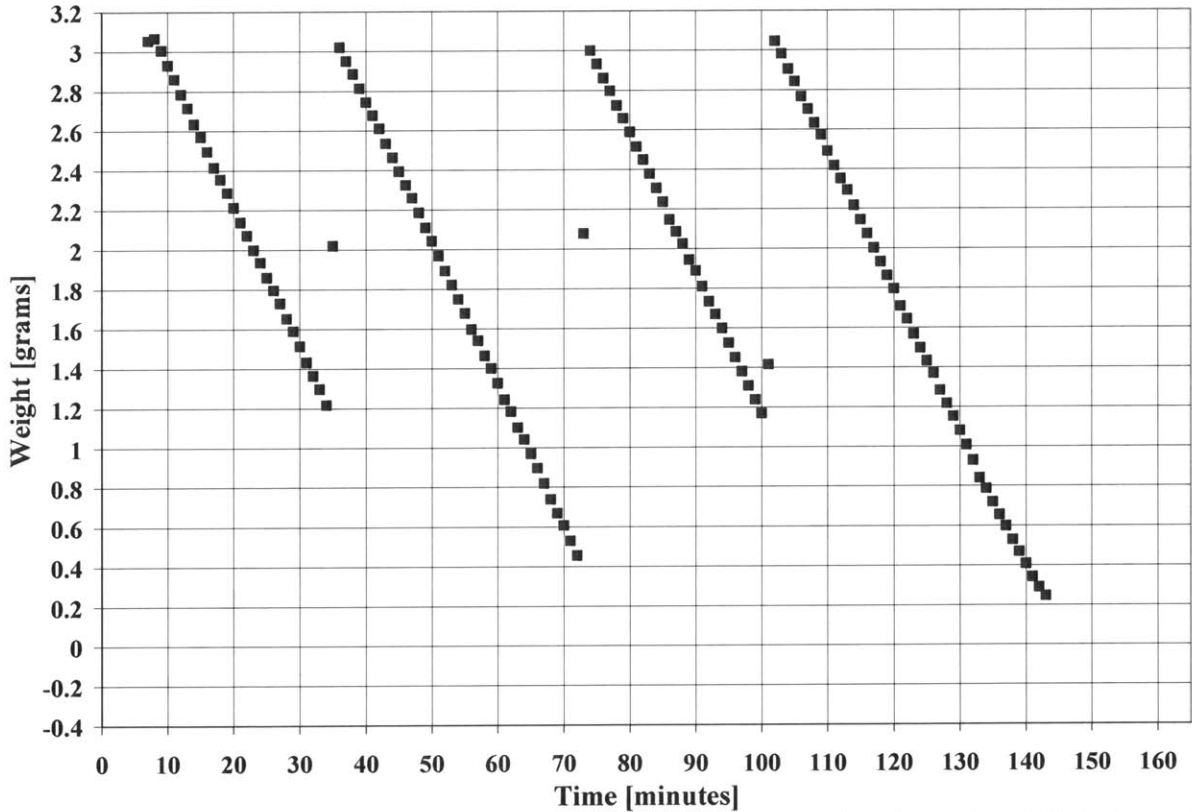
Figure A4.26: Weight-time history for HAMTA2 running open chamber with 100 °C nozzle temperature on 2007-02-01.
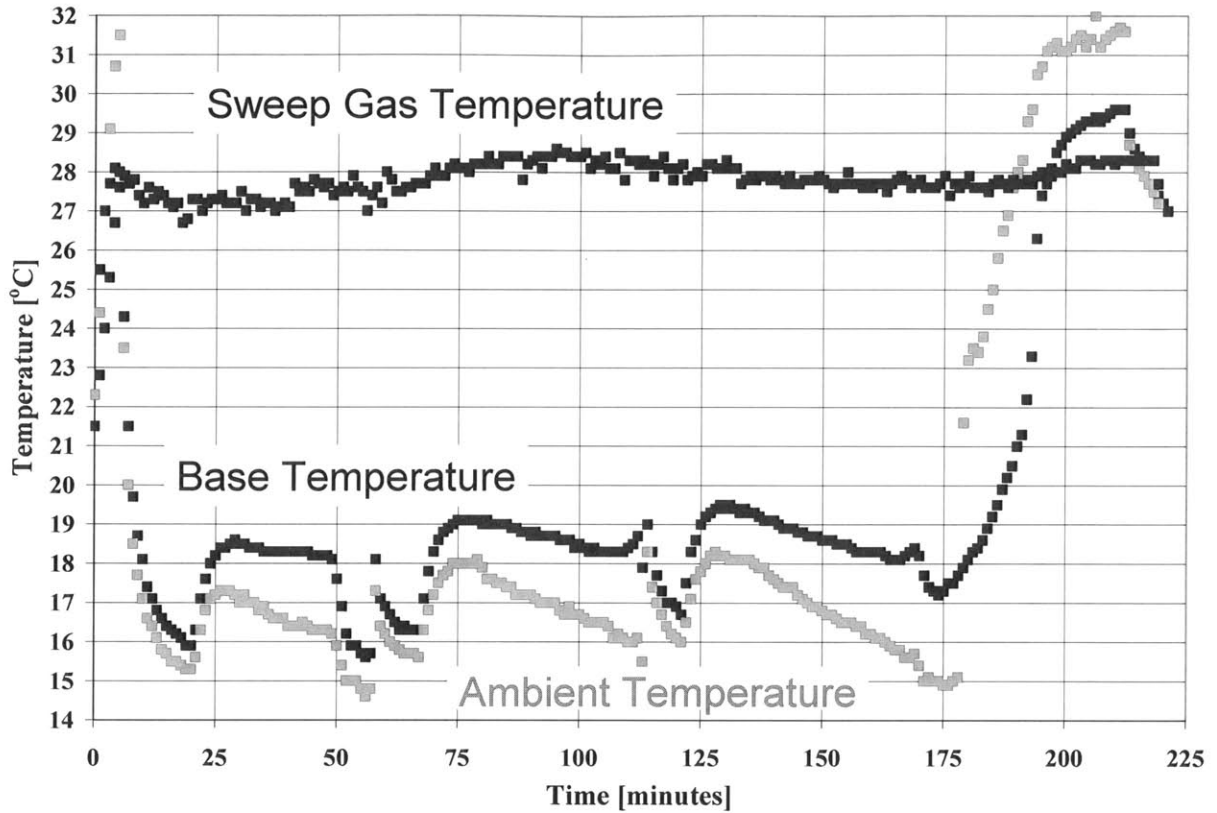
Figure A4.27: Temperature-time history for HAMTA2 running open chamber with 50 °C nozzle temperature on 2006-12-29.
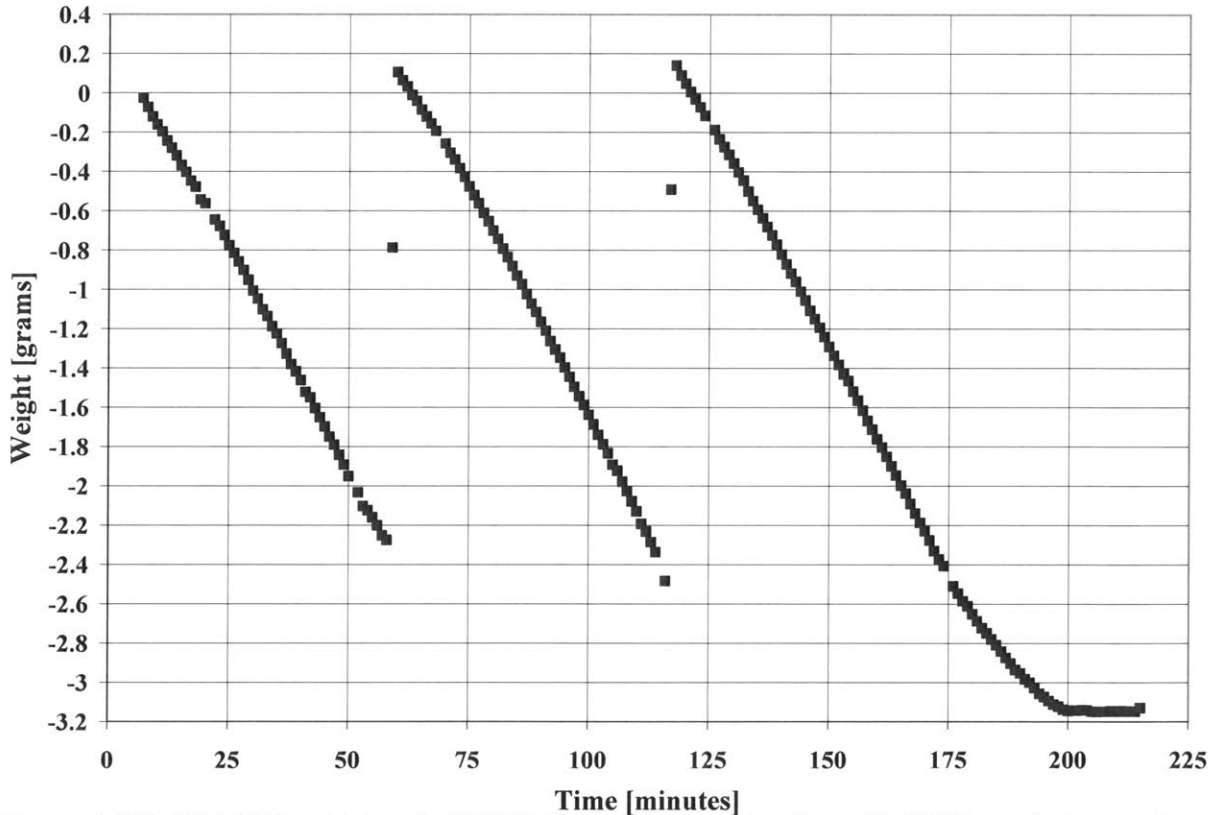
Figure A4.28: Weight-time history for HAMTA2 running open chamber with 50 °C nozzle temperature on 2006-12-29.
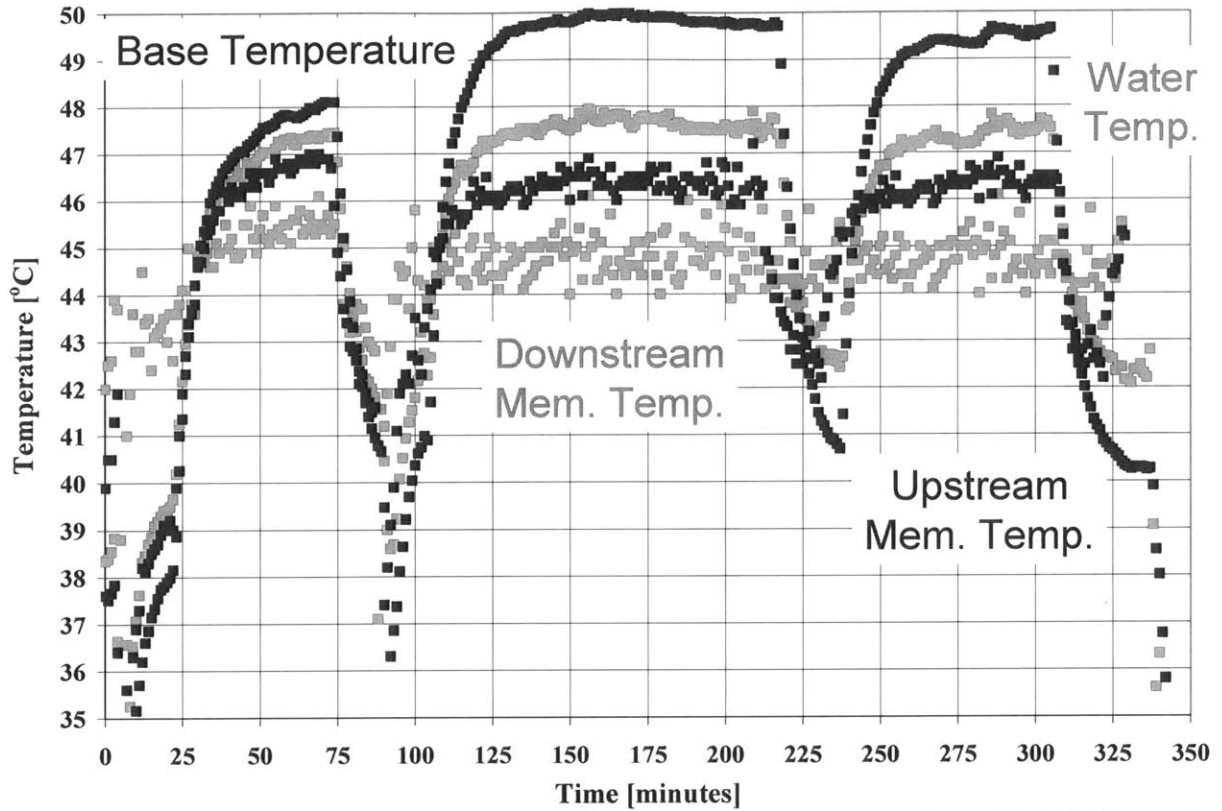
Figure A4.29: Temperature-time history for HAMTA2 running closed chamber with 100 °C nozzle temperature on 2007-02-04.
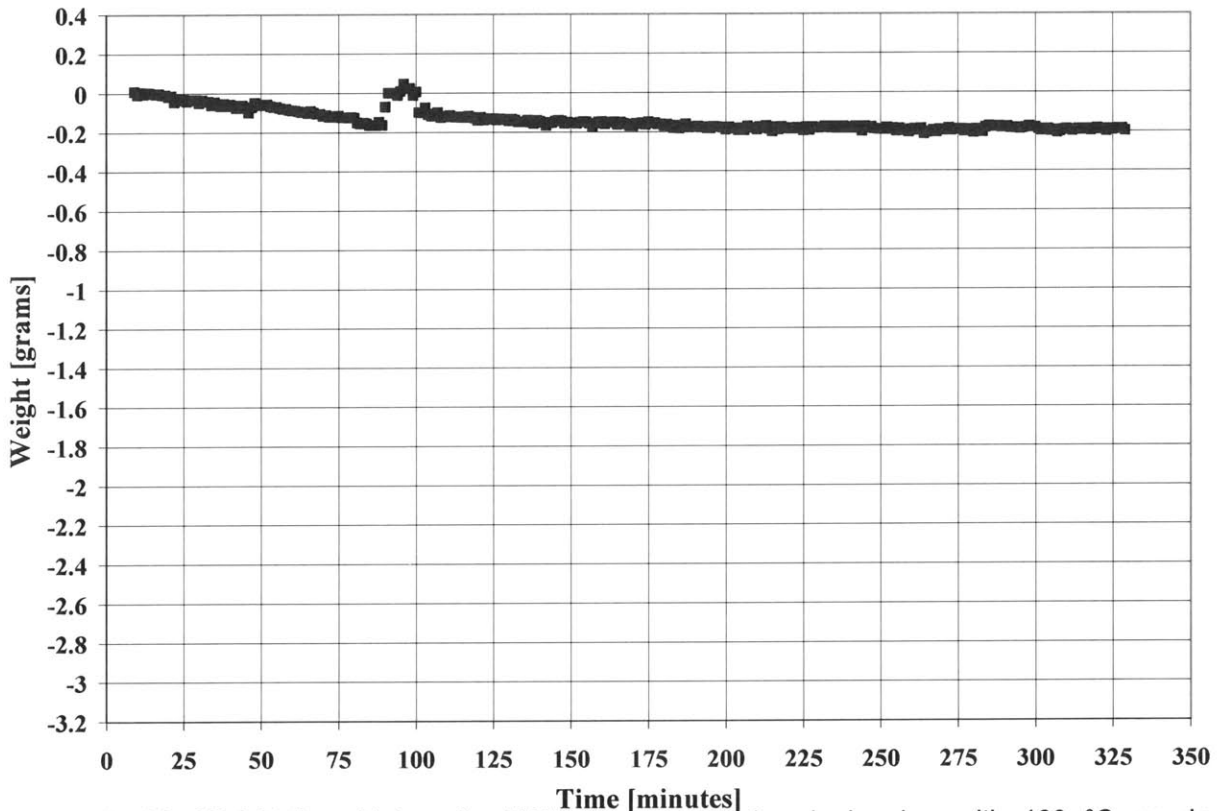
Figure A4.30: Weight-time history for HAMTA2 running closed chamber with 100 °C nozzle temperature on 2007-02-04.
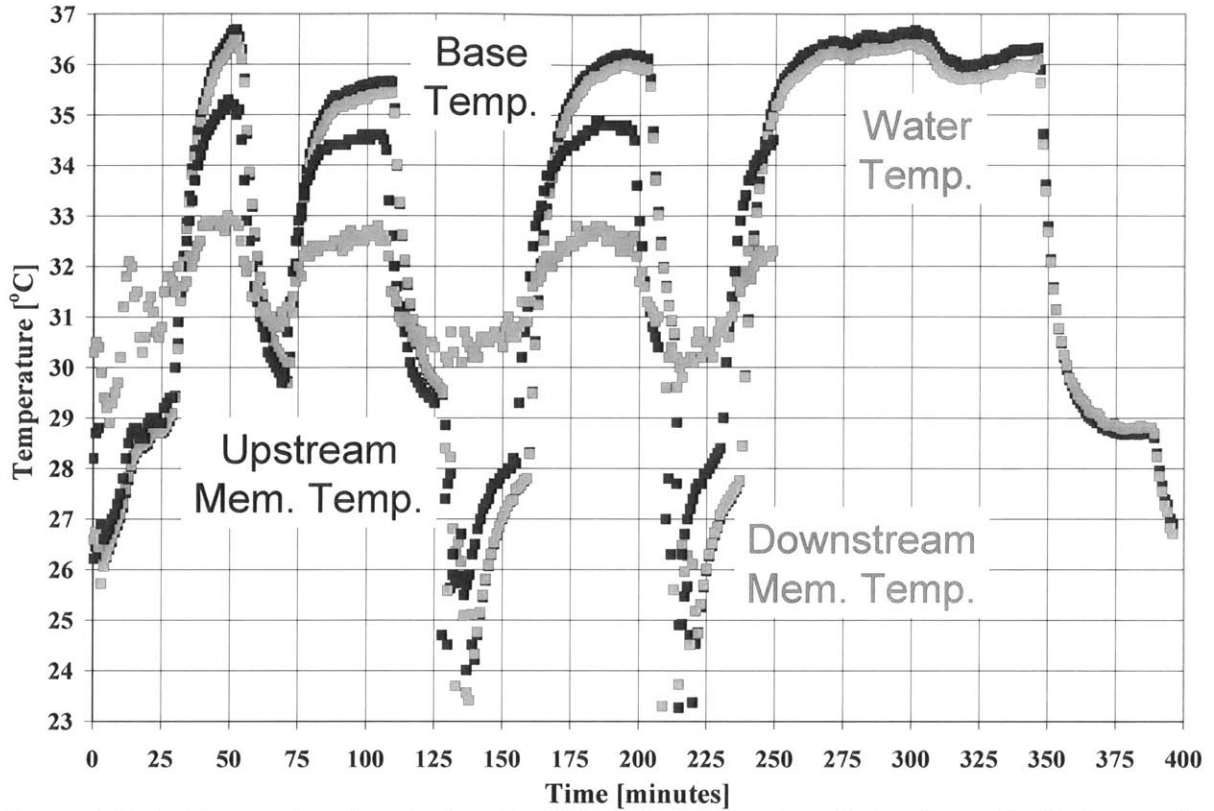
Figure A4.31: Temperature-time history for HAMTA2 running closed chamber with 50 °C nozzle temperature on 2007-02-03.
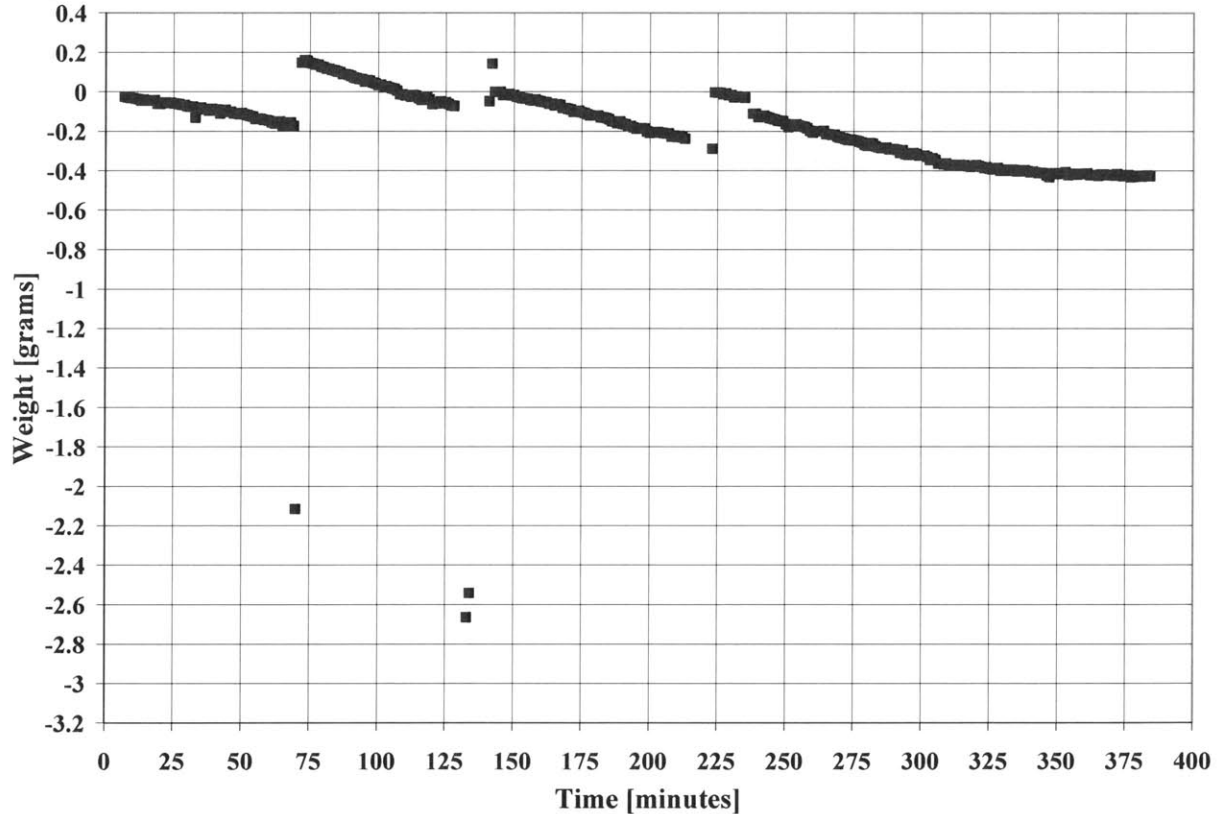
Figure A4.32: Weight-time history for HAMTA2 running closed chamber with 50 °C nozzle temperature on 2007-02-03.
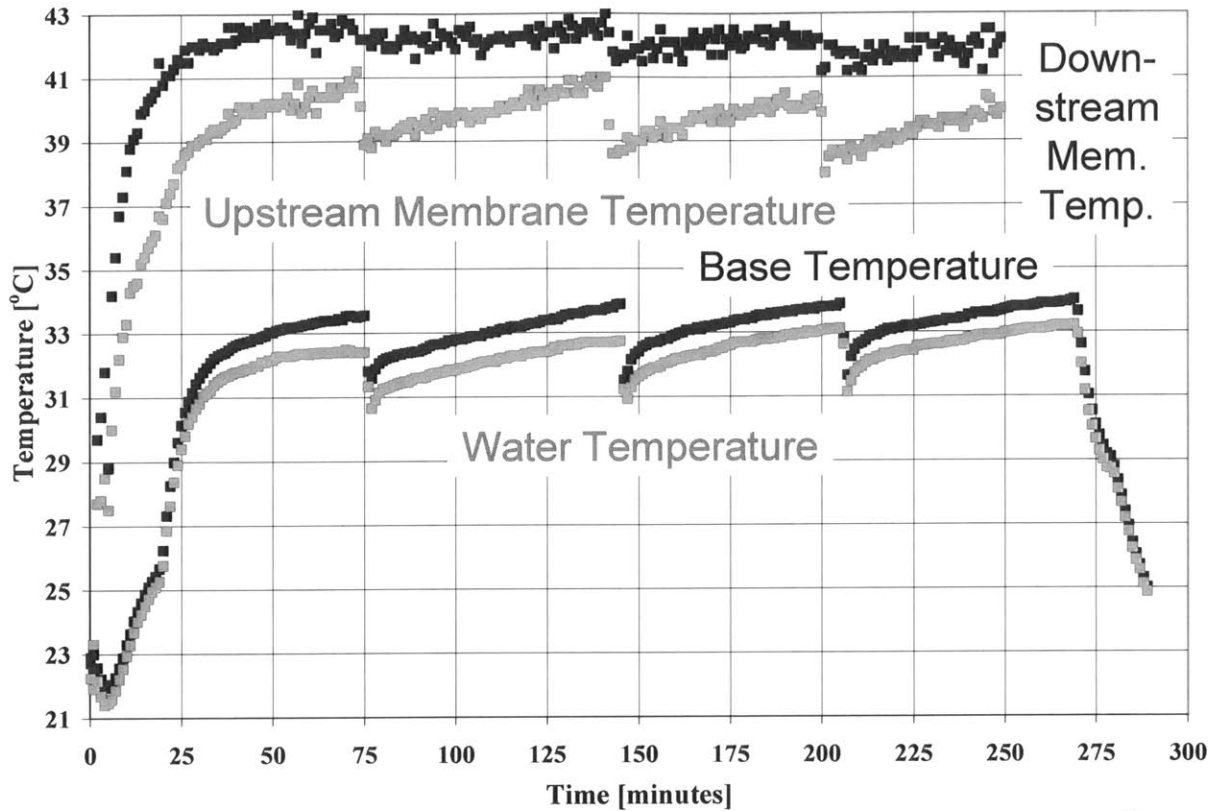
Figure A4.33: Temperature-time history for HAMTA2 running a 12 μm (14.4 μm measured) pore diameter track-etched membrane with 100 °C nozzle temperature on 2007-01-21.
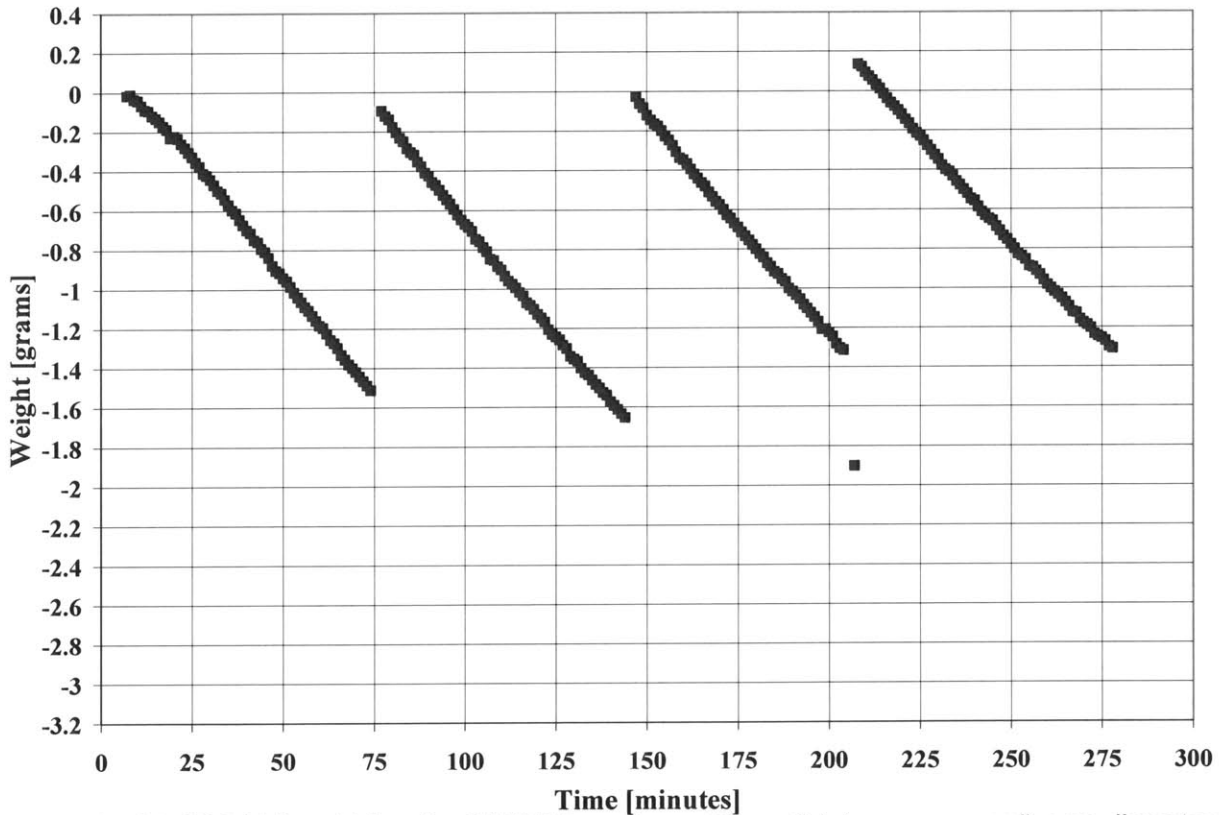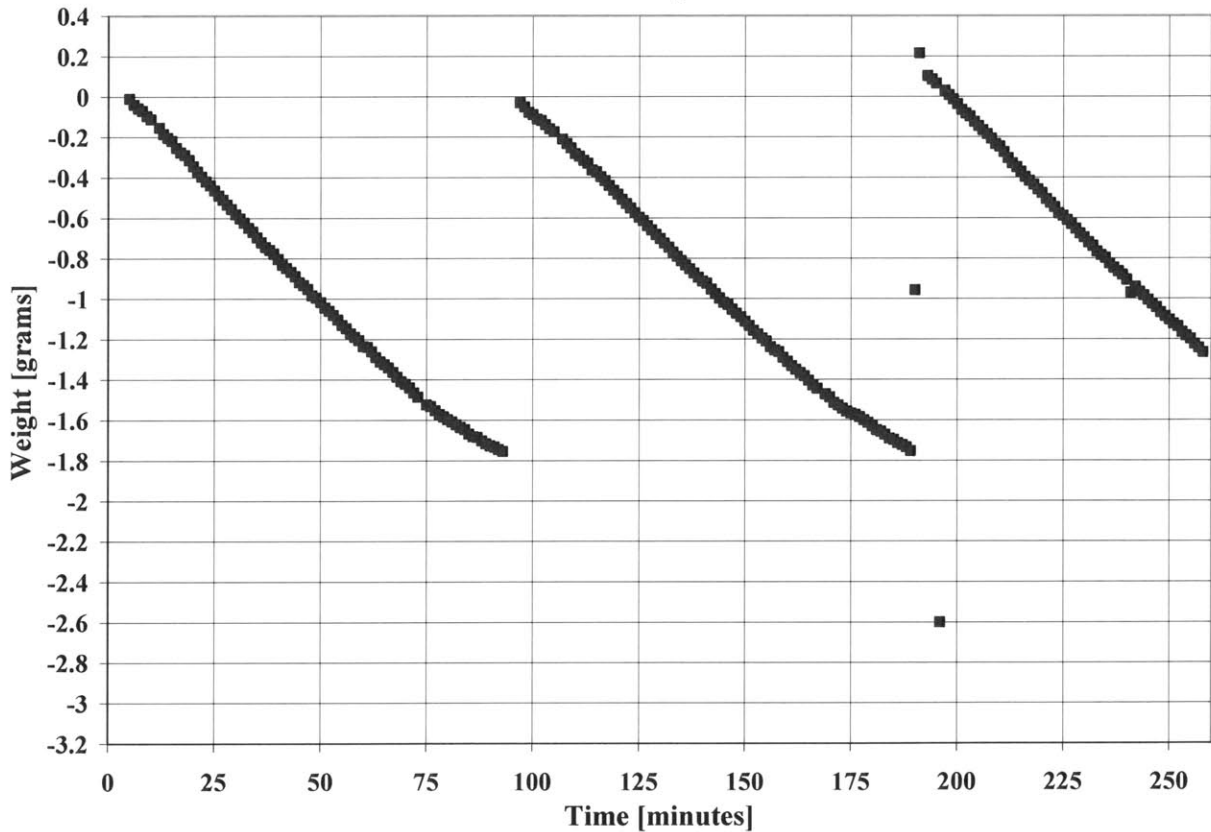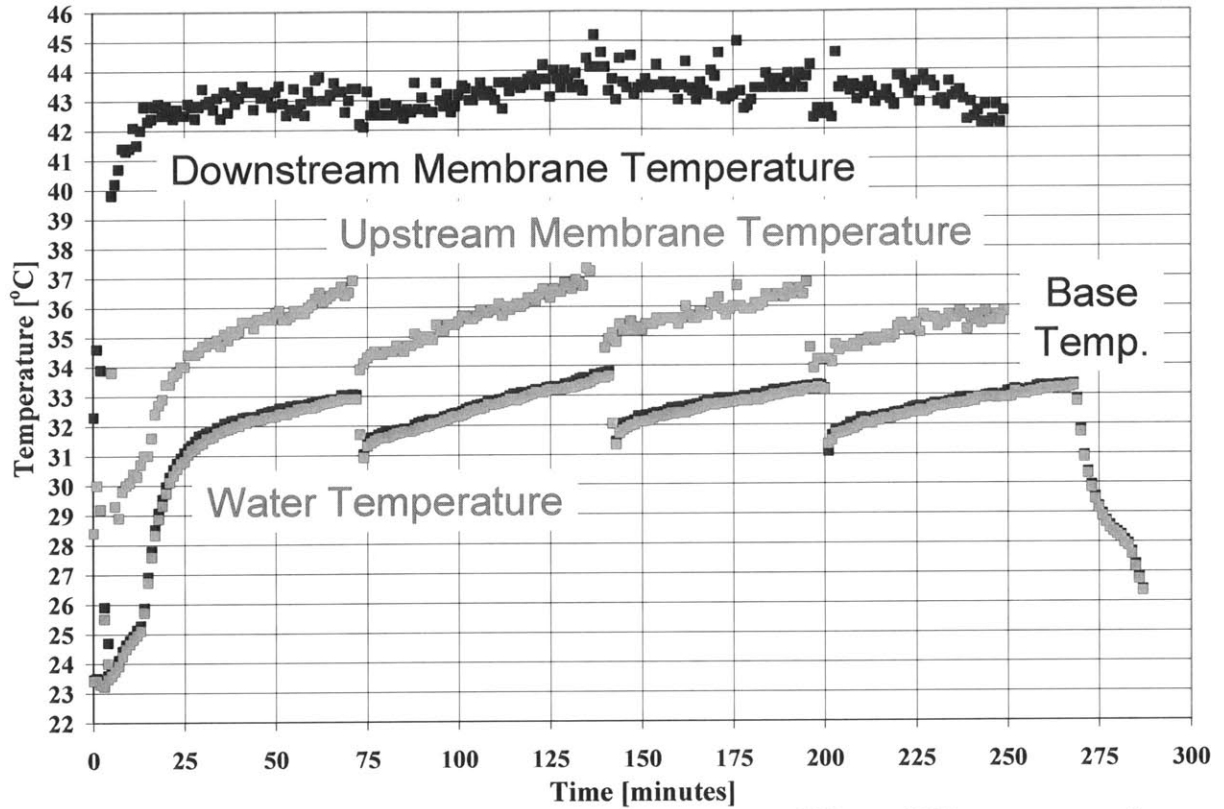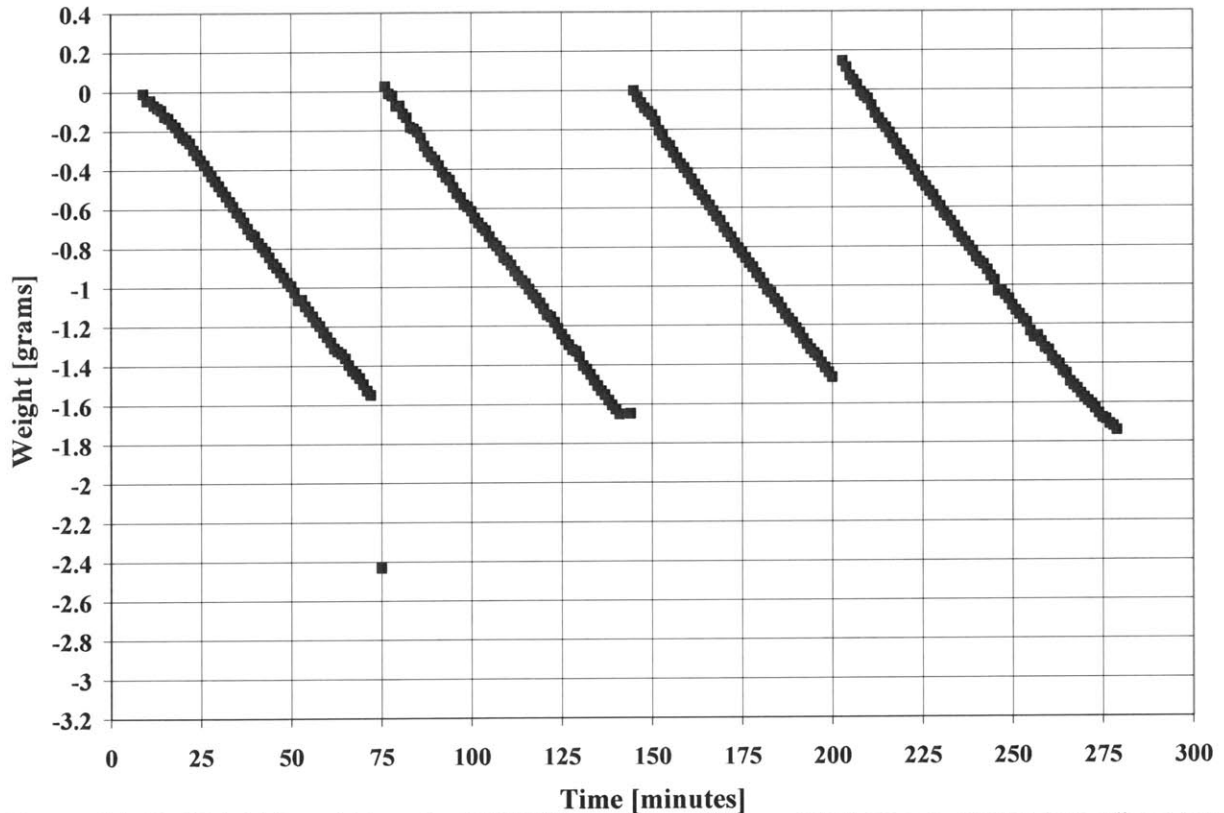

Figure A4.34: Weight-time history for HAMTA2 running a 12 μm (14.4 μm measured) pore diameter track-etched membrane with 100 °C nozzle temperature on 2007-01-21.

185
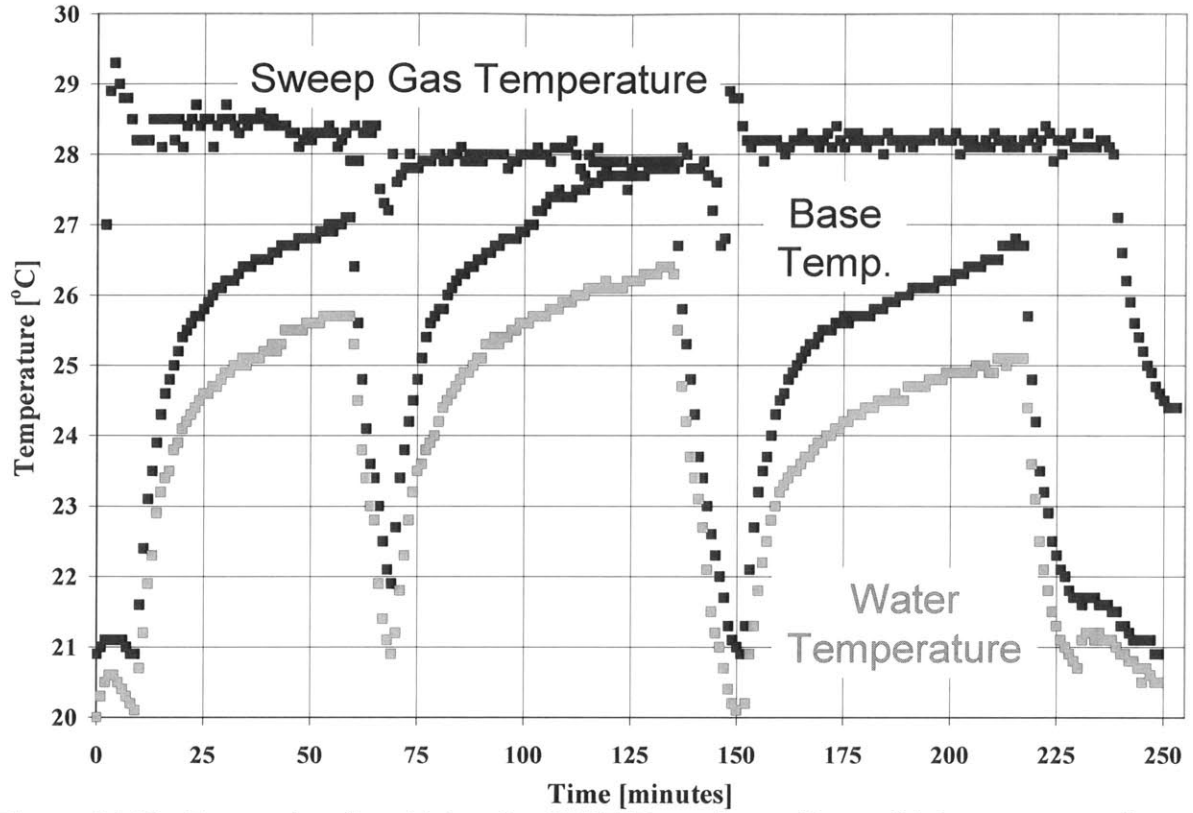
Figure A4.35: Temperature-time history for HAMTA2 running a 12 μm (14.4 μm measured) pore diameter track-etched membrane with 50 °C nozzle temperature on 2007-12-20.
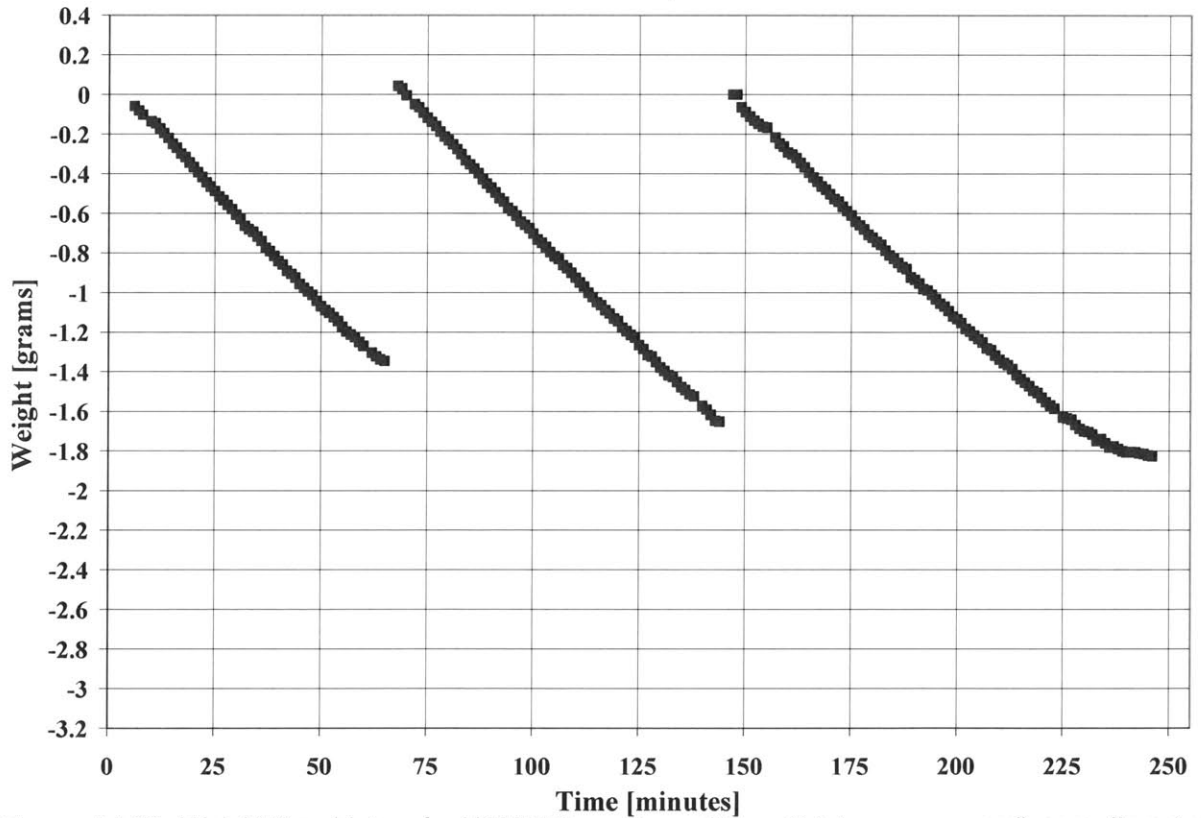
Figure A4.36: Weight-time history for HAMTA2 running a 12 μm (14.4 μm measured) pore diameter track-etched membrane with 50 °C nozzle temperature on 2007-12-20.
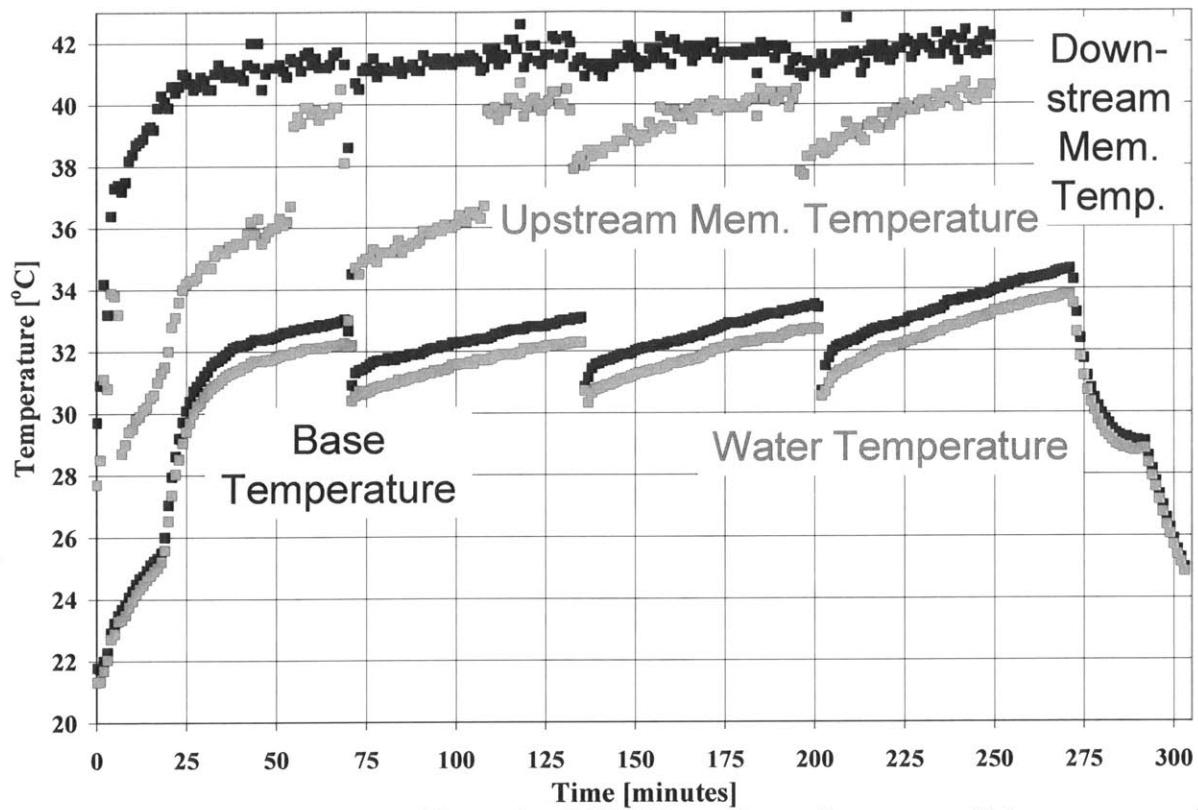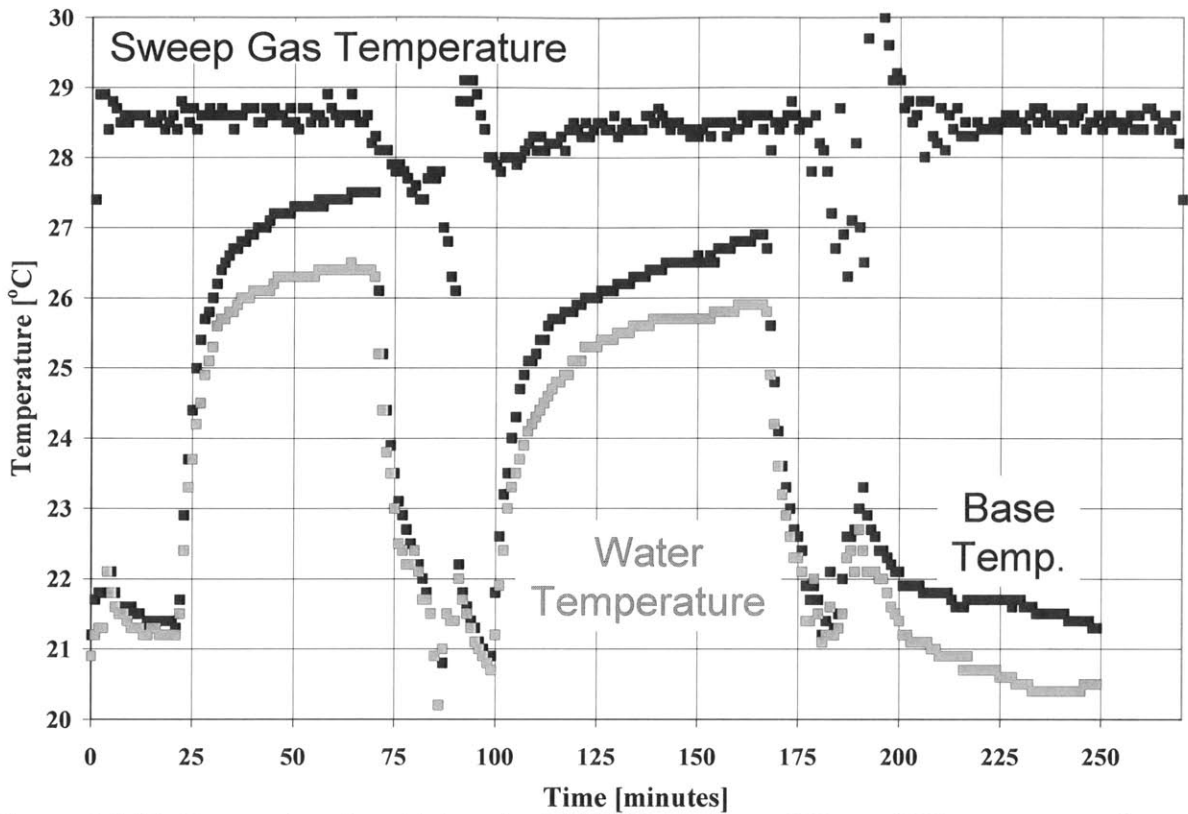
Figure A4.37: Temperature-time history for HAMTA2 running a 5 μm pore (5.4 μm measured) diameter track-etched membrane with 100 °C nozzle temperature on 2007-01-22.
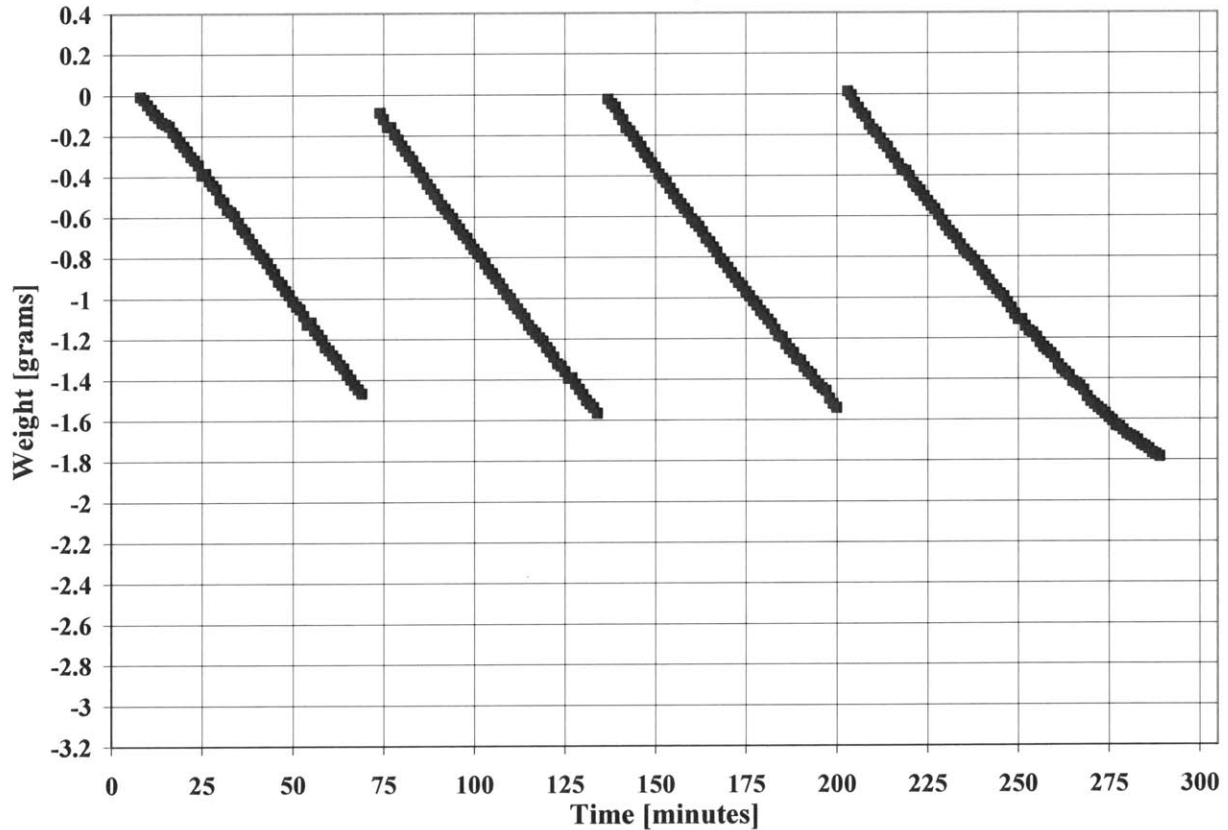
Figure A4.38: Weight-time history for HAMTA2 running a 5 μm (5.4 μm measured) pore diameter track-etched membrane with 100 °C nozzle temperature on 2007-01-22.
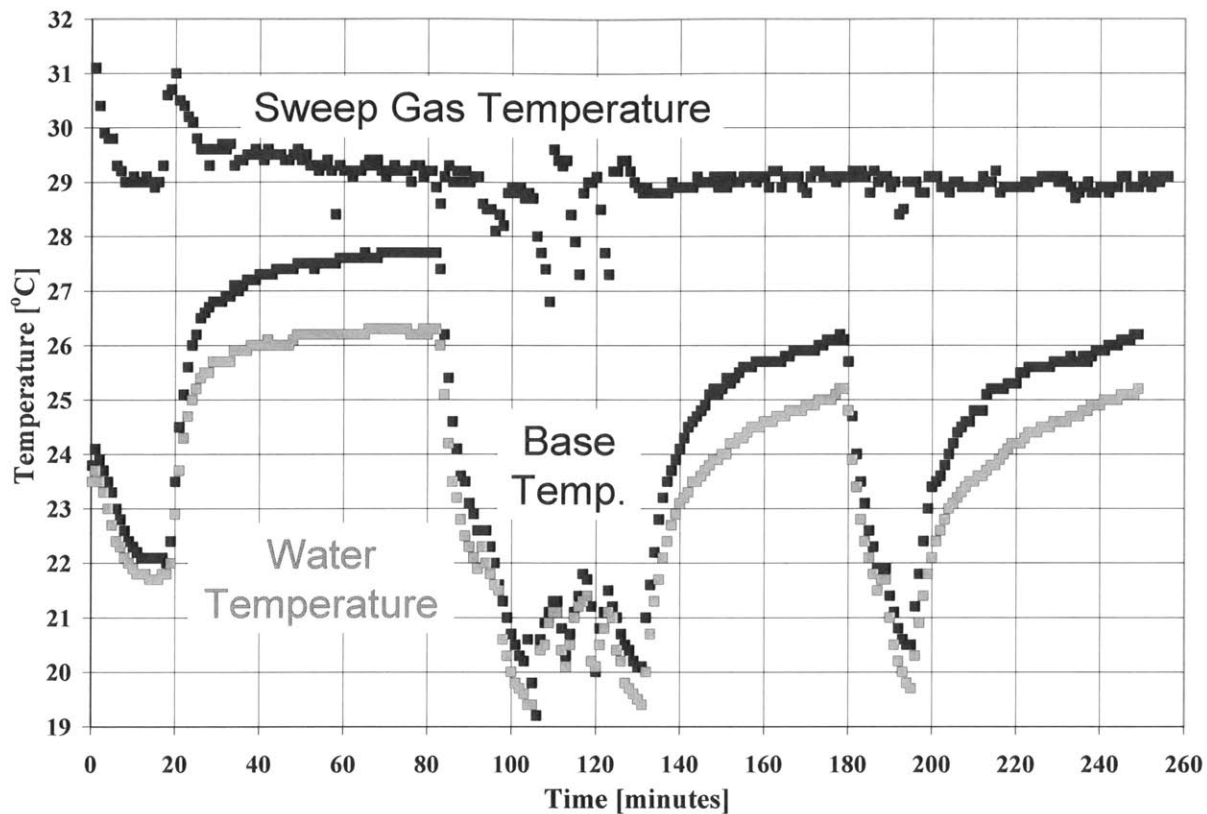
Figure A4.39: Temperature-time history for HAMTA2 running a 5 μm (5.4 μm measured) pore diameter track-etched membrane with 50 °C nozzle temperature on 2006-12-21.
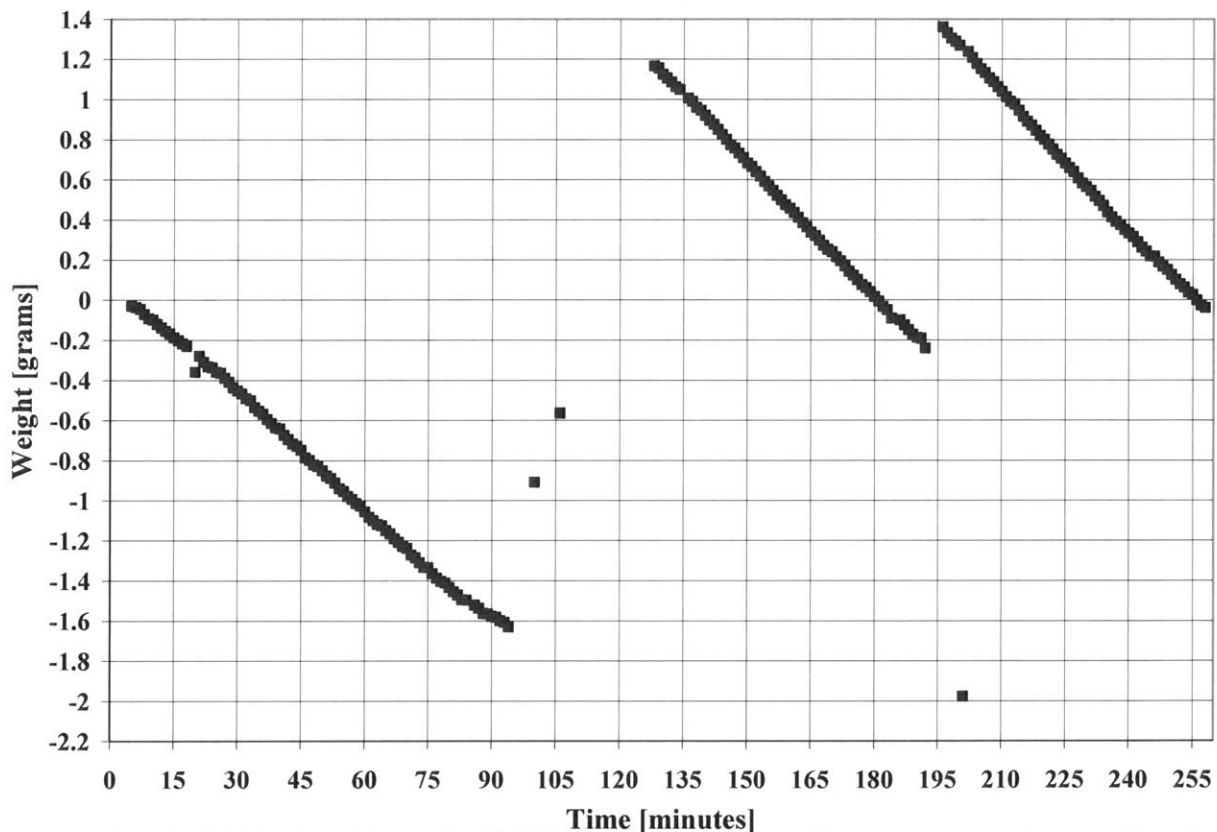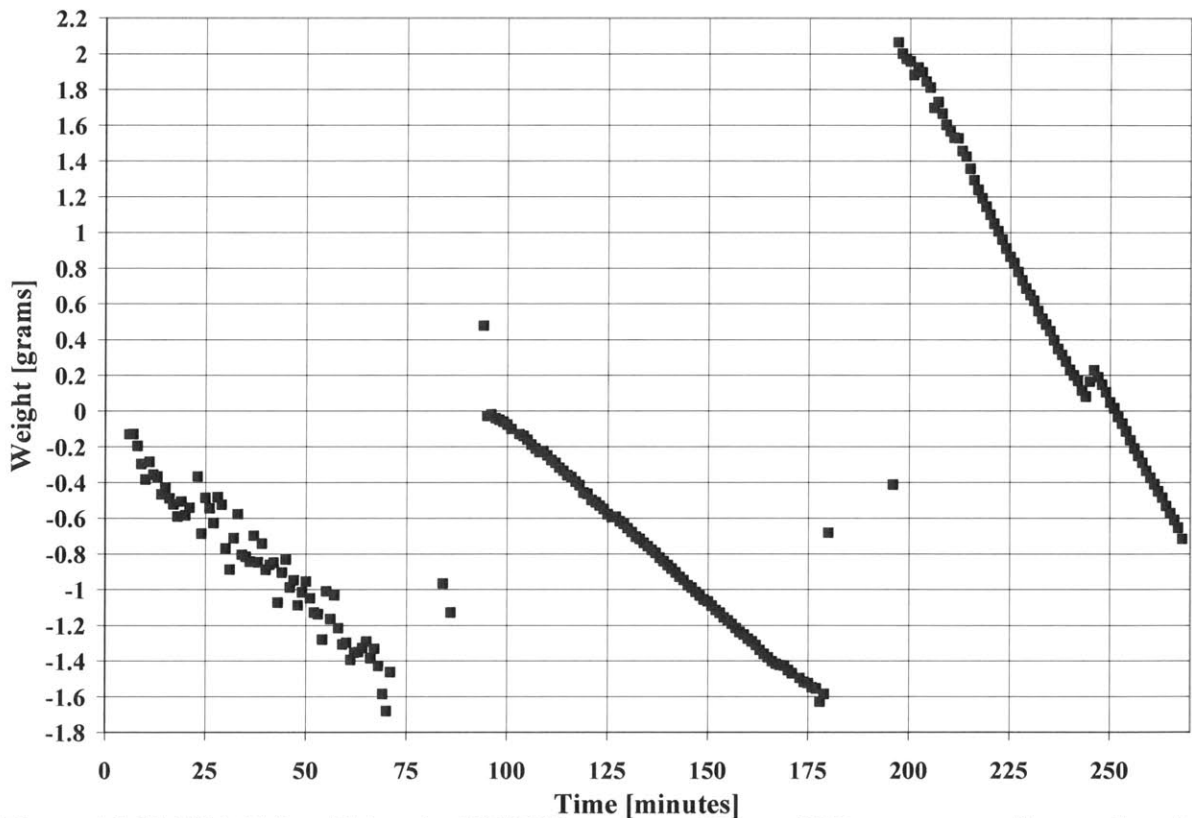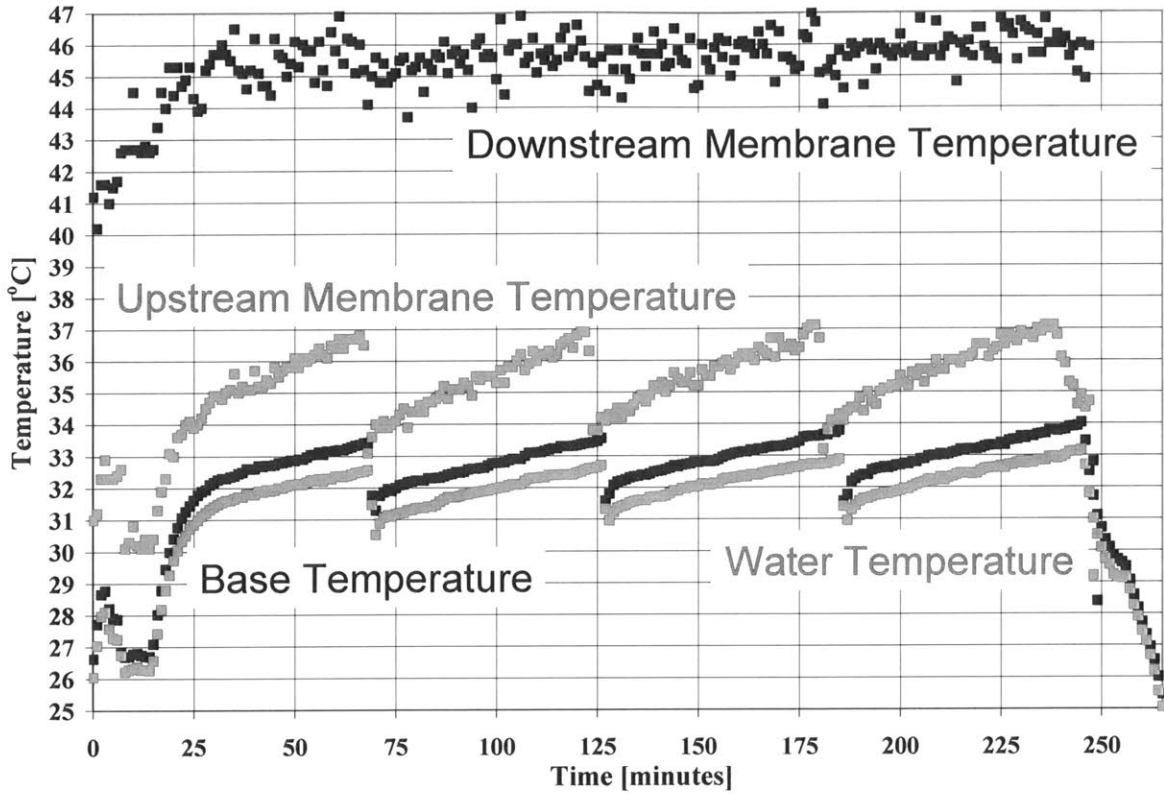

Figure A4.40: Weight-time history for HAMTA2 running a 5 μm (5.4 μm measured) pore diameter track-etched membrane with 50 °C nozzle temperature on 2006-12-21.
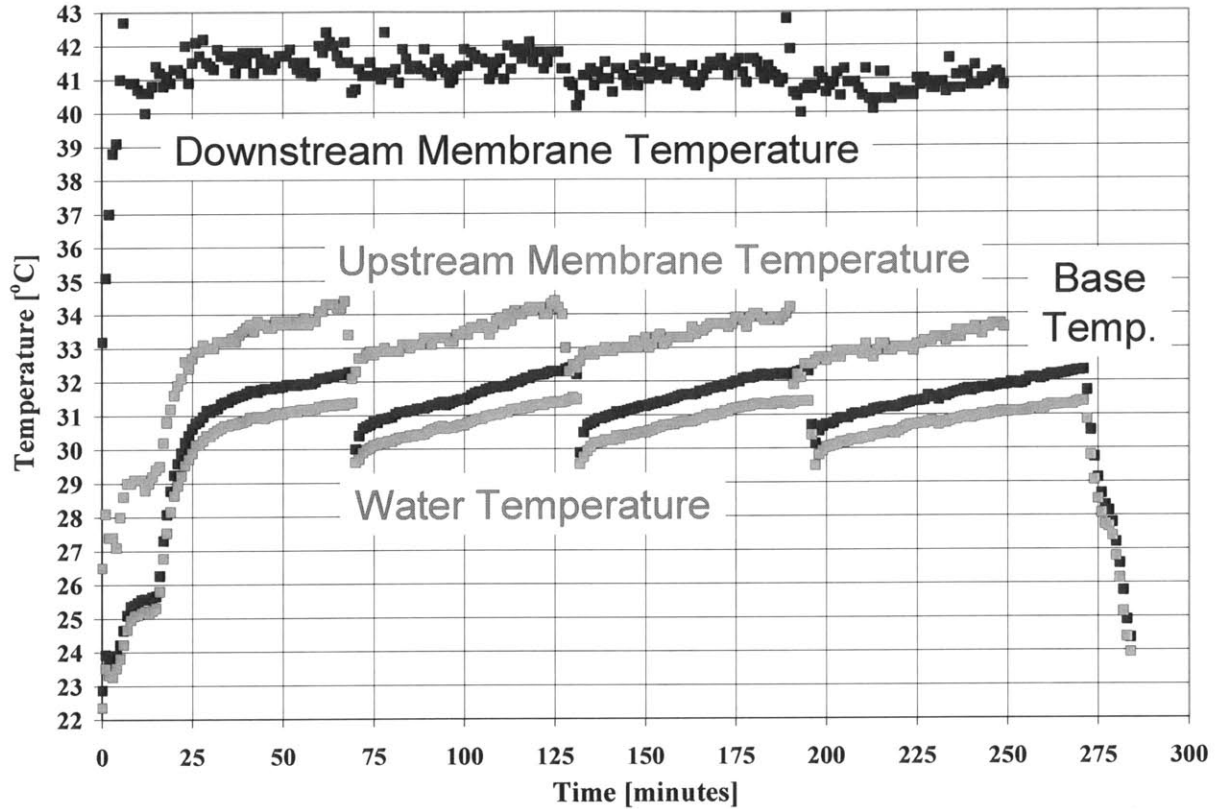
Figure A4.41: Temperature-time history for HAMTA2 running a 1200 nm (890 nm measured) pore diameter track-etched membrane with 100 °C nozzle temperature on 2007-01-25.
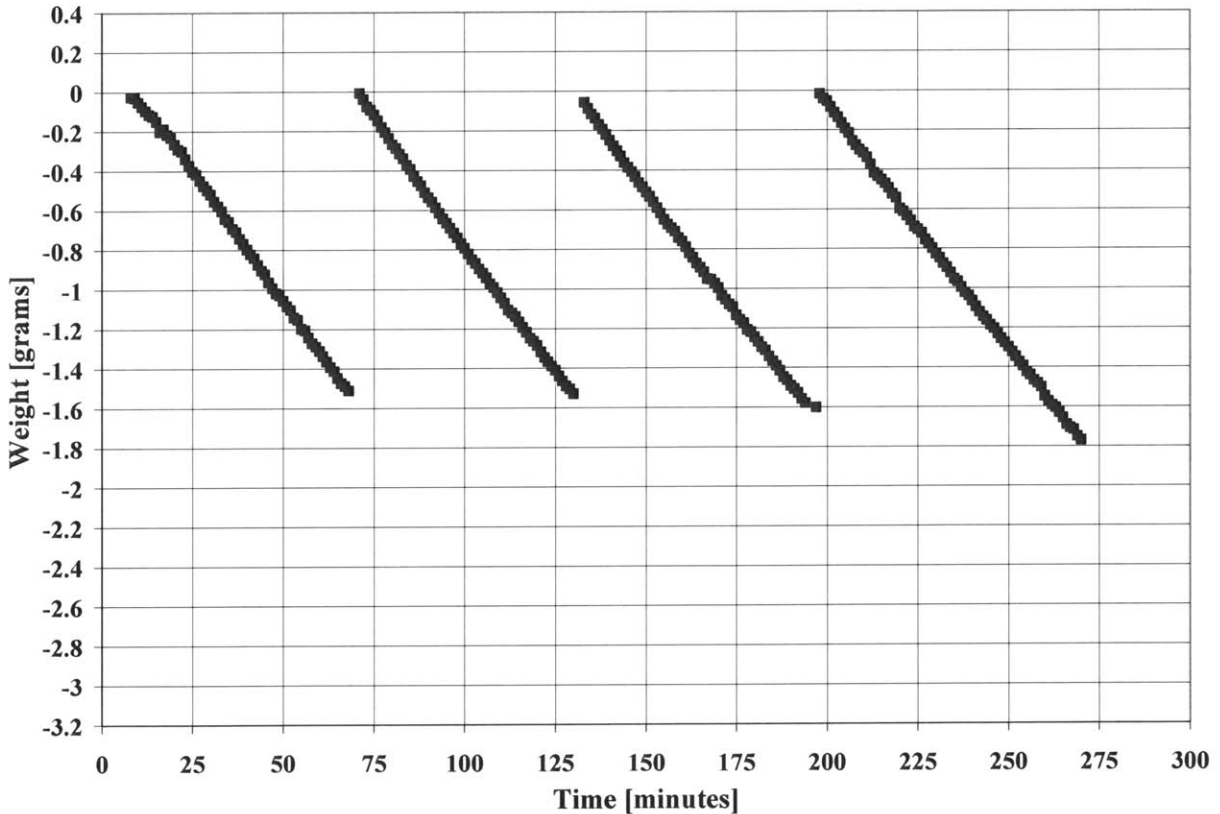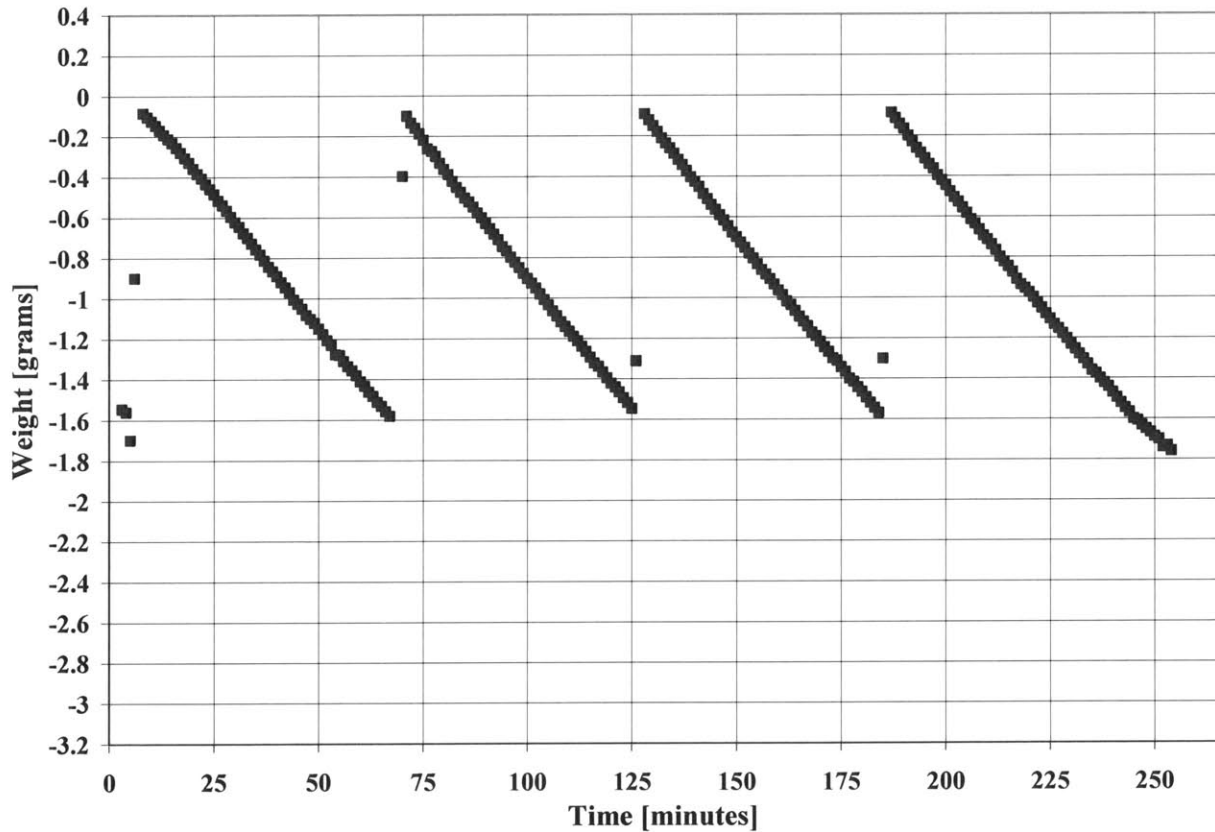

Figure A4.42: Weight-time history for HAMTA2 running a 1200 nm (890 nm measured) pore diameter track-etched membrane with 100 °C nozzle temperature on 2007-01-25.
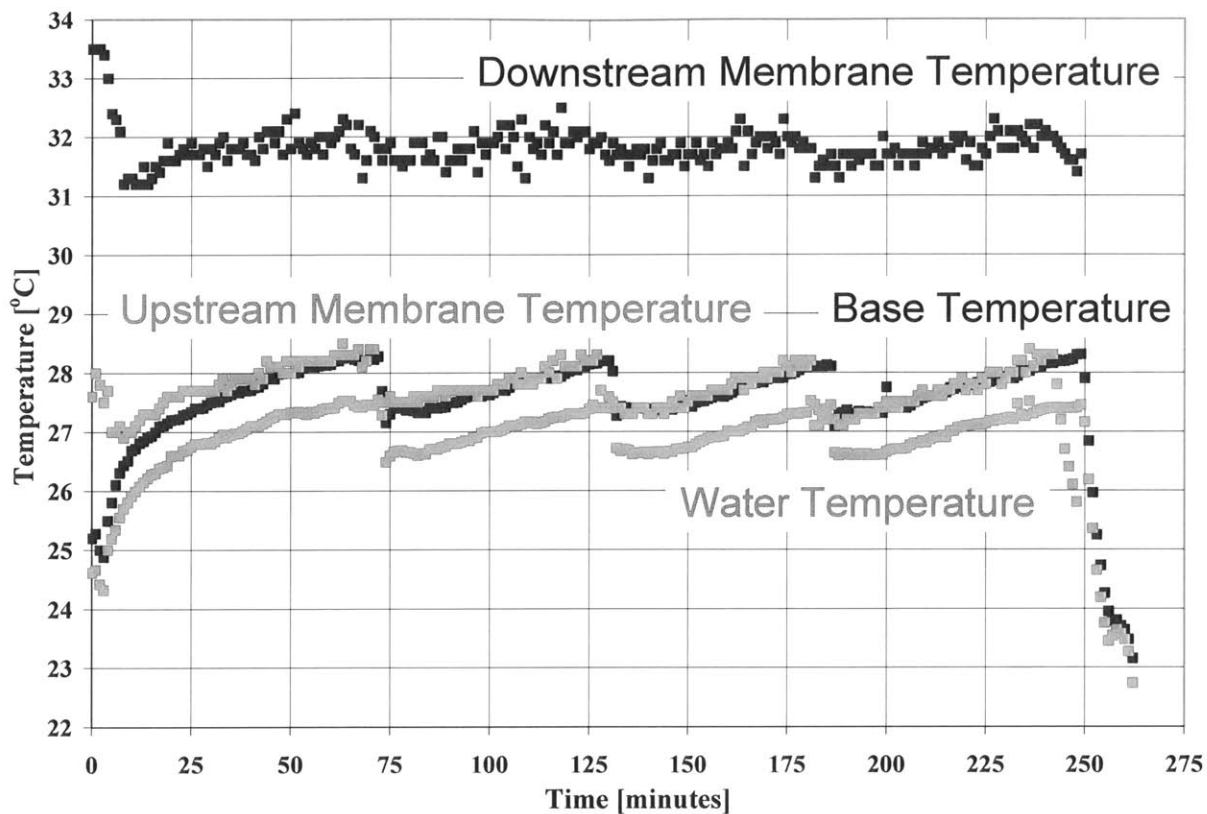
189
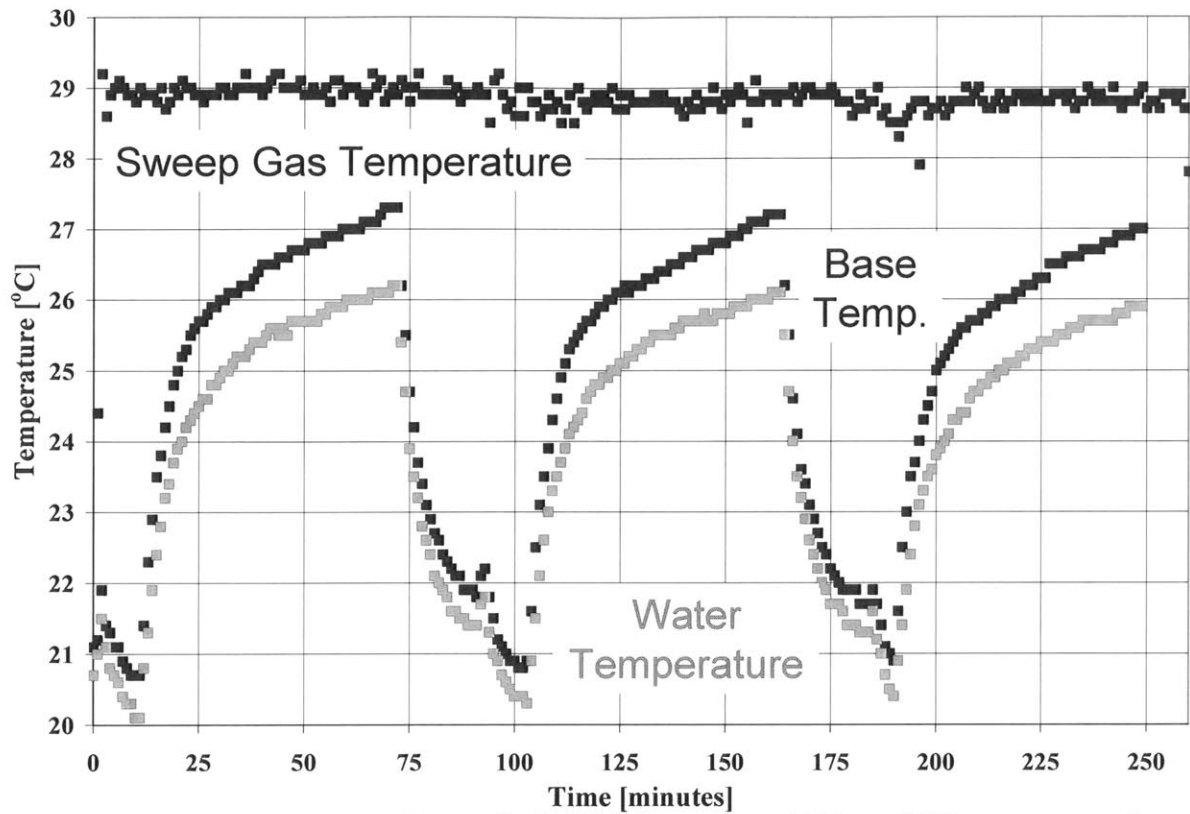
Figure A4.43: Temperature-time history for HAMTA2 running a 1200 nm (890 nm measured) pore diameter track-etched membrane with 50 °C nozzle temperature on 2006-12-22.

Figure A4.44: Weight-time history for HAMTA2 running a 1200 nm (890 nm measured) pore diameter track-etched membrane with 50 °C nozzle temperature on 2006-12-22.

Figure A4.45: Temperature-time history for HAMTA2 running a 600 nm (700 nm measured) pore diameter track-etched membrane with 100 °C nozzle temperature on 2006-01-20.
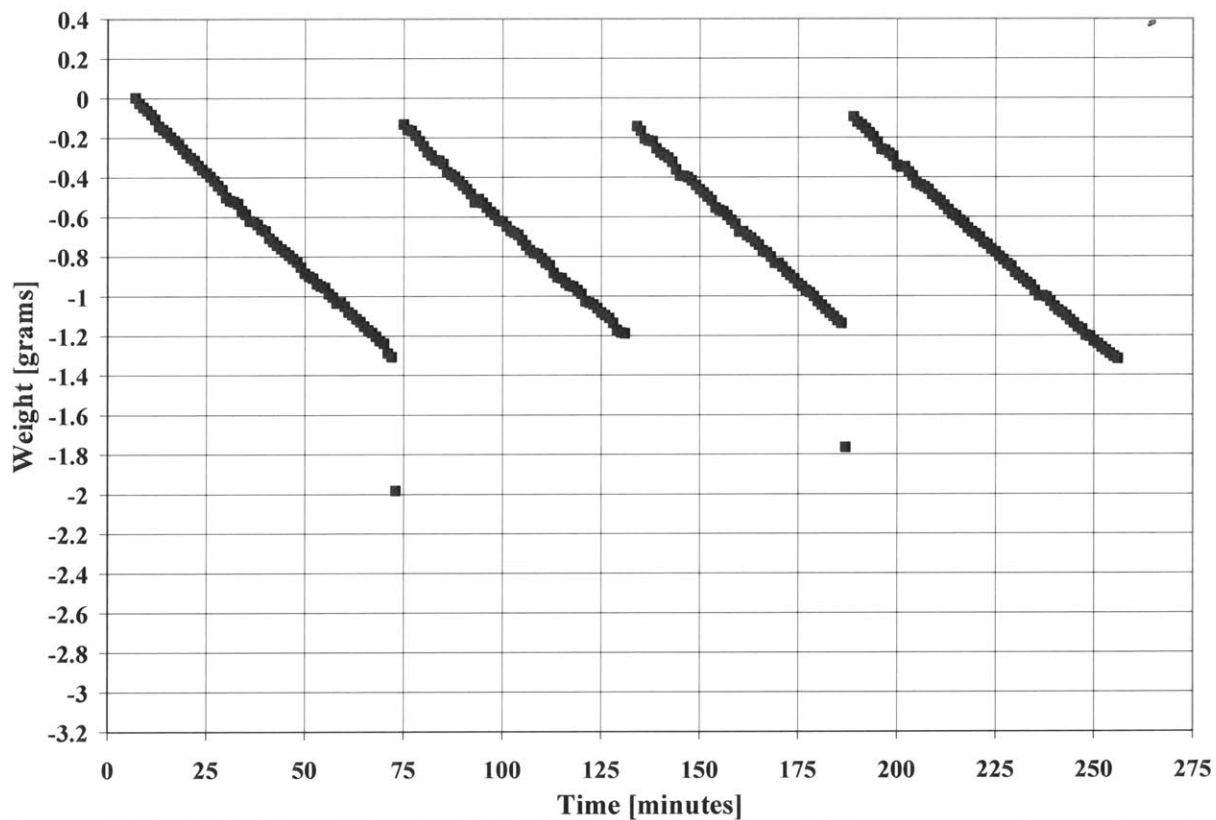

Figure A4.46: Weight-time history for HAMTA2 running a 600 nm (700 nm measured) pore diameter track-etched membrane with 100 °C nozzle temperature on 2006-01-20.

Figure A4.47: Temperature-time history for HAMTA2 running a 600 nm (700 nm measured) pore diameter track-etched membrane with 50 °C nozzle temperature on 2006-12-23.

Figure A4.48: Weight-time history for HAMTA2 running a 600 nm (700 nm measured) pore diameter track-etched membrane with 50 °C nozzle temperature on 2006-12-23.
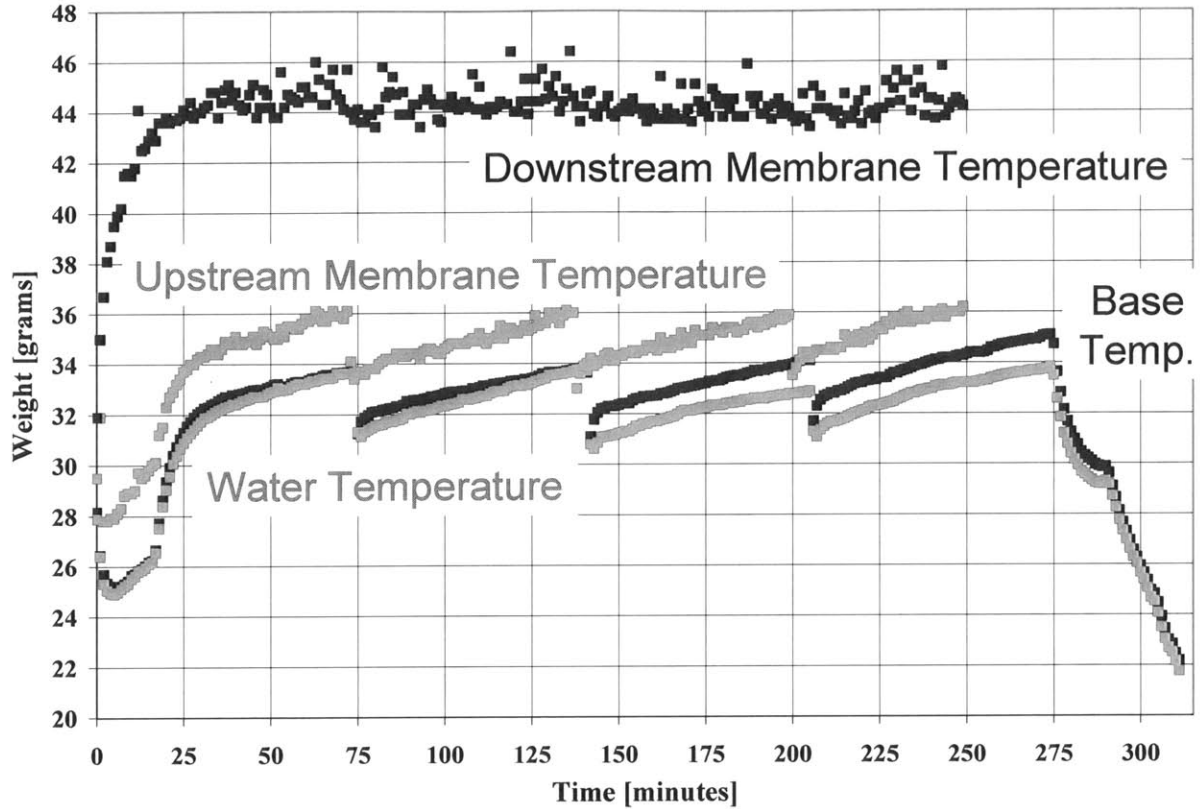
Figure A4.49: Temperature-time history for HAMTA2 running a 400 nm (410 nm measured) pore diameter track-etched membrane with 100 °C nozzle temperature on 2007-02-02.
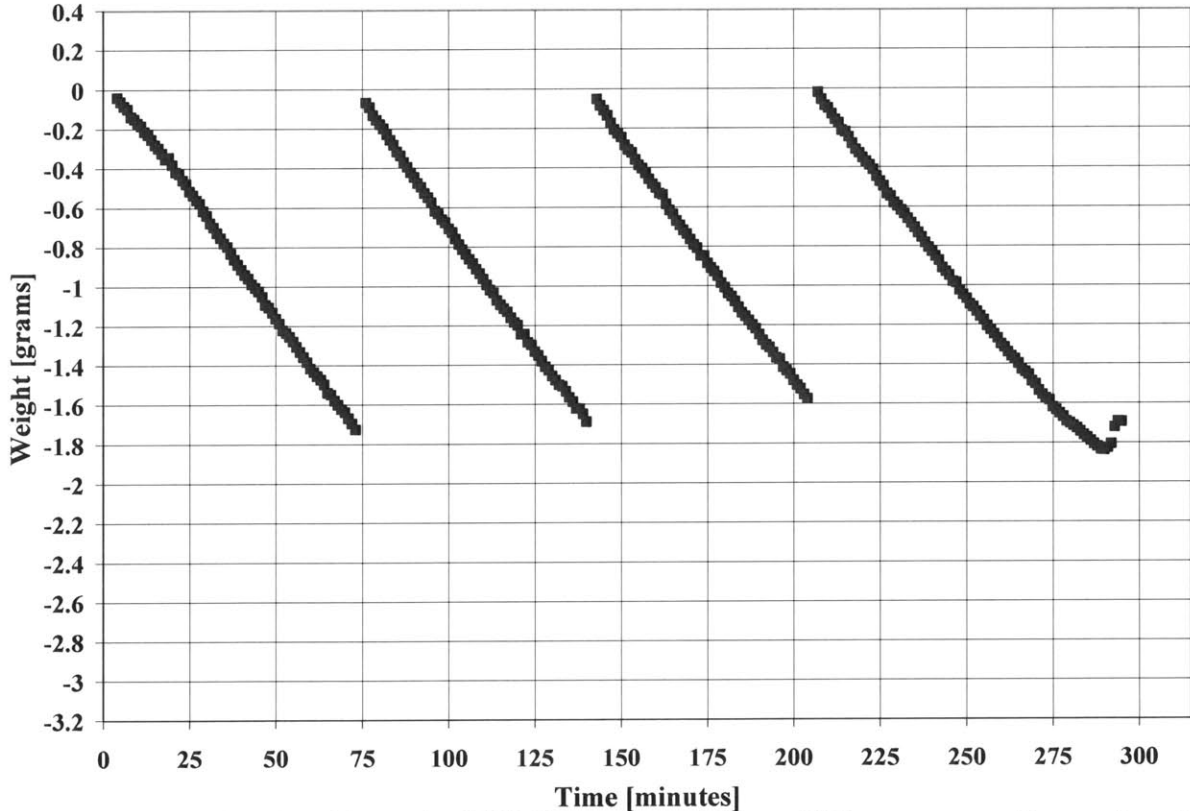

Figure A4.50: Weight-time history for HAMTA2 running a 400 nm (410 nm measured) pore diameter track-etched membrane with 100 °C nozzle temperature on 2007-02-02.
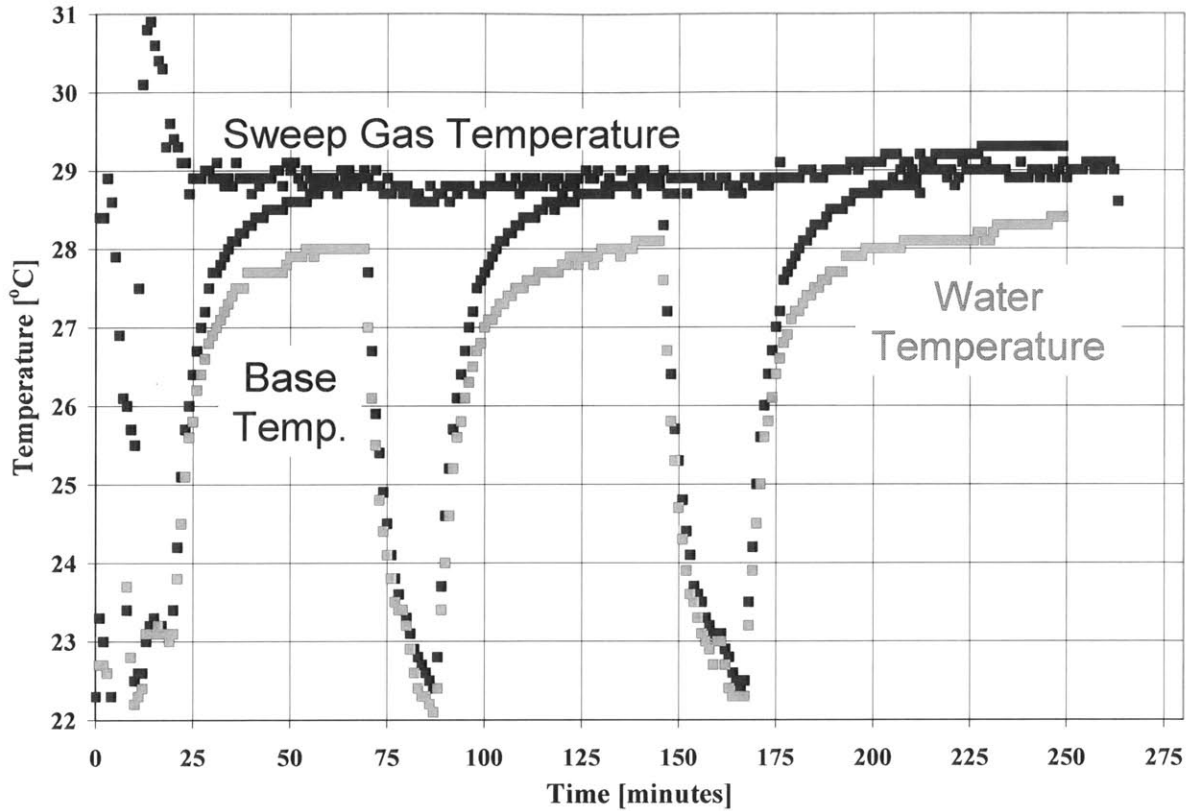
Figure A4.51: Temperature-time history for HAMTA2 running a 400 nm (410 nm measured) pore diameter track-etched membrane with 50 °C nozzle temperature on 2007-02-02.

Figure A4.52: Weight-time history for HAMTA2 running a 400 nm (410 nm measured) pore diameter track-etched membrane with 50 °C nozzle temperature on 2007-02-02.

Figure A4.53: Temperature-time history for HAMTA2 running a 220 nm (150 nm measured) pore diameter track-etched membrane with 100 °C nozzle temperature on 2007-01-23.
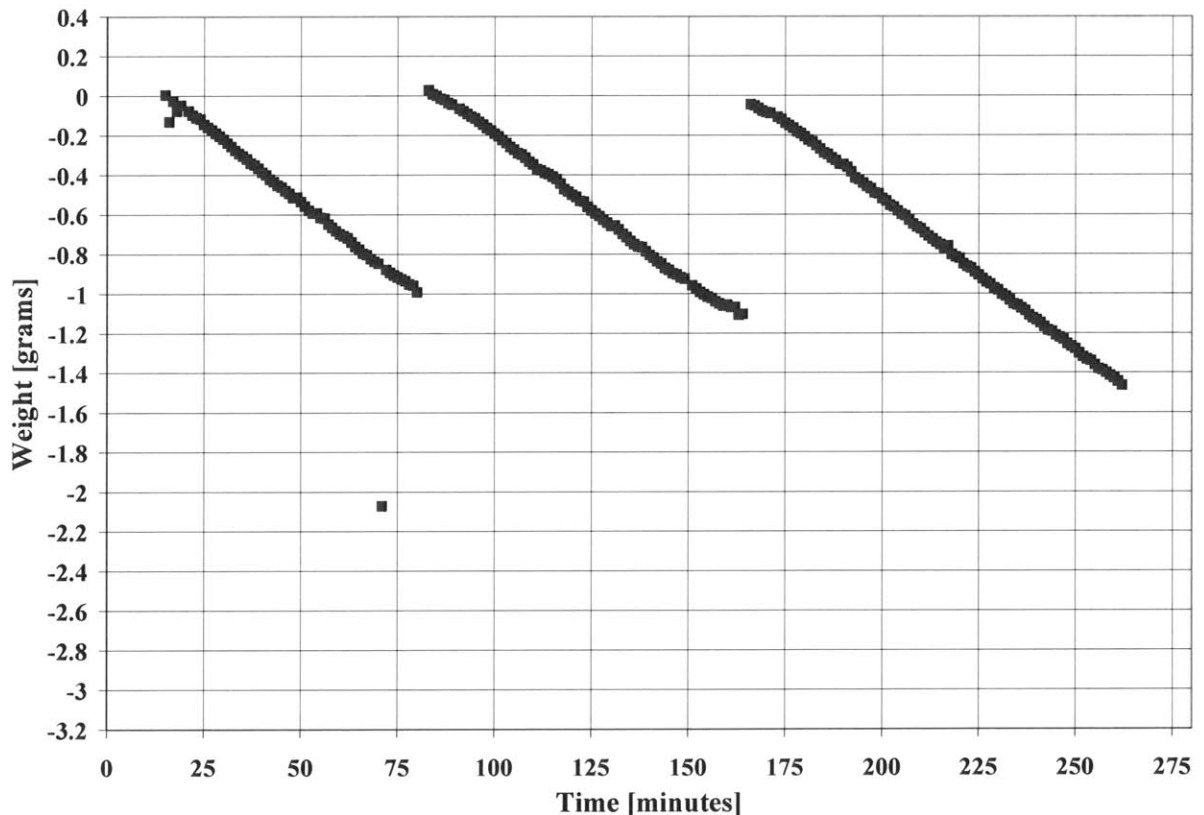

Figure A4.54: Weight-time history for HAMTA2 running a 220 nm (150 nm measured) pore diameter track-etched membrane with 100 °C nozzle temperature on 2007-01-23.

195

Figure A4.55: Temperature-time history for HAMTA2 running a 100 nm (95 nm measured) pore diameter track-etched membrane with 50 °C nozzle temperature on 2006-12-26.

Figure A4.56: Weight-time history for HAMTA2 running a 100 nm (95 nm measured) pore diameter track-etched membrane with 50 °C nozzle temperature on 2006-12-26.
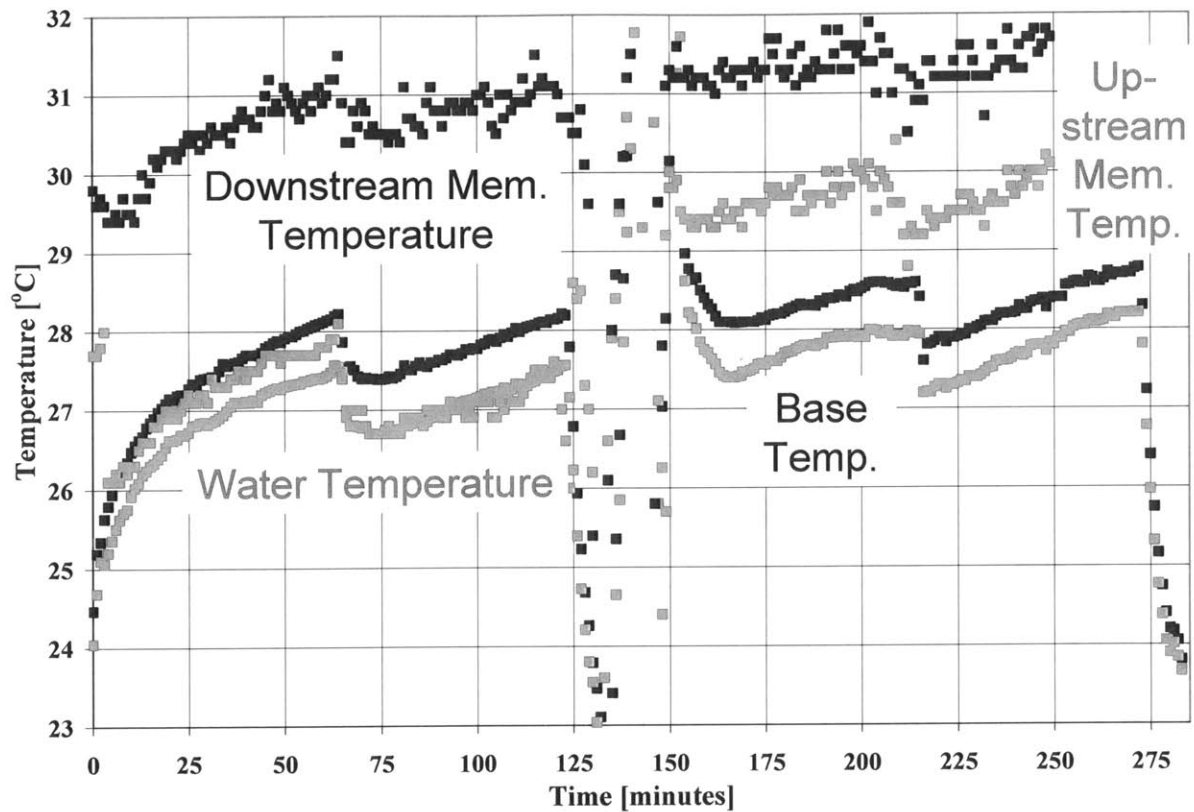
196

Figure A4.57: Temperature-time history for HAMTA2 running a 100 nm (95 nm measured) pore diameter track-etched membrane with 50 °C nozzle temperature on 2007-02-01.
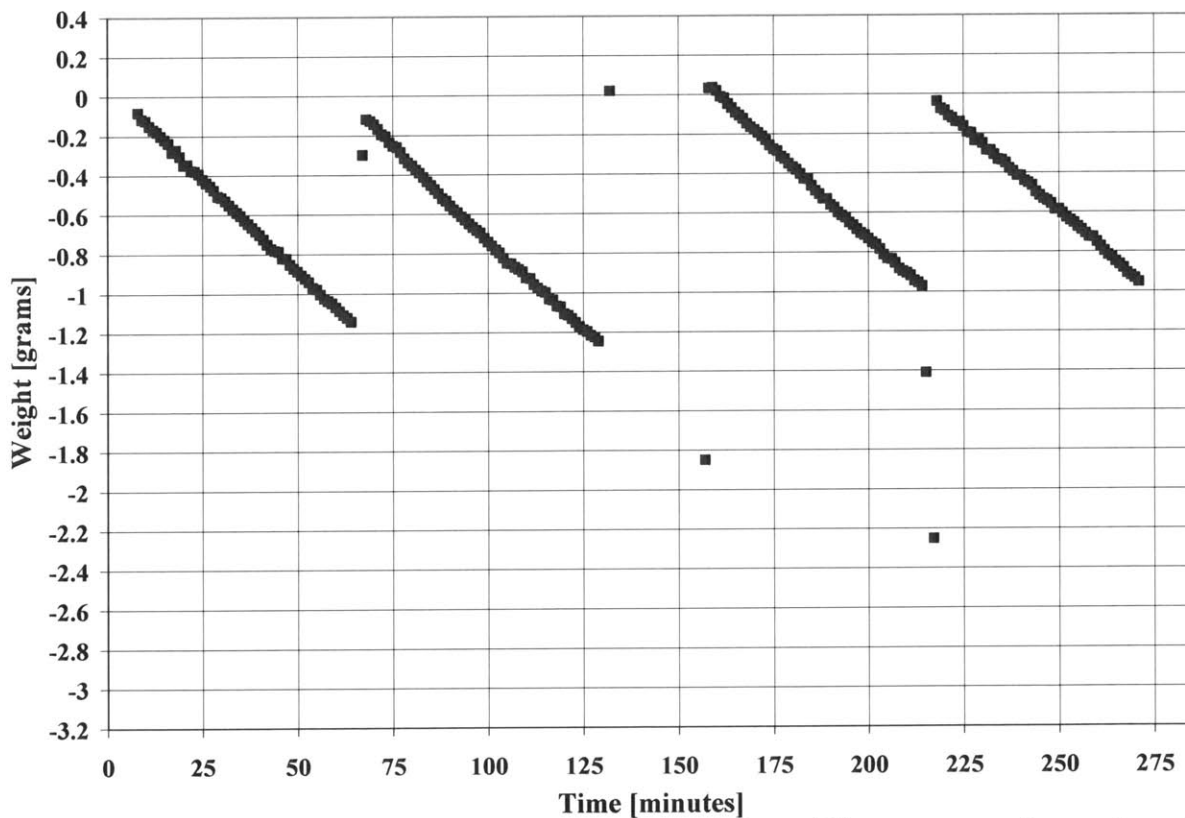

Figure A4.58: Weight-time history for HAMTA2 running a 100 nm (95 nm measured) pore diameter track-etched membrane with 50 °C nozzle temperature on 2007-02-01.
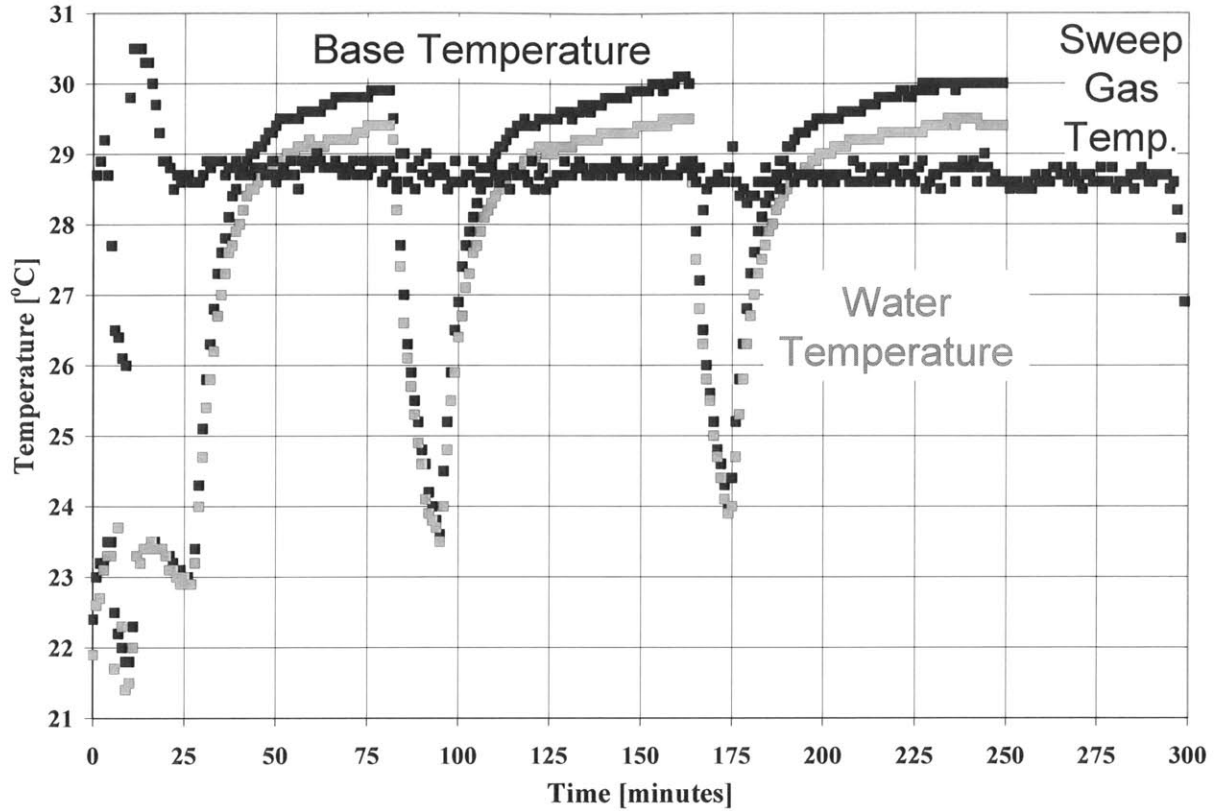
Figure A4.59: Temperature-time history for HAMTA2 running a 50 nm (60 nm measured) pore diameter track-etched membrane with 50 °C nozzle temperature on 2006-12-27.
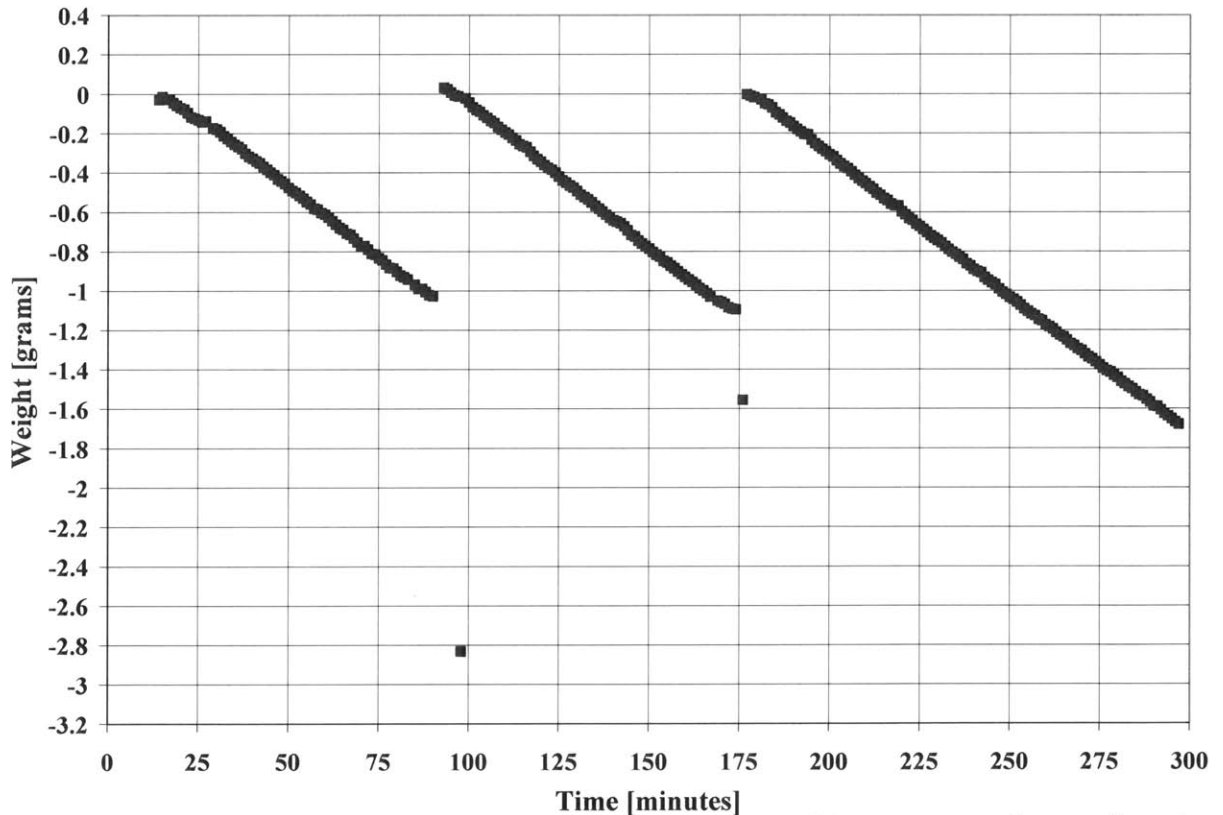

Figure A4.60: Weight-time history for HAMTA2 running a 50 nm (60 nm measured) pore diameter track-etched membrane with 50 °C nozzle temperature on 2006-12-27.

Figure A4.61: Temperature-time history for HAMTA2 running a 50 nm (60 nm measured) pore diameter track-etched membrane with 50 °C nozzle temperature on 2007-01-18.

Figure A4.62: Weight-time history for HAMTA2 running a 50 nm (60 nm measured) pore diameter track-etched membrane with 50 °C nozzle temperature on 2007-01-18.
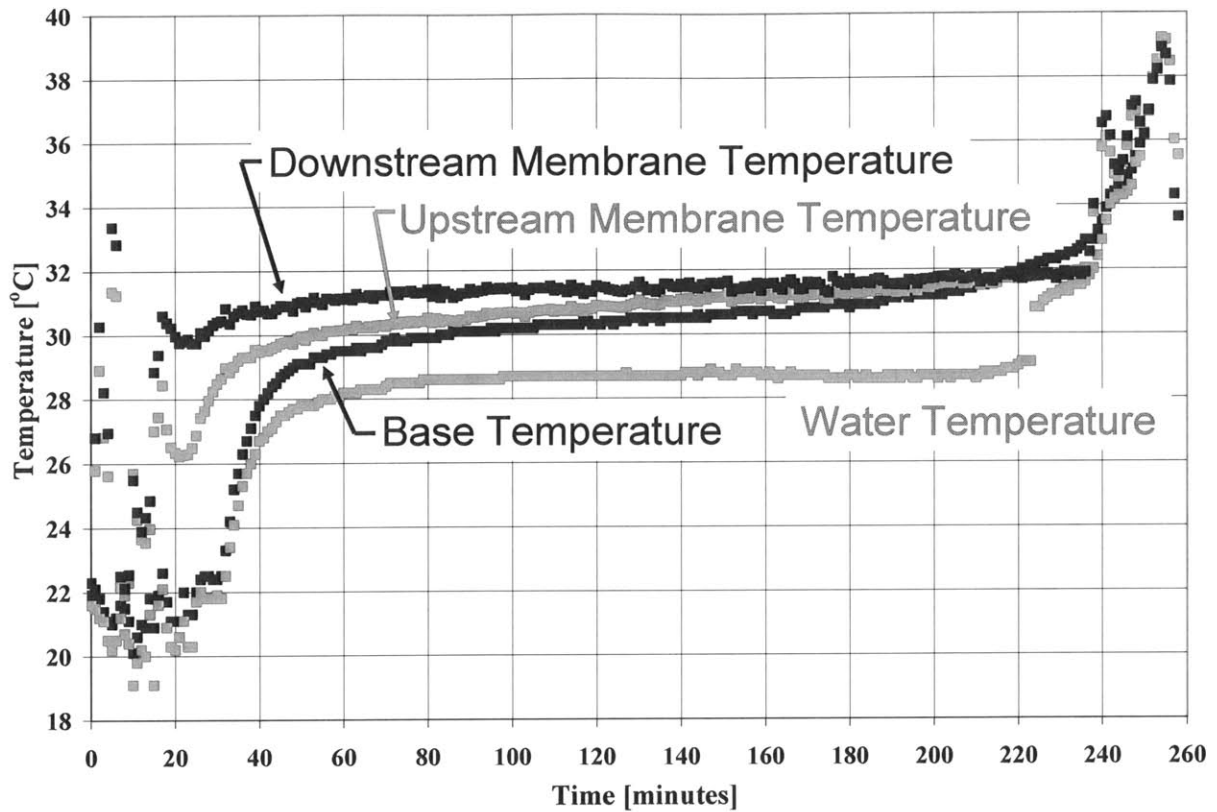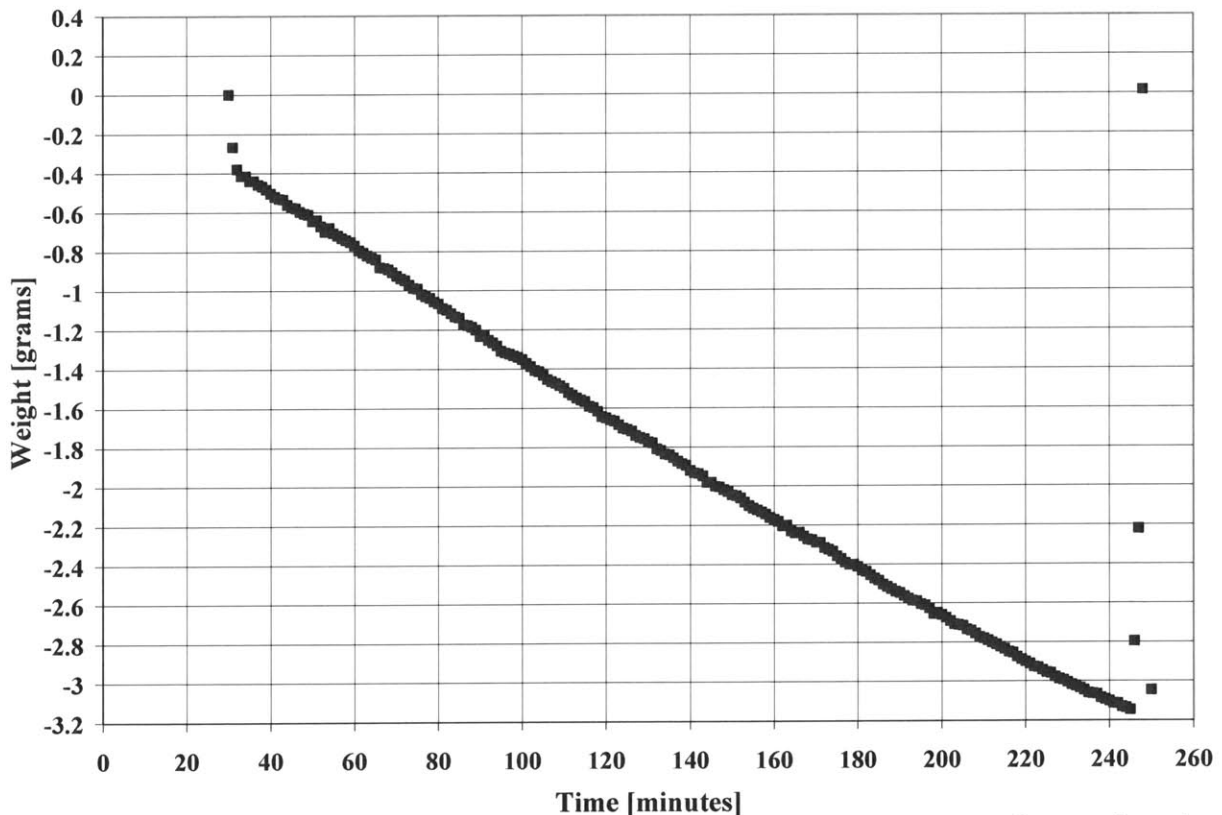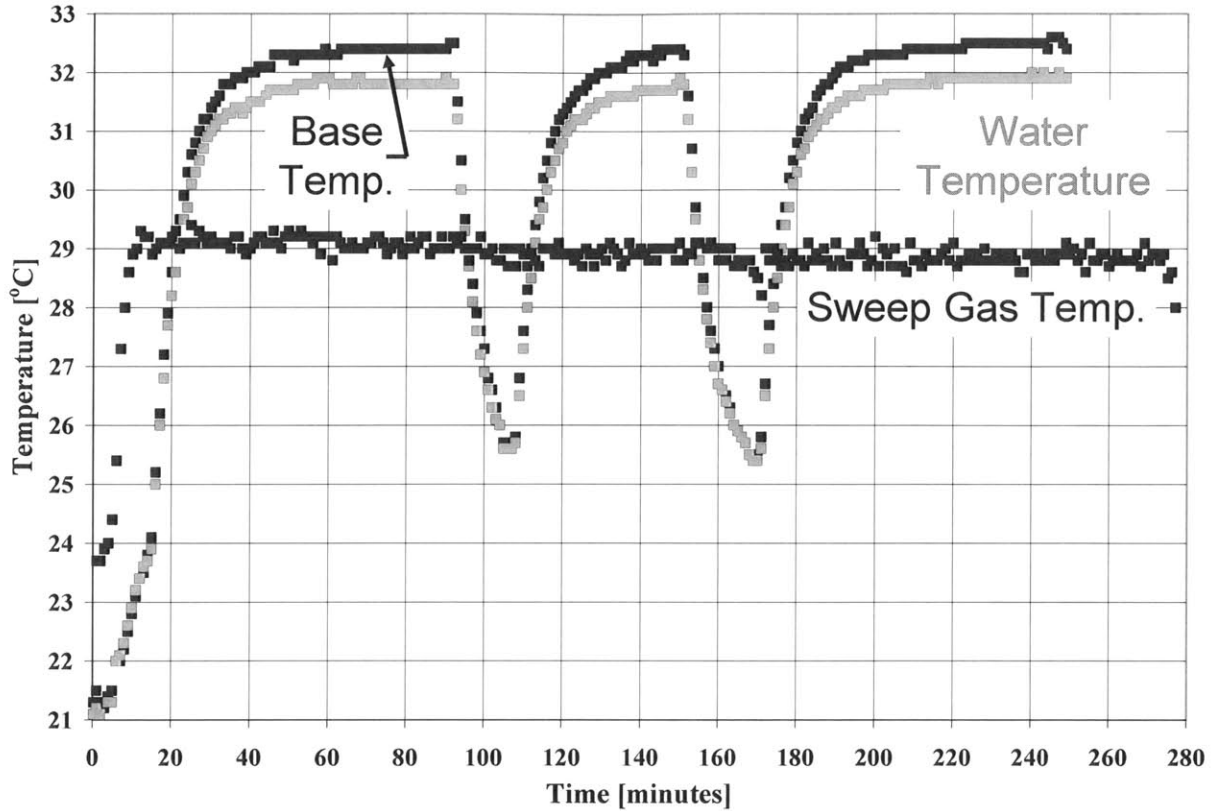
Figure A4.63: Temperature-time history for HAMTA2 running a 10 nm (39 nm measured) pore diameter track-etched membrane with 50 °C nozzle temperature on 2006-12-28.
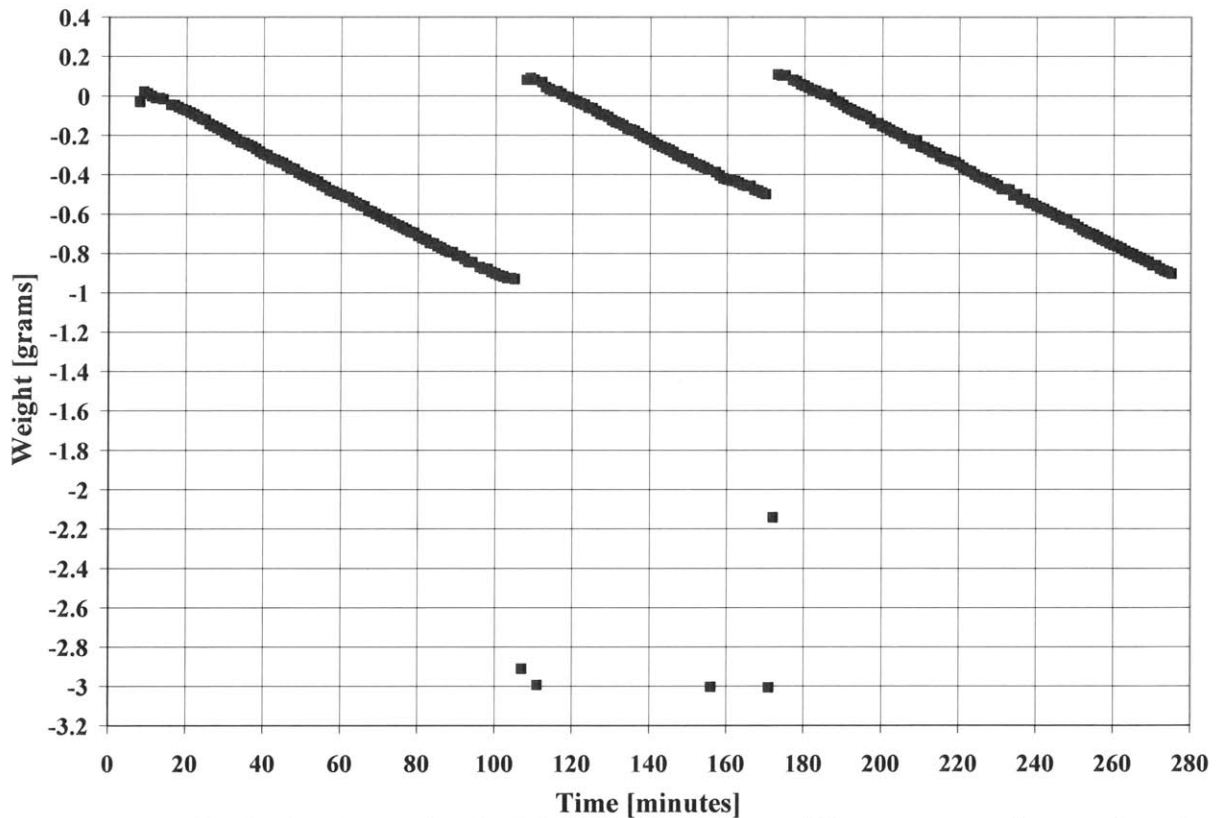

Figure A4.64: Weight-time history for HAMTA2 running a 10 nm (39 nm measured) pore diameter track-etched membrane with 50 °C nozzle temperature on 2006-12-28.

200

Bibliography

ASHRAE (2005) Chapter 8, "Thermal Comfort", ASHRAE Handbook of Fundamentals.

ASTM (1999) "Standard Test Methods for Water Vapor Transmission of Materials: Upright Cup Method", American Society for Testing and Materials Annual Book of ASTM Standards, Part 3.01, ASTM E 96, Procedure B. Conshohocken, PA.

Baker, H.D., Ryder, E.A., and Baker, N.H. (1953) Temperature measurement in engineering, Wiley, New York.

Balachandar, R. and Patel, V.C. (2002) "Rough wall boundary layer on plates in open channels", *Journal of Hydraulic Engineering-ASCE*, **128**(10), 947-951.

Barker, R. (2006) Director of the North Carolina State University Textile Protection and Comfort Center (T-PACC). *Private Communication*, North Carolina State University, Raleigh, NC.

Blasius, H. (1908) "Grenzschichten in Flussigkeiten mit kleiner Reibung", *Z. Math. Phys.*, **56**(1-37.

Bunger, U. and Zittel W. (2001) "Hydrogen storage in carbon nanostructures - still a long road from science to commerce?" *Applied Physics A - Materials Science & Processing*, **72**(2), 147-151.

Calvo, J.I., Bottino, A., Capannelli, G., and Hernandez, A. (2004) "Comparison of liquid-liquid displacement porosimetry and scanning electron microscopy image analysis to characterize ultrafiltration track-etched membranes", *Journal of Membrane Science*, **239**(2), 189-197.

Carl's Electronics (2007a) On-line Catalogue: http://www.electronickits.com/kit/complete/powe/ck403.htm, last accessed 3/19/2007.

Carl's Electronics (2007b) On-line Catalogue: http://www.electronickits.com/kit/complete/elec/ck1600.htm, last accessed 3/19/2007.

Celgard (2007) Celgard Web site: http://www.celgard.com/products/product-information.cfm, last accessed 4/25/2007.

Chen, G. (2005) Nanoscale energy transport and conversion : a parallel treatment of electrons, molecules, phonons, and photons, Oxford University Press, New York.

Choi, T., Jang, J.-H., Ullal, C.K., LeMieux, M.C., Tsukruk, V.V., Thomas, E.L. (2006) "The Elastic Properties and Plastic Behavior of Two-Dimensional Polymer Structures Fabricated by Laser Interference Lithography", *Advanced Functional Materials*, **16**(1324-1330).

Choi, T.Y. (2005) Atomic Force Micrograph of Cellulose Membrane, *Personal Communication*, Massachusetts Institute of Technology, Cambridge, MA.

Dean, Charlie [Colonel, US Army – retired] (2003) *Personal Communication*, Massachusetts Institute of Technology, Cambridge, MA.

Cravalho, E.G. and Smith, J.L. (1981) Engineering thermodynamics, Pitman, Boston, Page 522.

Cussler, E.L. (1997) Diffusion: mass transfer in fluid systems, Cambridge University Press, New York.

Deen, W.M. (1998) Analysis of transport phenomena, Oxford University Press, New York.

DeWALT (2007) DeWALT Company Web Site: http://www.dewalt.com/36v/, last accessed 11/24/2006.

Dushman, S. (1962) Scientific foundations of vacuum technique, Wiley, New York.

Eurotherm (2007) Eurotherm Product Catalogue: http://www.eurotherm.com/products/controllers/2100.htm, last accessed 3/19/2007.

Extech (2007a) Extech Product Catalogue: http://www.extech.com/instrument/products/alpha/EA10_15ThermoCouple.html, last accessed 3/19/2007.

Extech (2007b) Extech Product Catalogue: http://www.extech.com/instrument/products/310_399/380900.html, last accessed 3/19/2007.

Findley, M.E., Tanna, V.V., Rao, Y.B., Yeh, C.L. (1969) "Mass and heat transfer relations in evaporation through porous membranes", *AIChE Journal*, 15(4), 483-489.

Fluke (2007) Fluke Products Catalogue: http://us.fluke.com/usen/products/Fluke+114.htm?catalog_name=FlukeUnitedStates&category=HMA, last accessed 5/4/2007.

Fridge Freeze (2007) Fridge Freeze Web Site: http://www.fridgefreeze.com/recreation/prod-performance.html, last accessed 5/4/2007.

Gary, J.H. and Handwerk, G.E. (1984) Petroleum refining: technology and economics, M. Dekker, New York.

GE (2007) General Electric Osmonics Web site: http://geosmolabstore.com/OsmoLabPage.dll?BuildPage&1&1&1070, last accessed 4/26/2007.

Gennes, P.-G.d., Brochard-Wyart, F., and Quere, V. (2004) Capillarity and wetting phenomena: drops, bubbles, pearls, waves, Springer, New York.

Gibson, P., Schreuder-Gibson, H., and Rivin, D. (2001) "Transport properties of porous membranes based on electrospun nanofibers", *Colloids and Surfaces A - Physicochemical and Engineering Aspects*, **187**, 469-481.

Goodfellow (2007) Goodfellow Corporation Web Site: http://www.goodfellow.com/, last accessed 3/23/2007.

Gorishnyy, T., Ullal, C.K., Maldovan, M., Fytas, G., and Thomas, E.L. (2005) "Hypersonic phononic crystals", *Physical Review Letters*, **94**(11).

Hanot, H., De Coninck, M., and Jones, K. (2002). "Expanding the use of track-etched membranes", *IVD Technology*, http://www.devicelink.com/ivdt/archive/02/11/002.html, last accessed 5/4/2007.

Hernandez, A., Calvo, J.I., Pradanos, P., Palacio, L., Rodriguez, M.L., and de Saja J.A. (1997) "Surface structure of microporous membranes by computerized SEM image analysis applied to Anopore filters", *Journal of Membrane Science*, **137**(1-2), 89-97.

Holt, J.K., Park, H.G., Wang, Y., Stadermann, M., Artyukhin, A.B., Grigoropoulos, C.P., Noy A., and Bakajin, O. (2006) "Fast mass transport through sub-2-nanometer carbon nanotubes", *Science*, **312**(5776), 1034-1037.

Itaya, K., Sugawara, S., Arai, K., and Saito, S. (1984) "Properties of Porous Anodic Aluminum-Oxide Films as Membranes", *Journal of Chemical Engineering of Japan*, **17**(5), 514-520.

Jang, J.-H., Ullal, C.K., Choi, T.Y., LeMieux, M.C., Tsukruk, V.V. and Thomas, E.L. (2006) "3D polymer microframes that exploit length-scale-dependent mechanical behavior", *Advanced Materials*, **18**(16).

Jessensky, O., Muller, F., and Gosele, U. (1998) "Self-organized formation of hexagonal pore arrays in anodic alumina", *Applied Physics Letters*, **72**(10), 1173-1175.

Johnson, D.W., Yavuzturk, C., and Pruis, J. (2003) "Analysis of heat and mass transfer phenomena in hollow fiber membranes used for evaporative cooling", *Journal of Membrane Science*, **227**(1-2), 159-171.

Kapur, V. (2005a) *Personal Communication*, DuPont Company, Wilmington, DE.

Kapur, V. (2005b) *Personal Communication*, Questions about Nucrel® and Hytrel®, DuPont Company, Wilmington, DE.

Kapur, V. (2006) *Personal Communication*, Porosity of DuPont Porous Membranes, DuPont Company, Wilmington, DE.

Kärger, J. and Ruthven, D.M. (1992) Diffusion in zeolites and other microporous solids, Wiley, New York.

Karniadakis, G. and Beskök, A. (2002) Micro flows: fundamentals and simulation, Springer, New York.

Knudsen, M. (1952) The Kinetic Theory of Gases, 3rd Edition, Wiley, New York.

Lewis, J.M. (1995) "The story behind the Bowen ratio", *Bulletin of the American Meteorological Society*, **76**(12), 2433-2443.

Luo, G., Malkova, S., Yoon, J., Schultz, D.G., Lin, B., Meron, M., Benjamin, I., Vanysek, P., and Schlossman, M.L. (2006) "Ion distributions near a liquid-liquid interface", *Science*, **311**(5758), 216-218.

McCullough, E.A., Kwon, M., and Shim, H. (2003) "A comparison of standard methods for measuring water vapour permeability of fabrics", *Measurement Science & Technology*, **14**(8), 1402-1408.

Mettler-Toledo (2007a) Mettler-Toledo Product Catalogue:
http://us.mt.com/mt/products/products-applications_laboratory-weighing_precision_excellence_xp_xp-s/XP5003SDR_Product-Product_1096374878218.jsp, last accessed 3/19/2007.

Mettler-Toledo (2007b) Mettler-Toledo Product Catalogue:
http://us.mt.com/mt/products/SR8001_0x000246700002716c0002ef57.jsp?v=, last accessed 3/19/2007.

Millipore (2007a) Millipore Product Catalogue:
http://www.millipore.com/catalogue.nsf/docs/C254, last accessed 3/19/2007.

Millipore (2007b) Millipore Product Catalogue:
http://www.millipore.com/catalogue.nsf/docs/C153, last accessed 5/4/2007.

Mills, A.F. (1999a) Basic Heat and Mass Transfer, 2nd Edition, Prentice Hall, Upper Saddler River, N.J.

Mills, A.F. (1999b) Basic Heat Transfer, 2nd Edition, Prentice Hall, Upper Saddler River, N.J.

Nellis, G.F., Evans, J., Klein, S.A., Albrecht, S. (February 2003) "Updated Assessment of Microclimate Cooling Options for the Individual Soldier", Technical Report, *U.S. Army Soldier & Biological Chemical Command*.

Nellis, G.F., Klein, S.A., and Evans, J.C. (August. 2003). "Assessment of Technologies for Microclimate Cooling", *Proceedings of the 21st IIR International Congress of Refrigeration*.

Nielsen-Kellerman (2007) Nielsen-Kellerman Web Site: http://www.nkhome.com/ww/4000.html, last accessed 3/19/2007.

NOAA (2007) National Oceanic & Atmospheric Administration Web Site: http://www.noaa.gov/, last accessed 5/4/2007.

Noels, L. (2006). *Personal Communication*, Massachusetts Institute of Technology, Cambridge, MA.

Omega (2006) Omega Engineering Web Site: http://www.omega.com/toc_asp/frameset.html?book=Temperature&file=TC_GEN_SPECS_REF , last accessed 4/26/2006.

Omega (2007a) Omega Engineering Product Catalogue: http://www.omega.com/pptst/HH2000.html, last accessed, 3/19/2007.

Omega (2007b) Omega Engineering Product Catalogue: http://www.omega.com/Temperature/pdf/OB-100_OB-200_OT-200.pdf, last accessed 3/16/2007

Pollard, W.G. and Present, R.D. (1948) "On Gaseous Self-Diffusion in Long Capillary Tubes", *Physical Review Letters*, 73(7), 762-774.

Roy, S., Cooper, S.M., Meyyappan, M. and Cruden, B.A. (2005) "Single component gas transport through 10 nm pores: Experimental data and hydrodynamic prediction", *Journal of Membrane Science*, 253(1-2), 209-215.

Roy, S., Raju, R., Chuang, H.F., Cruden, B.A., and Meyyappan, M. (2003) "Modeling gas flow through microchannels and nanopores", *Journal of Applied Physics*, 93(8), 4870-4879.

Sadasivan, V., Richter, C.P., Menon, L., and Williams, P.F. (2005) "Electrochemical self-assembly of porous alumina templates", *AIChE Journal*, 51(2), 649-655.

Satterfield, C.N. (1991) Heterogeneous catalysis in industrial practice, McGraw-Hill, New York.

Schmidt-Nielsen, K. (1979) Desert Animals - Physiological Problems of Heat and Water, Dover Publications, New York.

Shier, D., Butler, J., Lewis, R. (1996) Hole's human anatomy & physiology, W.C. Brown Publishers, Dubuque, IA.

Sigma Aldrich (2007) Sigma Aldrich Product Catalogue: http://www.sigmaaldrich.com/catalog/search/ProductDetail/SUPELCO/23991, last accessed 3/19/2007.

Smith, R.W. (1994) "Effect of Reynolds Number on the Structure of Turbulent Boundary Layers", *Doctoral Thesis in the Department of Mechanical and Aerospace Engineering*, Princeton University.

SPI (2007) SPI Product Catalogue: http://www.2spi.com/catalog/spec_prep/filter6.shtml, last accessed 5/4/2007.

Sypeck, D.J. and Wadley, H.N.G. (2001) "Multifunctional microtruss laminates: Textile synthesis and properties", *Journal of Materials Research*, **16**(3), 890-897.

Thomas, E. L. (2005), *Personal Communication*, Massachusetts Institute of Technology.

Toader, O., T. Y. M. Chan and S. John (2004) "Photonic band gap architectures for holographic lithography", *Physical Review Letters*, 92(4),

Tomlins, P.E., Grant, P., Vadgama, P., James, S., and Mikhalovsky, S. (2004). "Structural Characteristics of Polymer Based Tissue Scaffolds" *UK Department of Trade and Industry*, Project MPP4.2 T1D4, DEPC-MN-02.

Tristan Technologies (2006) Tristan Technologies Web Site: http://www.tristantech.com/prod_geomagnetic.html, last accessed 11/29/2006.

Tritton, D.J. (1977) Physical fluid dynamics, Van Nostrand Reinhold Co., New York.

Turner, J.S. (1973) Buoyancy effects in fluids, University Press, Cambridge, UK.

Ullal, C.K., Maldovan, M., Thomas, E.L., Chen, G., Han, Y,J., and Yang, S. (2004) "Photonic crystals through holographic lithography: Simple cubic, diamond-like, and gyroid-like structures", *Applied Physics Letters*, **84**(26), 5434-5436.

VWR (2007) VWR Product Catalogue: http://www.vwrsp.com/catalog/product/index.cgi?catalog_number=46610-028, last accessed 4/27/2007.

Whatman (2007) Whatman Product Catalogue: http://www.whatman.com/products/?pageID=7.25.5, last accessed 3/22/2007

Wilson, E. (1915) "A basis for rational design of heat transfer apparatus", *Transactions of the American Society of Mechanical. Engineers*, **37**, 47-82.

Yu, B.M. and Li, H.M. (2004) "A geometry model for tortuosity of flow path in porous media", *Chinese Physics Letters*, **21**(8), 1569-1571.

Yu, J. (January 2007) *Personal Communication*, Massachusetts Institute of Technology, Cambridge, MA.

Permissions to Reuse Copyrighted Material

**AMERICAN INSTITUTE OF PHYSICS LICENSE
TERMS AND CONDITIONS**

May 11, 2007

This is a License Agreement between Matthew J Traum ("You") and American Institute of Physics ("American Institute of Physics"). The license consists of your order details, the terms and conditions provided by American Institute of Physics, and the payment terms and conditions.

License Number	1706221229570
License date	May 11, 2007
Licensed content publisher	American Institute of Physics
Licensed content title	Self-organized formation of hexagonal pore arrays in anodic alumina
Licensed content author	O. Jessensky
Type of Use	Republish Portions
Requestor Type	Third Party
Include other media	Yes
Number of portions	1
Title of your work	Latent Heat Fluxes Through Nano-engineered Porous Materials
Publisher of your work	Ph.D. Thesis at the Massachusetts Institute of Technology
Publication date of your work	06/01/2007
PO Number	Pending
Total	$0.00

Terms and Conditions

American Institute of Physics -- Terms and Conditions: Permissions Uses

American Institute of Physics ("AIP") hereby grants to you the non-exclusive right and license to use and/or distribute the Material according to the use specified in your order, on a one-time basis, for the specified term, with a maximum distribution equal to the number that you have ordered. Any links or other content accompanying the Material are not the subject of this license.

1. You agree to include the following copyright and permission notice with the reproduction of the Material: "Reprinted with permission from [FULL CITATION]. Copyright [PUBLICATION YEAR], American Institute of Physics." For an article, the copyright and permission notice must be printed on the first page of the article or book chapter. For photographs, covers, or tables, the copyright and permission notice may appear with the Material, in a footnote, or in the reference list.
2. If you have licensed reuse of a figure, photograph, cover, or table, it is your responsibility to ensure that the material is original to AIP and does not contain the copyright of another entity, and that the copyright notice of the figure, photograph, cover, or table does not indicate that it was reprinted by AIP, with permission, from another source. Under no circumstances does AIP, purport or intend to grant permission to reuse material to which it does not hold copyright.
3. You may not alter or modify the Material in any manner. You may translate the

Material into another language only if you have licensed translation rights. You may not use the Material for promotional purposes. AIP reserves all rights not specifically granted herein.

4. The foregoing license shall not take effect unless and until AIP or its agent, Copyright Clearance Center, receives the Payment in accordance with Copyright Clearance Center Billing and Payment Terms and Conditions, which are incorporated herein by reference.

5. AIP or the Copyright Clearance Center may, within two business days of granting this license, revoke the license for any reason whatsoever, with a full refund payable to you. Should you violate the terms of this license at any time, AIP, American Institute of Physics, or Copyright Clearance Center may revoke the license with no refund to you. Notice of such revocation will be made using the contact information provided by you. Failure to receive such notice will not nullify the revocation.

6. AIP makes no representations or warranties with respect to the Material. You agree to indemnify and hold harmless AIP, American Institute of Physics, and their officers, directors, employees or agents from and against any and all claims arising out of your use of the Material other than as specifically authorized herein.

7. The permission granted herein is personal to you and is not transferable or assignable without the prior written permission of AIP. This license may not be amended except in a writing signed by the party to be charged.

8. If purchase orders, acknowledgments or check endorsements are issued on any forms containing terms and conditions which are inconsistent with these provisions, such inconsistent terms and conditions shall be of no force and effect. This document, including the CCC Billing and Payment Terms and Conditions, shall be the entire agreement between the parties relating to the subject matter hereof.

This Agreement shall be governed by and construed in accordance with the laws of the State of New York. Both parties hereby submit to the jurisdiction of the courts of New York County for purposes of resolving any disputes that may arise hereunder.

Matthew J. Traum
Doctoral Candidate in Mechanical Engineering
Institute for Soldier Nanotechnologies at MIT
77 Massachusetts Avenue
NE47-587
Cambridge, MA 02319

May 11, 2007

Re: Request for Permission to Reprint Guarded Sweating Hotplate Image

Dear Mr. O'Niell:

I am preparing my Doctoral thesis at Massachusetts Institute of Technology ("M.I.T") and wish to reprint the Guarded Sweating Hotplate image from your product manual in my dissertation. M.I.T., as the copyright holder to my thesis, will publish it in its library and make it available upon request.

Therefore, I respectfully request that Measurement Technology Northwest grant to me a non-exclusive, world-wide, royalty-free license to copy, edit, display and distribute, in either electronic or hardcopy format, for personal and academic purposes, the Guarded Sweating Hotplate image from the following on-line document:

http://www.mtnw-usa.com/pdf/Sweating_Hotplate.pdf

The image will be reprinted as a Figure in the following work: Traum, Matthew, "Latent Heat Fluxes Through Nano-engineered Porous Materials" (Ph.D. thesis, M.I.T. Department of Mechanical Engineering, 2007). I understand that any right to copy and/or distribute the image other than for academic purposes shall require further permission of Measurement Technology Northwest.

If this is acceptable, please acknowledge Measurement Technology Northwest's permission by signing below and returning to my attention at FAX number (617) 253-5859. Thank you and if you have any questions, please call me immediately at (617) 233-9735
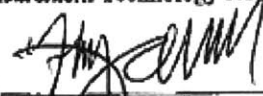
Sincerely yours,

Matthew J. Traum

PERMISSION GRANTED:

Measurement Technology Northwest

By: _____

Title: _____ President

Date: _____ May 14 2007

209

Matthew J. Traum
Doctoral Candidate in Mechanical Engineering
Institute for Soldier Nanotechnologies at MIT
77 Massachusetts Avenue
NE47-587
Cambridge, MA 02319

May 16, 2007

Re: Request for Permission to Reprint Celgard® 2400 Micrograph Image

Dear Barbara:

I am preparing my Doctoral thesis at Massachusetts Institute of Technology ("M.I.T") and wish to reprint the Celgard® 2400 micrograph image from your product manual in my dissertation. M.I.T., as the copyright holder to my thesis, will publish it in its library and make it available upon request.

Therefore, I respectfully request that Celgard, Inc. grant to me a non-exclusive, world-wide, royalty-free license to copy, edit, display and distribute, in either electronic or hardcopy format, for personal and academic purposes, the Celgard® 2400 micrograph image from the following on-line document:

http://www.celgard.com/documents/2400%20Rev1104.pdf

The image will be reprinted as a figure in the following work: Traum, Matthew, "Latent Heat Fluxes Through Nano-engineered Porous Materials" (Ph.D. thesis, M.I.T. Department of Mechanical Engineering, 2007). I understand that any right to copy and/or distribute the image other than for academic purposes shall require further permission of Celgard, Inc.

If this is acceptable, please acknowledge Celgard's permission by signing below and returning to my attention at FAX number (617) 253-5859. Thank you and if you have any questions, please call me immediately at (617) 233-9735
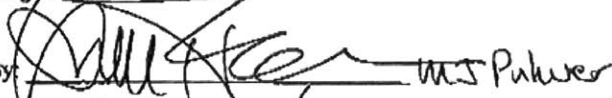
Sincerely yours,

Matthew J. Traum

PERMISSION GRANTED:

Celgard, Inc.

By _____ M J Pulver

Title: _Vice President / General Manager_

Date: _17 May 07_